UNIVERSITY OF Southampton

University of Southampton Research Repository
ePrints Soton

Copyright © and Moral Rights for this thesis are retained by the author and/or other copyright owners. A copy can be downloaded for personal non-commercial research or study, without prior permission or charge. This thesis cannot be reproduced or quoted extensively from without first obtaining permission in writing from the copyright holder/s. The content must not be changed in any way or sold commercially in any format or medium without the formal permission of the copyright holders.

When referring to this work, full bibliographic details including the author, title, awarding institution and date of the thesis must be given e.g.

AUTHOR (year of submission) "Full thesis title", University of Southampton, name of the University School or Department, PhD Thesis, pagination

http://eprints.soton.ac.uk

UNIVERSITY OF SOUTHAMPTON

FACULTY OF NATURAL AND ENVIROMENTAL SCIENCES

School of Chemistry

Bi-functional oxygen catalysts for metal-air flow-batteries

by

Stephen Jeffrey Thompson

Thesis for the degree of Doctor of Philosophy

August 2015

University of Southampton

ABSTRACT

FACULTY OF NATURAL AND ENVIRONMENTAL SCIENCES

Chemistry

Thesis for the degree of Doctor of Philosophy

Bi-functional oxygen catalysts for metal-air flow-batteries

Stephen Jeffry Thompson

The rise in wind, solar and tidal renewable power generation presents a new challenge for the future stability of electrical networks on the national and international scale. The modal nature of renewable power and its incompatibility with consumer demand necessitates a means for large-scale energy storage with high efficiency and relatively low cost. Zinc-air flow batteries represent one possible solution to this problem. The energy is stored in the metallic zinc, and reversed with the oxidation to form zincate releasing the energy on demand. The majority of energy losses in the zinc-air battery are for the O_2 evolution and reduction reactions on the air electrode. A stable, durable and low-cost bi-functional air electrode would allow the introduction of zinc-air flow batteries to support the power grids of the future.

The work in this thesis will investigate the activity of $NiCo_2O_4$ electrocatalysts prepared by various methods, for their use as bi-functional electrocatalysts in the air-electrode. The electrocatalyst prepared on to a gas diffusion electrode, to determine activity in lab-scale half-cells. Improvements to catalyst activity are then considered through the addition of metal nanoparticles to the surface of $NiCo_2O_4$, with in-situ X-ray absorbance measurements to determine the oxidation states of ruthenium during the O_2 evolution reaction. The activity of $NiCo_2O_4$ was compared to alternative perovskite mixed metal oxide electrocatalysts.

Table of Contents

List of Tables

List of Figures

DECLARATION OF AUTHORSHIP

I, Stephen Jeffrey Thompson

declare that this thesis and the work presented in it are my own and has been generated by me as the result of my own original research.

Bi-functional oxygen catalysts for metal-air flow-batteries

The rapid growth in renewable power generation will require a new level of energy grid storage. Renewable power is in strong demand, The modal energy output from renewable sources requires novel methods for storing large quantities of power with high efficiency and relatively low cost.

I confirm that:

1. This work was done wholly or mainly while in candidature for a research degree at this University;
2. Where any part of this thesis has previously been submitted for a degree or any other qualification at this University or any other institution, this has been clearly stated;
3. Where I have consulted the published work of others, this is always clearly attributed;
4. Where I have quoted from the work of others, the source is always given. With the exception of such quotations, this thesis is entirely my own work;
5. I have acknowledged all main sources of help;
6. Where the thesis is based on work done by myself jointly with others, I have made clear exactly what was done by others and what I have contributed myself;
7. Parts of this work have been published as:

   a. Price, S. W. T.; Thompson, S. J.; Li, X.; Gorman, S. F.; Pletcher, D.; Russell, A. E.; Walsh, F. C.; Wills, R. G. A. *Journal of Power Sources*. 2014, pp 43–49.
   b. Li, X.; Pletcher, D.; Russell, A. E.; Walsh, F. C.; Wills, R. G. A.; Gorman, S. F.; Price, S. W. T.; Thompson, S. J. *Electrochemistry Communications*. 2013, pp 228–230.

Signed: .....

Date:.....

Acknowledgements

First of all I would like to thank my supervisor Professor Andrea E. Russell, for giving me the opportunity to study for this PhD, and her support, advice and motivation for the last four years. I would also like to acknowledge Derek Pletcher, Frank C. Walsh and Richard Wills for their valuable knowledge and discussions. Further, I would like to thank Stephen Price for the rapid introduction to electrochemistry and all the support he provided to me, and for Xiahong Li and Scott Gorman for teaching me of all the challenges of scaling up electrodes into large prototypes.

A big thanks to all the support staff at the uni*vs.*erity who keep the magic happening behind the scenes; Karl, Alistair, Sally, Anne,; Alan, Rob and Konstant of the mechanical workshop; and Lee, Pzemslaw and Paul in the glass blowing workshop. Also, to the electrochemistry department for their wide array of discussions keeping us motivated through all the trials of a PhD.

I would like to thank the members of our research group past and present, for all their advice and friendship. Pete Richardson and Laura Calvillo for bringing me along to Diamond and Alba to assist in XAS measurements and Stephen Price again, for teaching me how to make sense of the data. Waldemir Paschoalino including me on his in-situ XRD work. To David, Danai and Turgut who have jumped in whole heartedly and helped whenever I needed you.

To my family for all their love and support in everything I have done, and finally to Vicky who has helped me through the ups and downs of a PhD. Thank you.

Chapter 1: Introduction

1.1 Energy storage

The shift from fossil fuel to renewable sources for energy production is of intense interest to provide secure and environmentally friendly sources of energy into the future. The integration of renewable sources of power generation requires additional energy storage due to the modal nature of its energy production. Energy storage is the mediator between the variable energy sources and energy loads. The storage of energy is the ability to dissociate the generation and consumption of power through time, allowing appropriate management of its future use and availability.

The storage of energy via electrochemical processes has been a fundamental key development for all modern electronics. It was not until 1800 when Allesandro Volta reported the electric pile that the first battery was invented. In this discovery a stack of dis-similar metals, zinc and copper discs, separated by brine soaked cloths were used to provide electrical current upon completion of the circuit.[1]

New mass produced commercial batteries were used to provide power for the telegraph network. Early electrical networks used lead-acid batteries to provide additional power during peak times. The batteries were also able to store excess energy generated during periods of low demand. The development of pumped storage, capable of storing megawatts of power, offered lower costs and increased capabilities in comparison with electrochemical energy storage technologies.

Research into energy storage for stationary applications was a rapidly expanding field from the late 1960s, where political, social and economic factors were coalescing to require a new form of energy stability.[2,3] A number of alternative energy technologies (Table 1) are currently being developed for energy grids of the future. Electrochemical technologies are of interest due to a number of factors, including capital installation costs, grid reliability, flexible location, scalable capacity and energy efficiency. A solution to the power requirements could be provided in the form of capacitors and batteries to provide electrical energy from seconds to hours, with near instant response with high energy efficiency.

Table 1: Worldwide operational grid energy storage capacity, by technology and rated capacity.[4]

Type of storage	Installations worldwide	Rated power / 10^3 kW Hr	Duration / Hrs
Mechanical - Compressed-air	4	0.05 – 160	1 – 250
Electrochemical - Capacitor	19	0.6 – 24	0.17 – 1
Electrochemical - Flow-battery	31	0.001 – 2.5	1 – 20
Electrochemical – Lead acid battery	49	0.0007 – 54	0.017 -15
Electrochemical - Lithium-ion battery	218	0.001 – 128	0.05– 15
Mechanical - Flywheel	6	0.01 - 5	0.006 – 0.25
Electrochemical – Hydrogen	6	0.4 - 2	1 – 27
Mechanical – pumped hydro	292	0.001 – 1,000	2 – 14,000

The range and frequency of technologies currently undergoing development and installation around the world highlights the desire and growth of the energy storage market. A system free from geographical location limitations and the risks of mechanical potential energy is desirable for its flexibility and relative low risk to the nearby environment. The environmentally benign and flexibility of an electrochemical energy storage solution is therefore desirable and dominates the solutions being developed to date.

The available electrochemical solutions typically are based upon early battery solutions from lead-acid to lithium ion batteries. However the lead-acid provides relatively low energy density and lithium-ion batteries incur increased capital costs and limited cycle-life when considering stationary power applications. This has focused some recent efforts on redox flow batteries, which operate on reversible electrochemical reactions.

1.2 Redox-flow batteries

Redox flow-batteries are an area of growth for energy storage with one of the main advantages being the effective decoupling of the energy density and power of the battery. The vanadium flow-battery, to name but one example, operates by separating four oxidation states of vanadium into two compartments separated by a membrane; the reaction between the oxidation states

allows either storage of energy in higher oxidation states or release of electrical energy through the reverse reaction to lower oxidation states. A number of other redox couples are possible (Table 2), each providing a different cell voltage or containment requirements for the final battery installation.

Table 2: Various redox-flow batteries redox couples and their corresponding theoretical potential.[5]

Type	Redox couple	Voltage
All Vanadium	V^{2+}/V^{3+} - VO^{2+}/VO_2^{+}	1.2
Vanadium/bromine	$ClBr_2^{+}/Cl^{-}$+$2Br_2^{-}$ - $2VCl_2$+$2Cl^{-}$ /$2VCl_3$	1.1
Iron/chromium	Fe3+/Fe2+ - Cr	1.2
Fe-EDTA/Bromine	2Fe(III)-EDTA/2Fe(II)-EDTA – $2Br^{-}/Br_2$	1.0
Zinc-cerium	$2Ce^{4+}/2Ce^{3+}$ - Zn^0/Zn^{2+}	2.6
Bromine/polysulfide	$Br_3^{-}/3Br^{-}$ - $2S_2^{2-}/S_4^{2-}$	1.5

The capacity of the battery is scalable by installation of larger electrolyte tanks and power is determined by the size of the electrodes. The charge/discharge process is efficient, but suffers from crossover of vanadium species through the membrane, resulting in a net loss of electrical efficiency. Current densities are often low, operating at 10 – 50 mA cm^{-2}. The quantity and toxicity of the vanadium compounds in the electrolyte requires careful controls to avoid damage to the environment and health of workers. In addition, initial capital costs are relatively high due not only to the electrochemical cells, but most significantly the cost of vanadium required to fill the two electrolyte reservoirs.[6]

Metal-air batteries have become areas of interest in recent years with a number of reviews published.[5-12] These technologies are desirable due to greater energy densities, reduced capital costs, and utilisation of more environmentally benign chemicals. The electrolytes used are typically alkaline or ionic liquids (in the case of alkali metals). Although high theoretical energy densities are possible, the addition of the electrode structures and ancillary components reduces these in demonstration and prototype systems. It does, however, still provide a degree of comparison between the available technologies. For stationary energy storage solutions, the capital cost of installation, energy capacity and efficiency and cycle life are the key metrics.

Table 3: Comparison of metal-air batteries currently in development.

Type	Electrically rechargeable?	Voltage /V	Gravimetric capacity /mAh g^{-1}	Gravimetric energy density /Wh kg^{-1}
Li-air	Y	2.91	3842[13]	11429
Na-air	Y	3.11	1165	2644
Mg-air	Y	3.10	2205	6836
Al-air	N	2.70	2965[13]	8046
Si-Air	N	2.19	3817	8359
Fe-air	Y	1.19	960	1142
Zinc-air	Y	1.65	820	1353

*** Faraday constant = 26.801 Ah mol^{-1}; Theoretical gravimetric capacity = Faraday constant × atomic weight × number of valence electrons; Gravimetric energy density = theoretical cell voltage × theoretical gravimetric capacity; All based on a metal-anode only.[11,12,14]**

Although a number of technologies are available, the need for electrical recharging and large energy capacity limits the suitability of redox species further. Iron-air and zinc-air both provide electrical recharging and large energy capacity suitable for use in redox-flow batteries. Both standard electrode potentials for the reduction of zinc ($Zn^{2+}_{(aq)} \rightarrow Zn_{(s)}$ -0.76 V) and iron ($Fe^{2+}_{(aq)} \rightarrow Fe_{(s)}$ -0.41 V) are positive of hydrogen formation ($H_2O_{(l)} \rightarrow H_{2(g)} + 2OH^-{}_{(aq)}$ -0.83 V) in alkaline solution.

1.2.1 The zinc-air flow battery

The zinc-air flow battery operates by the reactions described in Equation 1 for the zinc-electrode and Equation 2 for the air-electrode. The zinc-electrode varies between electrodeposition of zinc during the charging of the battery and zinc stripping during the discharge. The air-electrode undergoes oxygen evolution during the charging of the battery and oxygen reduction for the discharge.

Equation 1

$$\boldsymbol{Zn(OH)_4^{2-} + 2e^- \rightleftharpoons Zn + 4HO^-}$$

Equation 2

$$\boldsymbol{O_2 + 2H_2O + 4e^- \rightleftharpoons 4HO^-}$$

The standard electrode potential, E^0, for zinc-electrode in Equation 1 is -1.25 V, and the reaction at the air-electrode in Equation 2 occurs at a standard electrode potential of 0.4 V, resulting in an overall voltage of 1.65 V for the zinc-air cell. However, due to the slow electron kinetics of the oxygen evolution and reduction reactions, a large overpotential is observed for the air-electrode (Figure 1).

The above equation utilises the 4-electron reduction of oxygen to hydroxide. It is possible for this to occur either as a direct 4-electron reaction or via a two-step 2-electron reduction of oxygen. The later occurs via the 2-electron reduction of oxygen to hydrogen peroxide. This reaction is undesirable as the hydrogen peroxide intermediate product is able to desorb back into the electrolyte, if not rapidly reacted in the second of the 2-electron steps. In the presence of a flowing electrolyte it is likely that the formation of hydrogen peroxide would be lost to the electrolyte reservoir, where it can be catalytically decomposed by transition metals. This loss of hydrogen peroxide would reduce the Faradaic efficiency of the cell, as the hydrogen peroxide present in solution may go onto react with the zinc metal deposit and result in self-discharge of the cell.

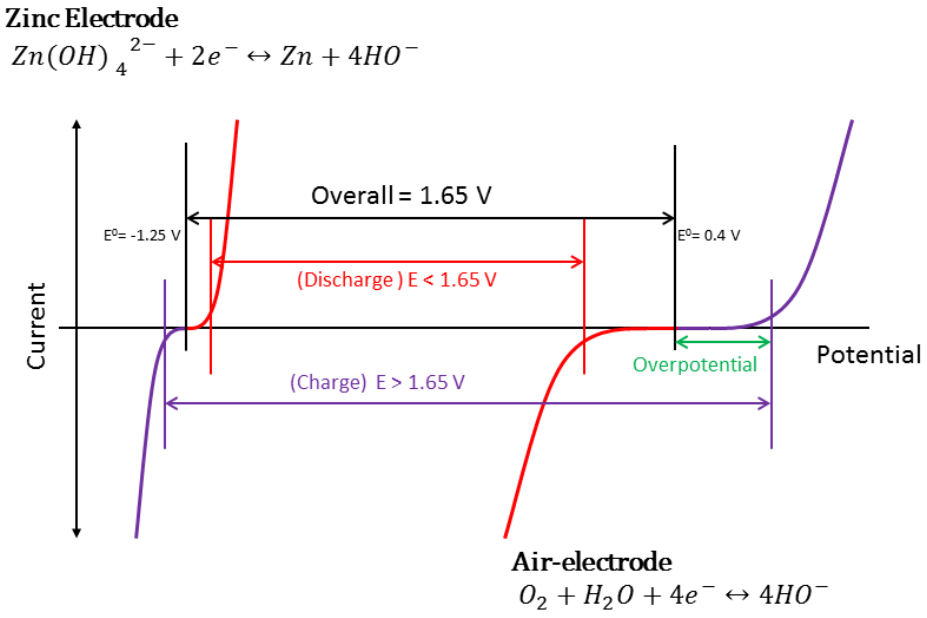

Figure 1: Schematic for the oxygen and zinc electrodes in the zinc-air battery.

The zinc-air flow battery is desirable because it avoids the need for storing two tanks of electrolyte, by using oxygen from the atmosphere for the second redox species. This results in a significant reduction in capital costs, allows the use of environmentally benign chemicals such as zinc and increases the energy density of the system relative to other redox flow batteries.

Further gains are achieved through the nature of the flowing electrolyte in comparison to other static metal-air batteries, whereby each cell is supplied with a continuous flow of soluble zinc

partially decoupling the energy density from a fixed volume of electrolyte in the cell. In a typical static electrolyte battery the solubility of zinc in the electrolyte as $Zn(OH)_4$ provides a practical limit for the maximum volumetric energy density achievable in such a system, unless it was stored as metal for a discharge only system.

During the charging process the zinc is electrodeposited typically onto a carbon or zinc plate current collector. This deposit, in a flowing electrolyte, avoids the previous limitation of relatively low solubility of zinc in alkali (~1 M $Zn(OH)_4$ in 8 M KOH), and allows further electrodeposition of metal. The volume occupied by the zinc deposit is variable by altering either the inter-electrode gap for the cells or by increasing the number of cells in the battery. Increasing the inter-electrode gap does however lead to an increased Ohmic drop across the cell. The flowing electrolyte supresses dendrite formation and potentially avoids the subsequent shorting of cells in the battery.

Although the theoretical energy densities of the metal-air batteries offer great improvements over current generations of lead-acid, nickel-metal hydride and lithium-ion, they are not achieving the expected level of performance with current designs. Typical laboratory scale lithium-air cells are providing 300 – 500 mAh g^{-1}, comparable to lithium-ion cells.[15] The zinc-air system, although achieving a partial decoupling of the power and energy density, is still limited by the solubility of zinc in the alkaline electrolyte and the volume of the cell in which the zinc can be deposited. The capacity of a working zinc-air flow-battery will therefore be determined by the concentration of the electrolyte (optimally 8 M KOH with 1 M zincate) and total volume of inter-electrode space that the zinc can occupy (ideally <1 cm^3 or the iR drop will become an overbearing factor on the cell efficiency).

The metal-air battery when using alkaline electrolyte must be careful to avoid the introduction of CO_2 into the air-inlet. The CO_2 present in the oxygen supply will readily react with the alkaline electrolyte forming carbonate salt precipitate. This may lead to blocking of the gas diffusion pore or coverage of catalytic sites. If using air from the atmosphere the CO_2 should be removed, using a CO_2 scrubber or the O_2 generated during the OER should be stored and fed back into the air electrodes during the discharge.

The electrical efficiency of the zinc-air battery is dependent upon the overpotential related to the zinc electrode, air-electrode and any Ohmic losses through the cell. As can be seen from the high overpotentials for the air electrode, the majority of energy losses for the battery stem from the oxygen activity. The high pH of the zinc-air battery allows the use of a wide selection of relatively low cost transition metal based electrocatalysts. However, the ability to catalyse both the oxygen

evolution and reduction reactions efficiently, limits the possible catalyst selection for the air-electrode.

The focus of the work presented in this thesis is the development of bi-functional oxygen electrocatalysts for applications in zinc-air batteries. A secondary goal is the incorporation of the electrocatalysts into gas diffusion electrodes for use as the air-electrode in a zinc-air flow-battery. This work is carried out as a small part of the collaboration on the POWAIR project (grant number 256759), carried out across Europe and involves six companies and two universities.

The POWAIR project aims to create a low-cost, modular and environmentally sustainable energy storage system using zinc-air flow batteries. The system is planned to be capable of storing kW to MWs of power and used for peak shaving (load-levelling) applications or the storage of renewable power. This requires the extension and improvement of zinc-air primary batteries into scalable redox-flow battery modules. Simultaneously with the zinc-air battery, a new distributed power converter will be developed to provide scale-up and rapid exchange of battery modules. The electronic control systems are to provide individual battery module load-balancing throughout the stack. This will allow the modules to be selectively charging/discharging as required and avoid a single cell failure affecting the integrity of the entire system, as is the case with existing systems.

1.3 Thesis outline

The work contained in this thesis is presented as a series of chapters as outlined below.

Chapter 1: Introduction will provide a brief history of energy storage technology. This will lead onto the electrical energy storage technology that is currently under development. The benefits of the various flow-battery chemistries will be compared, with a more detailed explanation of the zinc-air flow battery. This is completed by a project outline and the overview of the thesis to follow.

Chapter 2: Methods, will discuss the physical and electrochemical methods used to characterise the catalyst samples prepared in this work. The physical methods will focus on the principals of the analytical techniques and the understanding each may provide. The electrochemical characterisation will focus on the experimental design and methodology behind the testing regimes used.

Chapter 3: Will discuss the activity of $NiCo_2O_4$ towards oxygen. The oxygen reduction activity is evaluated using rotating disc electrodes. A comparison is made to platinum and carbon. The mechanism of the reaction is further elucidated using rotating ring disc electrodes, to resolve the generation of hydrogen peroxide. The addition of carbon to the catalyst layer is also evaluated

and the effect it may elicit on the oxygen reduction reaction. The impact of synthesis method and fundamental oxygen activity of the $NiCo_2O_4$ is outlined, with the potential use as an oxygen electrocatalyst assessed.

Chapter 4: Will present the developments in gas diffusion electrodes completed in this work. The work evolved the carbon paper commonly found in PEM fuel cells, through to metallic foam and mesh current collectors with porous catalyst layers. This work highlights potential alternatives to inherently unstable carbon based electrodes for metal-air batteries.

Chapter 5: This chapter considers methods of improving the oxygen activity of the $NiCo_2O_4$. The $NiCo_2O_4$ was modified through the addition of precious metal nanoparticles onto the metal oxide surface. The addition of ruthenium dioxide results in the lowest potential gap between the ORR and OER of the electrocatalysts investigated in this work.

Chapter 6: The future work section of this report presents a context for this work, with a comparison to other activity mixed metal oxides reported in the literature. This work also focused on understanding the limitations of metal dopants to alter the electronic structure and the electrochemical activity of the $NiCo_2O_4$.

Chapter 7: Conclusions will provide a summary of the aims of this thesis and the results reported herein. A theoretical cost analysis of the electrodes will outline the cost effectiveness of a mixed metal oxide electrocatalysts.

1.4 References

(1) Thackeray, M. M.; Wolverton, C.; Isaacs, E. D. *Energy Environ. Sci.* **2012**, *5*, 7854–7863.

(2) Bockris, J. O.; Srinivasan, S. *Journal of Electroanalytical Chemistry (1959)* **1966**, *11*, 350–389.

(3) Tantram, A. D. S. *Energy Policy* **1974**, *2*, 55–66.

(4) DOE Global Energy Storage Database http://www.energystorageexchange.org/ (accessed Dec 1, 2014).

(5) Weber, A. Z.; Mench, M. M.; Meyers, J. P.; Ross, P. N.; Gostick, J. T.; Liu, Q. *J. Appl. Electrochem.* **2011**, *41*, 1137–1164.

(6) Kear, G.; Shah, A. A.; Walsh, F. C. *Int. J. Energy Res.* **2012**, *36*, 1105–1120.

(7) Ponce-de-León, C.; Frías-Ferrer, A.; González-García, J.; Szánto, D. A.; Walsh, F. C. *J. Power Sources* **2006**, *160*, 716–732.

(8) Skyllas-Kazacos, M.; Chakrabarti, M. H.; Hajimolana, S. A.; Mjalli, F. S.; Saleem, M. *J. Electrochem. Soc.* **2011**, *158*, R55–R79.

(9) Leung, P.; Li, X.; de León, C. P.; Berlouis, L.; Low, C. T. J.; Walsh, F. C. *RSC Adv.* **2012**, *2*, 10125–10156.

(10) Wang, W.; Luo, Q.; Li, B.; Wei, X.; Li, L.; Yang, Z. *Adv. Funct. Mater.* **2013**, *23*, 970–986.

(11) McKerracher, R. D.; Ponce de Leon, C.; Wills, R. G. A.; Shah, A. A.; Walsh, F. C. *ChemPlusChem* **2014**, n/a–n/a.

(12) Dunn, B.; Kamath, H.; Tarascon, J.-M. *Science* **2011**, *334*, 928–935.

(13) Kraytsberg, A.; Ein-Eli, Y. *J. Power Sources* **2011**, *196*, 886–893.

(14) Wang, L.; Liu, F.; Wang, W.; Yang, G.; Zheng, D.; Wu, Z.; Leung, M. K. H. *RSC Adv.* **2014**, *4*, 30857–30863.

(15) Ottakam Thotiyl, M. M.; Freunberger, S. A.; Peng, Z.; Chen, Y.; Liu, Z.; Bruce, P. G. *Nat. Mater.* **2013**, *12*, 1050–1056.

Chapter 2: Catalyst Characterisation

The preparation of the catalysts will be presented in the relevant results chapters (3-6). This chapter contains the general information and methodology used to characterise the catalysts, electrode preparation and electrochemical testing.

2.1 Physical Characterisation

Prepared electrocatalysts were physically characterised by SEM-EDX, TEM, BET and XRD to determine bulk elemental concentration, metal distribution, particle size, morphology, surface area, crystallite size and phase.

2.1.1 SEM-EDX

Scanning electron microscopy (SEM) with energy dispersive X-ray (EDX) spectroscopy was used to characterise samples at lower magnification and to determine elemental concentrations over an area of the sample. The SEM operates on a similar basis to TEM, whereby a high-energy beam of electrons is focused onto a sample and moved by a process of rastering across the surface. The electrons interact with those of the sample, generating secondary electrons (used in imaging), characteristic X-rays (used in EDX) as well as back scattered electrons and light. The secondary electrons are emitted from the sample and picked up by the detector; the systematic rastering of the electron beam is recombined to provide an electron micrograph of the sample surface.

In EDX analysis, X-rays are generated from the sample by bombardment of electrons from the electron beam. This process can be applied across a surface to provide information from a single point, or with the rastering of the electron beam, to resolve elemental concentrations across a sample. The relative intensities of the characteristic energy of the X-rays generated from the sample can be used to calculate the concentrations of each element of which the sample is composed.

Sample specimens were prepared by attaching catalyst powders onto adhesive carbon tabs on aluminium sample studs. The SEM Mmeasurements were carried out on a Phillips XL30 SEM with a Thermo-Scientific UltraDry EDX system.

The morphological information gained is limited by the resolution of the instrument and the particle size of the sample under investigation. A typical SEM micrograph can be seen in Figure 2 with corresponding EDX data in Figure 3.

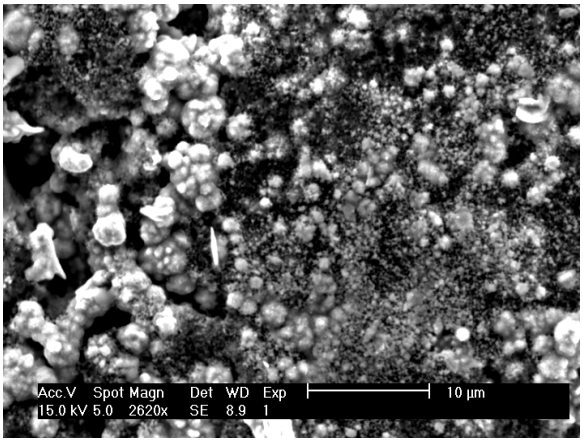

Figure 2: SEM micrograph of $NiCo_2O_4$ on nickel foam electrode.

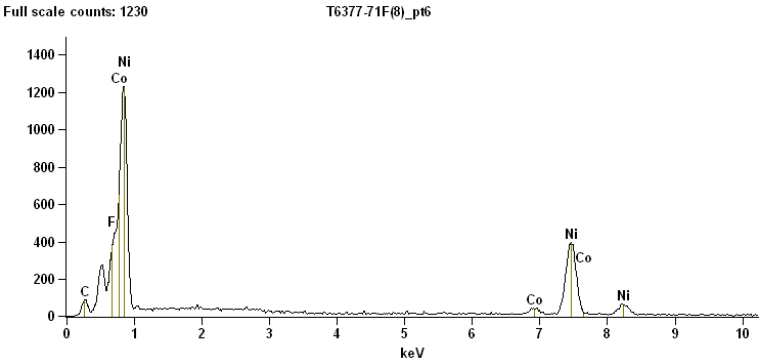

Figure 3: SEM-EDX data for $NiCo_2O_4$ on nickel foam electrode.

2.1.2 Transmission electron microscopy

Transmission electron microscopy was used to determine particle size and morphology of the electrocatalysts. The wavelength of the visible spectrum at between 380 – 750 nm is larger than the nanoparticles prepared, making it impossible to record visible images of nano-structures synthesised in this work; as such electron imaging techniques such as SEM and TEM are commonly used. The wavelength of an electron as resolved from the de Brogile equation (Equation 3) is significantly smaller than that of interatomic distances. A high-energy beam of electrons is focused onto a thin sample; electrons that pass through the sample are then detected by a fluorescent screen or charge couple device (CCD) sensor with the resulting 2-D projection of sample analysed to yield particle size and shape. This mode of detection is known as bright field (BF).

$$\lambda = \frac{h}{mv}$$

Equation 3

Samples were prepared by grinding in an agate pestle and mortar, dispersed in solvent (2 mL H_2O or MeOH), with 15 μL drop cast on to a Cu TEM grid (1000 mesh holey carbon, VWR). An example of TEM micrographs of silver nanoparticles prepared onto $NiCo_2O_4$ is given in Figure 4. In the micrograph the dark polygonal particles are silver supported onto $NiCo_2O_4$ substrate. The lattice planes of the supporting $NiCo_2O_4$ are clearly visible as interference lines in both images. Particle size and shape is calculated by analysis of particles from several images. A JEOL JEM-2100 LaB_6 Transition Electron Microscope with 200 kV accelerating voltage was used to collect the micrographs.

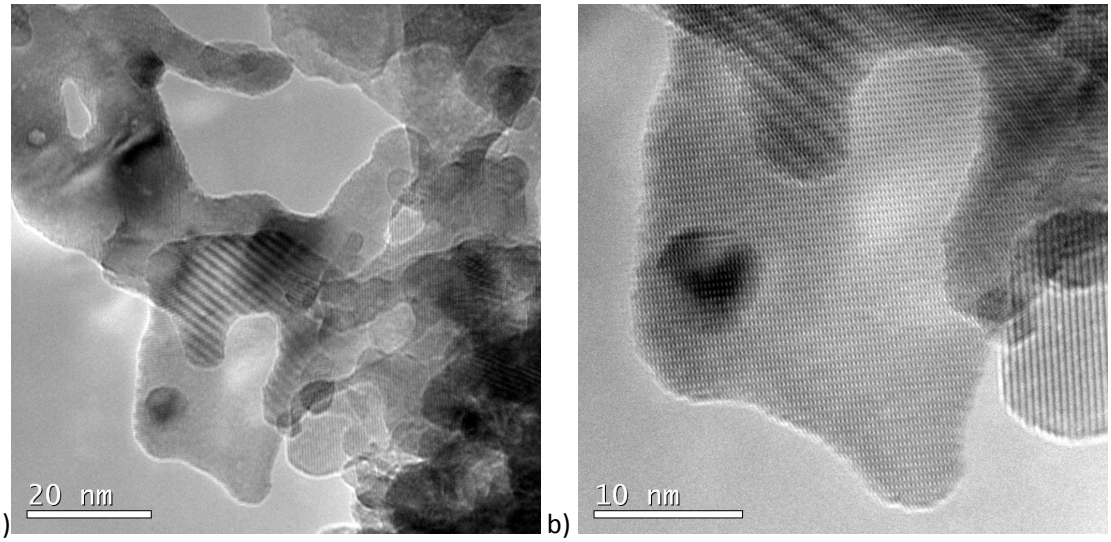

Figure 4: TEM micrographs of silver nanoparticles supported on $NiCo_2O_4$.

2.1.3 Powder X-ray Diffraction

Powder X-ray diffraction (XRD) is a non-destructive technique used to analyse crystallite size and crystalline phases present in a sample. Due to fluorescence from the nickel and cobalt present in the sample, when using a copper radiation source, the analysis was carried out using an Agilent supernova diffractometer with molybdenum K_α X-ray source. The instrument was used to provide reasonable X-ray powder diffraction patterns (Figure 6) later used for Rietveld refinement to determine unit cell, crystallite size and strain of the electrocatalysts.

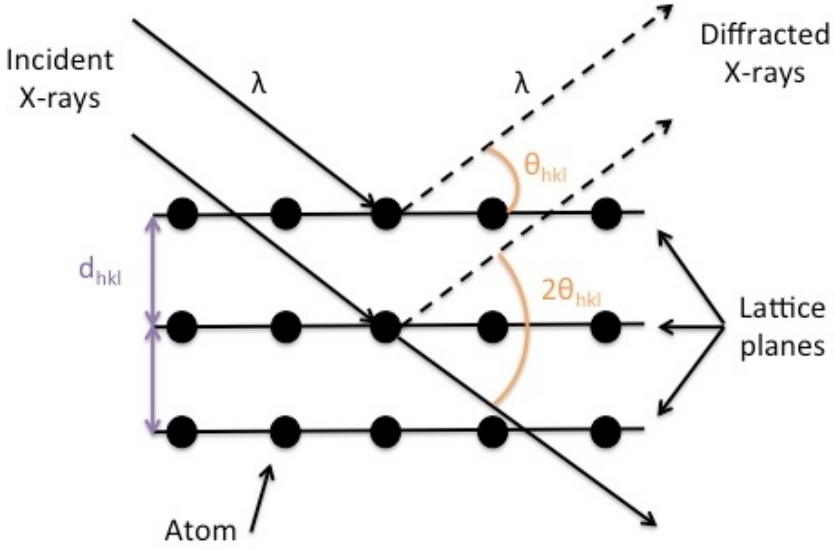

Figure 5: Illustration of incident and diffracted x-rays on a crystal lattice to demonstrate Bragg's law.

The X-ray powder diffraction is possible by the application of X-rays onto the sample with an increasing angle of incidents, when Bragg's Law is fulfilled (Figure 5) the X-rays are diffracted to the detector. The d spacing (d_{hkl}) can be calculated using the Bragg equation (Equation 4). Where n is the order of diffraction, λ the wavelength of the incident X-rays, θ the angle of peak at maximum intensity and d the lattice plane spacing. The X-ray pattern recorded is over a range of angles 2-theta to produce intense peak at points of constructive interference, whilst the interim spaces are periods of destructive interference.

$$n\lambda = 2d\sin\theta$$

Equation 4

Crystallite size can be calculated using the Scherrer equation (Equation 5). Where K is the shape factor, typically 0.9 for spherical particles, λ is the wavelength of the incident X-rays, β the line broadening at full width half maximum (FWHM) intensity in radians, θ the Bragg angle of peak at maximum intensity and L the linear dimension of the crystallite.[1]

$$L = \frac{\mathrm{K}\lambda}{\beta\cos\theta}$$

Equation 5

An improved method in resolving crystallite information involves the Rietveld refinement method resolved computationally using GSAS and EXPGUI.[2,3] The method for Rietveld analysis, first

outlined by Rietveld[4,5], whereby a theoretical diffraction pattern is sequentially fitted to the whole of the measured data. The process can be simplified into the initial fitting of intensity and background. This is followed by least squares fitting of instrument and sample parameters against the measured diffraction pattern to achieve good fit of the peak shape, and finally thermal and unit cell parameters. This method was recently described in greater detail by McCusker and within the GSAS software manual.[2,6]

An example of a completed Rietveld refinement fitting can be seen in Figure 6, where a reasonable fit has been achieved. A reasonable fit in this work is defined as the weighted R-factor profile, wRp or Rwp, being less than six. The weighted wRp is calculated using Equation 6, where the intensity values for the observed, $y_{o,I}$ intensity values for the calculated, $y_{c,i}$, and uncertainty in the $y_{o,i}$, $\sigma[y_{o,i}]$, are computed during the Rietveld algorithm. However, the critical factor when determining the quality of fit must be a visual comparison of the theoretical model with the collected diffraction pattern. The use of a non-ideal diffractometer for the screening of samples resulted in a complex background contribution from the glass capillary, limiting the quality of fit that can be derived. However, the error factor, (wRp), reported in the GSAS software to assist in determining the quality of a fit, was less than five percent for all fits. The refinement fitting process was deemed complete upon no further significant changes to unit cell, instrument and sample parameters with repetitive cycles, whilst maintaining a high quality fit to the data.

$$R_{wp}^2 = \frac{\sum_i w_i \left(y_{c,i} - y_{o,i}\right)^2}{\sum_i w_i \left(y_{o,i}\right)^2}$$

Equation 6

$$\boldsymbol{w_i = \left(\frac{1}{\sigma^2[y_{o,i}]}\right)}$$

Equation 7

Catalyst powder samples were prepared for XRD analysis by grinding in an agate pestle and mortar. Freshly ground powder was transferred into 0.3 mm diameter glass capillaries. Each capillary was sealed with epoxy resin and set into a brass mount for use with the Agilent supernova diffractometer, with Mo X-ray tube and Atlas CCD detector. The measurement obtained a diffraction pattern over the 5 – 80° 2θ.

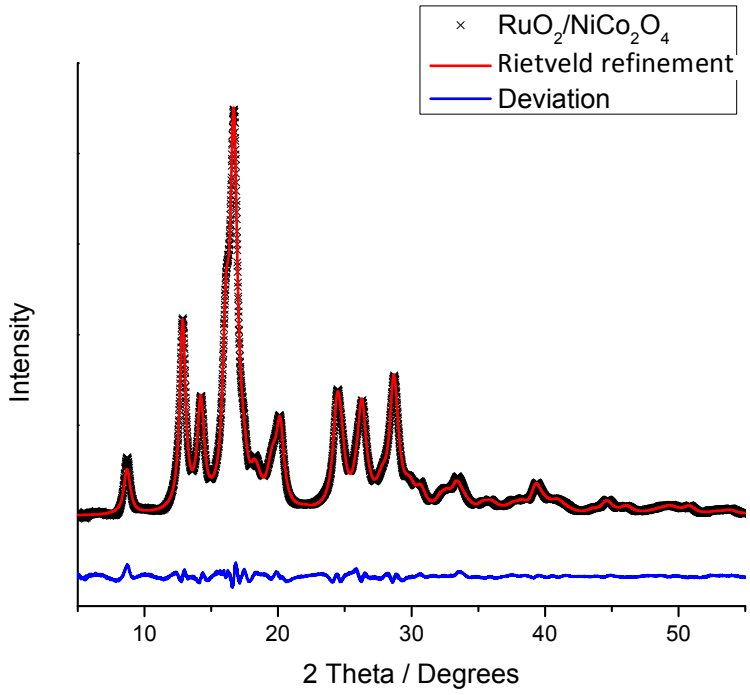

Figure 6: Rietveld refinement of powder diffraction pattern for sample of RuO_2 supported on $NiCo_2O_4$.

2.1.4 BET

Catalyst surface area was measured using Brunauer, Emmett and Teller (BET) isotherm analysis, first reported in 1937.[7] A multilayer of nitrogen gas was adsorbed onto the sample surface at 77 K, the sample was then returned to room temperature recording the partial pressure within the sample tube. Several assumptions are made: The nitrogen molecules are assumed to not interact with one another; the surface is uniformly accessible; and all adsorption sites are equivalent. At saturation pressure the molecule layer number will tend to infinity; the desorption is kinetically-limited process.

The sample was inserted into a BET instrument, Micromeritrics – Gemini, to measure the surface area of each catalyst sample. The automated system used the BET equation, Equation 8, can be used to determine the surface area of the sample. The equilibrium pressure, P_0 is the vapour pressure of the adsorbate gas at standard conditions; V is the volume of the gas adsorbed at a particular partial pressure $\left(\frac{P}{P_0}\right)$; V_m is the volume of gas required to form a monolayer of the sample surface and C is the temperature dependant constant related to the enthalpies of adsorption of the monolayer and multilayers of adsorpbate.

$$\frac{P}{V\left(P_0 - P\right)} = \frac{1}{V_m C} + \frac{\left(C-1\right)}{V_m C}\left(\frac{P}{P_0}\right)$$

Equation 8

A plot of $\frac{P}{V\left(P_0 - P\right)}$ against $\left(\frac{P}{P_0}\right)$ should produce a straight line with an intercept of $\frac{1}{V_m C}$ and gradient of $\frac{\left(C-1\right)}{V_m C}$, from which *C* and V_m can be determined. In practice the BET isotherm is typically linear over the range of 0.05 and 0.3, with these limits used to construct the plots. The surface area of the catalyst sample can then be calculated from Equation 9.

$$SA = V_m \left(\frac{N_A}{V_A}\right) A$$

Equation 9

Where *SA* is the surface area, $\left(\frac{N_A}{V_A}\right)$ is Avogadro's number per cubic meter of gas and *A* is the area of the adsorbate molecule.

$$\text{Specific surface area} = \frac{\text{Surface area}}{\text{Mass of sample}}$$

Equation 10

To compare different samples the surface area is divided by the mass of sample to yield the specific surface area in $m^2\ g^{-1}$. All surface area measurements were carried out using nitrogen; with examples of the measured surface area in Table 4.

Table 4: Surface area results for $NiCo_2O_4$ samples by synthesis method.

Sample	Surface Area / $m^2\ g^{-1}$
Co-precipitation	70
Thermal decomposition from methanol	10
Thermal decomposition from water	7

2.2 Electrochemical Characterisation

Electrochemical characterisation of the electrocatalysts was used to understand the link between material properties and the activity towards oxygen evolution and reduction reactions.

2.3 Preparation of electrodes

Electrocatalysts were prepared into suitable electrodes for electrochemical experiments by the methods described below.

2.3.1 Rotating Disc Electrode (RDE)

Experiments were carried out using glassy carbon (GC) encased in PTFE electrodes (Pine research instrumentation, approximately 0.2 cm^2) coated with a thin-film catalyst layer. The electrocatalyst was prepared into an ink with a composition of 2 mg catalyst and 6 mL H_2O. The ink was irradiated with ultrasonic radiation for 30 minutes (Fisherbrand FB15046), followed by 2 minutes shear force stirring (homogeniser Fisher Powergen 1000). The ink, totalling 45 μL, was applied in 15 μL aliquots and allowed to dry on the GC electrode (heated by IR heat lamp, ~ 353 K). A thin-film of Nafion® solution (15 uL of 0.1 wt.% in water) was drop cast on top of the catalyst layer for improved stability and dried by IR heat lamp.

2.3.2 Carbon Gas Diffusion Electrode

The electrocatalyst (100 mg), 564 μL Nafion®, 916 μL H_2O, 200 μL IPA was irradiated with ultrasonic radiation for 30 minutes followed by two minutes of homogeniser mixing. The resulting catalyst ink was applied to wet-proofed Toray paper (TGP-H-60), via transfer from a brush, with a dry loading of 0.5 mg cm^{-2}. A final hot-pressed heat-treatment at 453 K and 4 kg cm^{-2} disperses the Nafion® across the electrode.

2.3.3 Mesh Gas Diffusion Electrode

For application to metals a modified ink formulation was used, whereby 100 mg of catalyst, 50 mg of PTFE (60 wt.% dispersion), 500 μL H_2O and 100 μL IPA was combined. The ink was irradiated with ultrasonic radiation for 30 minutes, homogenised for 2 minutes after which it is ready to be applied. Dexmet microgrid® expanded nickel mesh, was irradiated with ultrasonic radiation initially in acetone for 20 minutes, followed by acid etching in 1 M HCl at 353 K for 1 hour, rinsed with water and dried in a desiccator. Catalyst ink was applied via airbrush to the electrode with an approximate target loading of 10 mg cm^{-2}; each layer is applied and air-dried (heat-gun), until the

desired loading is achieved. The sample was pressed (4 kg cm^{-2}) and heated (453 K) for 3 minutes, the low pressure and high temperature to promote PTFE migration through the structure, improving catalyst adhesion to the support and overall hydrophobicity.

2.3.4 Nickel Foam Gas Diffusion Electrode

Goodfellows nickel foam was degreased by irradiating with ultrasonic radiation in acetone for 20 minutes, then acid etched in 1 M HCl at 353 K for ~1 hour. Samples were prepared using a 200 mg mixture of catalyst and PTFE, at a ratio of 10:3 (as dry solids), suspended in 8.94 mL of IPA / H_2O. The suspension was irradiated with ultrasonic radiation for 20 minutes, then homogenised for 4 Minutes. Nickel-PTFE paste (200 mg wet weight or approximately 120-150 mg dry weight) was applied to 1.2 cm^{-2} nickel foam and pressed at 153 kg cm^{-2}. The gas diffusion electrode was dip-coated in a solution of (2.91 g) cobalt nitrate and (1.45 g) nickel nitrate in 10 mL water for 5 minutes, dried (648 K, 10 minutes) three times with a final calcination step at 648 K for 3 hours.

2.4 Electrochemical Methods

Electrochemical techniques were used to study the behaviour and activity of synthesised electrocatalysts. The techniques employed for evaluating catalysts and electrodes included cyclic, linear and galvanostatic voltammetry. Initially samples were evaluated by cyclic voltammetry for characterisation of redox activity within a defined electrochemical window. Linear sweep voltammetry on rotating disc electrode (RDE) was used to investigate the electrochemical activity for oxygen reactions. Selected catalysts were then made into gas diffusion electrodes and performance measured with linear sweep voltammetry to compare kinetics to RDE measurements. The final measurements carried out on the electrodes were under galvanostatic control to record the voltage gap between the oxygen evolution and reduction reactions, used to approximate the performance of the air electrode in a working battery.

2.4.1 Experimental Aspects

All measurements were carried out in a three electrode cell as illustrated in Figure 7 and Figure 8, using a Pt mesh as counter and mercury-mercuric oxide reference electrode (0.943 V *vs.* RHE in 1 M KOH). The potential and current control measurements were achieved using an Autolab PGSTAT128N. A Pine modulated speed rotator maintained rotation control. Pine AF3M glassy carbon RDE electrodes with a disc diameter of 0.2 cm. RDE experiments were typically carried out in 1 M KOH, whilst half-cell measurements used 8 M NaOH or KOH. The low solubility of oxygen in

potassium and sodium hydroxide solutions limits the ORR current densities that can be achieved in the RDE set-up, hence the lower KOH concentration used for the RDE measurements.[8]

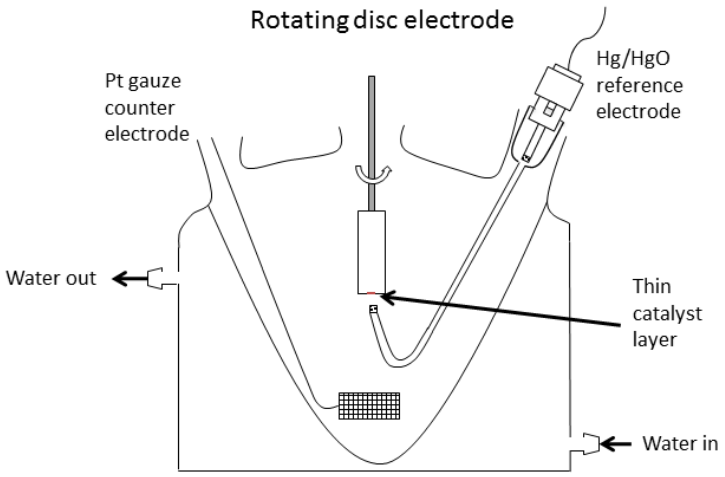

Figure 7: Schematic jacketed electrochemical cell used for RDE measurements.

(a)

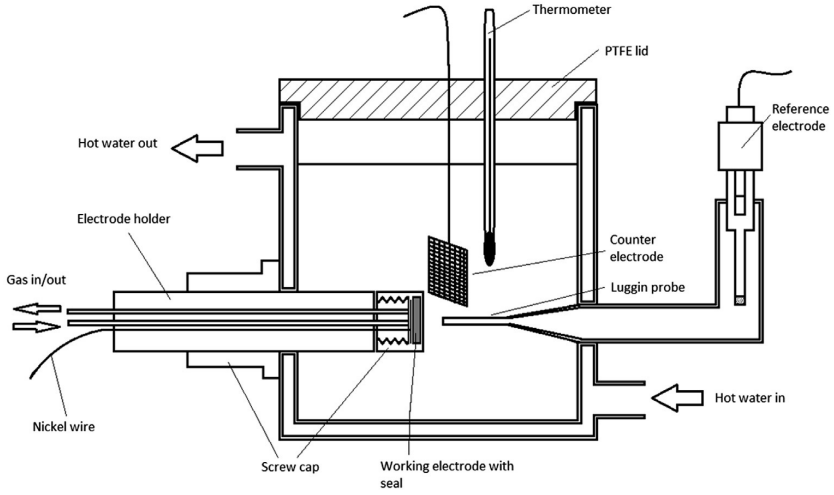

(b)

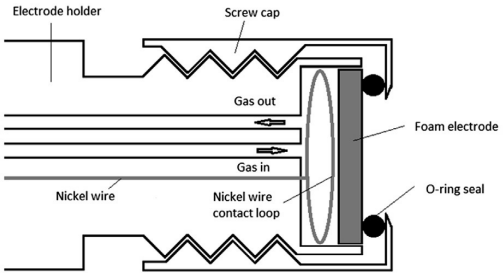

Figure 8: Schematic of cell used for testing of GDE electrodes (a) with an expanded view of the insert (b).[9]

Galvonstatic measurements were carried out in the gas diffusion cell to evaluate how the catalyst performs as a function of time and these more closely simulated the flow-cell, where the electrocatalyst is prepared on a gas diffusion layer. Samples were mounted vertically to maximise oxygen flow to the air–side of the electrode, whilst also ensuring the electrode was hydrated to maximise the three-phase activity region, and to better simulate how the electrode would be mounted in an operational flow-cell.

2.4.2 Voltammetry – cyclic, linear and galvanostatic

Cyclic voltammetry is used to measure the electrochemical response of the catalyst samples in the aqueous electrolyte. The voltammetry provides information on any double layer charging, changes in the oxidation state of the electrocatalyst, and reactions with the electrolyte. The potentiostat controls the potential between the working and reference electrodes and records the current measured between the working and counter as a function of potential. The working electrode potential relative to the reference is swept from an initial potential E_1 to another E_2 and back again at a constant rate, repeating as required as shown in Figure 9.

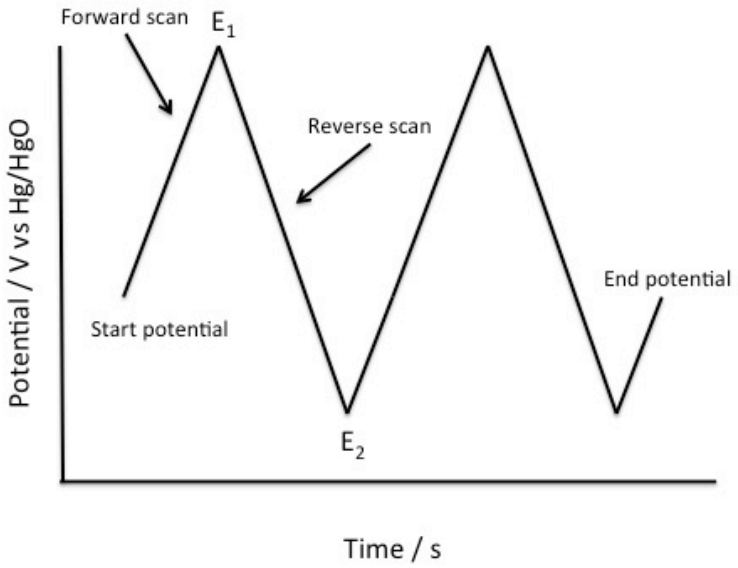

Figure 9: Example waveform for cyclic voltammetry.

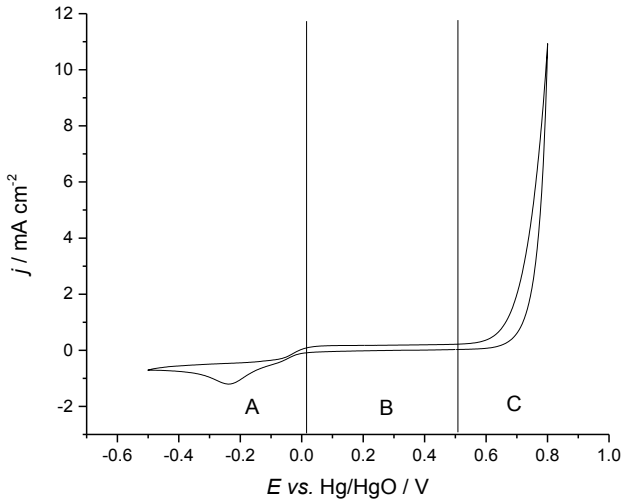

Figure 10: CV of a bulk Pt disc (0.2 cm^2) in oxygen saturated 4 M KOH, 333 K. Rotation rate 400 rpm and scan rate 10 mV s^{-1}, division depicting: A, oxygen reduction, B, hydroxide formation region, and C, oxygen evolution.

The resulting CV for bulk platinum RDE rotated at 400 rpm in potassium hydroxide electrolyte can be seen in Figure 10. Three distinct regions are identified, A, oxygen reduction, B, hydroxide formation, and C, oxidation and oxygen evolution. The platinum forms platinum hydroxide in the region 0 to 500 mV *vs.* Hg/HgO, similar to the formation of platinum oxide before the OER in acidic media. The oxidation region begins by initial surface oxide formation at 500 mV, followed by oxygen evolution at 600 mV. The oxygen reduction region is observed below 0 mV, a maximum peak is from the initial saturation of oxygen at the electrode layer being consumed, followed by a lower concentration of oxygen being driven to the electrode through forced convection (rotation of the electrode).

The $NiCo_2O_4$ thin layer electrodes prepared on GC appear with similar features with oxygen reduction occurring approx. -100 mV and oxygen evolution 600 mV. There is an additional redox couple observed at approx. 400 mV on the forward scan and reversed on the back at 270 mV. The redox couple is associated with the reversible change in oxidation state of the nickel and cobalt present in the spinel. The oxygen reduction peak from bulk platinum (2 mA cm^{-2} in Figure 10) is significantly smaller than that observed from the charging of the mixed metal oxide surface (approx. 10 mA cm^{-2} in Figure 11) for RDE CV experiments, due to the low solubility of oxygen in the KOH electrolyte.

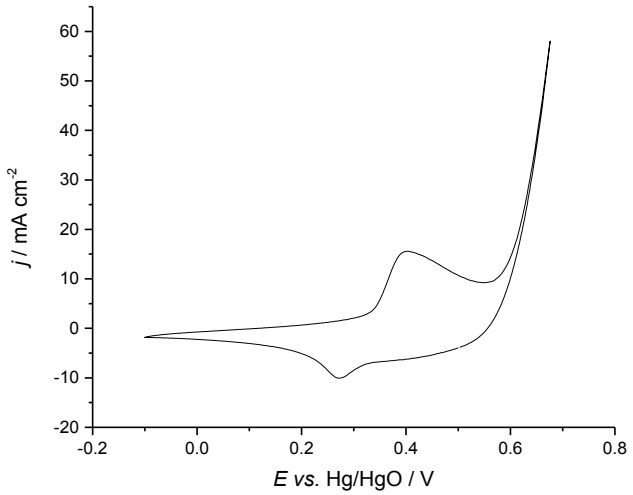

Figure 11: CV of $NiCo_2O_4$ thin film electrode (15 μg) on GC RDE (0.2 cm^2) in oxygen saturated 4 M KOH, 333 K. Rotation rate 400 rpm. Scan rate 10 mV s^{-1}.

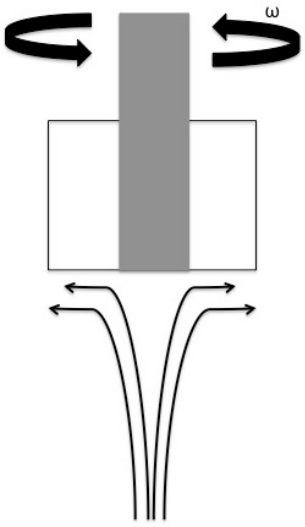

Figure 12: Illustration of forced convection from a rotating disc electrode in solution.

Linear sweep polarisation curves at slow sweep rates and in combination with RDE were used to investigate electrochemical reaction kinetics. The rotating disc electrode controls the convection, providing a constant stream of reactants to the working electrode; reactions are carried out in large excess of conductive electrolyte (1 M KOH), limiting the contribution from migration, leaving a thin diffusion layer near to the surface of the electrode controlling reactants and products leaving this thin region at the electrode surface. The hydrodynamics are controlled by the applied rotation rate of the RDE, allowing higher rotations to increase the forced convection and in effect

the mass transfer of reactants to the electrode. The polarisation curve response is observed in Figure 13, where with increasing rotation rate the limiting current (at ~ 0.5 V) increases.

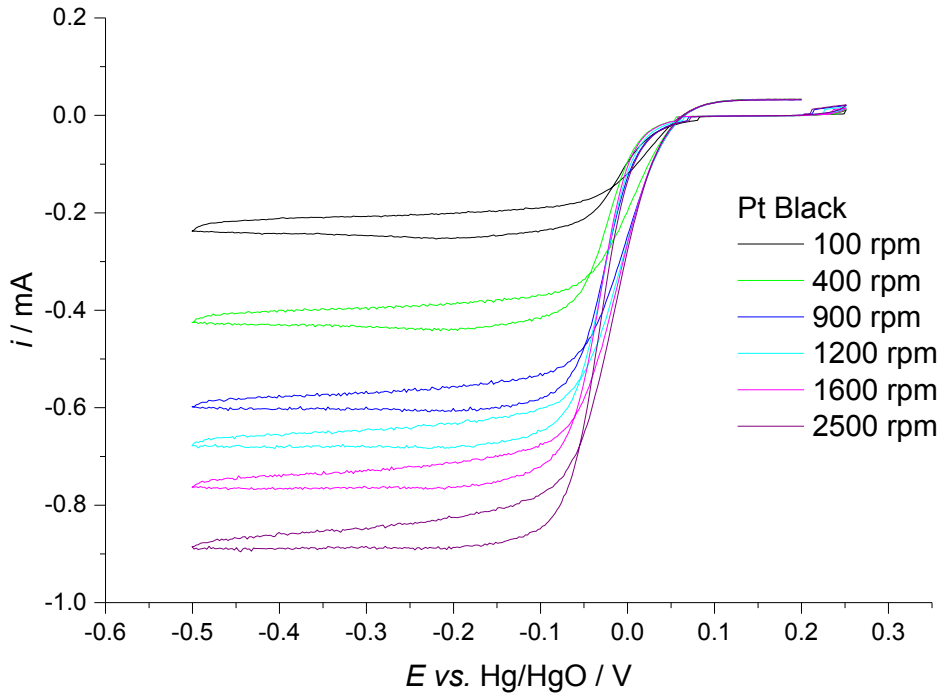

Figure 13: Polarisation curves of platinum black on GC RDE, in oxygen saturated 1 M KOH at 298 K. Catalyst loading 15 µg, 0.2 cm^2 GC RDE, sweep rate 10 mV s^{-1}.

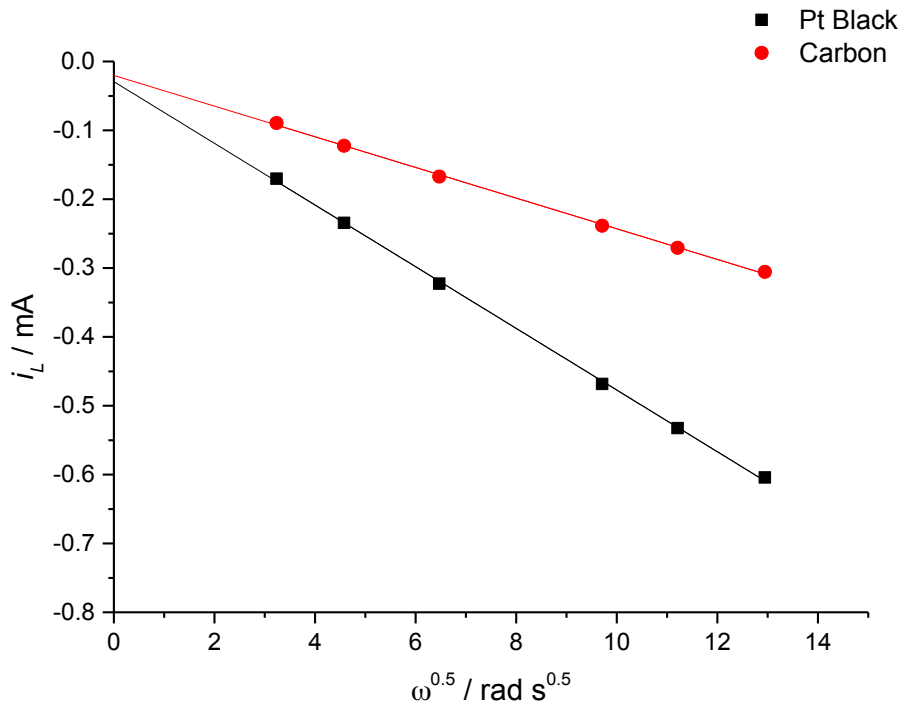

Figure 14: Levich plot for thin-film electrodes on GC RDE in oxygen saturated 1 M KOH at 298 K.

The number of electrons involved in the ORR can be elucidated using the Randel Sevich equation (Equation 11). A plot of the limiting current against the rotation rate to the power ½ (Figure 15) yields should yield a linear response.

Equation 11

$$i_c = \left(0.620nFAD_{O_2}^{\frac{2}{3}} v^{-\frac{1}{6}} C_{O_2}\right) \omega^{\frac{1}{2}}$$

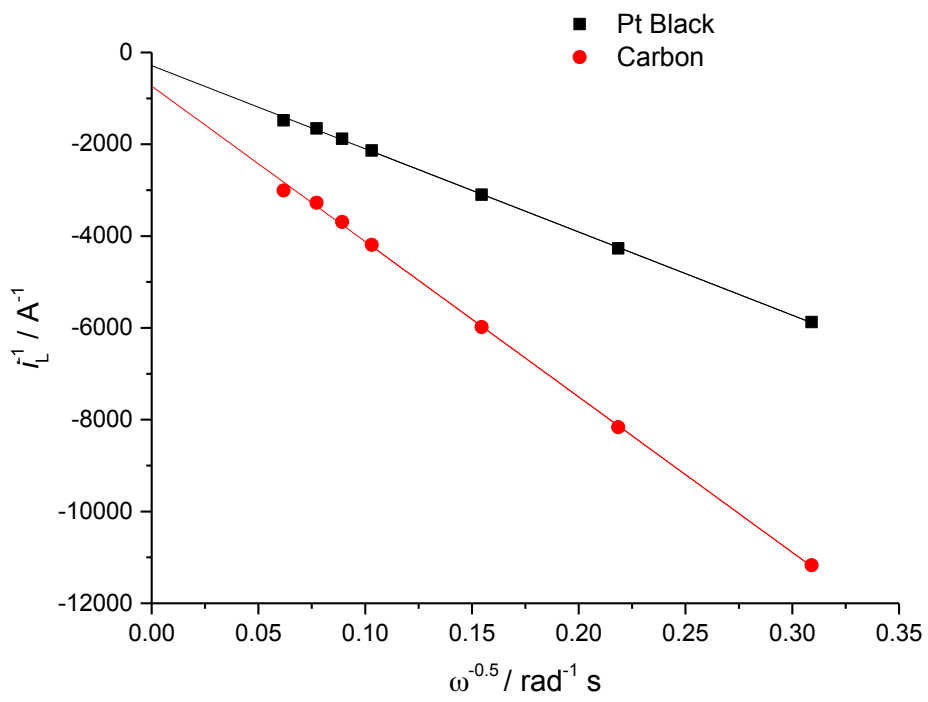

Figure 15: Koutecky-Levich plot for the ORR of $NiCo_2O_4$ in oxygen saturated 1 M KOH at 298 K.

RDE studies were carried out to determine the number of electrons transferred and reaction kinetics, and rotating ring disc electrode (RRDE) studies to measure intermediate species that may be generated during the reaction (Figure 16). The disc is swept to a negative potential, with the ring potential held at a potential to oxidise hydrogen peroxide. The passage of the intermediate species generated at the disc to the ring is controlled by the forced convection of the rotating electrode. The geometry of the disc to ring determines the theoretical collection efficiency.

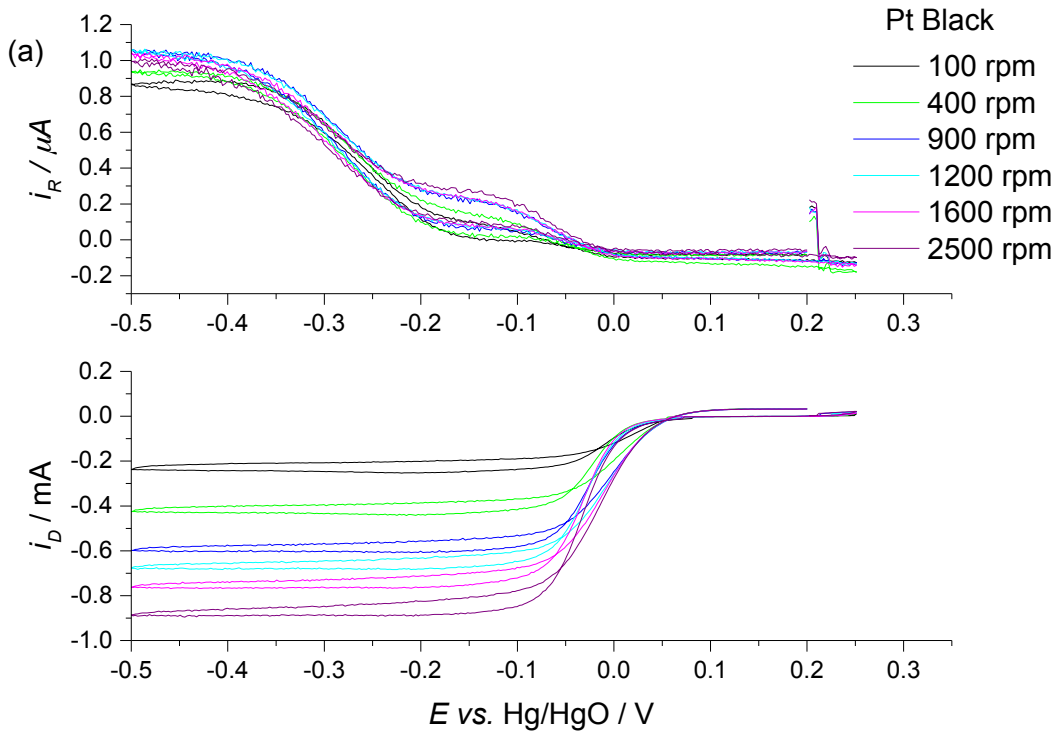

Figure 16: Polarisation curves of platinum black on GC-disc (lower) and at a fixed potential (0.1 V *vs.* Hg/HgO) for Pt-ring RDE (upper), in oxygen saturated 1 M KOH at 298 K.

Galvanostatic measurements set a fixed current between the working and counter electrode, with the potentiostat altering the potential until the desired current is achieved. Measuring the potential as a function of time for a desired current density provides a comparison for how the air-electrode would be operated in a working battery when charging (OER) or discharging (ORR). Galvanostatic measurements were carried out on gas diffusion electrodes (GDE) developed for the air-electrode, which overcome the low oxygen availability of the RDE measurements. As a result the GDE was not used to study reaction kinetics. However, information on the catalyst and electrode stability was used in the further development of a functional and durable GDE for metal-air batteries.

2.5 X-ray absorption spectroscopy

2.5.1 Introduction

The X-ray absorption spectroscopy (XAS) technique is used to resolve long-range structure of an element from the absorption of monochromatic X-rays at a characteristic energy. The energy, where the X-rays are most strongly absorbed, is known as the 'absorption edge' and was first reported by de Broglie in 1913.[10] The technique is the measurement of the absorption coefficient μ(E) as a function of the X-ray energy. In the 1920's Fricke et al.,[11,12] identified the fine edge

oscillations post of the absorption edge, shortly followed by the first theory proposed by Kronig.[13,14] It was not until the 1970s, when synchrotron radiation became stable, with the addition of storage rings and hard X-rays to measure high K-edges, that the theory was further developed. Two theories were proposed in the literature to explain the oscillations and the information they may hold, short range order and long range order, until an experiment with perovskites of $CaTio_3$, $CaZrO_3$, $SrTiO_3$ and $SrZrO_3$ was able to provide enough evidence for the SRO theory to be widely accepted.[15] Soon after, the modern theory of EXAFS was outlined by Sayers,[16] and improved upon by both Stern and Lee.[17-19]

2.5.2 Theory of XAS

The passage of X-rays through a material is described by Beer-Lambert law, but with the added probability of absorption from the absorption coefficient, μ, as described in Equation 12. The intensity of X-rays from the incident intensity, (I_0), is reduced upon passage through the samples, yielding the transmitted intensity, (I_t), as an exponential of the sample thickness, (x), and absorption coefficient.

$$I_t = I_0 e^{-\mu x}$$

Equation 12

With increasing X-ray energy (hν), the absorption coefficient declines, with the corresponding increase in the penetration of X-rays, until the next binding energy is reached. As the monochromatic X-ray energy increases, it will equal that of the binding energy (E_b) of a core electron. At this point, due to the photoelectric effect, the energy can be transferred from the incoming X-rays to the electron and a sharp rise in the absorption occurs, known as the absorption edge. The excited electron from the absorbing atom has energy (E_k), determined by the incoming X-ray energy less that of the binding energy of the electron (Equation 13).

$$E_k = h\nu - E_b$$

Equation 13

The absorption coefficient, μ, which determines the intensity of the absorption, is proportional to the probability of absorbing an incoming X-ray photon, according to 'Fermi's gold rule' (Equation 14).[20]

$$\mu \propto \sum_f \left|\langle \varphi_f | p.A(r) | \varphi_i \rangle\right|^2 \delta(E_f - E_i - \hbar v)$$

Equation 14

Where φ_i and φ_f describe the initial and final states upon absorption of an X-ray photon of energy $\hbar v$, p is the momentum operator, and $A(r)$ the vector potential of the incident electromagnetic field. The final states are dependent on the outgoing and backscattered waves of the photoelectron. This is clear from the oscillatory nature observed in the EXAFS, where the outgoing and backscattered waves result in constructive and destructive interference.

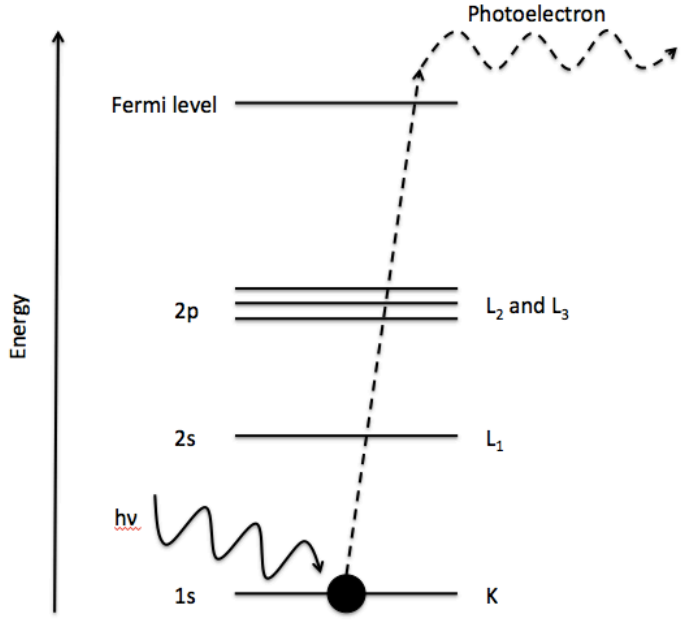

Figure 17: Schematic of the photoelectric effect, excitation of 1s electron to photoelectron emission, giving rise to the K-edge absorption.

The absorption of the X-ray photon followed by emission of a photoelectron is described graphically in Figure 17. The notation used for the absorption edges (K, L_1, L_2, L_3 etc.) is based upon the principal quantum number from which the electron was ejected. The K edge corresponds to an electron excitation from the 1s orbital, and L_1 — L_3 edges for 2s, $2p_{1/2}$ and $2p_{3/2}$ respectively. An XAS spectrum of Ruthenium metal collected on B18 at the Diamond light source is shown in Figure 18. The spectrum is separated into two components, XANES and EXAFS, which are brought about by the interactions of this photoelectron propagating from the absorbing atom.

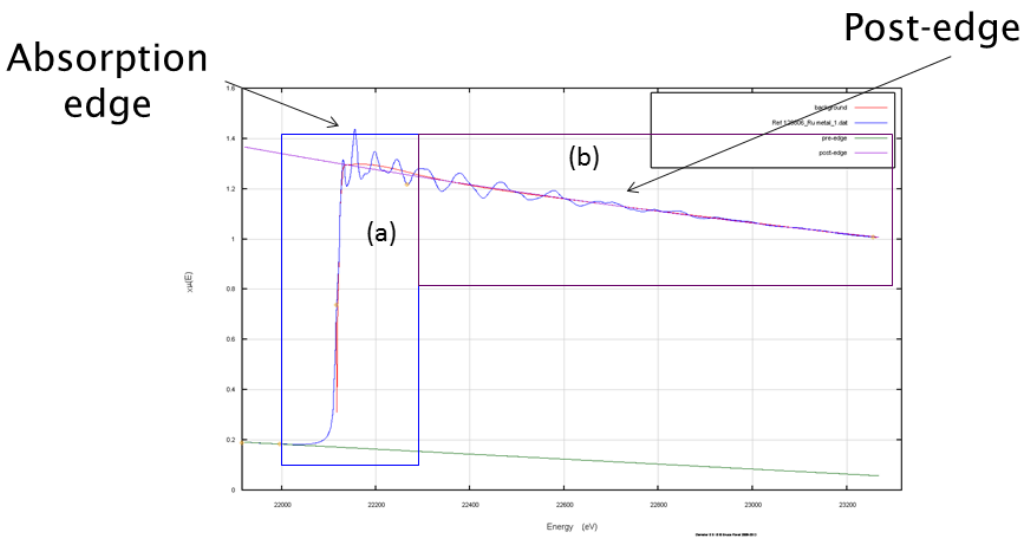

Figure 18: Normalised XAS spectra for Ruthenium metal foil describing the (a) XANES and (b) EXAFS regions.

The emitted photoelectron propagates as spherical wave from a central absorbing atom. The immediate region surrounding the initial absorption is described as the XANES region. From the peak position the oxidation state can be determined from a linear relationship of the binding energy and that of reference samples with a well-characterised oxidation state. The XANES region is however also sensitive to bonding geometry and electron donating or withdrawing effect from any surrounding atoms. As such the ideal standard reference samples consist of various oxidation states with the same coordinating atoms and a similar geometry.

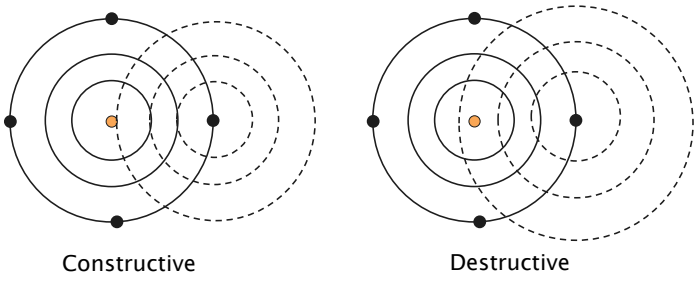

Figure 19: Schematic of photoelectron wave propagating (solid) from the central absorber (orange), and scattering (dashed) off surrounding atoms (black) resulting in constructive and destructive interference.

The EXAFS region consists of the XAS spectrum beyond that of the initial absorption edge. The EXAFS results in a region of declining absorption, influenced by the multiple scattering paths of the photoelectron wave propagated from the central absorbing atom. At energies where constructive interference occurs from the scattering atoms then the absorption is increased, whilst at energies where destructive interference occurs from the scattering atoms the absorption will be reduced. The outgoing photoelectron wave can be related to the energy of the photon,

Equation 15, with k representing the vector of the outgoing wave, m_e the mass of the electron and E_o the energy of the absorption edge.

$$k = \sqrt{\left(\frac{8\pi^2 m_e}{\mathrm{h}^2}\right)\left(h\nu - E_o\right)}$$

Equation 15

The EXAFS signal, $\chi(k)$, is extracted from the X-ray absorption spectrum using Equation 16, where $\mu_{tot}(k)$ is the total absorption and $\mu_0(k)$ is the background absorption.

$$\chi(k) = \frac{\mu_{tot}(k) - \mu_0(k)}{\mu_0(k)}$$

Equation 16

Analysis of the EXAFS signals was carried out through computer simulations of EXAFS signals on pre-defined atomic structures. This is possible by solving of the EXAFS equation, as outlined below, for photoelectron waves propagating from central absorbing atoms of interest.

2.6 XAS experimental aspects

To successfully carry out electrochemical operando (in-situ) studies it was necessary to select the optimal synchrotron beamline to carry out the desired analysis. Further to this electrochemical cells had to be designed for the type of measurement and any potential disruptions to the spectra, such as gas bubbles and liquid scattering, avoided.

2.6.1 Diamond Light Source - B18

The B18 beamline at the Diamond Light Source was selected for the XAS measurements. The synchrotron operates by accelerating bunches of electrons, initially using a linear accelerator followed by a booster ring, taking them to near light speed, before passing them to the outer storage ring. A series of bending magnets are used to deflect the electron path ensuring they maintain a path around a closed loop. Each deflection results in the emission of X-rays to conserve the angular moment of the electrons.

The beamline is capable of providing X-ray energies in the range of 2.05–35 KeV with a double-crystal monochromator using either Si(111) for low energy (2-20KeV) or Si(311) crystals for higher energies (4-35 KeV), with a typical energy resolution of 2 x 10^{-4}. Focusing of the X-ray beam was

achieved with a Pt coated collimating mirror and a pair of toroidal mirrors before and after the monochromator. The configuration was capable of achieving a flux of 5 x10^{11} photons per second, with a beam spot size of 0.6 mm by 1 Mm. The B18 beamline with quick EXAFS utilised either ionisation chamber detectors for transmission or a 9-element Ge fluorescence detector for fluorescence measurements. Measurements were carried out on the Ru K edge at 22117 eV, by scanning the X-ray energy from 21900 to 22900 eV.

2.6.2 XAS experiments

The X-ray absorption measurements were carried out in transmission and fluorescence modes of operation. The difference in geometry can be seen in Figure 20, where the transmission measurements are operated in a linear path with ion chambers used to detect X-ray intensity at different points along the beamline. This is in contrast to the fluorescence measurements, where the sample is held at 45 degrees from the incidence beam of X-rays towards the germanium detector. For samples with low loadings, as required by the carbon electrodes in the in-operando cell, the fluorescence set-up was used. This can be seen in Figure 21, where the cell is situated in position on the beamline measurement table.

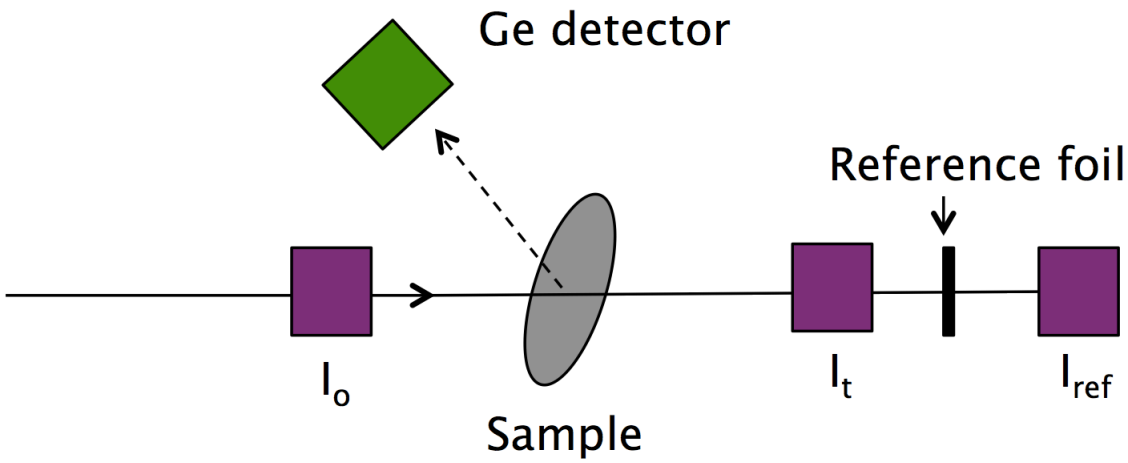

Figure 20: Illustration of the fluorescence and transmission geometry for XAS measurements.

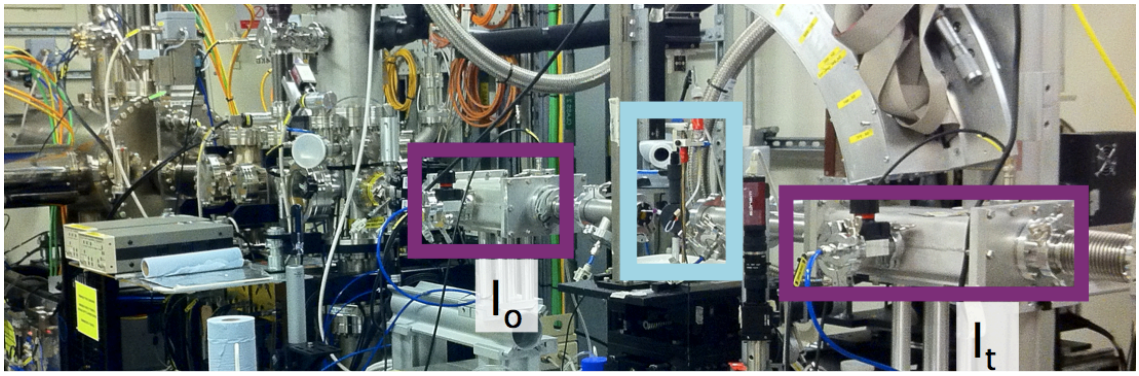

Figure 21: Digital image of in-operando cell (Blue) in position on the B18 beamline.

2.6.3 Cell for in-operando experiments

The development of a new electrochemical cell was required for in-operando synchrotron radiation experiments to measure XANES and EXAFS of mixed metal oxide catalysts. This work was carried out with the help of Peter Richards and Professor Andrea E. Russell, with the cell built at the University of Southampton mechanical workshop by Konstant Venter. The key parameters of the in-operando cell are as follows:

- Wide aperture X-ray transparent window
- Alkali and leak resistant design
- Rapid removal of evolved gas
- Versatile mounting for different beamline configurations

The cell design was based upon previous cells,[21] but provide high volume liquid transfer near to the electrode surface. A peristaltic pump (Masterflex C/L 77120-62) provided a constant stream of electrolyte flowing through the cell to ensure removal of gas during measurements. Fresh electrolyte is introduced at the bottom of the cell, ensuring that a constant flow across the electrode is maintained. A coiled 0.5 mm gold wire was used to make the connection to the working electrode, with a 0.5 mm platinum wire used as counter electrode. Cyclic voltammetry recorded with scan rates above 20 m*Vs.*$^{-1}$ resulted in a large IR drop due to the large distance between working and reference electrodes. All voltammetry in the cell were carried out at a scan rate of 10 m*Vs.*$^{-1}$ or under potentiostatic control for X-ray measurements. The final cell design can be seen on the B18 beamline at Diamond Light Source in Figure 22.

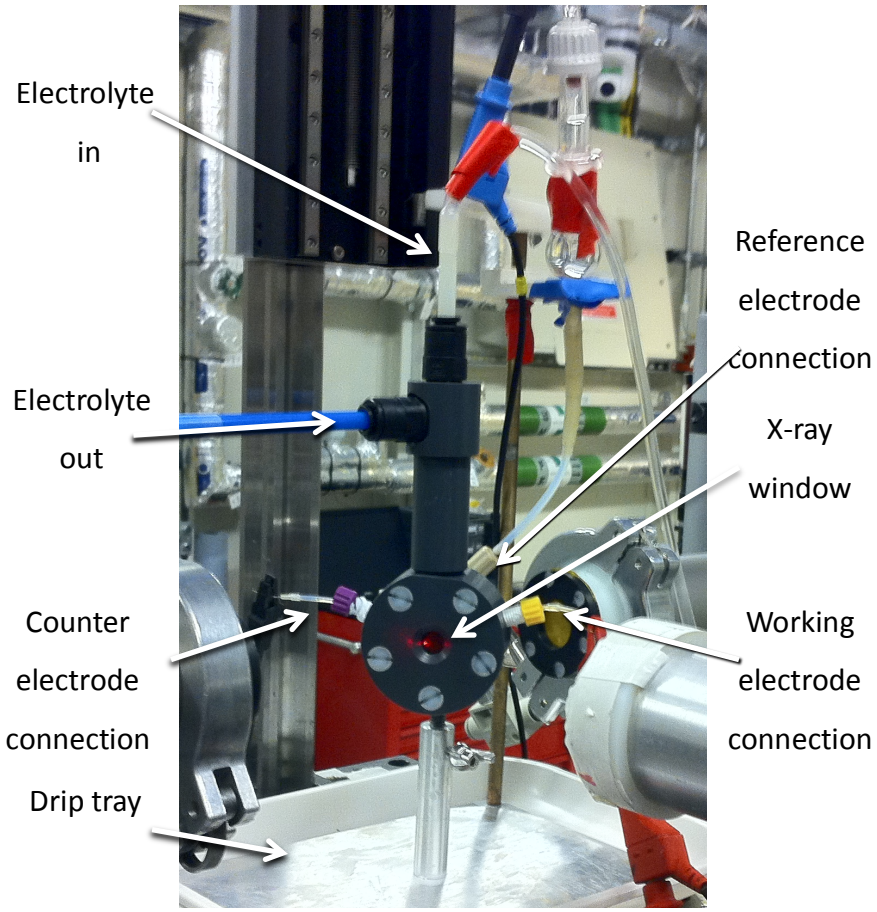

Figure 22: In-operando electrochemical cell for X-ray absorption spectroscopy.

Internal electrolyte flow was key to avoid the accumulation of evolved gas on the electrode. The top push fittings allow a secondary internal tube to pass the incoming fresh electrolyte directly to the base of the cell, at the bottom of the x-ray window. The evolved gas was displaced, by the incoming electrolyte flow, into a large headspace chamber to the electrolyte exit. Flow rates were relatively high during operation to ensure gas bubbles did not build up on the electrode at high overpotential.

2.6.4 Experimental regime for XAS measurements

The standard procedures used in X-ray absorption measurements were two-fold in nature. Powdered samples with a known oxidation state were prepared as pellets. The ex-situ pellets were typically 50 mg of active material and 100 mg Polyethylene powder 10,000 wt.%, homogenised in a pestle and mortar followed by compression at 10 tons, however the composition was adjusted to account for the X-ray absorption of the active material. These pellets were measured in transmission on the beamline with a ruthenium reference foil to provide an accurate energy position for all measurements.

Electrochemical studies were carried out on carbon paper gas diffusion electrodes measured in fluorescence, due to low loading of active material on the electrode making transmission measurements unfeasible. All carbon paper electrodes undergo cyclic voltammetry to confirm electrochemical redox peaks and currents corresponding to the oxygen evolution and reduction reactions occur in at the expected potentials. Secondly potentiostatic measurements were carried out with simultaneous XAS measurements to measure effects of potential on the oxidation state and coordination of the electrocatalysts.

2.7 References:

(1) Patterson, A. *Phys. Rev.* **1939**, *56*, 978–982.

(2) Larson, A. C.; Dreele, Von, R. B. *Los Alamos National Laboratory Report LAUR* **2004**, 86–748.

(3) Toby, B. *J Appl Crystallogr* **2001**, *34*, 210–213.

(4) Rietveld, H. *Acta Cryst.* **1967**, *22*, 151–152.

(5) Rietveld, H. *J Appl Crystallogr* **1969**, *2*, 65–71.

(6) McCusker, L. B.; Dreele, Von, R. B.; Cox, D. E.; Louër, D.; Scardi, P. *J Appl Crystallogr* **1999**, *32*, 36–50.

(7) Brunauer, S.; Emmett, P. H.; Teller, E. *J. Am. Chem. Soc.* **1938**, *60*, 309–319.

(8) Tromans, D. *Hydrometallurgy* **1998**, *50*, 279–296.

(9) Price, S. W. T.; Thompson, S. J.; Li, X.; Gorman, S. F.; Pletcher, D.; Russell, A. E.; Walsh, F. C.; Wills, R. G. A. *J. Power Sources* **2014**, *259*, 43–49.

(10) Broglie, M. de. *Comptes Rendus* **1913**, *157*, 924–926.

(11) Lytle, F. W. *urn:issn:0909-0495* **1999**, *6*, 123–134.

(12) Wende, H. *Rep. Prog. Phys.* **2004**, *67*, 2105–2181.

(13) de L Kronig, R. *Z. Physik* **1931**, *70*, 317–323.

(14) de L Kronig, R. *Z. Physik* **1932**, *75*, 191–210.

(15) Perel, J.; Deslattes, R. *Phys. Rev. B* **1970**, *2*, 1317–1323.

(16) Sayers, D.; Stern, E.; Lytle, F. *Phys. Rev. Lett.* **1971**, *27*, 1204–1207.

(17) Stern, E.; Sayers, D. *Phys. Rev. Lett.* **1973**, *30*, 174–177.

(18) Stern, E. *Phys. Rev. B* **1974**, *10*, 3027–3037.

(19) Lee, P.; Pendry, J. *Phys. Rev. B* **1975**, *11*, 2795–2811.

(20) Rehr, J. J. *Rev. Mod. Phys.* **2000**, *72*, 621–654.

(21) Maniguet, S.; Mathew, R. J.; Russell, A. E. *J. Phys. Chem. B* **2000**, *104*, 1998–2004.

(22) Tang, C. Diamond Light Source - Engineering and Environment - Welcome to I11 http://www.diamond.ac.uk/Beamlines/Engineering-and-Environment/I11.html (accessed Feb 4, 2015).

Chapter 3: Effects of preparation method on the oxygen activity of $NiCo_2O_4$ spinels

This chapter discusses the synthesis of spinel-based electrocatalysts for the oxygen evolution and reduction reactions.

3.1 Introduction

A number of publications have recently focused on the development of pyrochlores[1-4], perovskites[5-13] and spinels[14-17] for their activity, stability and low cost. This work focuses on the use of $NiCo_2O_4$ spinel and understanding the electrocatalytic activity towards oxygen.

3.1.1 Oxygen reduction

The mechanism of the oxygen reduction and evolution reactions are not fully understood. It is proposed to operate via direct 4-electron reduction of the oxygen to hydroxide, or by a two-step 2-electron reduction via the hydrogen peroxide species, HO_2^-, to form hydroxide (Figure 23).

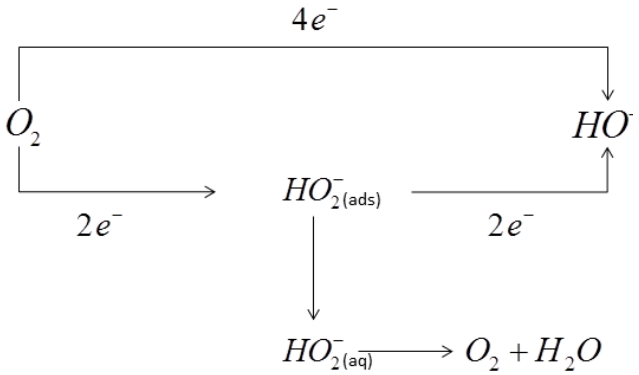

Figure 23: General reaction scheme for the oxygen reduction reaction in alkaline electrolyte.

The oxygen reduction is believed to involve a multiple step mechanism, with platinum operating primarily through the 4-electron pathway and carbon only the first step of the 2-electron mechanism to HO_2^-.[18-21] Mixed metal oxide electrocatalysts with metal-oxygen bonded surfaces have been found to behave differently to those with metallic surfaces such as platinum. The oxygen activity is reported to operate with a key step involving a metal bound hydroxy-oxide species. The same reaction occurring on perovksites has been suggested by Bockris[7], and further refined by Shao-horn[13] to operate as per Figure 24.

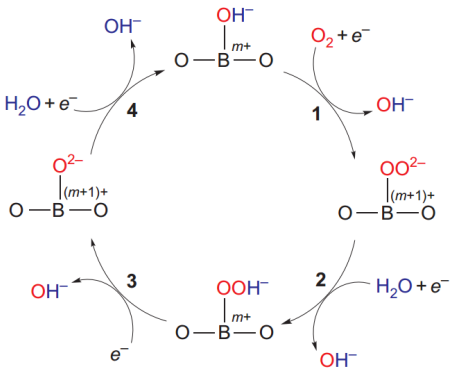

Figure 24: Proposed mechanism for the ORR reaction on perovskite electrocatalysts.[13]

The $NiCo_2O_4$ is likely to operate through similar processes to those suggested for perovskites, whereby multiple charge transfer steps are required to complete the ORR.[22] The mechanism involved on $NiCo_2O_4$ is unclear, however it is reported to provide excellent activity towards both oxygen reduction and hydrogen peroxide reduction.[23,24]

3.1.2 Oxygen evolution

The oxygen evolution reaction mechanism on $NiCo_2O_4$ is less well characterised and thought to operate via an increased oxidation state. The initial step is likely to involve the oxidation of the surface (Equation 17). This initial step in the reaction is the formation of a surface hydroxyl species (Equation 18), followed by conversion to hydrogen peroxide (Equation 19) with a final catalytic decomposition step to water and oxygen (Equation 20) on a tetravalent metal centre.[15] The mechanism shown is in contrast to those proposed by others, whereby the surface hydroxyl reacts with hydroxide to form surface oxides, followed by formation of di-oxygen species, and subsequent loss as oxygen[25], or a similar mechanism as below, but the decomposition of the peroxide is of the HO_2^- species in alkaline electrolyte.[20]

Equation 17

$$\mathbf{M^{2+} \rightarrow M^{3+} \rightarrow M^{4+}}$$

Equation 18

$$\mathbf{M + OH^- \leftrightarrows M - OH + e^-}$$

Equation 19

$$M - OH + OH^- \rightarrow M..H_2O_2 + e^-$$

Equation 20

$$2M..2H_2O_2 \rightarrow 2M + 2H_2O + O_2 \uparrow$$

3.1.3 Structure

Depending on the preparation method, the $NiCo_2O_4$ is reported to contain a mixture of 2+, 3+ and 4+ oxidation states for both the nickel and cobalt.[14,26,27] The distribution of the various oxidations states found in the spinel are inconsistently distributed for nickel and cobalt across the tetrahedral and octahedral sites.[26-33] A general form of $(Co^{3+})_{tet}[Ni^{2+}Co^{3+}]_{oct}O_4$ in an inverse spinel structure encompasses the reported structures. The reported variations in the composition may be derived from poor mixing of the metal salts during the synthesis, producing inhomogeneous mixtures of product, or the use of different thermal treatments. This variation in composition is likely to affect not only the surface species, but also the oxidation states and reactivity of the nickel and cobalt surface.

The spinel has been synthesised by a number of methods including thermal decomposition[16,17], co-precipitation (CP)[14,16], sol-gel[34,35], hydrothermal[36,37] and freeze drying[14,16,38]. The preparation method of the $NiCo_2O_4$ has been shown to affect the oxygen activity of the electrocatalyst.[39] This effect has been explored by considering physical characteristics of the prepared samples. The highest surface areas, 60 - 70 $m^2 g^{-1}$ have been reported when using co-precipitation or cryochemical synthesis methods.[16] The increased surface area of $NiCo_2O_4$ has not been studied in terms of both the oxygen reduction and oxygen evolution activity, leaving a gap in the necessary understanding of spinel-type electrocatalysts activity towards oxygen and their suitability in bi-functional oxygen electrodes.

The conductivity of the $NiCo_2O_4$ has been reported to change with calcination temperature.[16] Samples prepared between 573 K and 673 K produce the highest conductivity of prepared $NiCo_2O_4$ powders. Samples prepared at temperatures greater than 673 K include a NiO impurity, as determined from the XRD pattern. For temperatures greater than 673 K the conductivity reduces, likely caused by the relatively poor conductivity of NiO. The increased conductivity of the lower temperature range samples is believed to be from the pure spinel, with highest conductivities for samples with high surface areas and small crystallites. The smaller particles will pack more efficiently than the larger particles, thereby increasing the number of point contacts and improving the inter-particle conductivity.

The synthesis by co-precipitation of the nickel and cobalt nitrates in sodium carbonate and potassium hydroxide is known to yield a pure phase of the $NiCo_2O_4$. The intermediate species formed during this process however were less clear. Upon initial precipitation an amorphous

nickel/cobalt hydroxy-carbonate structure is formed in addition to NiO. Partial oxidation results in the intermediate formation of a nickel-cobalt hydroxy-carbonate and a loss of NiO. A maximum surface area of 90 $m^2\ g^{-1}$ was reported for samples prepared at the lowest temperatures and with the highest metal-nitrate concentration of 1.2 mol dm^{-3}.[40]

The synthesis method of the $NiCo_2O_4$ electrocatalyst is believed to strongly influence the oxygen activity. Recent reports suggest the composition of the spinel can be altered by the use of different preparation methods. Marco et al. reported synthesis methods can achieve similar nominal compositions, however they show variations of the bulk and surface metal ratios.[27,30,41] The XANES analysis showed the nickel occupying the octahedral sites was a mixture of Ni^{2+} and Ni^{3+}, with the greatest amount of Ni^{3+} observed in the co-precipitated sample. The cobalt on the tetrahedral sites shows a comparable trend with the relative ratio of Co^{2+} and Co^{3+}, with the lowest concentration of Co^{3+} present in the co-precipitation method in comparison to the sol-gel or thermal decomposition methods. A comparison with the XPS suggested the surface of the thermally decomposed samples was enriched in cobalt, whilst the sol-gel produced a nickel enriched surface and an equal ratio of surface nickel and cobalt for the co-precipitated sample. The thermal treatments for these samples were however different, with the co-precipitated calcined at 593 K, in comparison to the thermally decomposed sample at 603 K and the sol-gel sample at 623 K. The increased temperature treatment could explain the nickel enrichment, with the formation of a NiO impurity at these temperatures. This temperature difference may also have influenced the oxidation states of the bulk sample.

The effect of synthesis method of the $NiCo_2O_4$ on the OER reaction was explored by Bocca et al. with a comparison between thermally decomposed, sol-gel and co-precipitated methods.[39] The co-precipitated samples yielded the highest current density for $NiCo_2O_4$ for a given potential.

The addition of alkali and transition metals into the cobalt based structure to enhance the activity has been of intense interest. The addition of lithium into the Co_3O_4 structure has been reported to reduce the OER overpotential, through increased conductivity and an increased proportion of Co^{3+} in the structure.[42,43] The lithium doped samples did suffer deactivation from aging, likely caused by a dissolution of the lithium from the structure.

Further synthesis of ternary metal spinels, reported by Singh et al., focused on modifications to $NiCo_2O_4$.[17,44] The addition of manganese into the structure was found to improve the ORR activity. The addition of lithium and copper resulted in improvements in OER activity when compared with pure Co_3O_4. The doping of copper into $Cu_xNi_{1-x}Co_2O_4$ resulted in the oxidation state of the cobalt remaining constant and significant variation in the nickel. The bulk spinel contained Ni(II), but the sample also included a mixture of NiOOH and NiO with a mixture of Cu(I) and Cu(II) sites.[45] The

enhancement in OER activity can be explained by the increase in the fraction of cobalt atoms in the surface of the structure, which are believed to be the active sites for the cobalt spinels and the addition of NiOOH, which is also an excellent OER catalyst.

Theoretical studies have been carried out on spinels and perovskites to determine trends in the oxygen activity. The activity of perovskites increase with the number of electrons on the B-site atom across the first row transition metals, but unlike the perovskite, the electron filling level has not been suggested as a descriptor for activity towards the ORR or OER for cobalt or nickel-cobalt spinels.[46] For perovskites based upon ABO_3 (A= Lanthanide and B = transition metal) the activity towards oxygen reduction and evolution reactions was linked to the electron density of the transition metal centre occupying the octahedral B-site.[47] The use of different transition metals doped into either the A or B sites on the perovskite affects the electron density of B-site metal-oxygen bond, which is important in both the oxygen evolution and reduction reactions. The mechanism of the ORR and OER on perovskites is believed to operate via surface bound oxygen species. Volcano plots for the OER and ORR reactions were achieved when considering the e_g filling of the B-site metal with the $Ba_{0.5}Sr_{0.5}Co_{0.8}Fe_{0.2}O_3$ (BSCF) and $LaMnO_3$ showing the maximum performance for each respective reaction.[12,13] The OER was optimal with an e_g filling of 1.25, in comparison the ORR obtained the highest activity with e_g filling of 0.75. The e_g orbital of the metal provides an interaction with the O-2p_σ orbital of the oxygen, which is reported to provide a characteristic for the activity towards the oxygen reactions. The difference in the optimal level for e_g filling highlights the difficulty in the selection of bifunctional electrocatalysts. It would be of interest if such a relationship for electron filling and oxygen activity can also be found in spinel-based electrocatalysts.

Beyond electronic effects of the bulk and surface structure, the effect of particle size has been explored on Co_3O_4 for the oxygen evolution reaction. A comparison of samples with a particle size of approx. 50, 100 and 150 nm show an increased surface area results in an increased current from oxygen evolution throughout the potential range for the OER.[25] Therefore catalyst development should aim for the highest possible surface area to take advantage, however the impact the surface area has on the ORR is unknown.

With the advent of numerous hard- and soft-templating methods the morphology of particles has become an area of great interest. Several studies have used hard-template, sol-gel and hydrothermal synthesis methods in an attempt to control the nanostructure of the spinel. Nano-cubes[48], spheres[36,49], wires[50-52], rods[53,54], core-ring[55] and roughened structures[37,56-59] have been reported in the literature. These structures typically provide high surface areas, however little is known regarding the influence on the oxygen activity as a result of these changes. The

comparison for several preparations of $NiCo_2O_4$ would suggest that particle size and not morphology is the most influential factor on sample conductivity, but little information extends to oxygen catalysis on such samples.[16]

Recent theoretical studies using density field theory calculations have suggested the active species for the OER reaction on Co_3O_4 to be CoOOH.[46] The addition of either nickel (x= 0.36) or vanadium (x=0.5) into the $Co_{3-x}O_4$ resulted in the lowest overpotentials for the OER. The theoretical increase in oxygen activity of a cobalt spinel with a nickel dopant agrees with experimental results with the lowest overpotentials observed for samples of $NiCo_2O_4$, whilst no experimental studies are available for the vanadium-doped spinel.

The work in this chapter will focus on exploring the oxygen reduction and evolution reactions on $NiCo_2O_4$. A comparison will be made of alternate preparation methods of the spinel and how these may impact both the ORR and OER activity. The $NiCo_2O_4$ samples have been characterised, both physically and electrochemically, to assess their suitability as ORR and OER electrocatalysts in metal-air batteries.

3.2 Preparation methods

3.2.1 Reagents

Table 5 details the materials and reagents used in this work, along with their respective suppliers.

Table 5: List of reagents and materials used including suppliers.

Material/Reagent	Supplier
Aqueous Nafion® solution (10.85 % solids)	Johnson Matthey
Cobalt Nitrate (ACS reagent > 98 %)	Sigma-Aldrich
Isopropyl Alcohol	Fischer Scientific
Methanol (HPLC grade)	Sigma-Aldrich
Nickel Nitrate (Puriss, > 98.5 %)	Sigma-Aldrich
Potassium Hydroxide (> 98 %)	Sigma-Aldrich
PTFE Suspension (60 wt.%)	Sigma-Aldrich
Sodium Bicarbonate (> 97 %)	Fisher Scientific
Water (18 MΩ cm)	Purite water purifier

3.2.2 Nanoparticle synthesis by thermal decomposition (TD-H_2O or TD-MeOH)

A solution of $Ni(NO_3)_2.6H_2O$ (14.539 g) and $Co(NO_3)_2.6H_2O$ (29.103 g) in 100 mL of H_2O (or methanol) was stirred and subsequently evaporated to dryness (373 K). The resulting deep red powder was ground to ensure homogeneity and calcined at 648 K in air. The powder was re-ground and passed through a 50 μm sieve, yielding a fine black powder as product.

3.2.3 Nanoparticle synthesis by CP in potassium hydroxide/sodium carbonate (CP-OH)

Co-precipitation of nanoparticles was carried out to yield a mixture of nano-spheres, rods, and platelets of the mixed metal oxides. The synthesis of $NiCo_2O_4$ is detailed below.

$Ni(NO_3)_2.6H_2O$ (14.5395 g) and $Co(NO_3)_2.6H_2O$ (29.103 g) were added to 100 mL of water (forming a deep red solution). A separate solution of Na_2CO_3 (52.995 g) and KOH (56.11 g) in 1.5 L H_2O was prepared (colourless). The metal nitrate solution was added drop-wise to the vigorously stirred hydroxide/carbonate solution (initially blue, then to green opaque suspension). The resulting solution was heated (353 - 363 K) for 20 hours. The suspension was filtered through a 0.02 μm polyamide filter (Whatman) under vacuum, and washed with 1 L of H_2O. The solids were dried in air (373 K), ground to a fine powder and then calcined at 648 K in air for 4 hours. The resulting black powder is ground for a final time to form a homogenous product of $NiCo_2O_4$.

3.2.4 Nanoparticle synthesis by CP in ammonia (CP-Am)

$Ni(NO_3)_2.6H_2O$ (1.4536 g) and $Co(NO_3)_2.6H_2O$ (2.9094 g) was added to 200 mL of water (red solution). The pH was adjusted to 10 by addition of ~ 30 % ammonia solution. The solution was transferred to an evaporating dish and heated (353 K), to dryness (dark red gel). The gel was then transferred to a crucible with a lid and decomposed and calcined at 648 K in air for 4 hours. The resulting black powder was ground to a fine homogenous product.

3.3 Physical characterisation

This section will discuss the physical properties of the prepared electrocatalysts.

3.3.1 TEM

All samples were characterised by electron microscopy techniques to determine particle size and elemental composition. Transmission electron micrographs of the samples of $NiCo_2O_4$ prepared by the methods outlined previously are shown in Figure 25. The micrographs show agglomerations of nano-sized particles of irregular polygonal shape, with the exception of the CP-OH sample where linear rod agglomerations were also present.

Initial SEM results appeared to suggest all samples were prepared with a particle size of 2-20 μm, however at higher magnification it was difficult to clarify the particles size due to appearance of 'soft' edges on the particles. Using TEM the larger particles observed on the SEM were agglomerates composed of smaller particles. The particle size for co-precipitated samples (CP-OH & CP-Am) was found to be approximately 10 – 20 nm, with agglomerated particles ranging from 200 – 2000 nm. The hydroxide-precipitated samples however show additional rod like morphologies in the sample ranging 100 to 500 nm in length and 15 – 100 nm in diameter. The rod like structures consist of agglomerated smaller particles, suggesting that they may be formed by an additive/agglomeration/aging process during the synthesis of the smaller 10 nm particles.

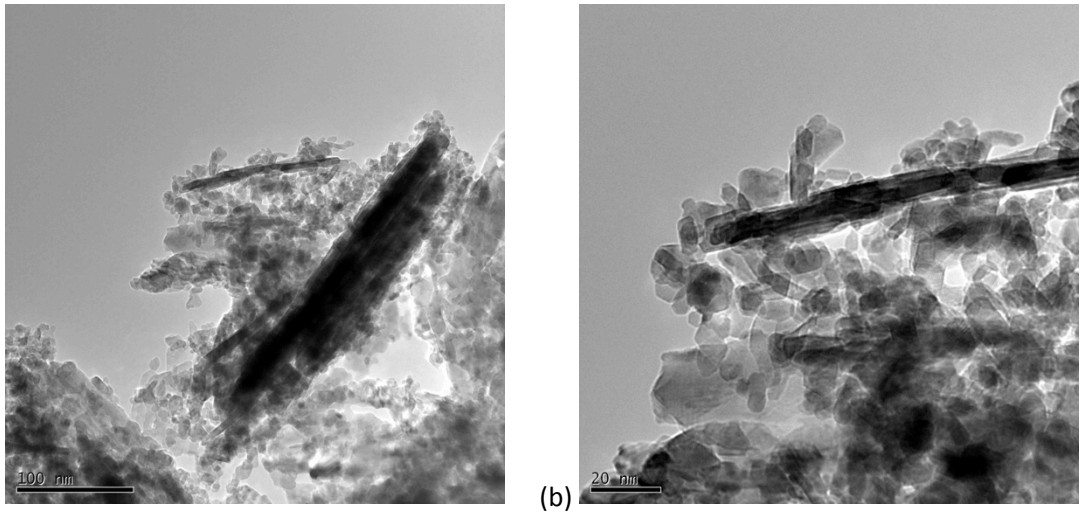

Figure 25: TEM micrographs of $NiCo_2O_4$ sample CP-OH (a & b) at a scale of100 nm (left) and 20 nm (right), prepared on copper grids.

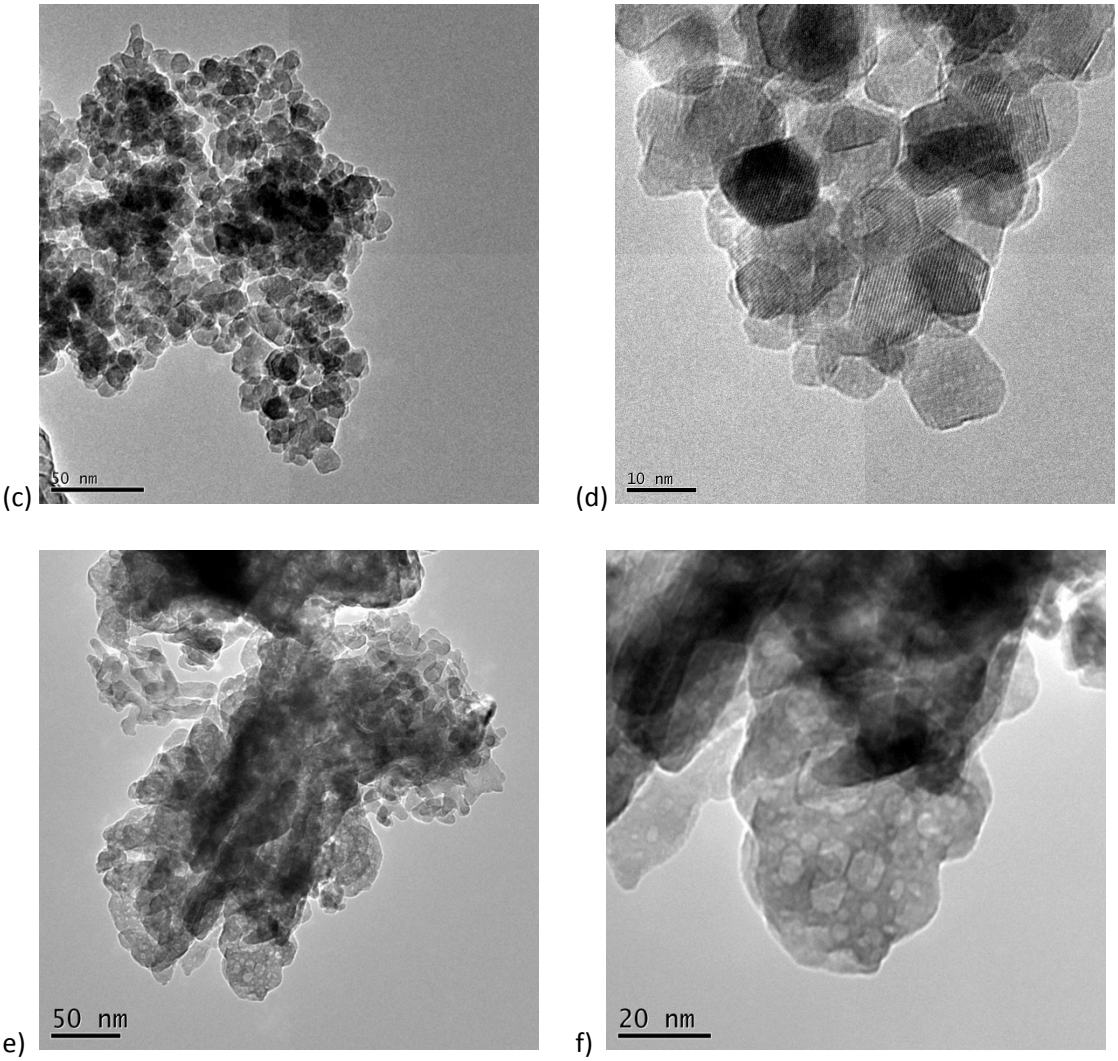

Figure 25 continued: TEM micrographs of $NiCo_2O_4$ sample CP-Am (c & d) and TD_H_2O (e & f) with scale bars of 50 nm on the left and 10 or 20 nm on the right. Prepared on copper grids.

Catalyst synthesis by thermal decomposition methods resulted in larger particles sizes (Figure 25 e – f) (Table 6). The particle shape is less ordered and controlled with size varying by 10 – 50 nm. None of the thermally decomposed samples yielded rod like structures, but appear to provide more compact agglomerates than the co-precipitated samples. The thermal stability of the $NiCo_2O_4$ spinel is limited to 673 K, above this point NiO is reported to form.[14]

The TEM provides an means for establishing the size of individual particles, as it provides high resolution images at small nm or sub nm range. The technique is limited, most notably by focusing on isolated particles . The results can be influenced by the preparation method transferring the sample onto the grids, which may exclude larger particles present in the sample.

The particle size of the agglomerate material was analysed using a second method, disc centrifuge particle analysis, was used to confirm particle size measurements on the catalyst. The powders were suspended in a carrier liquid, the suspension transferred onto a rotating plate where the particles were carried out distances proportional to their particle size, (Table 6). The particles separate across the optically clear rotating plate and accumulate as sediment at the edge. The shadowing effects are detected by a continuous light sensor and its signal used to calculate the particle size distribution. An example of the results for the $NiCo_2O_4$ can be seen in Figure 26.

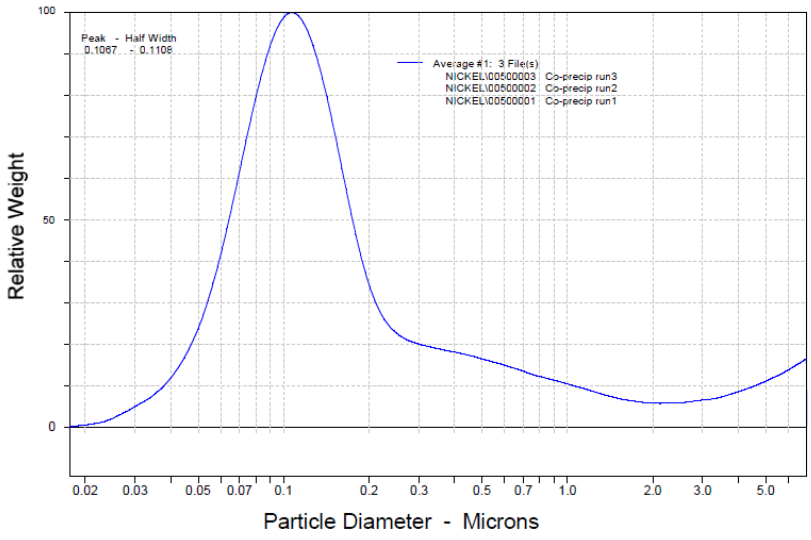

Figure 26: Results of particle size analysis for $NiCo_2O_4$, prepared by the CP –OH method.

Table 6: Particle size analysis of different preparations of $NiCo_2O_4$, characterised by disc centrifuge.

Sample	Primary peak / μm	Secondary peak / μm
TD - H_2O	0.655	3.052
TD – MeOH	0.721	-
CP – Am	0.195	0.852
CP – OH	0.107	-

Particles size distributions for all samples are submicron, with the exception of TD–H_2O. The smallest particles are observed in the co-precipitated samples averaging 150 nm. In comparison, thermally decomposed samples average 700 nm. A secondary minor peak is observed at 750 nm in the CP–Am sample suggesting the particles are distributed over two major particles sizes. The TD–H_2O sample provides a major peak at 650 nm, but also a minor peak at 3 μm. From the TEM results small spherical particles were observed to agglomerate into larger bulk particles. It is therefore likely the secondary peak is formed of large agglomerations of smaller particles.

3.3.2 BET

The specific surface areas of $NiCo_2O_4$ catalysts, prepared by the various methods outlined above, were determined by BET theory as outlined in Chapter 2. The surface area measurements, outlined in Table 7, are consistent with those previously reported in the literature.[14,60] The thermally decomposed methods produce a $NiCo_2O_4$ with relatively low surface areas of the order 10 $m^2 g^{-1}$. In comparison, the co-precipitation methods yield $NiCo_2O_4$ with higher surface area 50 - 70 $m^2 g^{-1}$.

The results from XRD and TEM suggest the samples with higher surface area also have smaller crystallite and particle sizes. The increased surface area is in agreement with the disc centrifuge measurements. Thermally decomposed samples yielded particle sizes of 700 – 800 nm; in comparison the co-precipitated samples were 100 – 300 nm. An alternative explanation for the increased measured surface area is an increased porosity in the sample.

Table 7: Surface area, as determined by BET, of $NiCo_2O_4$ samples prepared by thermal decomposition and co-precipitation methods.

Sample	Surface area / $m^2 g^{-1}$
TD – H_2O	6.8
TD – MeOH	13
CP – Am	48
CP – OH	68

3.3.3 X-ray Diffraction

Rietveld analysis of the whole diffraction pattern was carried out for the $NiCo_2O_4$ prepared in this work. Analysis was carried out using GSAS software, and fit against crystallographic standard patterns available on the ICSD database. Further details on the fitting procedure are outlined in methods section 2.1.3.

The spinel crystal structure is ideally composed of a close packed cubic structure, with the cations present in 8 tetrahedral co-ordinated A sites, 16 octahedral co-ordinated B sites relative to the 32 oxygen anions.[61,62] The possibility of multiple oxidation states occupying both tetrahedral and octahedral sites, increased the complexity of the structure, requiring the differentiation between 'normal' and 'inverse' spinel structures. The 'normal' structures are described with $X^{2+}[Y^{3+}]O_4$ or $X^{4+}[Y^{2+}]$ in the respective $A_{Tet}[B_{Oct}]O_4$ sites, and 'inverse' is possible through sharing of the octahedral sites by $Y^{3+}[X^{2+}Y^{3+}]O_4$ or $Y^{2+}[X^{4+}Y^{2+}]O_4$ of the spinel structure. [63-65]

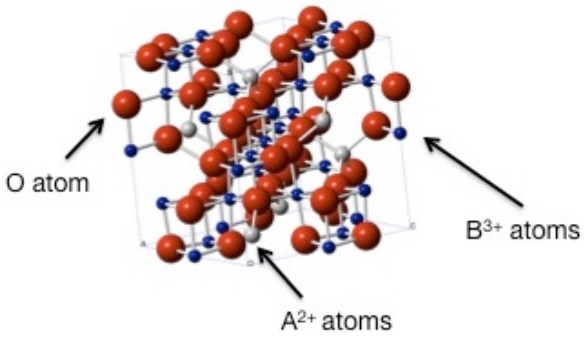

Figure 27: Crystal structure of $NiCo_2O_4$ spinel, Oxygen (Red), Tetrahedral A-site (white), Octahedral B-sites (Blue).

In the case of Co_3O_4, an inverse spinel structure is apparent with the A-site filled with Co^{3+} ions, whilst the B-site would be composed of Co^{2+} and Co^{3+}.[66] $NiCo_2O_4$ follows a similar structure with the presence of $Co^{3+}[Ni^{2+}Co^{3+}]O_4$, however, this simple description has been elaborated by recent studies in the literature.[14,30,32] The oxidation states and location of each metal centre on either a tetrahedral or octahedral sites have been shown to vary, with the main variable being the synthesis method.

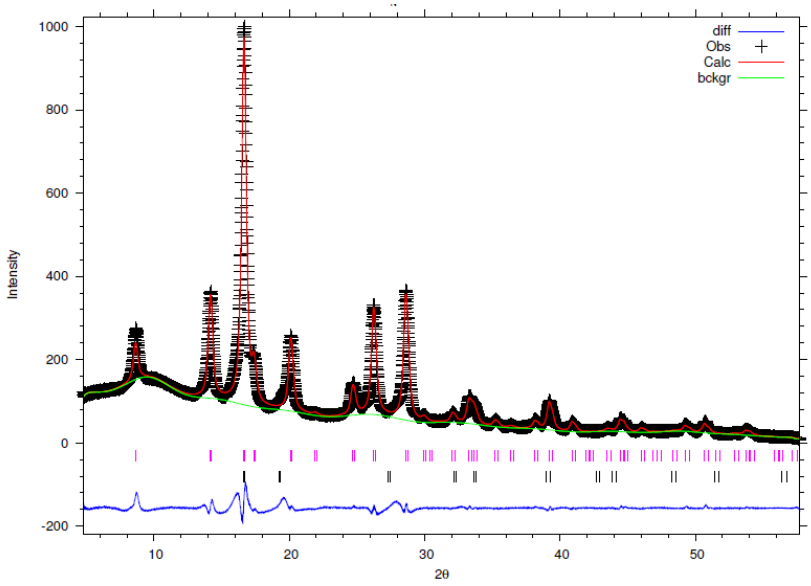

Figure 28: XRD pattern of $NiCo_2O_4$ (Black cross), background fit (Green line), Rietveld refinement fit (Red line), $NiCo_2O_4$ peaks (pink dashes), and difference between measured and fitted pattern (blue line).

The measured diffraction patterns of the $NiCo_2O_4$ (Figure 28) agree with a pure spinel crystal structure. The unit cell of $NiCo_2O_4$ prepared by CP-OH was 8.10 Å, in comparison the samples prepared by thermal decomposition resulted in a slightly larger unit cell of 8.11 Å. The pure cobalt Co_3O_4 structure results in a reduced unit cell to approx. 8.08 Å, and the $NiCo_2O_4$ approx. 8.11 Å.[16,17] The small contraction in the lattice parameter of the sample CP-OH is reported with a larger degree of error than other samples, due to the smaller crystallite size and difficulty fitting the broadening peaks. The ICP results found the CP-OH sample to have the lowest concentration of impurities; this may also allow a slight relaxation of the structure, in comparison to others samples with greater impurities, which may have incorporated into their structure. Another explanation would be, if the sample was nickel deficient, some inhomogeneity would be possible producing a mixture of overlapping peaks for $NiCo_2O_4$ and Co_3O_4.

Table 8: Results from Rietveld refinement of powder diffraction patterns of $NiCo_2O_4$ samples.

Sample	Crystallite size / nm	Lattice parameter (a = b = c) / Å	wRp / %	Rp / %
TD – H_2O	87.4 ± 4.1	8.115	2.6	2.1
TD – MeOH	46.3 ± 3.4	8.111	3.0	2.7
CP – Am	13.8 ± 0.6	8.112	2.1	2.1
CP – OH	9.5 ± 0.9	8.103	5.2	4.5

*Note: Lattice parameter for pure Co_3O_4 is 8.08 Å.[16,17]

3.3.4 Elemental analysis

Elemental analysis was carried out by inductive coupled plasma optical emission spectroscopy (ICP-OES). Medac Ltd. carried out all sample analysis in accordance with standard sample digestion and analysis procedures.

Table 9: Elemental analysis of $NiCo_2O_4$ by thermal decomposition and co-precipitation methods, as determined by ICP-OES.

Catalyst	Nickel / wt. %	Cobalt / wt. %	Co/Ni ratio	Impurities / ppm		
TD – H_2O	22.90	48.73	2.12:1	Ca – 130	Na – 220	K – 174
TD – MeOH	23.77	48.87	2.05:1	Ca – 247	Na – 1700	K – 1300
CP – Am	25.01	45.75	1.83:1	Ca – 212	Na – 699	K – 1700
CP – OH	22.99	49.03	2.13:1	Ca – 436	Na – 69	K – 61
Co_3O_4	-	68.80	-	Ni – 414	Ca – 513 Na – 394	K – 432

The results show that the ratio of cobalt to nickel for all samples is close to the ideal ratio of 2:1 (Table 9). However, each preparation results in a small variation in this ratio. The TD–MeOH sample is close to ideal with a ratio (Table 9) and the TD-H2O and CP-OH both have a slight excess of cobalt, but the CP–Am sample is rich in nickel. The results suggest a deficiency in the nickel doping of the TD–H_2O and CP–OH, whilst the CP–Am sample shows significant excess. The presence of NiO in the catalyst is therefore likely from different rates of precipitation for the two

metals in the case for co-precipitated samples, whilst if it was found in the thermally decomposed samples equally, then the calcination temperature is likely the cause.

Table 10: Empirical formula derived from the ICP results, normalised to four oxygen atoms in the structure.

Catalyst	Nickel	Cobalt	Oxygen
TD – H_2O	0.88	1.87	4
TD – MeOH	0.96	1.96	4
CP – Am	0.94	1.71	4
CP – OH	0.90	1.91	4
Co_3O_4	-	2.40	4

The empirical formulas derived from the ICP results suggest the samples are deficient in metal in all examples and this is most apparent in the pure cobalt sample. This may be due to the formation of oxygen rich impurities in the sample, errors in the ICP calibration for samples with high concentrations of cobalt, or differences in water content of the samples. Assuming that the ICP analysis by Medac Ltd. was correctly analysed, it is likely that a small proportion of NiO_x and CoO_x is present in all samples. This was not obvious on the XRD results, suggesting that if such material was present it is not crystalline.

The same samples were analysed by SEM-EDX to determine the concentration of cobalt and nickel in the sample (Table 11). The results from the EDX suggest that a slight excess of nickel is present in all samples. Oxygen is excluded from the quantification due to poor sensitivity of the technique for analysing light elements. The ratio of nickel and cobalt is correct at 1:2 when considering the error of 2 – 5 wt.% for the technique.

Table 11: Nickel and cobalt composition as determined by SEM-EDX for $NiCo_2O_4$ samples.

Sample	Cobalt / wt.%	Nickel / wt.%
TD-H_2O	55.0	28.2
TD-MeOH	61.7	36.3
CP-OH	63.2	36.8
CP-Am	61.9	34.8

3.4 Electrochemical characterisation and performance

This section will discuss the electrochemical response of the synthesised mixed metal oxide catalysts. The electrochemical characterisation of catalyst materials was carried out, as outlined in methods section 2.2.

Thin-film catalyst layers were formed on glassy carbon, with subsequent measurements for activity of oxygen reduction and evolution reactions on glassy carbon rotating disc electrodes (RDE) with a Nafion® binder. In chapter 4, the application of these active materials onto gas diffusion electrodes and their stability under cycling will be further discussed.

3.4.1 Cyclic voltammetry

The cyclic voltammetry of $NiCo_2O_4$ in alkaline electrolyte produces four distinct regions (Figure 29). This example of the electrocatalyst is prepared on a gas diffusion electrode to provide an increased current during the oxygen reduction reaction. The oxygen reduction occurs in section (a), typically at potentials negative of 0 V *vs.* Hg/HgO. The double layer for these samples is relatively small, encompassing section (b). The electrocatalyst produces a redox couple in potential range (c), which is likely to be related to the Ni^{2+} to Ni^{3+} and Co^{3+} to Co^{4+} transitions termed M-O/M-OH henceforth, with equally sized anodic and cathodic peaks. The exact nature of this peak is still under discussion.[15,39,42,67,68] Finally, section (d) corresponds to the current obtained during the oxygen evolution reaction.

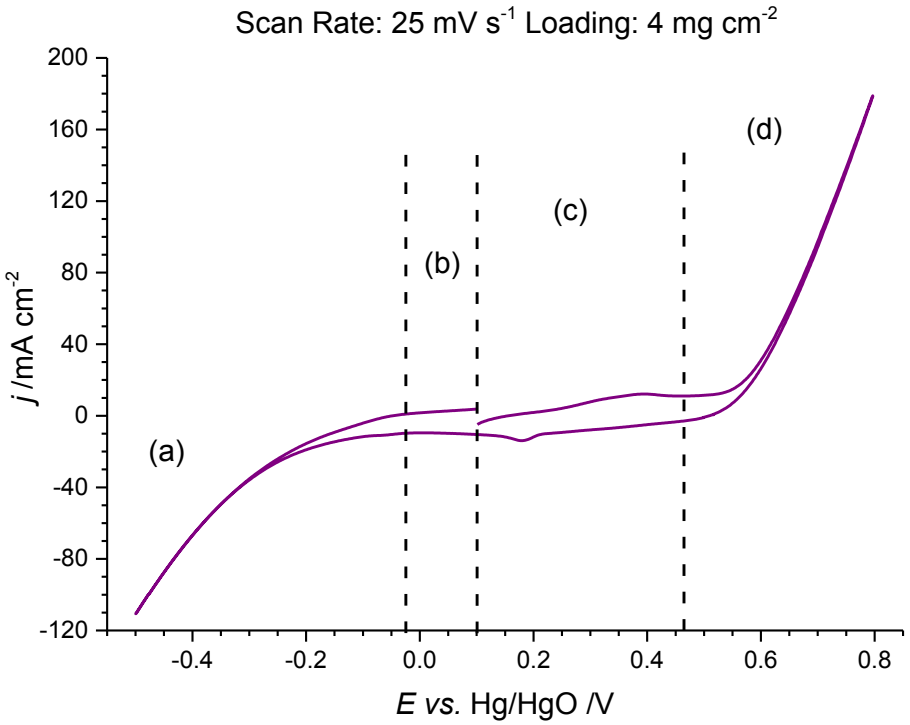

Figure 29: CV of $NiCo_2O_4$ (10:3 Catalyst to PTFE) on carbon paper GDE in 8 M KOH at 333 K with 200 cm^3 min^{-1} O_2.

The cycling stability of the electrocatalyst was evaluated by comparing the first cycle of the CV and the 10^{th} cycle (Figure 30). The voltammetry shows the redox couple occurring at 450 mV on the anodic sweep, for the oxidation of the Co^{2+} to Co^{3+}, with the reverse true for the cathodic sweep at a peak at 390 mV. With subsequent cycling the redox couple occurs at the same potential with each cycle, suggesting the chemical species involved are not changing, nor is a resistive film being formed (Figure 30).

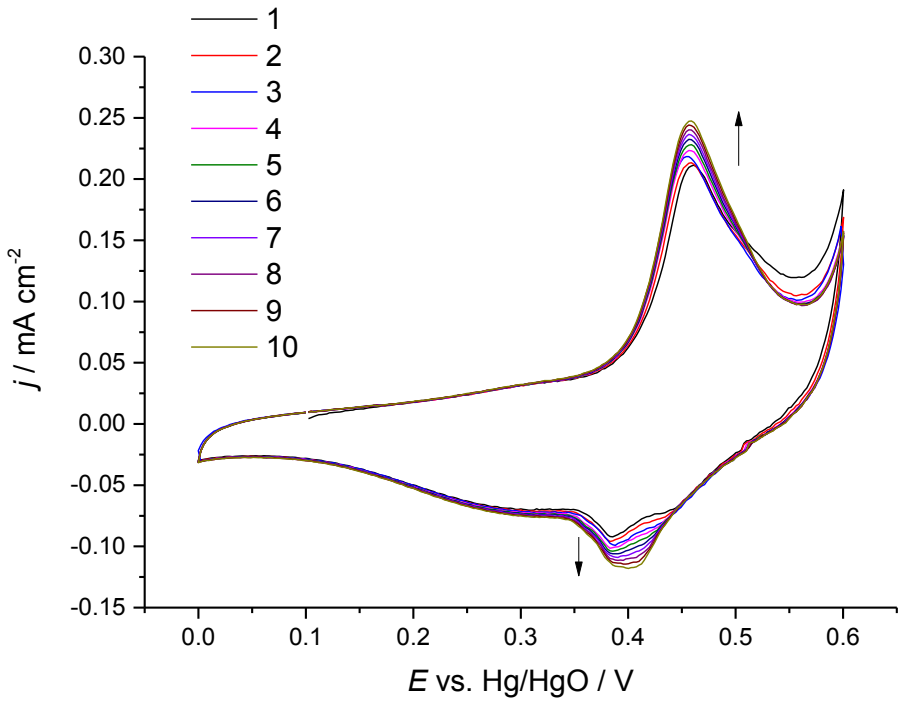

Figure 30: Cyclic voltammogram of $NiCo_2O_4$ (15 µg) drop cast on glassy carbon electrode (0.2 cm^2); measured in oxygen saturated 1 M KOH, 298 K at a scan rate of 10 mV s^{-1}.

The charge from the oxidation peak is equal to that of the reduction peak, when accounting for a small overlap with the OER during the anodic sweep and including the broad reduction peak centred at 390 mV, but extending down to 170 mV. The balancing of charge during the oxidation and reduction is expected for the surface oxidation state of the spinel. Furthermore, the peak current was found to be proportional to scan rate, consistent with a surface process. When comparing the 1st and 10th cycles a small increase in the current is observed, however, the change is negligible and the layer deemed stable. The small variation may be due to a surface roughening from cycling into the region where oxygen evolution may take place, but the change in the peak shape may indicate a change in the oxidation state of suface species.

Although the charge passed, corresponding to the M-O/M-OH redox couple at 450 mV, was found to slowly increase with cycling, the onset of the oxygen evolution reaction was independent of this process.[69] The spinel surface oxidation peak complicates the determination of the precise onset potential of the OER reaction, due to the slight overlap between 500 and 600 mV. The OER is further studied under steady state conditions in section 3.4.5.

There is a noticeable change in the open circuit potential (OCP) when cycling the $NiCo_2O_4$ (Figure 31). This behaviour is one of the reasons for this material also being of interest as a supercapictor; this pseudo-capacitance stems from the M-O/M-OH surface species, suggesting that the materials

oxidation state of the material is being altered. After oxygen reduction, the open circuit potential is observed to rapidly return to a value close to 0.16V; however, after the oxygen evolution, the slow return to the OCP suggests a slow reaction of the surface with the electrolyte until the original oxidation state is achieved, which is beyond 100 seconds.

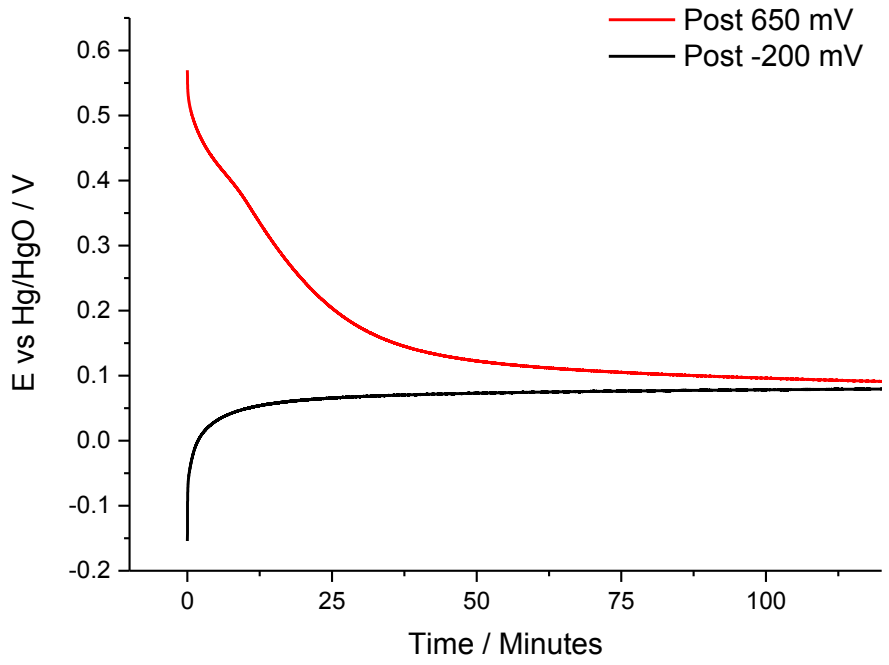

Figure 31: Open circuit potential post oxygen evolution (0.6 V *vs.* Hg/HgO for 60 seconds) and reduction (-0.2 V *vs.* Hg/HgO for 60 seconds) for $NiCo_2O_4$ on GC electrode in oxygen saturated 1 M KOH at 298 K.

The observed redox couple was then probed further by the use of varied scan rates. The CV was carried out with scan rates ranging 10 mV s^{-1} to 300 mV s^{-1} as seen in Figure 32. The cathodic and anodic peaks increase linearly with scan rate, suggesting the reaction is a surface reaction.

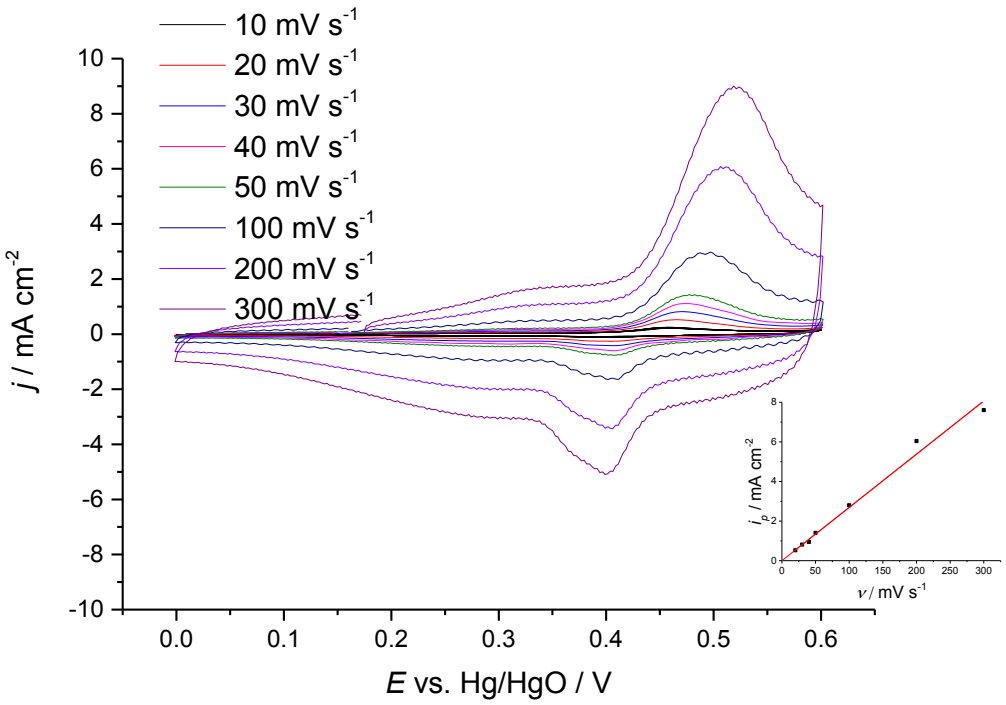

Figure 32: CV of $NiCo_2O_4$ (15 µg) on GC (0.2 cm^2), in nitrogen purged 1 M KOH, 298 K at varied (10 – 300 mV s^{-1}) scan rates. Insert a plot of peak current against scan rate (i_p *vs.* ν).

Voltammograms for the electrodes using other preparations of $NiCo_2O_4$ and Co_3O_4 are shown in Figure 33. The CP-Am sample produces two redox couple peaks at 380 mV and 480 mV. The voltammetry reported in the literature shows a wide range of responses,[14,16,39,45] where it is not uncommon to observe a similar broad double set of peaks. The current response for the CP–OH sample (Figure 30) yields a higher current for the corresponding redox couple than other samples (Figure 33), indicative of an increased surface area, in agreement with the BET results. All electrodes were prepared using the same mass of catalyst in the ink. The mass loading will vary due to the process used in casting catalyst films, however the major contribution is suggested to be the surface area of each preparation.

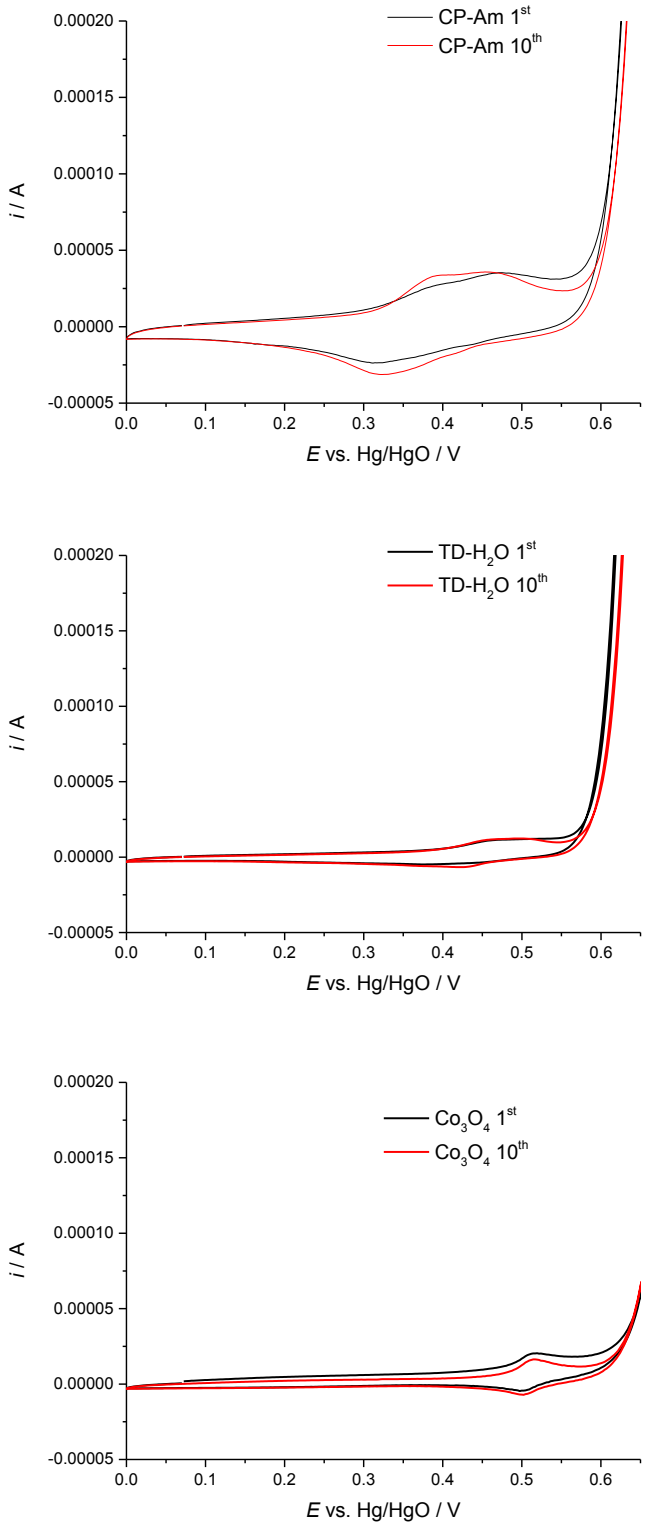

Figure 33: CV of $NiCo_2O_4$ prepared by CP–Am (Top), TD–H_2O (Middle) and CO_3O_4 by thermal decomposition (Bottom) in 1 M KOH, with 15 µg of catalyst on 0.2 cm^2 GC RDE, 10 mV s^{-1} sweep rate.

The current was normalised to the surface area of each sample, as measured using BET. The resulting plots are shown in Figure 34. The electrochemical response shows a similar, if

complicated trend. Peaks for the nickel and cobalt oxidation are observed at 0.40 and 0.46 V. The magnitude of the current observed from the CP-Am sample is lower than either the TD-H_2O or CP-OH samples. The changes in peak position and current intensity observed in the CVs suggest different surface sites/quantity of sites that are accessible depend upon the synthesis method. The thermally decomposed sample also appears to have the lower overpotential for the oxygen evolution reaction, when the activity is normalised to surface area. Although maintaining the activity, whilst increasing the surface area to that of the CP-OH samples may not be a simple process.

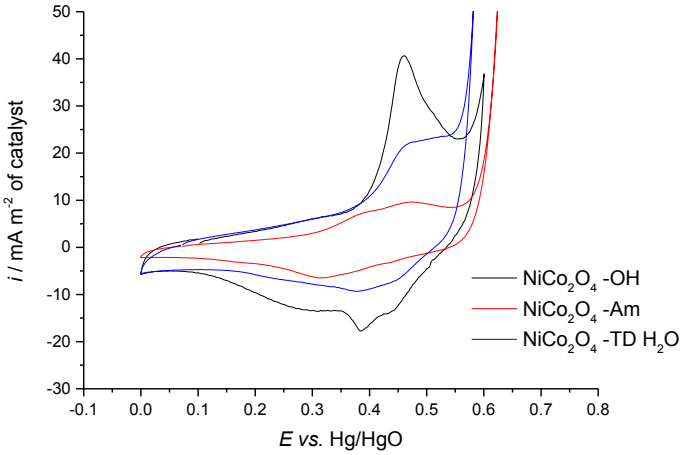

Figure 34: Plot of the CV for $NiCo_2O_4$ prepared by CP-OH, CP-AM and TD-H_2O. CV measured between 0 and 0.65 V *vs.* Hg/HgO, 10 mV s^{-1} sweep rate in 1 M KOH at 298 K. Current normalised to BET surface area. Each thin-film prepared consisted of a 15 ug cm^{-2} catalyst loading.

3.4.2 Oxygen reduction mechanism

Thin-film catalyst layers on glassy carbon rotating disc electrodes were used to study the oxygen reduction reaction activity. This technique allows the separation of kinetically controlled and mass transport controlled region. The thin catalyst layer was prepared as outlined in section 3.2.

The linear sweep voltammetry for $NiCo_2O_4$ is reported in Figure 35, with carbon and platinum black included for reference under the same conditions. All electrodes provide a sigmoidal response with clear plateaux regions. The resulting three regions of the voltammograms are described by, (i) kinetically controlled; (ii) mix controlled; and (iii) mass transport controlled currents.

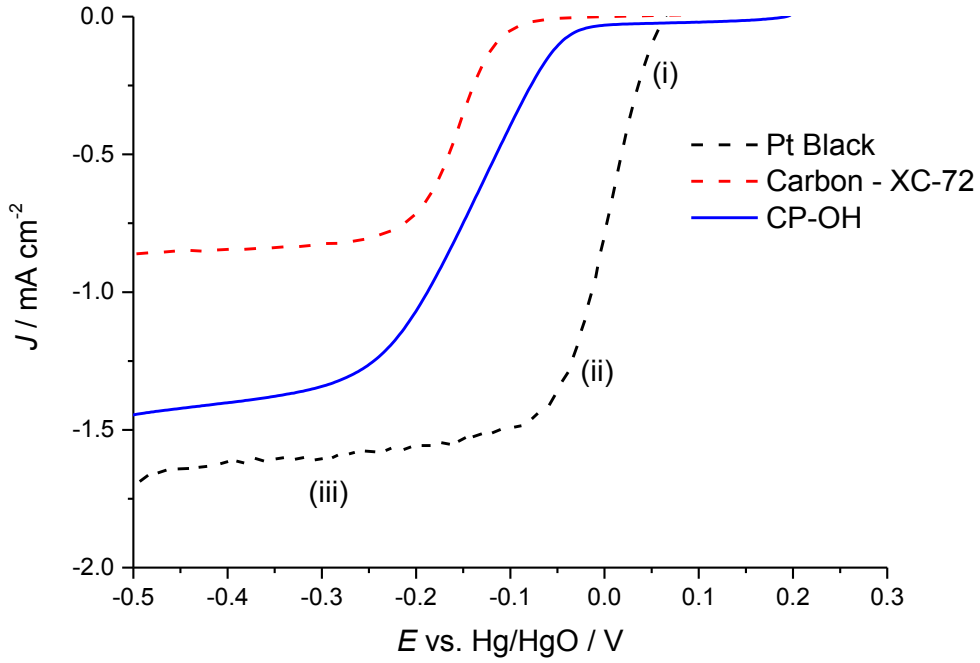

Figure 35 : Linear sweep voltammograms of Pt (Black), Carbon (Red), $NiCo_2O_4$ (Blue) in oxygen saturated 1 M KOH at 298 K. Catalyst loading fixed at 15 µg on 0.2 cm^2 GC RDE and 10 mV s^{-1} sweep rate.

As explained previously (Section 3.1.1) platinum catalyses the 4-electron reduction, whilst carbon results in a 2-electron reduction. The polarisation curve (Figure 35) obtained from the $NiCo_2O_4$ demonstrates its effectiveness as an ORR catalyst, with the lowest overpotential of the synthesised catalysts without carbon or precious metals. A large overpotential for the ORR on carbon is observed, in comparison to platinum, due to the low activity of carbon as an oxygen catalyst.

The limiting current for carbon corresponds to the 2-electron oxygen reduction to hydrogen peroxide. Twice the limiting current is observed for platinum, which is able to catalyse the 4-electron reduction of oxygen. A suitable catalyst to replace platinum must aim to achieve similar 4-electron efficiency per oxygen molecule. Further analysis of the limiting currents for the carbon and platinum showed the square root of varied rotation rates (Levich Plots) provide a linear response that does not pass through the origin (Figure 36).

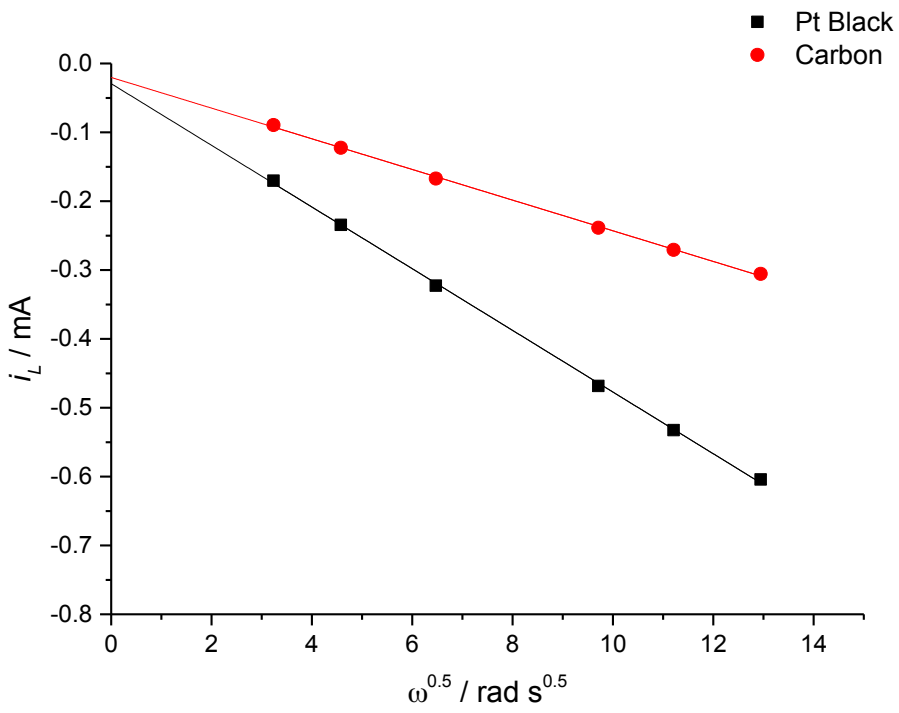

Figure 36: Levich plot of Pt black and carbon on GC RDE in 1 M KOH at 298 K. Catalyst loading 15 µg, 0.2 cm^2 GC RDE, sweep rate 10 mV s^{-1}.

The theory would predict that a linear response is observed that passes through the origin, if the platinum and carbon catalysts are under pure mass transport limitation. To deviate from a zero intercept, it would suggest the measurement is not under ideal mass transport control, with either a kinetic limitation or diffusional limitation distorting the results. The platinum and carbon catalysts are expected to operate with negligible kinetic limitations for this reaction when in the mass transport control region of -0.5 V. The diffusion through the thin film of Nafion is expected to be negligible. If a diffusion limitation was distorting the intercept, any effect it may have on the results should be consistent, as the same catalyst ink formulation was used in preparing all samples in this chapter.

The limiting current for the $NiCo_2O_4$ sample, unlike the carbon or platinum black, results in a shallow slope during the polarisation curve (Figure 35). The response of the limiting current with the square root of varied rotation (i_L *vs.* $\omega^{1/2}$) rates is not linear, nor does it pass through the origin, demonstrating the reaction is not wholly mass transport limited. Further analysis of the RDE data by Koutecky-Levich plots ($1/i_L$ *vs.* $1/\omega^{1/2}$) is reported in Figure 37.

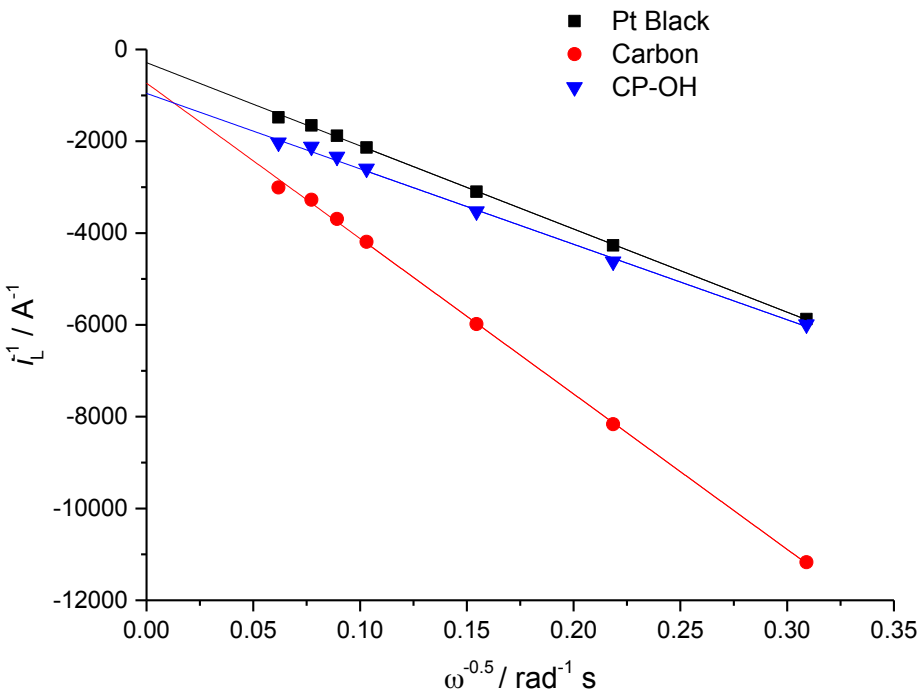

Figure 37: Koutecky-Levich plot for the ORR on thin-film electrodes at varied rotation rates in oxygen saturated 1 M KOH at 298 K. Catalyst loading 15 µg, 0.2 cm^2 GC RDE, sweep rate 10 mV s^{-1}.

The Koutecky-Levich equation (Equation 21), is valid in the region of the LSV where the response is mass transfer limited. The equation is an extension of the Levich equation, where the electrochemical response measured at the disc, i_d, is correlated with the kinetic current density, i_k, diffusion limiting current due to film, i_f, and catalyst diffusion limiting current density, i_c. Each component is described in Equation 22 - Equation 24, where n is the number of electrons in the reaction, F is faraday constant (96485 C mol^{-1}), A is the area of the electrode (0.25 cm^2), D_{O_2} is the diffusion coefficient of oxygen (145 x10^{-7} cm^2 s^{-1}), C_{O_2} is the concentration of oxygen in the electrolyte (0.8 x10^{-6} mol cm^{-3}), v is the kinematic viscosity of the electrolyte (1.0 x10^{-2} cm^2 s^{-1}) and ω is the rotation rate (rad s^{-1}). [70-74]

Equation 21

$$\frac{1}{i_d} = \frac{1}{i_K} + \frac{1}{i_f} + \frac{1}{i_c}$$

Equation 22

$$\mathbf{i_k = nFAkC_{O_2}}$$

Equation 23

$$\mathbf{i_c = \left(0.620nFAD_{O_2}^{\frac{2}{3}} \nu^{-\frac{1}{6}} C_{O_2}\right) \omega^{\frac{1}{2}}}$$

Equation 24

$$\mathbf{i_f = nFAC_{O_2}^{f} D_{O_2}^{f}}$$

The electrochemical response for platinum black and carbon produce a linear response passing near to the origin, as expected for a mass transport limited reaction, but with a slight deviation attributed to a diffusion limitation. A linear relationship is also observed for the $NiCo_2O_4$, however, so is an intercept is observed. The intercept in the $1/i_L$ axis strongly suggests a kinetic limitation during the ORR. The intercept is larger than both the platinum and carbon. When considering the initial slope of the CP-OH was closely following that of platinum, the deviation at higher rotation rates is a significant limitation. As the mass transport limited response is independent of overpotential, a kinetic limitation would suggest a chemical step during the mechanism is limiting the reaction. This may occur via initial oxygen splitting through to decomposition of surface hydroxy-species, but requires further analysis of the reaction intermediates to determine the details of the mechanism. The slope of the Koutecky-Levich plot for $NiCo_2O_4$ appears close to that of platinum, suggesting the oxygen reduction is operating by an approximate 4-electron transfer.

The number of electrons transferred during the ORR, as calculated using Equation 23, is reported in Table 12. The results at 100 rpm result in a higher value than expected with 2.2 and 4.2 electrons for the carbon and platinum black samples respectively. The calculated number of electrons for the $NiCo_2O_4$ is lower than expected ranging from 4.0 down to 2.8 at 100 rpm.

Table 12: Number of electrons transferred during the ORR for each sample.

ω / rpm	Carbon	Pt Black	CP-OH	CP-AM	TD-H_2O
100	2.20	4.19	3.29	3.99	2.83
400	1.97	3.90	2.59	3.13	2.23
900	1.83	3.80	2.39	2.68	1.91
1600	1.73	3.67	2.01	2.31	1.67
2500	1.62	3.51	1.72	1.97	1.45

All samples display a reduction in the number of electrons transferred with increasing rotation rate. This trend is clearly seen in Figure 38. This change in the number of electrons transferred for the platinum and carbon samples is unexpected as any kinetic parameters should be very small on the limiting current. The lower number of electros with rotation rate was observed on three different rotators and when using different glassy carbon rotating disc electrodes. The $NiCo_2O_4$ samples follow the same trend, but with a steeper gradient. With close to 4 electrons and low rotation rate and less than 2 electrons at 2500 rpm it is likely the reaction kinetics of the ORR is different on the spinel than that of either carbon or platinum.

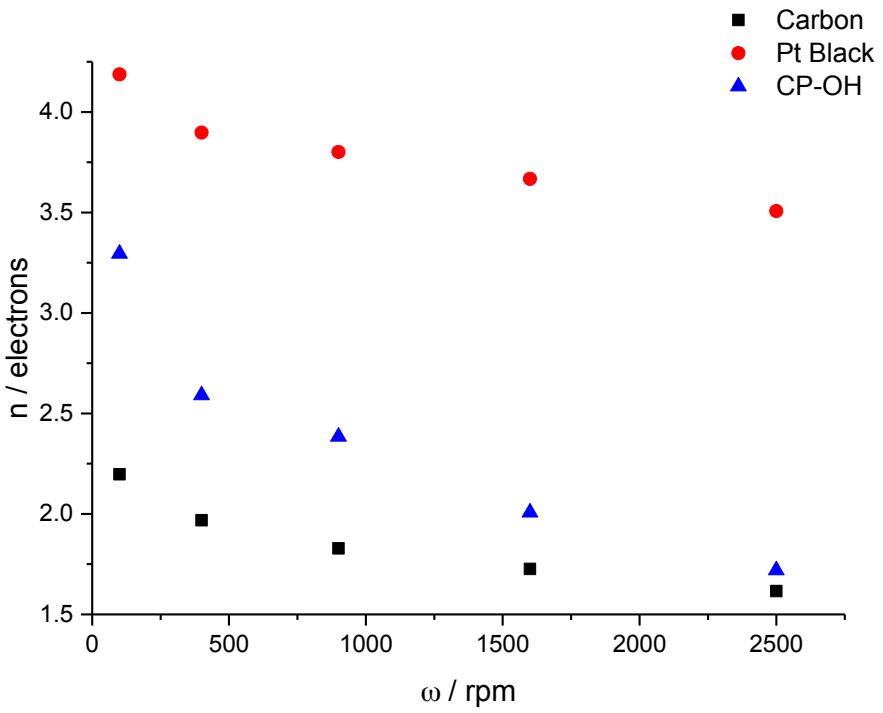

Figure 38: The number of electrons in the ORR reaction for different rotation rates. Measurements carried out on thin-film RDE electrodes

3.4.2.1 RRDE studies of oxygen reduction

Rotating ring disc electrode studies have commonly been employed to determine the percentage of the limiting current utilised in the partial (2-electron) reduction of oxygen. The rotating ring disc relies on a thin, electrochemically isolated, gap separating the disc electrode and a 'sensing' ring electrode. The disc is swept using the normal potential range to study the reaction of interest, in this case oxygen reduction. Whilst sweeping the potential of the disc, the ring is held at fixed potential of +0.2 V *vs.* Hg/HgO.

During the oxygen reduction reaction, if hydrogen peroxide is generated, a proportion of the generated species is forced away from the disc electrode by the laminar flow created by the rotation. Due to the small and fixed gap between the ring and disc, a well-characterised percentage of the species carried from the disc will be carried to the region of diffusional influence from the ring. The generation of hydrogen peroxide at the disc is subsequently oxidised at the ring, the proportion of disc to ring current is then used to calculate the percentage of H_2O_2 production and overall number of electrons transferred. The disc current, i_D, accounts for the total oxygen reduction to both water and hydrogen peroxide. The ring current, $i_{R,}$ accounts for 37 % of reduction to hydrogen peroxide via the 2-electron pathway. The collection efficiency at the ring, *N*, and how this is related to the disc current is described by Equation 25.

Equation 25

$$\mathbf{i_D = i_{H_2O} + i_{H_2O_2}\ \ where\ i_{H_2O_2} = \frac{i_R}{N}}$$

Equation 26

$$\mathbf{\frac{i_D}{n_e} = \frac{i_{H_2O}}{4} + \frac{i_{H_2O_2}}{2}}$$

The average number of electrons transferred, n_e, is shown in Equation 26. Rearranging the equation the average number of electrons is derived from the current measured in the RRDE experiment (Equation 27). This analysis does assume the total current correlates to a 4-electron transfer.

Equation 27

$$\mathbf{n_e = \frac{4i_D}{i_D + i_R/N}}$$

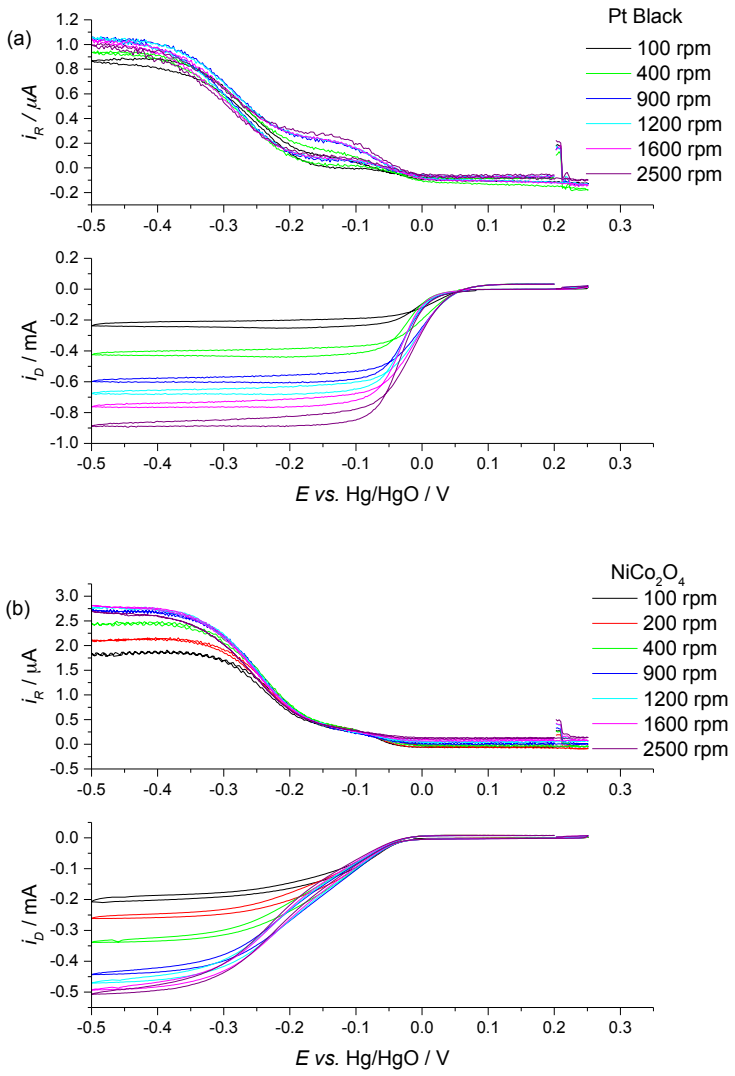

Figure 39: Oxygen reduction LSV on platinum ring, glassy carbon disc RRDE (Ring current top, Disc curent bottom), with the disc coating in a thin-film catalysts layer (a) Platinum black ; (b) $NiCo_2O_4$. All measurements carried out in oxygen saturated 1 M KOH at 298 K. Catalyst loading 15 µg, 0.2 cm^2 GC RDE, sweep rate 10 mV s^{-1}.

The current recorded at the ring electrode provides a response proportional to the onset of the oxygen reduction from the disc, indicative that the HO_2^- species reaching the electrode is being oxidised at the 0.2 V *vs.* Hg/HgO. To confirm optimal HO_2^- collection, an additional experiment was carried out with the disc held at -0.5 V with the ring current swept from 0 V to 0.4 V, with the anodic current peaking at 0.2 V. All further experiments operated with the ring at a fixed potential of 0.2 V *vs.* Hg/HgO.

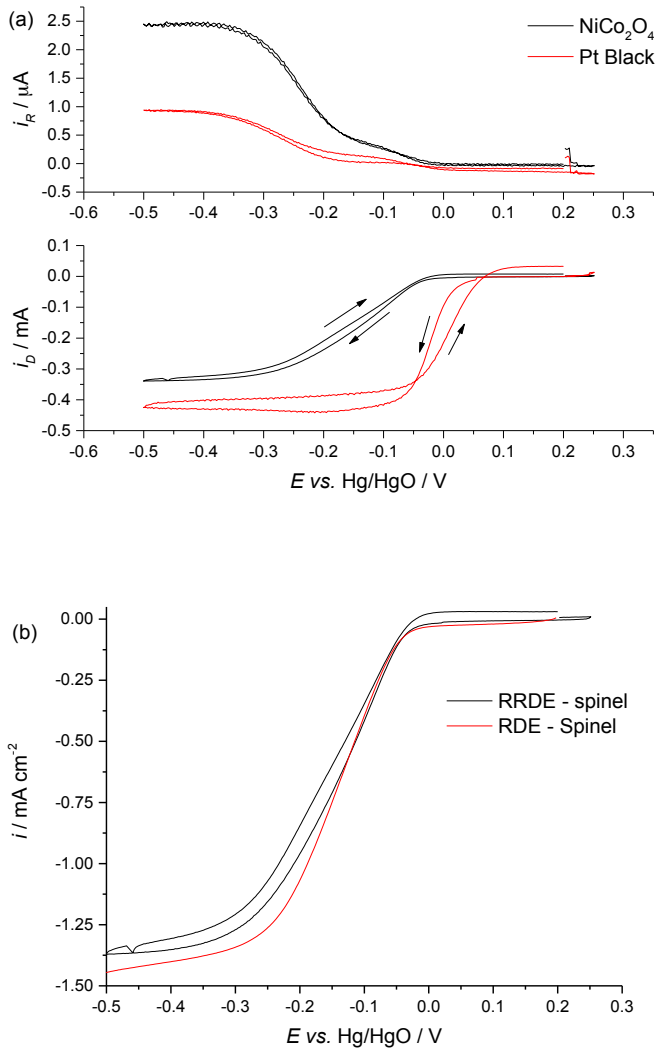

Figure 40: Oxygen reduction LSV using platinum ring, glassy carbon disc RRDE (Ring current top, Disc curent bottom), with the disc coated in a thin-film catalysts layer; (a) Comparison between RDE and RRDE at 400 rpm; (b) comparison of $NiCo_2O_4$ on RRDE and RDE. All measurements carried out in oxygen saturated 1 M KOH at 298 K. Catalyst loading 15 µg, 0.2 cm^2 GC RDE, sweep rate 10 mV s^{-1}.

The electrochemical response for the ORR on a thin-film catalyst layer of platinum black at varying rotation rate is shown in Figure 39 (a). The lower graph is the current detected on the disc, and the upper graph the response from the oxidation of products at the platinum ring. The platinum reduces the oxygen via the 4-electron pathway, as a result only a negligible current (1µA) is detected at the ring. The $NiCo_2O_4$ catalyst produces a similar response to the platinum with currents attributed to the generation of hydrogen peroxide of < 3 µA. This compares to carbon where the 2-electron reduction of oxygen results in large quantities of hydrogen peroxide being generated (80 µA) (Table 13). The carbon sample yielded a lower than expected 63.5 % of hydrogen peroxide detected at the ring. This may be due to a defect in the ring-disc that would

impact the collection efficiency of the electrode, but the electrode collection efficiency was calibrated using a standard solution of 10 mM $K_4Fe(CN)_6$. The disc electrode may have a slight leak down the glassy carbon that would potetnail yield a different ratio of electroactive area from low and high rotation rates, as electrolyte may be forced down a narrow gap. The solution may not have been fully saturated with oxygen between experiments, but the solution was purged for a 10 minute period between linear sweep scans. A number of factors may impact the accuracy of the measurement, but a clear trend can be seen in the results shown in Table 13, with low concentrations of peroxide observed when using platinum black and $NiCo_2O_4$ – OH electrocatalyst.

Table 13: Limiting currents on RRDE in 1 M KOH at 1600 rpm and percentage of current generating hydrogen peroxide.

Sample	i_D / mA	i_R / μA	n	n_e	% HO_2^-
Platinum black	-0.763	1.0	3.85	3.99	0.4
Carbon – XC72	-0.342	80.5	1.72	2.44	63.5
$NiCo_2O_4$ CP – OH	-0.494	2.8	2.49	3.94	1.5

3.4.3 The effect of synthesis method on ORR

The ORR activity for the $NiCo_2O_4$ was found to be dependent on the synthesis method as seen in Figure 41. All $NiCo_2O_4$ samples result in a sigmoidal curve with clear plateaux regions at high overpotential, indicative of mass transport limitation. The synthesis method employed was correlated to a change in the slope of the polarisation curve in the kinetic region. Thermally decomposed samples required higher overpotentials and had shallower gradients than the co-precipitated samples. This would indicate the smaller particle and crystallite sized samples, with high surface areas, form a less resistive layer than the low surface area thermally decomposed samples. This may be due to interconnections between the smaller particles, with fewer points of contact for the larger particles.

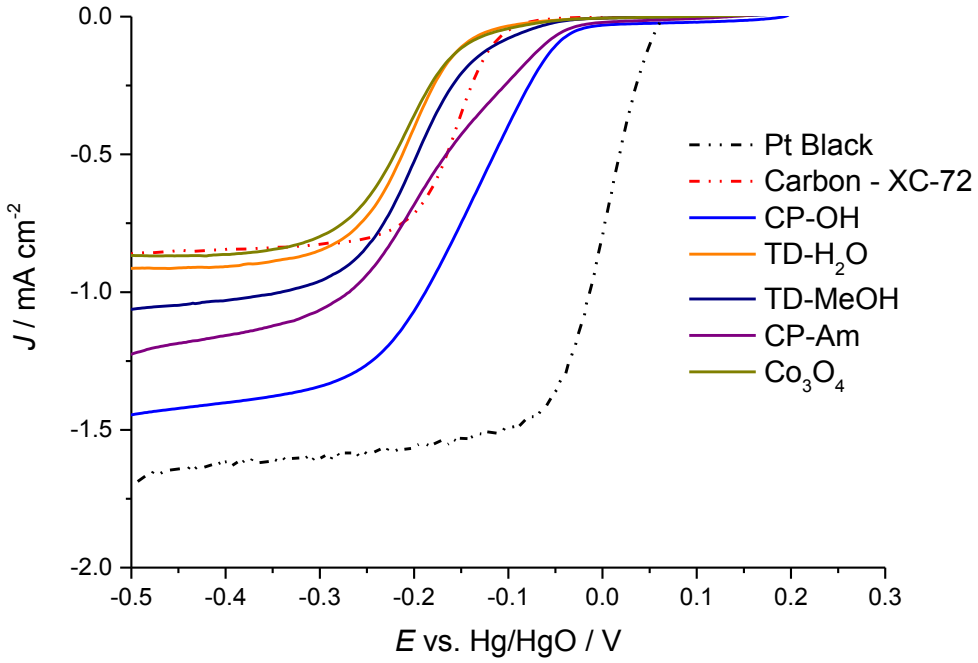

Figure 41: Comparison of ORR LSV for different preparations of $NiCo_2O_4$ on GC RDE in oxygen saturated 1 M KOH at 298 K. Catalyst loading 15 µg, 0.2 cm^2 GC RDE, sweep rate 10 mV s^{-1}.

The plateaux region for all $NiCo_2O_4$ samples was not constant, having a shallow gradient. Limiting currents for TD–H_2O and Co_3O_4 were found to be of the same order of magnitude as that observed for carbon. This would suggest the reaction is limited to a 2-electron ORR process. Alternatively, the oxygen reduction may undergo a slow chemical step, before undergoing electrochemical reaction, which limits the turn-over of reactions on the active sites. The limiting current increases depending on the preparation method, with the following trend: TD-H_2O<TD–MeOH<CP–Am<CP–OH. The thermally decomposed samples appear to achieve a limiting current consistent with a 2-electron reduction to hydrogen peroxide, whilst the co-precipitated samples achieve limiting currents close to a full 4-electron reduction of oxygen. To confirm the kinetics analysis and RRDE results will be compared in sections 3.4.3.1 and 3.4.3.2.

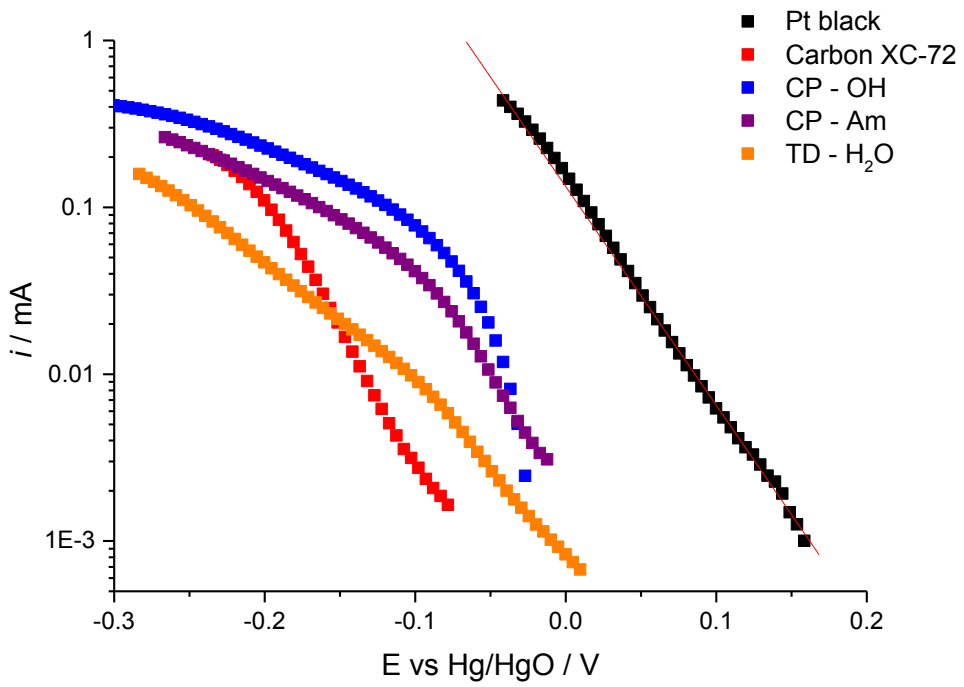

Figure 42: Tafel slope of $NiCo_2O_4$ in oxygen saturated 1 M KOH at 298 K. Catalyst loading 15 µg, 0.2 cm^2 GC RDE, sweep rate 10 mV s^{-1}.

The Tafel analysis of the various $NiCo_2O_4$ preparations is shown in Figure 42. The kinetic controlled region for the ORR for all of the $NiCo_2O_4$ samples occurs at approx. 0 V *vs.* Hg/HgO. In addition to the slight shift in the kinetic region, the slope for several samples is shallow in comparison to the CP-OH sample (Table 14). The gradient of the slope is greater for samples with smaller particle size, and provides further evidence of the activity being influenced by the preparation method.

Table 14: The activity of $NiCo_2O_4$ towards oxygen reduction reaction in oxygen saturated 1 M KOH at 298 K on GC RDE at 400 rpm.

Sample	$E_{\frac{1}{2}}$ / V	E @ 0.5 mA cm^{-2} / V	Tafel slope / mV dec^{-1}
Pt black	-0.001	0.018	-61 (5)
Carbon	-0.157	-0.165	-58 (1)
TD–H_2O	-0.213	-0.212	-92 (2)
TD–MeOH	-0.197	-0.196	-66 (3)
CP–Am	-0.187	-0.165	-68 (5)
CP–OH	-0.146	-0.114	-77 (4)
Co_3O_4	-0.210	-0.220	-100 (2)

The thermally decomposed samples result in half wave potentials approximately 20 – 30 mV negative of preparations by co-precipitation. The Tafel slope results suggest a similar mechanism is observed for all samples with typical values 50 – 70 mV dec^{-1}. However, the thermally decomposed samples result in slopes of 90 – 100 mV dec^{-1}, when also considering the difference in the limiting current this further suggests a shift in the reaction pathway towards the 2-electron route.

Due to the slight slope during the mass transport limited region, further analysis is required to separate the contribution from the kinetic component distorting the potential independent response. Koutecky-Levich analysis was used to discern the contribution due to the chemical and electrochemical response, thus providing the information on the reaction occurring on the catalyst in the mass transport limited region.

3.4.3.1 Koutecky-Levich

The RRDE results were further analysed by Koutecky-Levich plots ($1/i_L$ *vs.* $1/\omega^{0.5}$) as seen in Figure 43. The mass transport limited current yields the electrochemical independent information in the i_c component of the response. Therefore the number of electrons transferred during the oxygen reduction reaction is dependent upon the gradient of the slope. The intercept of the $1/i_L$ provides information regarding a slow kinetic step involved during the oxygen reduction reaction that is independent of the applied overpotential.

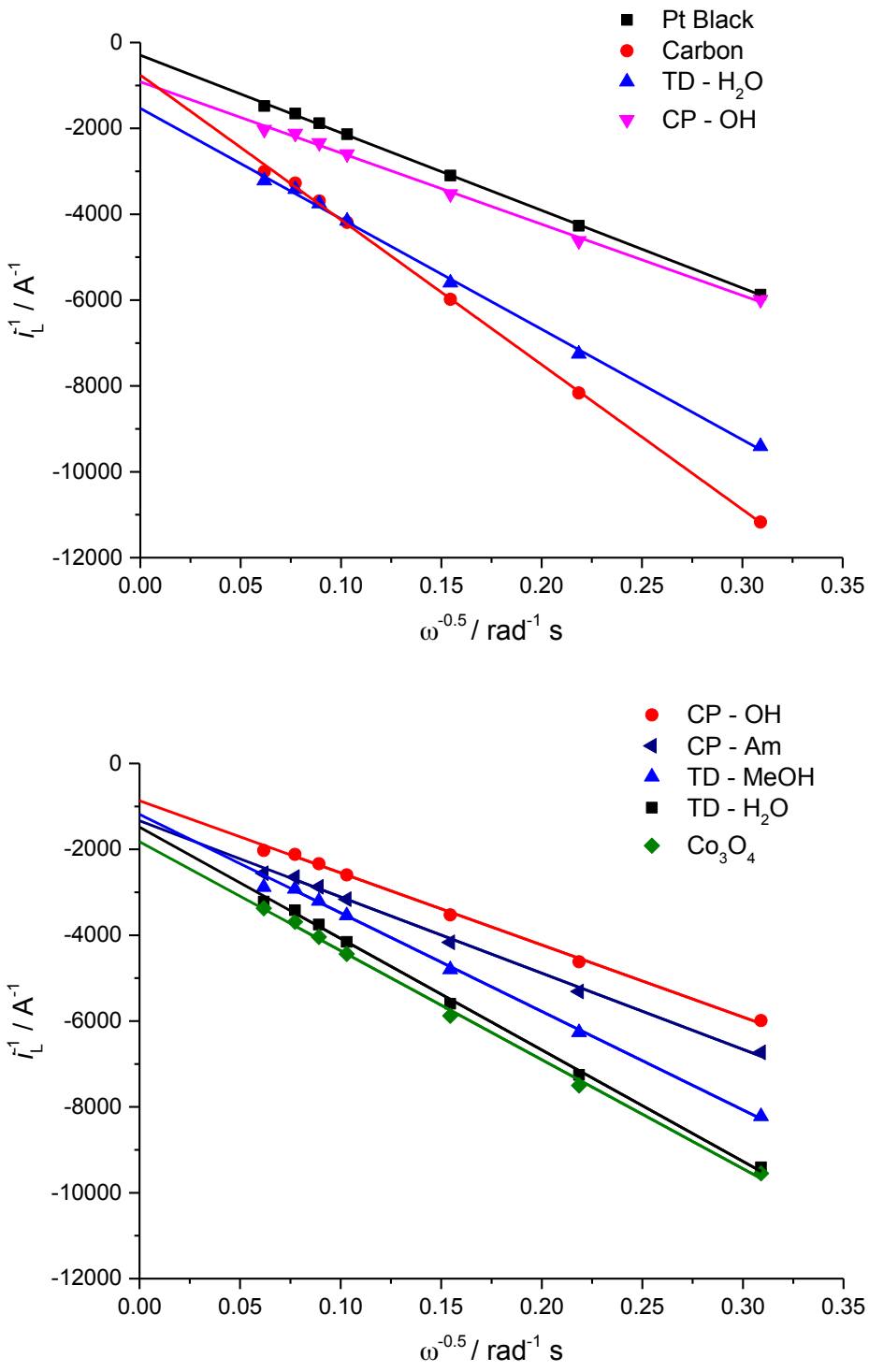

Figure 43: Koutecky-Levich plot for electrocatalysts on GC RDE in oxygen saturated 1 M KOH, 298 K with limiting current measured at -500 mV *vs.* Hg/HgO. Catalyst loading 15 µg, 0.2 cm^2 GC RDE, sweep rate 10 mV s^{-1}.

A linear relationship is observed for all samples in the Koutecky-Levich plot ($1/i_L$ *vs.* $1/\omega^{0.5}$). This would suggest the number of electrons transferred is independent of rotation rate and therefore constant for all samples. The slope for CP samples correlate closely to that of platinum

(approx. -18 mA^{-1} $rad^{-0.5}$ $s^{-0.5}$), suggesting the total electron transfer is on the order of 4-electrons. However, low surface area samples, prepared by thermal decomposition, yield slopes of -25 mA^{-1} $rad^{-0.5}$ $s^{-0.5}$, half-way between those is observed for platinum and carbon at -34 mA^{-1} $rad^{-0.5}$ $s^{-0.5}$. The carbon slope is approximately twice that of platinum and represents a 2-electron reduction of oxygen to hydrogen peroxide. The limiting current should be dependant upon the number of electrons involved in the ORR, with the reduction reaction from 4-electrons for platinum down to 2-electrons for carbon the reason for the lower limiting current in the mass transport region. This limiting current is, within reason, independent of thin-film loading and surface area, but is reliant on the electrode preparation providing a reproducible geometric area.

Analysis of the electrochemically independent kinetic component of the limiting current is important to elaborate intrinsic differences in catalytic activity provided by the preparation methods of the catalysts. It should be noted that for all samples the y-axis intercept deviates from zero. This deviation from the model result can be explained by a number of possible reasons: (1) diffusion limitation through the catalyst and Nafion film[75]; (2) surface roughness or porosity of the catalyst deposit; (3) slow chemical kinetic step during the reaction.

The thin-film method for preparing films was used to limit the impact of the Nafion film on the limiting current during the oxygen reduction. This method has been reported to yield reliable results in acid[75] and in base[10] to reduce the contribution to the limiting current.

The non-zero y-axis intercept values provide information on reaction kinetics of a slow chemical kinetic step involved in the oxygen reduction reaction. The slow kinetic step is likely related to the initial oxygen bond breaking. Platinum and carbon both yield relatively low values for the intercept (Table 15), with the highest activity samples also being linked with smallest intercept values.

Table 15: Values of i_K determined from Koutecky-Levich plots.

Sample	*Intercept* ($1/i_k$ / mA^{-1})	Slope (mA cm^{-2} $rad^{-0.5}$ $s^{-0.5}$)
CP – OH	-0.85 ±0.06	-16.8 ± 0.3
CP – Am	-1.35 ±0.08	-17.8 ± 0.4
TD – MeOH	-1.20 ±0.05	-23.0 ± 0.3
TD – H_2O	-1.50 ±0.08	-29.6 ± 0.5
Co_3O_4	-1.80 ±0.11	-25.4 ± 0.6
Platinum Black	-0.26 ±0.02	-18.3 ± 0.1
Carbon	-0.67 ±0.04	-34.1 ± 0.2

The synthesis method strongly affects the activity of the $NiCo_2O_4$ towards the ORR. The slope from the Koutecky-Levich plot changes from values close to platinum for co-precipitated samples to those half-way between platinum and carbon for the thermally decomposed samples. The results would suggest the mechanism for all samples operates close to a 4-electron transfer pathway with a slow initial chemical step. The RRDE study of the CP-OH sample confirms the catalyst produces a negligible portion of hydrogen peroxide (1.5 %), which is comparable to platinum (0.4 %) and significantly less than that produced by carbon (>60 %). Further RRDE measurements were carried out on other preparations of the $NiCo_2O_4$ to determine if hydrogen peroxide is generated during the ORR, which would explain the difference in the mass transport limited current.

3.4.3.2 Synthesis method – RRDE study

Thin-film electrocatalyst layers were prepared for the different synthesis methods of $NiCo_2O_4$. The ORR was carried out by sweeping the potential from 0.3 V to -0.5 V, followed by a return sweep in the opposite direction. The limiting current was taken at -0.5 V for all samples, to provide a consistent potential for comparison of all samples. As discussed previously (Section 3.4.2.1), the slopes produced by all electrodes are comparable to that produced on RDE electrodes. A clear sigmoidal response is achieved, with a slightly sloping limiting current for all samples (Figure 41).

The oxidation of hydrogen peroxide was achieved by holding the ring at a fixed potential of 0.2V *vs.* Hg/HgO.

Table 16: Limiting currents on RRDE in 1 M KOH at 1600 rpm and percentage of current generating hydrogen peroxide.

Sample	i_{LD} / mA	i_{LR} / µA	n_e	% HO_2^-
Platinum black	-0.763	1.0	3.99	0.4
Carbon – XC72	-0.342	80.5	2.44	63.5
CP – OH	-0.494	2.8	3.94	1.5
CP – Am	-0.458	22.4	3.53	13.2
TD – H_2O	-0.597	21.8	3.64	9.9
Co_3O_4 TD	-0.270	21.7	3.29	20.8

The limiting current for the disk (i_{LD}) and (i_{LR}) is reported in Table 16. The percentage of HO_2^- generation for platinum and the CP-OH sample is very low (< 2 %), consistent with early studies by Bagotzky et al.[23]. This result is in agreement with the RDE results, suggesting a 4-electron transfer is occurring, with minimal loss of hydrogen peroxide as an intermediate.

The TD-H_2O and CP-Am samples result in a greater proportion of hydrogen peroxide detected on the ring (approx. 10%), than that observed for CP-OH or platinum. All samples show a decrease in the hydrogen peroxide detected at the ring with increased rotation rates (Figure 44).

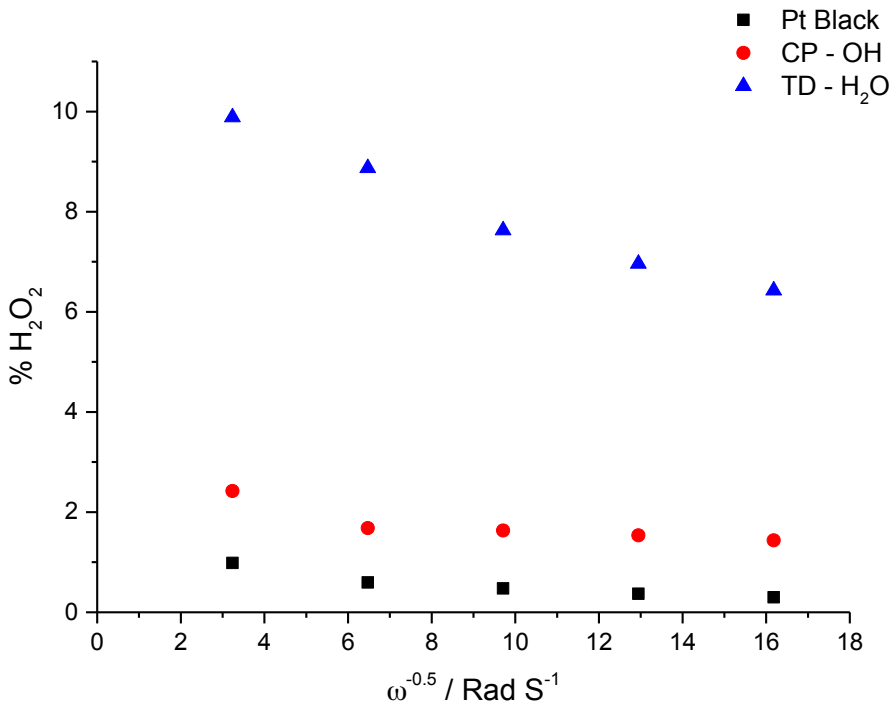

Figure 44: Percentage of H_2O_2 production on the RRDE in oxygen saturated 1 M KOH at 298 K. Catalyst loading 15 µg on GC disc and Pt ring RRDE, sweep rate 10 mV s^{-1}.

The apparent number of electrons transferred for CP-Am (3.99) is greater than the TD-H_2O (2.83). The difference in electron transfer and yet comparable yields of hydrogen peroxide for the ORR are explained by a slow kinetic step for the ORR. An early kinetic step, such as splitting of an oxygen bond, is therefore limiting the oxygen reduction reaction. The degree of kinetic limitation is dependent upon the synthesis method, with high surface area samples prepared by co-precipitation providing relatively fast kinetics and larger particles prepared by thermal decomposition relatively slow kinetics.

3.4.4 The effect of carbon added to the catalyst layer

The addition of carbon into electrode layers is common practice when investigating oxygen reduction in alkaline electrolyte to promote conductivity of mixed metal oxide electrocatalysts.[10] The carbon, however, has also been shown to be an excellent oxygen reduction catalyst to hydrogen peroxide, whilst also providing a roughened and porous layer for the dispersion of catalyst centres. A comparison was therefore made with the $NiCo_2O_4$ samples with and without carbon to understand how these impact the performance for ORR.

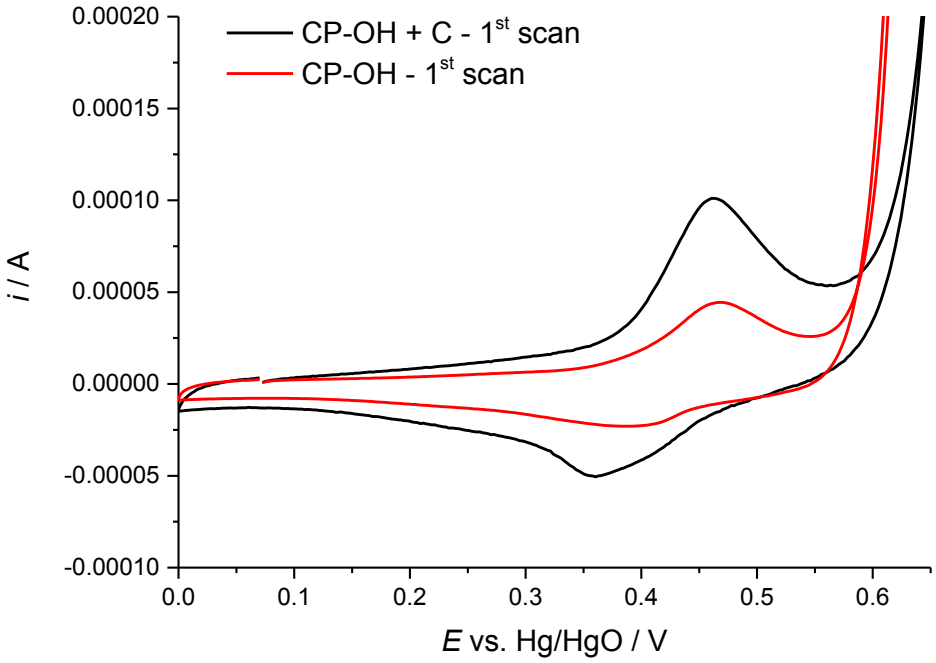

Figure 45: Cyclic voltammetry of thin-films of $NiCo_2O_4$ with carbon (black) and without (red) prepared on GC electrode, at 10mV s^{-1} in oxygen saturated 1 M KOH at 298 K. Catalyst loading 15 µg, 0.2 cm^2 GC RDE, sweep rate 10 mV s^{-1}.

Total material loading was maintained at approximately 70 ug cm^{-2} for all samples by the drop casting method Section 2.1. A 1:1 ratio of $NiCo_2O_4$ to carbon was used for all of the carbon comparison samples. The combination of $NiCo_2O_4$ and carbon produces an increased double layer charge, which is expected with the addition of a high surface area carbon to a catalyst layer. The Faradaic currents show increased current in both oxidation and reduction peaks, consistent with the conductivity of the material being improved and new surface sites being accessed. Surface sites may have been disconnected via grain boundaries in the crystallites, point connections between agglomerates and layer resistance.

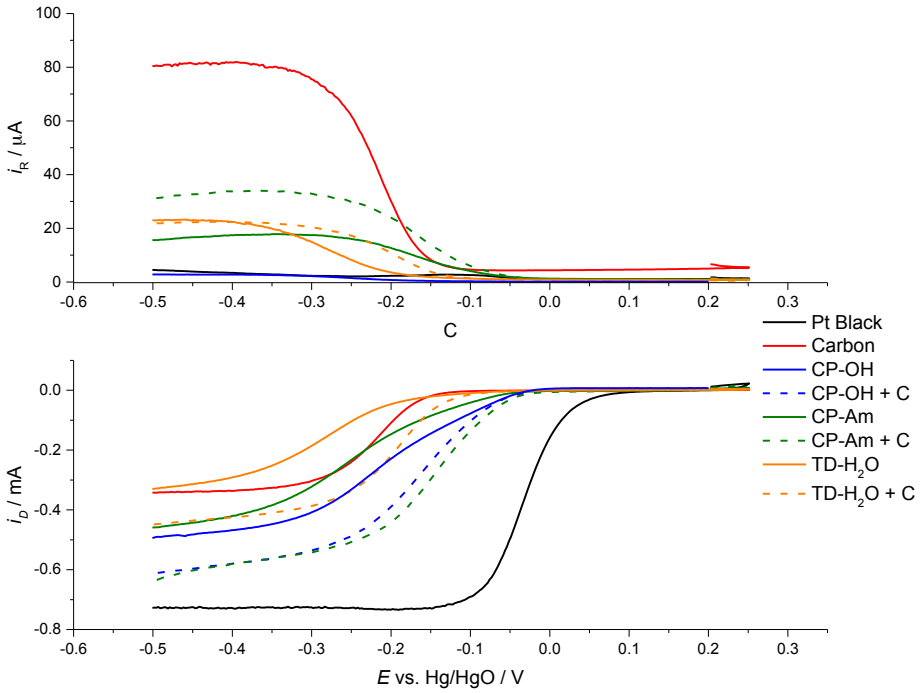

Figure 46: Oxygen reduction of thin-film catalyst layers with carbon (Dash) and without (Solid) on GC-Pt RRDE in oxygen saturated 1 M KOH at 298 K at 1600 rpm. Catalyst loading 15 µg, 0.2 cm^2 GC RDE, sweep rate 10 mV s^{-1}.

The addition of carbon to the thin-film layers strongly influences the resulting electrochemistry observed on the RRDE. All results maintain a sigmoidal curve for the oxygen reduction, with slight slopes for the mass transport limited region. Similar limiting currents were achieved for both co-precipitated samples when mixed with carbon. In addition, a positive shift in the mixed control region of the linear sweep would suggest the thermally decomposed samples are limited by relatively low conductivity/limited point contacts between agglomerates in the catalyst layer.

All samples mixed with carbon resulted in increased H_2O_2 production at higher overpotentials (Figure 46). This increase in peroxide production is likely due to a small amount of oxygen reduction occurring on the carbon in the catalyst layer.

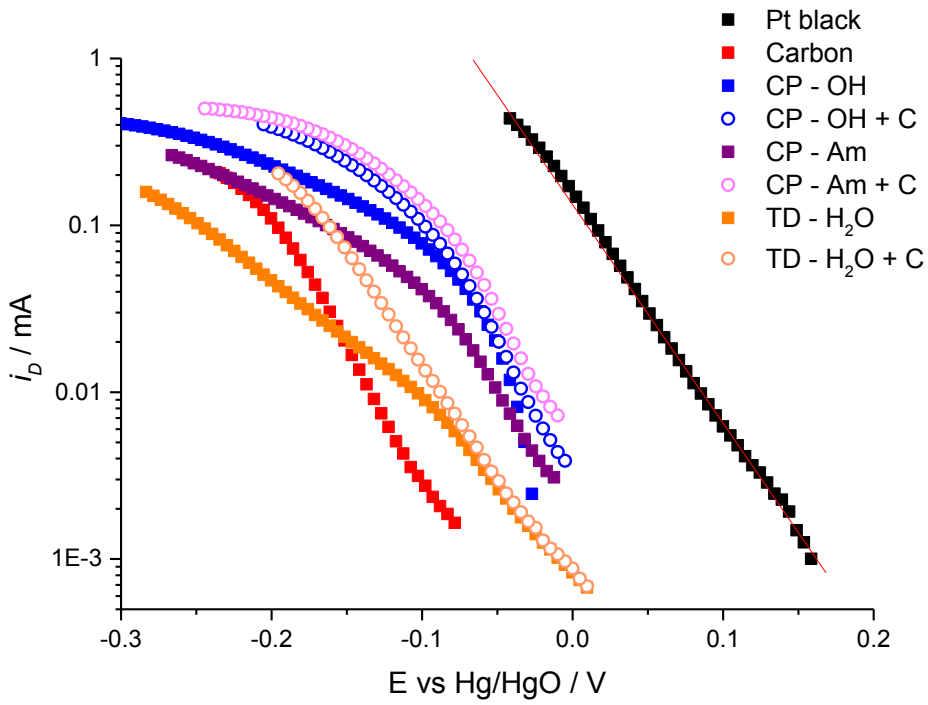

Figure 47: Tafel plots of thin-film electrodes with (non-solid) and without carbon (solid) prepared on GC-Pt RRDE in oxygen saturated 1 M KOH at 298 K. Catalyst loading 15 µg, 0.2 cm^2 GC RDE, sweep rate 10 mV s^{-1}.

The effect is clear on the Tafel slope of the thermally decomposed samples with and without carbon Figure 47, where samples result in similar slope in the low current range but, half way, the sample without carbon shows a rapid deviation followed by a second linear region at higher currents. In comparison, the same sample with added carbon results in a continuation of the linear mixed control region, until the limiting current then interferes.

The sources of variation for these samples are loading of active material, conductivity, dispersion of catalyst and surface roughing/porosity provided by the carbon. The variation observed in the mixed control region is most strongly influenced by the conductivity and porosity of the sample. Changes to the active sites would strongly dominate the kinetically controlled region at low current densities, whilst the reduced loading of active material would hinder the limiting current towards the mass transfer limited region. However, increased conductivity provides a negligible effect at lower current densities; increased porosity/roughening and dispersion of the catalyst on the electrode, by the addition of carbon, would promote high current densities and influence the limited current that can be achieved by deviating from the planar geometry provided by glassy carbon.

Table 17: Comparison of $NiCo_2O_4$ samples prepared with and without carbon on GC-Pt RRDE in 1 M KOH at 298 K.

Sample	$E_{\frac{1}{2}} / V$	*E @ 0.5 mA cm^{-2} / V*	Tafel slope / mV dec^{-1}
Pt Black	-0.001	0.018	-61
Carbon	-0.157	-0.165	-58
CP – OH	-0.208	-0.134	-74
CP – OH + C	-0.171	-0.108	-55
CP – Am	-0.187	-0.165	-68
CP – Am + C	-0.152	-0.094	-55
TD – H_2O	-0.213	-0.212	-92
TD – H_2O + C	-0.201	-0.170	-74

The addition of carbon has demonstrated an improvement to both the limited current region and mixed control regions. The mixed control region is highly sensitive to conductivity, as clearly demonstrated by the response from the thermally decomposed sample. The increase in the limited current can be partially accounted for by increased conductivity, whereby new catalyst centres may be accessible, but this should be a minor contribution as during the mass transport limited response should be achieved in theory by only singular catalytic centres. The thin-film catalyst layers when formed with carbon was prepared with half the catalyst loading of carbon free layers, where an overall reduction in the number of available catalytic centres is more likely. The carbon may also provide improved catalyst dispersion and will provide a high surface area across the glassy carbon surface, suggesting these parameters may play an important role in promoting the oxygen reduction reaction on thin-film rotating disc electrodes.

3.4.5 Oxygen evolution on $NiCo_2O_4$

The oxygen evolution reaction, essential for the charging of the metal-air, operates via the splitting of water molecules into oxygen and hydroxide. Initial catalyst screening towards the OER was carried out on the RDE, as it provides planar electrode geometry with controlled mass transfer. The same catalyst layers used in the study of the ORR were subsequently characterised for their activity towards OER.

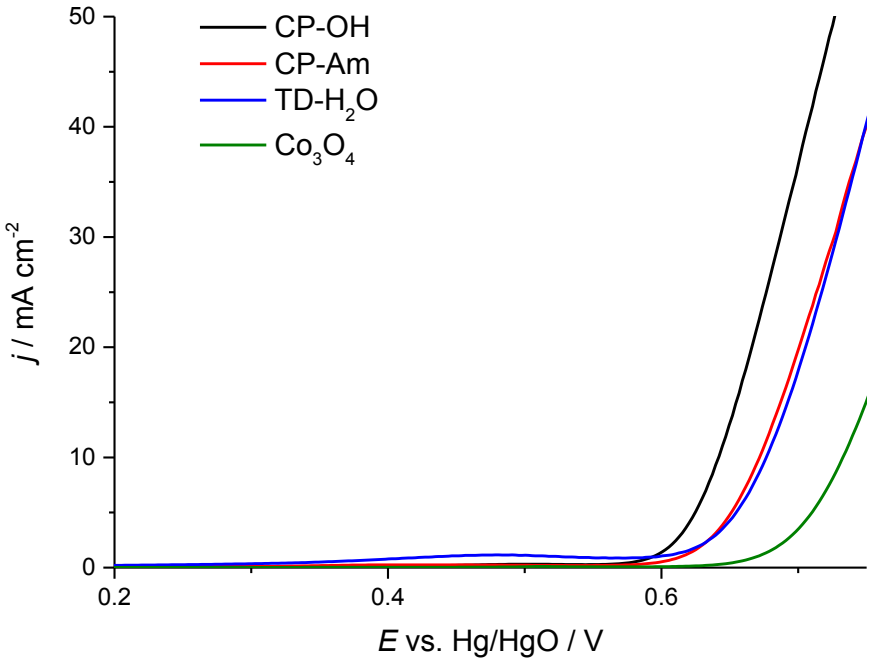

Figure 48: LSV of $NiCo_2O_4$ electrocatalysts cast on GC RDE at 400 rpm, in oxygen saturated 1 M KOH at 298 K. Catalyst loading 15 µg, 0.2 cm^2 GC RDE, sweep rate 10 mV s^{-1}.

The thin-film electrodes on GC RDE were swept from 0.1 V positive to 0.75V *vs.* Hg/HgO in 1 M KOH at 298 K at a sweep rate of 10 mV s^{-1} and a rotation rate of 400 rpm. The voltammogram produced during the screening for OER activity yields a flat region, before an exponential rise corresponding with the OER. Initial results (Figure 29 and Figure 33) from screening several preparation methods of the $NiCo_2O_4$ show similar exponential rises followed by a linear portion with increasing overpotential for the OER. The cyclic voltammetry, section 3.4.1, yields an oxidation peak at approximately 0.5 V for all samples, followed by subsequent oxygen evolution. The steady state LSV measurements (Figure 48) produce similar results, but isolate the contributions from double layer and surface redox couple observed in the CV. Measured currents during the reaction showed minimal effect from the rotation rate at 400 rpm and above.

A small rise in the current is visible for the TD-H_2O sample in Figure 48. Reducing the scale of the current, a small rise in the current is observed for all samples. This correlates to the redox couple seen in the cyclic voltammetry in Figure 33. Lowering of the scan rate for these measurements below 10 mV s^{-1} would likely remove this feature from the voltammetry.

The inferior performance of Co_3O_4 compared to $NiCo_2O_4$ would suggest the addition of nickel increases in the conductivity of the catalyst layer, in agreement with results reported in the literature.[16] Another explanation is that the nickel doped into the spinel results in increased

oxidation state of the cobalt to a greater proportion of Co^{3+} and greater activity towards the OER. The CP-OH results in a reduced overpotential for the OER, compared to other preparations of the $NiCo_2O_4$. The difference between the Co_3O_4 and $NiCo_2O_4$ is most likely to be attributed to a difference in conductivity. However, small variations in the $NiCo_2O_4$ can be partially explained by different surface species. The CV for all samples suggests an increase in oxidation state occurs before the OER begins. It is therefore proposed that the higher oxidation state surface species will be the active sites for the OER.

The nature of the oxidation state of the nickel and cobalt in the spinel, as determined by ex-situ XANES and XPS measurements, has been reported to be dependent upon the preparation method.[27,30,32,76] As all samples appear to undergo an increase in oxidation state before the OER, the determination of the oxidation state ex-situ is unlikely to provide the necessary insight into the active species for the OER.

Further investigation of the mechanism of the OER was carried out by Tafel analysis of the polarisation curves. All samples produced a deviation from 'ideal' linear Tafel behaviour at high current densities due to Ohmic losses associated with electrode and electrolyte resistance. A correction for this deviation has been reported in previous studies for the involving the oxygen evolution reaction from metal oxides.[77-81]

3.4.5.1 iR correction

Correction was achieved by extrapolating the linear portion of the polarisation curve graphically. The uncompensated Ohmic resistance was calculated by the difference between the potential for the experimental data and the linear extrapolation from the linear portion of the data at low current densities (Figure 49). The deviation between the linear extrapolation and the experimental data, ΔE, was plotted as a function of the corresponding current.

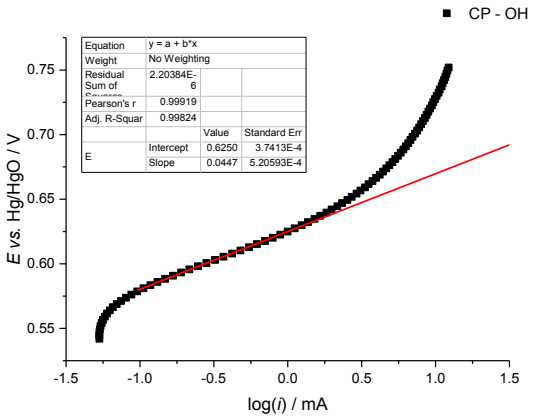

Figure 49: Tafel plot of $NiCo_2O_4$ catalyst (75 µg cm^{-2}) in 1 M KOH, 298 K.

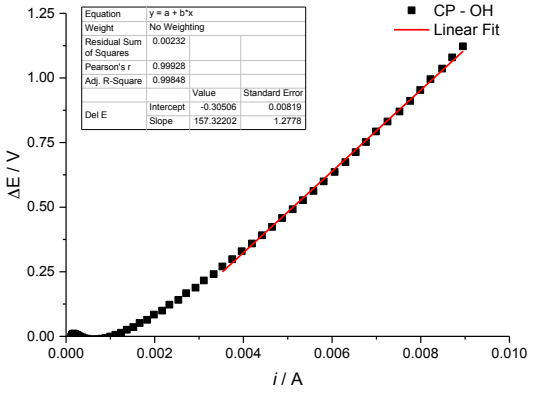

Figure 50: Plot of ΔE *vs.* j used to estimate the uncompensated resistance in the $NiCo_2O_4$ (75 µg cm^{-2}) thin-film.

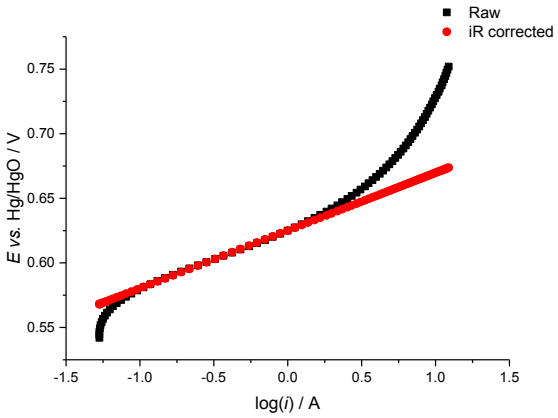

Figure 51: Comparison of Tafel plots for iR corrected $NiCo_2O_4$ (Red) and uncorrected (Black) during OER in 1 M KOH at 298 K.

The iR correction was applied to all $NiCo_2O_4$ samples and results presented in Table 18. The activity towards the OER was compared at a current of 10 mA cm^{-2}. The co-precipitated samples

with high surface area achieve a 10 – 20 mV reduction in overpotential compared to thermally decomposed $NiCo_2O_4$. An improvement of 80 – 90 mV is possible in comparison to the Co_3O_4 sample.

Table 18: Comparison of OER activity for different electrocatalysts in oxygen saturated 1 M KOH at 298 K on GC RDE at 400 rpm.

Catalyst	*E vs.* Hg/HgO at *J* = 10 mA cm^{-2} / mV (iR corrected)	Tafel slope / mV dec^{-1}
CP – OH	637	43
CP – Am	665	50
TD – H_2O	675	66
Co_3O_4	721	51

The oxygen evolution occurs between the solid sample and the liquid electrolyte, avoiding the complex relationship during ORR. There are several mechanisms reported for the OER in alkali media.[6,44,82-87] The rate determining step, and therefore the reaction mechanism, can be derived from the Tafel slope of a steady state polarisation measurement. The Tafel equation (Equation 28) is used to analyse a plot of the overpotential, η, with the log of the current, i, will be linear with a slope, b, and intercept, a.

Equation 28

$$\boldsymbol{\eta = a + b \log (i)}$$

A Tafel slope of ca. 120 mV dec^{-1} would suggest the rate determining step (RDS) is the first electron transfer of a multi-electron transfer reaction, a slope of ca. 40 mV dec^{-1} would correspond with the second electron transfer step being the RDS and a slope of ca. 60 mV dec^{-1} would suggest a chemical step for the RDS.[88]

All samples display Tafel slopes > 40 mV dec^{-1}. The magnitude of the slope is found to increase from 43 to 66 mV dec^{-1} for the CP-OH through to the TD-H_2O sample. The Tafel slope of ca. 40 mV dec^{-1} for the co-precipitated samples would suggest an electrochemically limited second step for the OER. The Tafel slope for the thermally decomposed samples rises to ca. 60 mV dec^{-1} suggesting a potential change in the rate-determining step.

This is in agreement with studies on the OER on Co_3O_4, whereby smaller particles were linked with reduced overpotential and increased Tafel slope for the oxygen evolution reaction.[25] The results here highlight the importance of the synthesis method on the activity of the $NiCo_2O_4$ towards the oxygen evolution reaction.

3.5 Conclusion

In this chapter a series of $NiCo_2O_4$ samples have been prepared via co-precipitation and thermal decomposition methods. XRD indicates a single pure spinel phase is present for all samples, with crystallite size 10 – 90 nm. TEM, disc centrifuge results identified the co-precipitated samples to yield the smallest particle size 100 – 200 nm, compared to 700 – 800 nm for thermally decomposed samples. BET measurements confirmed the smaller particle size co-precipitated samples yielded the highest surface area of 50 – 70 $m^2\ g^{-1}$.

Cyclic voltammetry suggests a consistent redox couple is present for all samples. The shape of the peak varies with synthesis method and is consistent with the values reported in the literature. The variation in peak shape can be explained by either a variable pore structure or surface species of the catalyst producing some variability depending on the preparation method. The addition of carbon appears to improve the electrocatalyst utilisation for a number of samples. However this may be biased on the RDE whereby dispersion of active sites, conductivity of the layer and a surface roughness are contributing to a complex result and incompatible with results when the material is bonded into a gas diffusion electrode.

Studies on $NiCo_2O_4$ towards the oxygen reduction and evolution reactions have consistently demonstrated the high activity of these materials. The activity over short-time scales on RDE is heavily influenced by the preparation of the electrocatalyst. The conductivity, porosity and surface area of the hydroxyl-carbonate co-precipitated product results in good activity.

The oxygen reduction reaction on $NiCo_2O_4$ produces a sigmoidal curve with a sloping limiting current when prepared on RDE in 1 M KOH at 298 K. The limited current response with rotation rate suggests a mainly 4-electron pathway for the spinel catalysts. This result was confirmed by the RRDE, whereby little to no hydrogen peroxide was observed. The reaction may still occur with a hydrogen peroxide species intermediate, but this is rapidly decomposed in a further step. The intercept in the Koutecky-Levich analysis would suggest the reaction involves a slow chemical step, and by reference to the literature[18,19,21,89-94] the chemical step is likely to involve the oxygen bond-breaking step.

The addition of carbon to the electrocatalytic layer improves the conductivity for all samples. The addition of carbon to thermally decomposed samples produces the largest shift in the electrochemical response. The improvement in conductivity is the dominant factor that it provides in the kinetic and mixed control response. However increased catalyst dispersion and surface roughness dominate the effects on the mass transport limited response. The inclusion of carbon into a bifunctional electrocatalytic layer is detrimental for long-term stability and, so, further work will focus on improvements achieved in the absence of carbon.

The $NiCo_2O_4$ activity towards the OER was excellent, with overpotential at 10 mA cm^{-2} of 637 mV. The Tafel slope of 43 was comparable to the 40 mV for ruthenium dioxide (results for RuO_2 included as part of Chapter 5).

The reduction in particle size and increase in surface area of the $NiCo_2O_4$ was found to reduce the Tafel slope and also the overpotential for the oxygen evolution reaction, consistent with results in the literature.[25,39]

The lowest overpotential for the combined oxygen reduction and oxygen evolution reactions was found when using the CP-OH samples. The lowest oxygen evolution overpotential is likely due to the small particle size and large surface area. The high surface area is also likely to be beneficial to the oxygen reduction reaction, where the $NiCo_2O_4$ requires a chemical step before the electrochemical reaction.

3.6 References

(1) Horowitz, H. S.; Longo, J. M.; Horowitz, H. H. *J. Electrochem. Soc.* **1983**, *130*, 1851–1859.

(2) Shukla, A. K.; Kannan, A. M.; Hegde, M. S.; Gopalakrishnan, J. *J. Power Sources* **1991**, *35*, 163–173.

(3) Prakash, J.; Tryk, D. A.; Aldred, W.; Yeager, E. B. *J. Appl. Electrochem.* **1999**, *29*, 1463–1469.

(4) Konishi, T.; Kawai, H.; Saito, M.; Kuwano, J.; Shiroishi, H.; Okumura, T.; Uchimoto, Y. *Top Catal* **2009**, *52*, 896–902.

(5) Meadowcroft, D. B. *Nature* **1970**, 847–848.

(6) Bockris, J. O.; Otagawa, T. *J. Electrochem. Soc.* **1984**, *131*, 290–302.

(7) Bockris, J. O.; Mine*vs.*ki, Z. S. *Electrochim. Acta* **1994**, *39*, 1471–1479.

(8) Jung, J. I.; Jeong, H. Y.; Lee, J.-S.; Kim, M. G.; Cho, J. *Angew. Chem.* **2014**.

(9) Poux, T.; Bonnefont, A.; Kéranguéven, G.; Tsirlina, G. A.; Savinova, E. R. *ChemPhysChem* **2014**.

(10) Poux, T.; Napolskiy, F. S.; Dintzer, T.; Kéranguéven, G.; Istomin, S. Y.; Tsirlina, G. A.; Antipov, E. V.; Savinova, E. R. *Cat. Today* **2012**, *189*, 83–92.

(11) Miyahara, Y.; Miyazaki, K.; Fukutsuka, T.; Abe, T. *J. Electrochem. Soc.* **2014**, *161*, F694–F697.

(12) Suntivich, J.; May, K. J.; Gasteiger, H. A.; Goodenough, J. B.; Shao-Horn, Y. *Science* **2011**, *334*, 1383–1385.

(13) Suntivich, J.; Gasteiger, H. A.; Yabuuchi, N.; Nakanishi, H.; Goodenough, J. B.; Shao-Horn, Y. *Nat. Chem.* **2011**, *3*, 546–550.

(14) King, W. J.; Tseung, A. *Electrochim. Acta* **1974**.

(15) Singh, R. N.; Hamdani, M.; Koenig, J. F.; Poillerat, G.; Gautier, J. L.; Chartier, P. *J. Appl. Electrochem.* **1990**, *20*, 442–446.

(16) Lapham, D. P.; Tseung, A. C. C. *J. Mater. Sci.* **2004**, *39*, 251–264.

(17) Hamdani, M.; Singh, R. N.; Chartier, P. *Int. J. Electrochem. Sci.* **2010**, *5*, 556–577.

(18) Markovic, N. M.; Gasteiger, H. A.; Philip, N. *J. Phys. Chem.* **1996**, *100*, 6715–6721.

(19) Geniès, L.; Faure, R.; Durand, R. *Electrochim. Acta* **1998**, *44*, 1317–1327.

(20) Damjanovic, A.; Genshaw, M. A.; Bockris, J. O. *J. Electrochem. Soc.* **1967**, *114*, 1107–1112.

(21) APPLEBY, A. J.; Savy, M. *J. Electroanal. Chem. Interfacial Electrochem.* **1978**, *92*, 15–30.

(22) Goodenough, J. B.; Cushing, B. L. *Oxide-based ORR catalysts*; John Wiley & Sons, Ltd: Chichester, UK, 2010.

(23) Bagotzky, V. S.; Shumilova, N. A.; Khrushcheva, E. I. *Electrochim. Acta* **1976**, *21*, 919–924.

(24) Cong, H. N.; Abbassi, K. E.; Chartier, P. *J. Electrochem. Soc.* **2002**, *149*, A525.

(25) Esswein, A. J.; McMurdo, M. J.; Ross, P. N.; Bell, A. T.; Tilley, T. D. *J. Phys. Chem. C* **2009**, *113*, 15068–15072.

(26) King, W. J.; Tseung, A. C. C. *Electrochim. Acta* **1974**, *19*, 493–498.

(27) Marco, J. F.; Gancedo, J. R.; Gracia, M.; Gautier, J. L.; Rıos, E.; Berry, F. J. *J. Solid State Chem.* **2000**, *153*, 74–81.

(28) Battle, P.; Cheetham, A.; Goodenough, J. *Mater. Res. Bull.* **1979**, *14*, 1013–1024.

(29) Kim, J.; Pugmire, D.; Battaglia, D.; Langell, M. *Appl. Surf. Sci.* **2000**, *165*, 70–84.

(30) Marco, J. F.; Gancedo, J. R.; Gracia, M.; Gautier, J. L.; Ríos, E. I.; Palmer, H. M.; Greaves, C.; Berry, F. J. *J. Mater. Chem.* **2001**, *11*, 3087–3093.

(31) De Faria, L. A.; Prestat, M.; Koenig, J. F.; Chartier, P.; Trasatti, S. *Electrochim. Acta* **1998**, *44*, 1481–1489.

(32) Lenglet, M.; Guillamet, R.; Dürr, J.; Gryffroy, D.; Vandenberghe, R. *Solid State Commun.* **1990**, *74*, 1035–1039.

(33) Nkeng, P.; Poillerat, G.; Koenig, J. F.; Chartier, P.; Lefez, B.; Lopitaux, J.; Lenglet, M. *J. Electrochem. Soc.* **1995**, *142*, 1777–1783.

(34) Feng, J.; Zeng, H. *Chem. Mater.* **2003**, *15*, 2829–2835.

(35) Singh, R.; Pandey, J.; Singh, N.; Lal, B.; Chartier, P.; Koenig, J. 2000; Vol. 45, pp 1911–1919.

(36) Liu, Z.-Q.; Xu, Q.-Z.; Wang, J.-Y.; Li, N.; Guo, S.-H.; Su, Y.-Z.; Wang, H.-J.; Zhang, J.-H.; Chen, S. *Int. J. Hydrogen Energ.* **2013**, *38*, 6657–6662.

(37) Lee, D.; Kim, B. J.; Chen, Z. *J. Mater. Chem. A* **2013**, –.

(38) Vassie, P. R.; Tseung, A. C. C. *Electrochim. Acta* **1975**, *20*, 763–765.

(39) Bocca, C.; Barbucci, A.; Delucchi, M.; Cerisola, G. *Int. J. Hydrogen Energ.* **1999**, *24*, 21–26.

(40) Klissurski, D. G.; Uzunova, E. L. *Chem. Mater.* **1991**, *3*, 1060–1063.

(41) Gautier, J.; Marco, J.; Gracia, M.; Gancedo, J.; Guadarrama, V.; Nguyen-Cong, H.; Chartier, P. *Electrochim. Acta* **2002**, *48*, 119–125.

(42) Bocca, C. *Int. J. Hydrogen Energ.* **1999**, *24*, 699–707.

(43) Wu, X.; Scott, K. *Int. J. Hydrogen Energ.* **2013**, *38*, 3123–3129.

(44) Nikolov, I.; Darkaoui, R.; Zhecheva, E.; Stoyanova, R.; Dimitrov, N.; Vitanov, T. *J. Electroanal. Chem.* **1997**, *429*, 157–168.

(45) Tavares, A.; Pereira, M.; Mendonca, M.; Nunes, M.; Costa, F.; Sa, C. *J. Electroanal. Chem.* **1998**, *449*, 91–100.

(46) Bajdich, M.; García-Mota, M.; Vojvodic, A.; Nørskov, J. K.; Bell, A. T. *J. Am. Chem. Soc.* **2013**, *135*, 13521–13530.

(47) Matsumoto, Y.; Yoneyama, H.; Tamura, H. *J. Electroanal. Chem. Interfacial Electrochem.* **1977**, *83*, 167–176.

(48) Li, Y.; Zhao, J.; Dan, Y.; Ma, D.; Zhao, Y.; Hou, S.; Lin, H.; Wang, Z. *Chem. Eng. J.* **2011**, *166*,

428–434.

(49) Liang, Y.; Li, Y.; Wang, H.; Zhou, J.; Wang, J.; Regier, T.; Dai, H. *Nat. Mater.* **2011**, *10*, 780–786.

(50) Jin, C.; Lu, F.; Cao, X.; Yang, Z.; Yang, R. *J. Mater. Chem. A* **2013**, *1*, 12170–12177.

(51) Li, Y.; Hasin, P.; Wu, Y. *Adv. Mater.* **2010**, *22*, 1926–.

(52) Lu, B.; Cao, D.; Wang, P.; Wang, G.; Gao, Y. *Int. J. Hydrogen Energ.* **2011**, *36*, 72–78.

(53) Xu, J.; Gao, P.; Zhao, T. S. *Energy Environ. Sci.* **2012**, *5*, 5333–5339.

(54) Kong, F. *Electrochim. Acta* **2012**, *68*, 198–201.

(55) Cui, B.; Lin, H.; Li, J.-B.; Li, X.; Yang, J.; Tao, J. *Adv. Funct. Mater.* **2008**, *18*, 1440–1447.

(56) Anu Prathap, M. U.; Srivastava, R. *Nano Energy* **2013**, *2*, 1046–1053.

(57) Padmanathan, N.; Selladurai, S. *Ionics* **2013**, 1–9.

(58) Prabu, M.; Ketpang, K.; Shanmugam, S. *Nanoscale VL - IS* - **2014**.

(59) Sa, Y. J.; Kwon, K.; Cheon, J. Y.; Kleitz, F.; Joo, S. H. *J. Mater. Chem. A* **2013**, *1*, 9992–10001.

(60) Rojas, R. M.; Kovacheva, D.; Petrov, K. *Chem. Mater.* **1999**, *11*, 3263–3267.

(61) Bragg, W. H. *Nature* **1915**, *95*, 561–561.

(62) Sickafus, K. E.; Wills, J. M.; Grimes, N. W. *Journal of the American Ceramic Society* **1999**, *82*, 3279–3292.

(63) Verwey, E. J. W.; Heilmann, E. L. *J. Chem. Phys.* **1947**, *15*, 174–180.

(64) Miller, A. *J. Appl. Phys.* **1959**, *30*, S24–S25.

(65) Richardson, J. T. **1964**, *35*, 664.

(66) Hill, R. J.; Craig, J. R.; Gibbs, G. V. *Phys Chem Minerals* **1979**, *4*, 317–339.

(67) Tseung, A. C. C. *J. Electrochem. Soc.* **1978**, *125*, 1660–1664.

(68) Tseung, A. C. C.; Jasem, S. M. *J. Appl. Electrochem.* **1981**, *11*, 209–215–215.

(69) Zhu, H.; Zhang, S.; Huang, Y.-X.; Wu, L.; Sun, S. *Nano Lett.* **2013**, 130509090232007.

(70) Zhang, D.; Wu, J. F.; Mao, L. Q.; Okajima, T.; Kitamura, F.; Ohsaka, T. *Indian Journal of Chemistry* **2004**, *42A*, 801–806.

(71) Zhang, C.; Fan, F.-R. F.; Bard, A. J. *J. Am. Chem. Soc.* **2009**, *131*, 177–181.

(72) Qiao, J.; Xu, L.; Ding, L.; Shi, P.; Zhang, L.; Baker, R.; Zhang, J. *Int. J. Electrochem. Sci.* **2013**, *8*, 1189–1208.

(73) Davis, R. E.; Horvath, G. L.; Tobias, C. W. *Electrochim. Acta* **1967**, *12*, 287–297.

(74) Gubbins, K. E.; Robert D Walker, J. *J. Electrochem. Soc.* **1965**, *112*, 469–471.

(75) Paulus, U. A.; Schmidt, T. J.; Gasteiger, H. A.; Behm, R. J. *J. Electroanal. Chem.* **2001**, *495*, 134–145.

(76) Knop, O.; Reid, K. I. G.; Sutarno; Nakagawa, Y. *http://dx.doi.org/10.1139/v68-576* **1968**, *46*, 3463–3476.

(77) Lyons, M. E. G.; Brandon, M. P. *Int. J. Electrochem. Sci.* **2008**, *3*, 1386–1424.

(78) Baronetto, D.; Kodintsev, I. M.; Trasatti, S. *J. Appl. Electrochem.* **1994**, *24*, 189–194.

(79) Tseung, A. C. C.; Jasem, S. *Electrochim. Acta* **1977**, *22*, 31–34.

(80) De Faria, L. A.; Boodts, J. F. C.; Trasatti, S. *J. Appl. Electrochem.* **1996**, *26*, 1195–1199.

(81) Da Silva, L. M.; Boodts, J. F. C.; De Faria, L. A. *Electrochim. Acta* **2001**, *46*, 1369–1375.

(82) Matsumoto, Y.; Yoneyama, H.; Tamura, H. *J. Electroanal. Chem. Interfacial Electrochem.* **1977**, *83*, 237–243.

(83) Bockris, J. O.; Otagawa, T. *J. Phys. Chem.* **1983**, *87*, 2960–2971.

(84) Willems, H.; Kobussen, A. G. C.; De Wit, J. H. W.; Broers, G. H. J. *J. Electroanal. Chem. Interfacial Electrochem.* **1984**, *170*, 227–242.

(85) Rasiyah, P.; Tseung, A.; Hibbert, D. B. *J. Electrochem. Soc.* **1982**, *129*, 1724–1727.

(86) Rasiyah, P.; Tseung, A. *J. Electrochem. Soc.* **1983**, *130*, 365–368.

(87) Doyle, R. L.; Lyons, M. E. G. *Phys. Chem. Chem. Phys.* **2013**, *15*, 5224–5237.

(88) Doyle, R. L.; Lyons, M. E. G. *Phys. Chem. Chem. Phys.* **2013**, *15*, 5224–5237.

(89) Tseung, A. C. C.; Bevan, H. L. *J. Electroanal. Chem. Interfacial Electrochem.* **1973**, *45*, 429–438.

(90) Miles, M. H.; Huang, Y. H.; Srinivasan, S. *J. Electrochem. Soc.* **1978**, *125*, 1931–1934.

(91) Fischer, P.; Heitbaum, J. *J. Electroanal. Chem. Interfacial Electrochem.* **1980**, *112*, 231–238.

(92) Angelo, A. C. D.; Gonzalez, E. R.; Avaca, L. A. *Int. J. Hydrogen Energ.* **1991**, *16*, 1–7.

(93) Matsumoto, Y.; Yamada, S.; Nishida, T.; Sato, E. *J. Electrochem. Soc.* **1980**, *127*, 2360–2364.

(94) Suntivich, J.; Gasteiger, H. A.; Yabuuchi, N.; Nakanishi, H.; Goodenough, J. B.; Shao-Horn, Y. *Nat. Chem.* **2011**, *3*, 546–550.

Chapter 4: Development of a gas diffusion electrode for bifunctional oxygen catalysis

4.1 Introduction

The overall goal of the PowAir project has been to design and prototype a working zinc-air flow battery for integration into a national electrical network. The work in this thesis is limited to the development of bifunctional oxygen electrocatalysts and their implementation into gas diffusion electrodes for the zinc-air battery. Any further work to scale and implement the electrodes in a full working flow-cell is outside of the scope of this thesis.

The zinc-air flow battery operates with a number of cells (depending upon the amount of energy that is to be stored), each comprising of two electrodes, one for the zinc and the other for the oxygen. The flowing electrolyte, composed typically of either sodium or potassium hydroxide and soluble zincate species, separates the electrodes. The battery cells are then cycled between the charging state corresponding to the OER and deposition of zinc and discharging state corresponding to the ORR and dissolution of zinc.

As already discussed in Chapter 3, the slow kinetics of the oxygen reactions remains one of the key factors determining the final battery performance. This limitation is the motivation behind the development of new electrocatalysts to promote the oxygen reduction and evolution reactions. The method by which the catalyst is incorporated into a working electrode structure will influence the operation of the cell in terms of electrical power and voltage efficiency. Electrical power is the transfer of the electrical energy into and out of the cell, as determined by Equation 29, where P is power in watts, V is the voltage, Q is the charge in coulombs and t is time in seconds. The current density and the overpotential are the two primary criteria for improvement.

Equation 29

$$\boldsymbol{P = \frac{VQ}{t}}$$

4.1.1 The gas diffusion electrode

To introduce the basics of electrode design and the relevant points of a gas diffusion electrode as those employed in this project, the following aspects will be reviewed: (i) the requirements of the structure and the three-phase interface, (ii) utilisation of such structures for PEM fuel cells as an example, (iii) The scale of the support and alternative to carbon, and (iv) The effect and choice of binder.

The gas diffusion electrode is typically comprised of a current collector, gas diffusion layer, and catalyst/active layer.[1] These structures/layers are formed as outlined below.

The current collector provides high electrical conductivity across the back of the electrode. This is usually formed using metal or carbon in the form of paper[2], mesh[3,4] or foam[5].

The gas diffusion layer provides a highly porous and electrically conductive layer to facilitate the transport of gases to and from the catalyst layer. It also provides the electrical contact between the current collector and the catalyst layer.[1] This layer is typically formed by preparing a suspension of small particles of carbon or metal with a polymer binder, which is then applied as a film/layer to the current collector.[2,6]

The catalyst layer typically includes a mixture of the active material and high surface area carbon.[4] A polymer binder is included to provide adhesion to the gas diffusion layer and to alter the properties (e.g. proton conductivity, hydrophilic, hydrophobic etc.) of the catalyst layer.[1,2,6,7]

Each layer can be formed individually and then bonded together to form a GDE or prepared directly on top of one other to form a continuous structure. The method of producing the gas diffusion electrode varies depending upon the application the electrodes are designed for. The electrolyte and electrochemical reaction will define the requirements of the electrode. An example of extensive GDE development has been for the hydrogen fuel cell.

4.1.2 Fuel cell GDEs

The study of hydrogen, as first observed in 1789,[8] lead to its industrialisation through the 19th and 20th centuries.[9] The gas is produced primarily through reformation of hydrocarbons, but also via hydrolysis of water. Electrolysis represents a benefit for hydrogen production, by not relying on fossil fuels and delivers high purity oxygen and hydrogen gases.

The hydrogen gas can be used to store energy, with the energy released by reaction with oxygen as outlined in Equation 30 - Equation 32. This reaction takes place inside of the hydrogen fuel cell. The reactions described below refer to the proton exchange membrane fuel cell (PEMFC), but other hydrogen fuel cells are available, such as the phosphoric acid (PAFC), alkaline (AFC) and solid oxide (SOFC) fuel cells.

Equation 30

$$Cathode: +2H^+ + 2e^- \rightarrow H_2O_{(l)} \qquad E^0 = 1.23\ V\ vs.\ RHE$$

Equation 31

$$Anode:\ H_{2\,(g)} \rightarrow 2H^+ + 2e^- \qquad E^0 = 0.00\ V\ vs.RHE$$

Equation 32

$$Overall: H_{2\,(g)} + {}^1/_2\, O_{2\,(g)} \rightarrow H_2O_{(l)} \qquad E^0 = 1.23\ V\ vs.RHE$$

The PEM fuel cell offers several advantages over the PAFC, AFC and SOFC. The thin polymer membrane separating the PEMFC electrodes facilitates high current densities and voltage efficiencies.[10] The rapid start-up time, flexible power production and low operating temperature allow for a wide range of applications.[11]

For applications in space, the platinum electrocatalyst was prepared with high surface area and onto a gas diffusion electrodes based on carbon paper, which was capable of operating at current densities in excess of 1 A cm^{-2}.[12] Although successful for such limited space applications, the main barrier to commercialisation for terrestrial applications remained the cost of the platinum electrocatalyst and storage of the reactants for such a system.

The alkaline fuel cell and subsequent acid and solid polymer fuel cells required a new range of gas diffusion electrodes to be developed. The high cost associated with the electrocatalysts drove the metal utilisation to be a key parameter in future works in acid and PEM fuel cells.

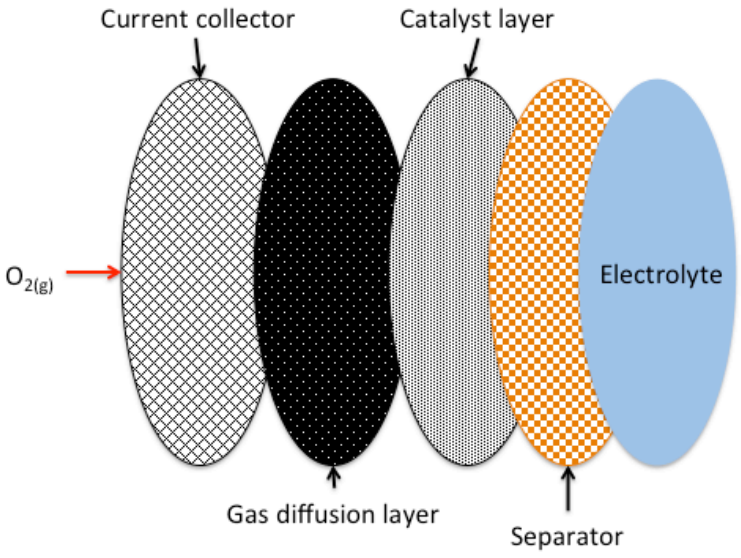

Figure 52: Schematic of the layers in a composite gas diffusion electrode.

The electrode structure evolved, commonly with a two- or three-layer composite (Figure 52).[13,14] The typical construction required a current collector to provide a conductive path across the electrode, a hydrophobic gas diffusion layer (GDL) and a catalyst layer. A two-layer structure would unify the GDL and catalyst layers.[13] The reactant gas diffuses through the hydrophobic GDL

to reach the catalyst layer. The other reactant was carried through either a solid polymer proton conductor or separators from the hydrogen electrode to the catalyst layer on the oxygen electrode, before completing the reaction to form water, in the case of fuel cells.

The catalyst layer provided a diffuse region of the necessary reaction media of oxygen, protons and water in which the reaction readily takes place. The combination of the gas, liquid and solid comprises the reactive area of the catalyst layer and is commonly referred to as the three-phase region of the electrode. The electrical contact to the electrocatalyst is critical to avoid excessive Ohmic losses in the catalyst layer, which would produce an undesirable loss in efficiency and thermal build up during operation in a cell stack. The gas permeation to the electrocatalyst centres is controlled by the porosity and thickness of the GDE. Further the porosity and binder in the carbon paper also provide a hydrophobic barrier to excess liquid flooding the electrode. This, however, is unable to prevent flooding by liquid produced during the reaction.

A desirable electrode structure is therefore, one that is stable foremost, is able to regulate the degree of flooding or liquid ingress into the electrode and one that maintains gas flow channels.[15] The porosity of the structure was designed with a fine pore structure at the gas interface and a coarse structure at the electrolyte interface.[16] Carbon based electrodes provide a mixture of macroporisity and mesoporosity, capable of sustaining both the water and gas channels, and have been an area of great interest.[17-20] The pore structure has been further tuned through the addition of pore-formers during the electrode manufacture, whereby soluble inorganic salts are included into the catalyst layer to increase porosity and catalyst utilisation.[21] Although progress has been made in the electrode pore structure, the catalyst utilisation remains challenging.

As carbon paper provides a suitable stable and low cost gas diffusion layer, the research focus shifted to catalyst utilisation. The current cost of platinum at $1,223 per ounce[22] motivated these efforts. This was achieved by changing synthesis methods to reduce particle size and, further, by creating core-shell structures to form thin films of platinum on relatively low cost base metals. This has resulted in a reduction in platinum loading from 1 mg cm^{-2} for platinum black to 0.01 – 0.05 mg cm^{-2} for state of the art platinum electrocatalysts.[23,24] The reduced loadings have been demonstrated to achieve high current densities (>1 A cm^{-2}) with only a small increase (20 mV) in the overpotential.[25] Progress on catalyst utilisation is shifting the main cost of fuel cells from the platinum catalyst to other components, such as flow field plates and ancillaries necessary for cell operation, but availability of precious metals will always remain a long-term concern for mass production.

4.1.3 Metal-air battery GDE

The development of electrodes for metal-air batteries typically focused on either the oxygen reduction reaction or the oxygen evolution reaction.[26-29] However, for an electrically rechargeable zinc-air battery both reactions are required. The use of a dual electrode design has been reported for secondary zinc-air batteries[30,31], with dedicated electrodes or catalyst layers for the ORR and OER. Inevitably, the increased cost, through added materials for two catalysts, or increased complexity of the cell design for multiple electrodes limited the appeal of such designs.

Efforts have focused on the development of novel catalysts using base metals, to overcome the cost implications of precious metal based electrocatalysts. A number of mixed metal oxide electrocatalysts have been developed based on MnO_x, perovskites, spinels and pyrochlores, with several compositions suggested as viable alternatives to precious metal catalysts. The development of the electrode structure has mimicked that found in fuel cells.

The conductivity of mixed metal oxides or any catalyst is a limiting factor when constructing electrodes. This is commonly overcome by the addition of highly conductive carbon additives. The use of conductive carbon additives in the air-electrode presents a significant complication when designing a bifunctional electrode. The carbon is stable for hundreds to thousands of hours during the ORR reaction and the conductivity and surface area benefit the structure. However, the carbon is unstable in the potential range for the OER, leading to the eventual loss of the catalyst layer and formation of non-conductive carbonate salts.

Alternative substrates were thus sought. The key parameters are corrosion resistance, electrical conductivity, mechanical support and porous for efficient gas and liquid transport. PEM water electrolysers have commonly used titanium foams or felt with added titanium powder as current collector.[32,33] Hydrogen embrittlement could be further reduced by the addition of a thin-film of gold.[32] Alkaline applications for the OER are carried out on flooded electrodes, with the catalyst layer prepared on metallic (nickel or stainless steel) mesh or foils.[34-37] The flooded electrodes provide excellent performance towards the OER, but are unsuitable as bi-functional electrode due to the low solubility of oxygen in the electrolyte limiting the ORR. Nickel is a suitable low cost current collector and is found in other nickel/alkaline based batteries.

Efforts to form a GDE suitable for ORR and OER reverted to using a mixture of catalyst and hydrophobic binder. Early work was carried out on electrodes prepared as pellets, which provided limited oxygen supply to the three-phase boundary interface resulting in relatively low current densities being achieved (<10 mA cm^{-2}).[38,39] Several reports have proposed the use of three electrode cells; this is possible with a solid zinc metal electrode, the oxygen catalysis is carried out

on a dedicated carbon based GDE for the discharge (ORR) and charged via the OER on a flooded nickel electrode (typically a mesh).[40] Although functional, the additional cost of a third electrode in the flow-battery would be undesirable. The suggested cell geometry would result in the zinc deposit being plated on one side and stripped on the other, creating a layer that shifts in the cell with each cycle until eventually the zinc electrode fails (Figure 53).

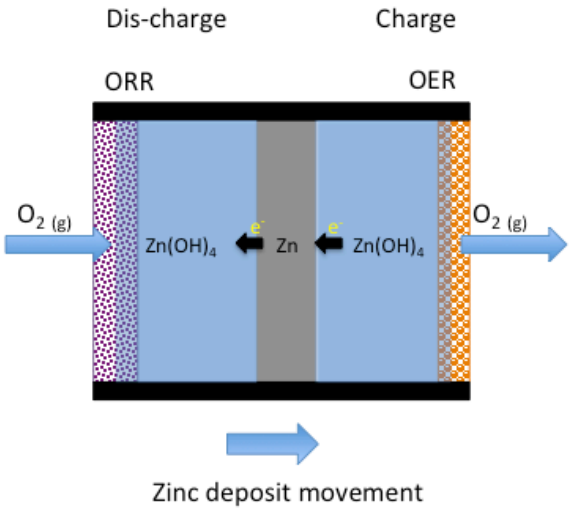

Figure 53: Schematic of twin oxygen electrode with central zinc electrode.

A single electrode capable of both the oxygen evolution and reduction reactions, avoiding the use of carbon, was therefore one of the goals of this project.

Bifunctional electrodes, capable of both the ORR and OER, have previously been manufactured using catalyst combined with polymer binder, carbon and formed onto a metallic current collector.[27,41-43] Mixed metal oxides combined with PTFE and roll-pressed onto nickel mesh have also been reported to achieve 10s to 100s of mA cm^{-2} and avoids the need for carbon.[38,44,45] Roll pressing of an electrode provides a well characterised and uniform layer. The film-thickness can easily be separation of the rollers, and any binder can be made flexible by the application of heat.

Initial reports used nickel mesh electrodes that appeared promising, but required high pressures and temperatures that would be undesirable for large energy storage applications with corrosive electrolyte.[12] Changes to lower the temperature or reduce operating pressures would overcome many of the safety concerns, but would likely adversely impact the performance of the battery.

It is therefore desirable to find a solution that achieves similar performance of 100s of mA cm^{-2}, but at lower temperatures and pressure. The mixture of carbon powders, PTFE and $La_{0.6}Ca_{0.4}CoO_3$ has been pressed between two nickel screens with the electrodes capable of 3 A cm^{-2} for the ORR only.[46] The greatest influence to the current densities of a titanium mesh electrode was from increasing the surface area of the perovskite catalyst from 2 $m^2 g^{-1}$ to 27 $m^2 g^{-1}$.[47]

All electrodes incorporate a polymer binder for affixing the catalyst in the electrode structure. A range of polymers can provide suitable solutions, with hydrophobic and hydrophilic properties, but are typically based on a fluorocarbon backbone. Alternatively, polyethylene has been combined with a pyrochlore-based catalyst and carbon to provide a reactive layer for an electrode and avoids the necessity of PTFE to provide hydrophobicity in the layer.[48] A similar preparation using a reactive layer hot-pressed between nickel screens produced a suitable electrode capable of both ORR and OER, but with inferior performance limited to 100 – 200 mA cm^{-2}. Further examples commonly employ the mixture of catalysts, carbon and PTFE[49-57] but are unsuitable for the long lifetime required in metal-air batteries for stationary power applications. The development of a new type of gas diffusion electrode is therefore needed to support bifunctional oxygen electrodes for alkaline media.

This chapter will discuss the design and development of a gas diffusion electrode for the catalysis of the oxygen reduction and evolution reactions. The progress will discuss the evolution of the structure to improve voltage efficiency of the cell and methods used to further reduce catalysts loading.

4.2 Methods

4.2.1 List of Reagents

Table 19: List of reagents and materials used inclusive of suppliers

Material/Reagent	Supplier
Aqueous Nafion® solution (10.85 % solids)	Johnson Matthey
Aqueous PTFE solution (60 wt. % solids)	Sigma-aldrich
Carbon Paper (wet proofed) Toray	Alfa-Aesar
Carbon Powder (XC-72)	Johnson Matthey
Isopropyl Alcohol	Fisher
Nickel foam	Goodfellows
Nickel mesh (Microgrid®)	Dexmet
Nickel (carbonyl) powder	Huizhou Wallyking Battery
Potassium Hydroxide (> 98 %)	Sigma-Aldrich
Sodium Hydroxide (>98 %)	Fisher
Stainless steel mesh (120 x 400 mesh)	H & B wire fabrications
Water (18 MΩ cm)	Purite water purifier

4.2.2 Electrode preparation

A description of the electrode preparation is included for each 'type' of electrode. Electrodes of the same substrate material (Carbon paper, Nickel foam, wire mess) were prepared as briefly described below, with a detailed description available in Chapter 2 section 2.3.

4.2.2.1 Carbon paper electrode

The catalyst ink was prepared by combing catalyst powder (70 mg), XC-72 carbon powder (30 mg) with 564 μL 10 wt.% Nafion solution, 916 μL H_2O and 200 μL IPA. The ink was sonicated for 30 minutes, followed by two minutes of mixing using a homogeniser.

The catalyst ink was brush-coated onto wet-proofed Toray paper in multiple layers. Each layer was dried at 393K, before hot-pressing at 453 K at 5 kg cm^{-2}. Electrodes were prepared with catalyst loadings of 1 – 10 mg cm^{-2}.

4.2.2.2 Nickel foam electrode

A suspension of nickel (or $NiCo_2O_4$) powder and PTFE (150 – 200 mg cm^{-2} at a ratio of 10:3 catalysts to PTFE) was suspended in water (2 mL) and IPA (2 mL). The suspension was then applied to a disc of nickel foam. This was then cold-pressed at 3 kg cm^{-2} for 30 seconds, forming the gas diffusion layer.

4.2.2.3 Mesh electrode

A catalyst ink of $NiCo_2O_4$ (100 mg), 60 wt.% PTFE solution (50 mg), water (4 mL) and IPA (4 mL) was combined, sonicated (30 min) and homogenised (2 min). The solution was then spray-coated onto stainless steel mesh using an airbrush. The mesh was then hot-pressed at 453 K at 5 kg cm^{-2}.

4.2.2.4 Dip-coating

Electrodes were dip-coated in a solution of nickel and cobalt nitrates, before calcining at 648 K. The solution consisted of a 2:1 ratio of cobalt to nickel dissolved in a 1:1 ratio of water and IPA to yield 0.5 to 3 M metal salt in solution. The soaking (5 minutes) and thermal treatment (10 minutes at 573 K) was repeated three times to improve coverage, before a final calcination stage of 573 K for 3 hours, unless stated otherwise.

4.2.2.5 Brush-coating

Catalyst ink was prepared consisting of 20 mg $NiCo_2O_4$, 10 mg of 60 wt.% PTFE, 3 mL H_2O and 3 mL IPA. The nickel foam GDL was calcined at 648 K for 1 hour. The ink was then brush-coated onto the nickel foam GDL, as described in section 4.2.2.2, to yield a loading of 1 mg cm^{-2}. The electrode was then hot pressed at 453 K and 5 kg cm^{-2}.

4.2.3 Electrochemical methods

Gas diffusion electrodes are evaluated on their activation potential and durability. The measurements typically compared polarisation curves from 0.3 V down to -0.5 V vs Hg/HgO. The initial polarisation data provides an insight into how the electrode responds at higher current densities, with short time scales to avoid significant degradation. Further electrochemical study included either galvanostatic or potentiostatic measurements to determine the performance of the electrodes during extended operation. This identifies performance in the steady state and

overall stability of the electrode. The steady state measurements provide a simulation that closely follows the expected operation in a working flow battery. It is for this reason the majority of work presented here will be in the form of galvanostatic measurements to achieve current densities of 10, 20 and 50 mA cm^{-2}. Durability was then evaluated by cycling between the ORR and OER for periods of 0.5 to 1 hour for each reaction.

An ideal response for the galvanostatic measurements can be seen plotted as the black line in Figure 54. The square wave demonstrates an instantaneous increase in potential until the desired current density is achieved. The potential remains constant through the operation before the current is changed. The potential would be independent of the current density, as plotted, if the reaction kinetics and diffusion were extremely fast.

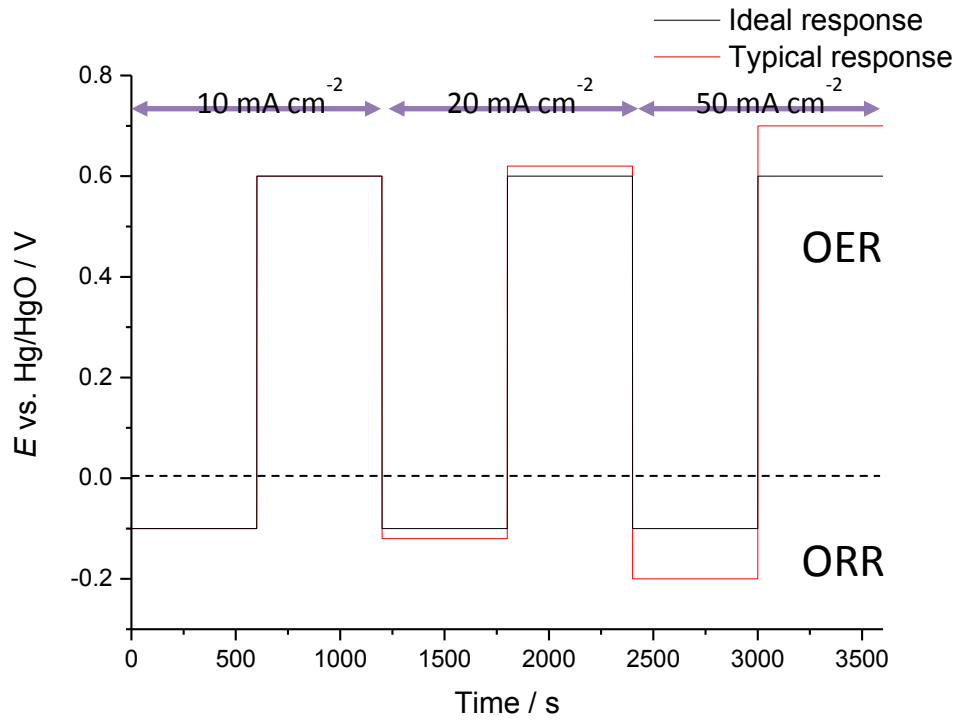

Figure 54: Example of an ideal and a expected electrochemical response for a galvanostatic measurement switching between the ORR and OER reactions and at increasing current densities.

The real response, plotted as the red line in figure 3, demonstrates that increased overpotentials are observed for operating at high current densities. The increasing overpotentials stem from a combination of slow electron kinetics for the oxygen reactions in addition to uncompensated resistance through the electrode and electrolyte. The slow kinetics of the oxygen reduction and evolution reactions require large overpotentials to achieve the desired current density. The increase in overpotential may not be equal for both ORR and OER, as they do not occur exclusively

on the same sites or necessarily follow similar mechanisms. The oxygen evolution reaction will occur in regions where the catalyst is flooded or partially flooded with electrolyte. In contrast, the oxygen reduction requires a three-phase boundary layer to combine the liquid and gas reactants at the catalyst surface. Although not shown in Figure 54, flooded portions would become severely limited in current density due to the low solubility of oxygen in the alkali electrolyte.

When considering the development of electrodes a wide array of variables are tuneable in the structure, from multi-layer construction through to pore-structure and individual layer composition. It is therefore important to identify criteria by which the electrodes can be compared. The parameters of merit for the air electrode are the potential gap, which is the potential difference observed between the OER and ORR, and the number of cycles the electrode can achieve before degradation/deactivation is observed, which is observed as a sudden increase in the potential gap.

The potential gap is determined as the difference in potential between the oxygen reduction and evolution reactions for a given current density on the air electrode. The difference provides the maximum voltage efficiency that the electrode is capable of achieving for the air electrode. The cell provides a theoretical voltage of 1.65 V, but due to the overpotential for the ORR and OER the actual voltage to charge the battery will be greater than 1.65 V, and the discharge voltage (corresponding to the ORR) lower than 1.65 V. The optimisation of the catalyst and the electrode structure are critical to minimise the losses associated with the voltage efficiency.

The number of cycles the electrode can achieve is important for determining the durability of the electrode. The number of cycles directly corresponds to the lifetime of the electrode and this is important consideration for energy storage capital costs. Increased electrode durability will provide a longer time period for depreciation of the installation, and therefore improve commercial opportunities.

Electrode degradation can occur through a series of modes. The activation overpotential is the potential required above the open circuit or equilibrium potential to achieve the desired current density. The battery will operate at 10 – 100 mA cm^{-2}, depending on the desired voltage efficiency to achieve profitability. Any deviation from the equilibrium potential can incur detrimental changes to the electrode, through mechanical, chemical, or electrochemical processes and may indicate the materials are unstable. The overpotential will typically increase with time to maintain the same current density, which can be attributed to either flooding during the ORR or drying out of the electrode during the OER. Finally the catalyst may undergo an activation or change in the surface structure. This can be seen in the cyclic voltammetry, shown in Chapter 3, whereby the cobalt undergoes oxidation state changes for the OER. Sustained cycling may result in this process

not being perfectly reversible and some effective deactivation of the catalysts. Finally, the oxygen evolution process is capable of generating high pressures in small pores of the electrode, which can cause physical degradation of the catalyst layer.

All electrodes were prepared as outlined as above and described in greater detail in chapter 2 section 2.3. All electrodes were tested in a thermostatically controlled three-electrode cell, as described in chapter 2 section 2.4. A nickel mesh was used to act as current collector on the back of the GDE. The electrolyte used in the experiment was either 8 M KOH or NaOH, operating at a temperature of 333 K. A continuous flow of oxygen was provided to the 'oxygen' side of the electrode at 200 cm^3 min^{-1}. A constant volume of electrolyte was supplied to the liquid side of the cell. A platinum mesh was used as the counter electrode and potential determined using a mercury/mercury oxide reference electrode in a Luggin capillary.

4.2.4 Scanning electron microscopy (SEM)

Gas diffusion electrodes were prepared onto conductive carbon layer on aluminium stubs. A Phillips XL30 SEM was used to measure the electron micrographs.

4.2.4.1 Carbon paper electrodes

The method of preparing the carbon paper based electrodes is outlined in section 4.2.2. In summary, a thin layer of catalyst and binder is applied through a brush coating process on the carbon paper. This undergoes a low-pressure (5 kg cm^{-2}) thermal treatment to ensure good adhesion. The resulting structure was analysed using scanning electron microscopy to determine surface morphology and layer thickness of the resulting electrode.

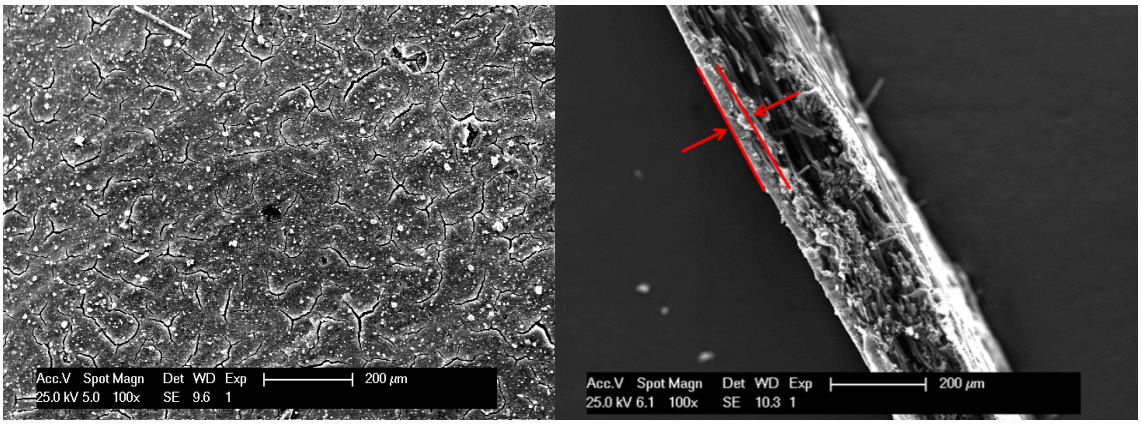

Figure 55: SEM micrograph of the $NiCo_2O_4$ prepared on carbon paper GDE. Top view, left, and side view of the same electrode, with the catalyst layer outlined in red on the right.

The $NiCo_2O_4$ coated top surface of the electrode is flat and uniform, with only small (50 – 100 μm) cracks covering the surface, as shown in Figure 55. The catalyst layer thickness was approximately 25 μm, as determined from the cross-section micrograph.

4.2.4.2 Nickel foam electrodes

The nickel foam electrode was produced as two variants, $NiCo_2O_4$ with PTFE binder and Ni powder with PTFE binder. The air face of the electrode is denoted by small wire-like structures, with the electrolyte face formed by the compacted mixed metal oxide surface. The $NiCo_2O_4$ yields a rough and porous surface electrolyte interface, with a relatively thick electrode at approximately 400 μm (Figure 56).

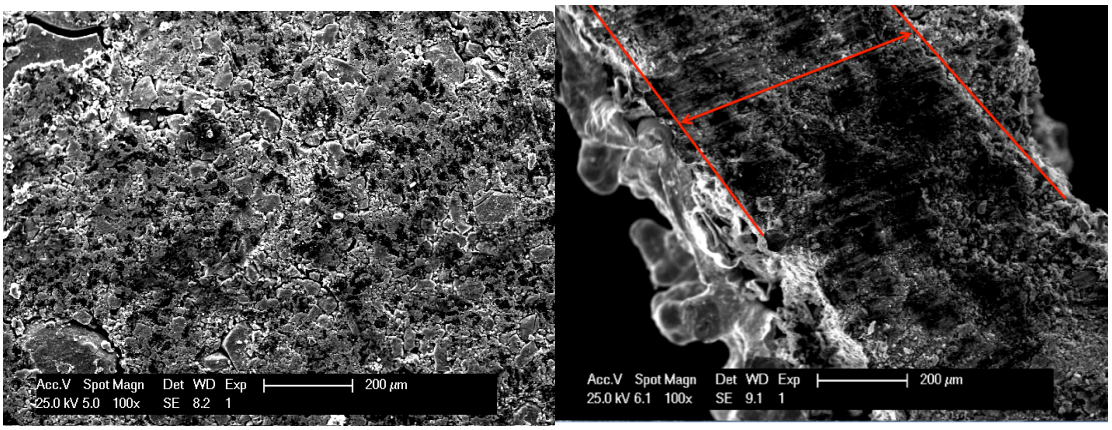

Figure 56: SEM micrographs of $NiCo_2O_4$ powder & PTFE packed into nickel foam. The catalyst layer (left) and side view (right) with the catalyst layer outlined in red.

In contrast, the nickel powder with PTFE on a nickel foam support yields a more uniform electrode surface, but remains a porous layer (Figure 57). The cross section view shows a compact structure with a thickness approximately 200 μm.

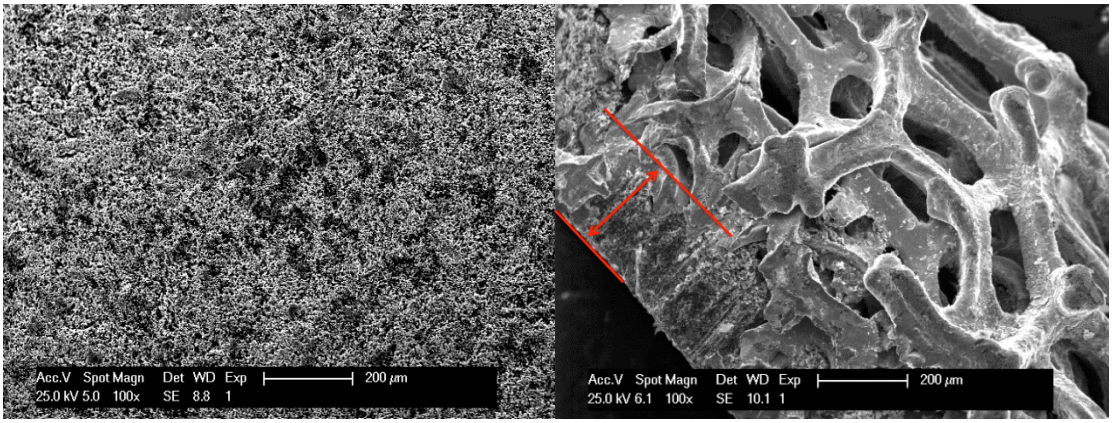

Figure 57: SEM micrographs of nickel foam electrode, electrocatalysts face (left) and cross section with nickel layer outlined in red (right).

4.2.4.3 Mesh electrode

The fabrication of a stable electrode structure on a metallic mesh presented a new engineering challenge. Previous electrodes utilised a dough-like paste to provide a pore structure that was mechanically reinforced through compression into a metal foam.[58-60] This was highly effective, if inefficient in regard to the loading of active and conductive material. A metallic mesh, expanded metal (Microgrid®), or woven twisted wire cloth may provide a viable alternative support. SEM images of the Microgrid® and a woven cloth are shown in Figure 58.

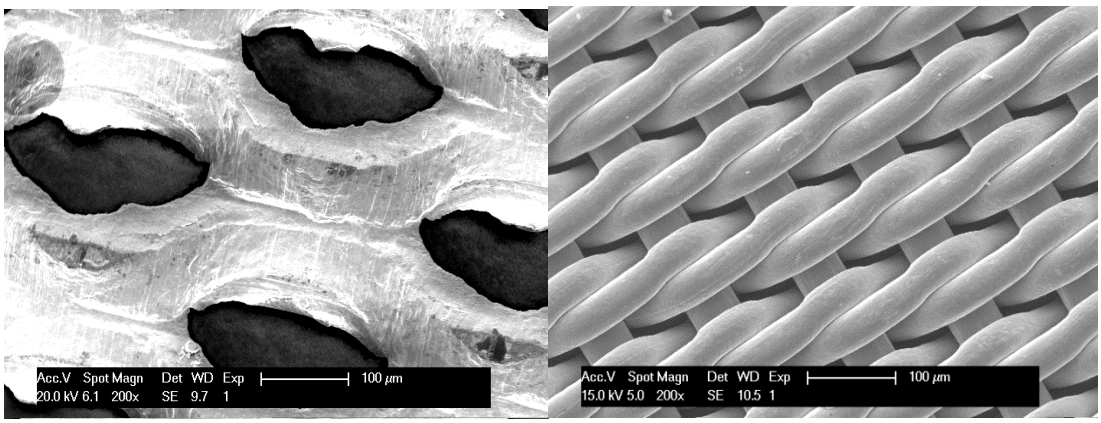

Figure 58: SEM micrographs of Microgrid® mesh (left) and woven cloth (right).

Initial attempts to prepare catalyst-loaded electrodes used the same Ni powder/PTFE dough as was used for the Ni foam electrodes. However, good adhesion could not be obtained. In place of the dough, an ink formulation was prepared with solutions of nickel or $NiCo_2O_4$ mixed with PTFE. Unfortunately the adhesion of the layer by brush-coating, screen-printing or roll-pressing was poor. The poor adhesion would result in the rapid failure of the electrode, resulting in leaking of electrolyte. Acid etching and sand blasting of the mesh both were insufficient to provide suitable substrate for the electrode layer. Spray-coating of dilute catalyst inks onto a heated mesh did however proved to be more successful. The heated mesh dried the fine spray of catalyst ink and the additive deposit was mechanically strong, whilst still maintaining a gas permeable structure.

The electrode layer prepared by spraying was intimately connected to the current collector as seen in electron micrographs (Figure 59). Spray-coating required a dilute ink comprised of a $NiCo_2O_4$ powder that was sieved to <50 μm and 60 wt.% PTFE at a 10:3 ratio by weight. This mixture was then suspended in 8 MΩ water and IPA at a 1:1 ratio by volume. The ink was sprayed onto the woven cloth using an Iwata HP-SB airbrush, propelled by a stream of nitrogen gas, from a distance of approximately 25 cm. Each layer was applied perpendicular to the previous layer and dried at 393 K on a hotplate. The electrode was then hot pressed and a film of $NiCo_2O_4$ applied by dip coating from metal nitrates and combustion at 573 K. The particle size was selected to avoid

blocking the spray-gun aperture (<300 μm). A low calcination temperature is desirable to avoid excessive decomposition of the PTFE binder in the electrode.

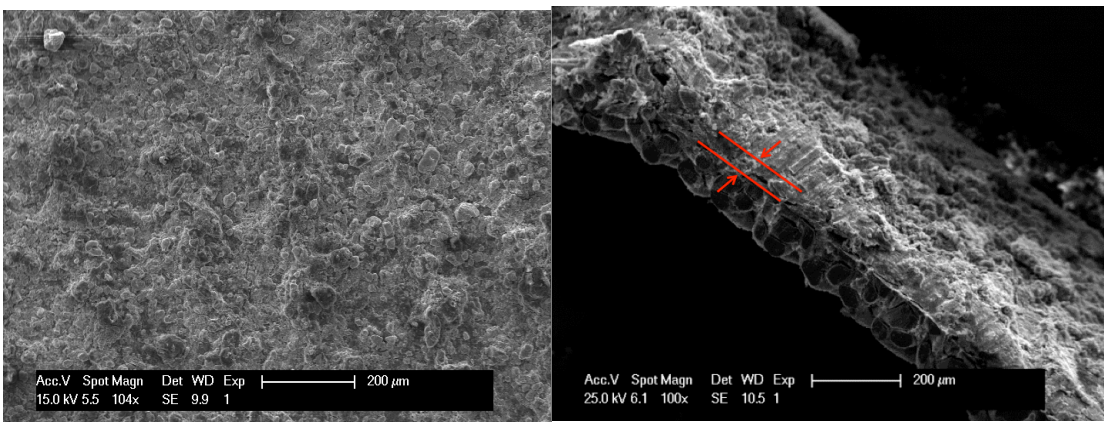

Figure 59: SEM micrographs of the catalyst layer of a spray-coated mesh electrode (left), and the side view of the same electrode with the catalyst layer outlined in red (right).

4.2.4.4 Brush-coated electrode

Brush-coated $NiCo_2O_4$ electrodes were prepared based upon nickel foam electrodes. A Ni foam electrode was prepared as outlined in section 4.2.2.2, using a pure Ni powder/PTFE composite. The brush-coated layer was then applied as outlined in section 4.2.2.5. This process avoids the need for dip-coating electrodes, but does still require the calcination step.

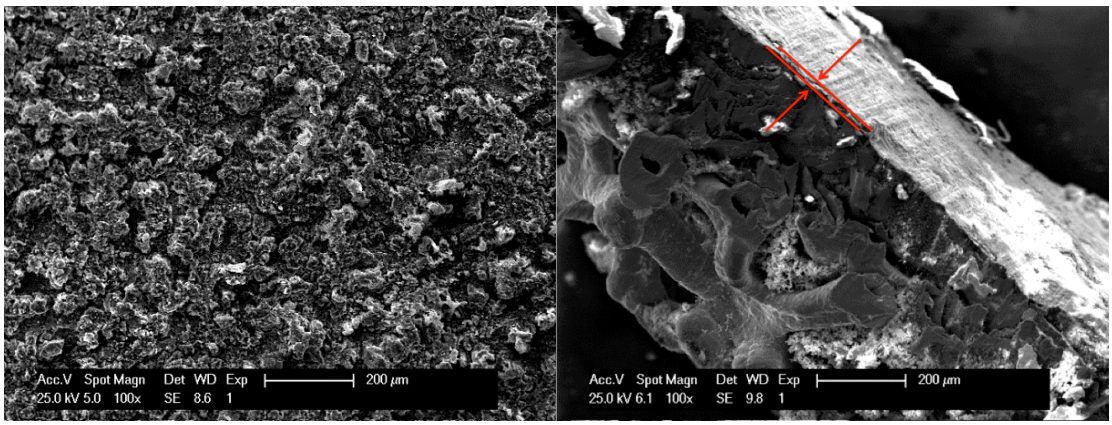

Figure 60: SEM micrographs of $NiCo_2O_4$ brush coated onto a nickel powder & PTFE in nickel foam GDL. Catalyst layer front (left) and side view of nickel foam, nickel paste and catalyst film outlined in red (right).

The brush-coated electrode surface appears to be covered by a range of agglomerated particles (Figure 60). The cross-section view from the SEM images above shows the airside of the electrode to the bottom left corner and the electrolyte face on the top right. The electrode composition is such that the airside is exposed to the Ni foam, with Ni paste layer ~ 150 – 200 μm on top, with

the final brush-coated layer (highlighted in red) facing the electrolyte. The brush-coated layer is formed as a thin-film, approximately 10 μm, on the Ni powder/PTFE layer.

4.2.5 Thermal gravimetric analysis

Thermal gravimetric analysis was carried out using a Mettler Toledo TGA with data analysed using STARe 8.0. Samples were prepared in pre-calcined alumina boat. A single electrode was cut down into small pieces ~<0.5 cm, to achieve a suitable sample for the sample boat. The intial mass of 93.48 mg is reduced to 93.29 mg through the loss of water from the electrode. The loss of mass to 92.08 mg is then the loss of the wetting agent commonly found in PTFE dispersions, up to a maximum temperature of 673 K, before the sample was allowed to cool. Overall, the 93 mg sample loses 1.5 mg of mass, suggesting excellent thermally stability up to 673 K.

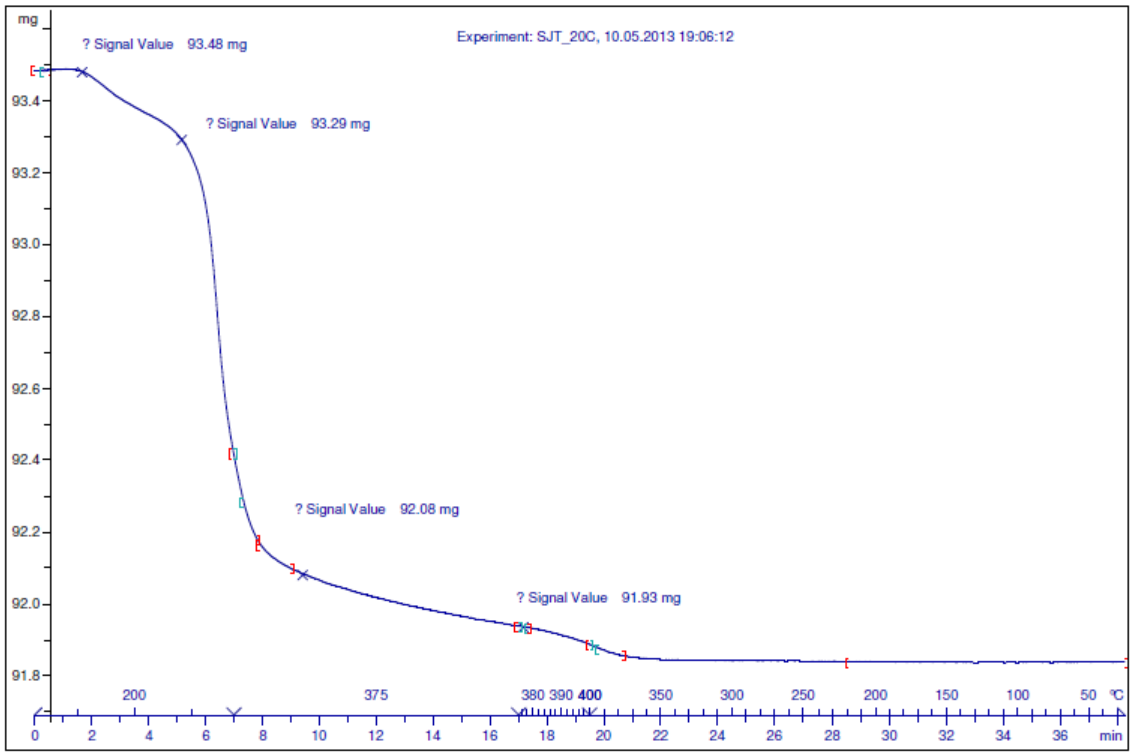

Figure 61: Plot from TGA of the loss of mass during thermal conditioning of a non-dip coated Ni foam electrode. Temperature is shown in degrees Celsius, with both time and temperature along the bottom axis.

4.3 Results

This section will discuss the electrochemical properties of a variety of gas diffusion electrodes developed for the zinc-air flow-battery. Results are ordered by the supporting structure employed in the manufacture of the electrode.

As a result of the significant change in reaction conditions (electrolyte, oxygen diffusion path and operating temperature) the measurements carried out on the gas diffusion electrodes are not directly comparable to those collected on the RDE. The gas diffusion electrode does not provide a smooth and flat surface to study the reaction kinetics of the electrocatalyst it does, however, provide a testing bed for how the electrocatalysts perform in conditions analogous to the final working flow cell. The zinc electrode is not included in these results, as this was evaluated as part of the thesis of Scott F. Gorman[61], who also worked on the POWAIR project. The zincate in the electrode was unlikely to strongly influence the air-electrode and it was important to identify the characteristics of the oxygen electrode in terms of performance and stability in isolation, before implementation in a working battery.

4.3.1 Carbon paper

Carbon paper gas diffusion electrodes were prepared to provide a baseline for the electrochemical performance that is achievable from the $NiCo_2O_4$ electrocatalysts. The electrocatalyst was selected due to the low overpotential towards both the oxygen reduction and evolution reactions; the synthesis requires relatively benign conditions and production is simple with low cost raw materials and relatively low temperature calcination step (< 693 K). These benefits combined with the high surface area of the $NiCo_2O_4$ produce an ideal electrocatalysts for manufacture into electrodes.

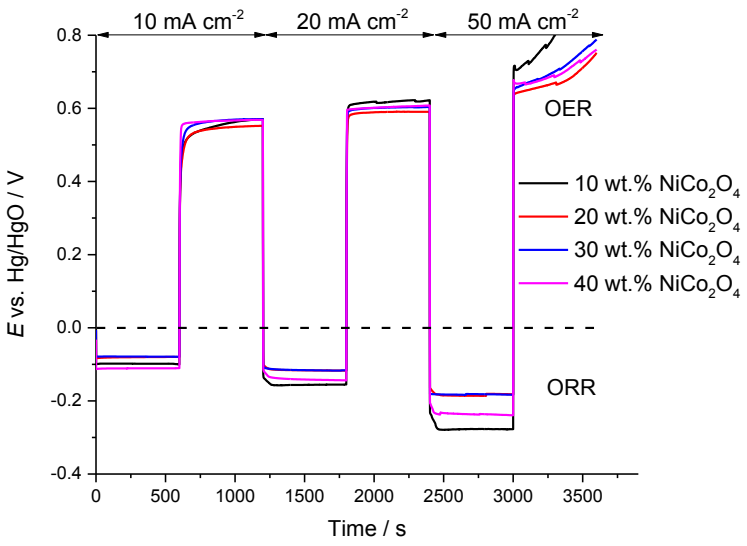

Figure 62: Constant current measurements at 10, 20 and 50 mA cm^{-2} (alternating ORR, followed by OER) on carbon paper GDE with different catalysts loadings. Loadings equate to 100-x mg Carbon, x mg $NiCo_2O_4$. All samples were measured in 8 M KOH at 333 K with 200 cm^3 min^{-1} of oxygen.

The constant current staircase measurements for a series of $NiCo_2O_4$ electrodes with varying amounts of carbon are shown in Figure 62. A loading of 20-30 wt. % of the $NiCo_2O_4$ electrocatalysts was found to be ideal (Figure 62). This composition achieved a potential gap between the oxygen reduction and evolution reactions of 707 mV at 20 mA cm^{-2} and 829 mV at 50 mA cm^{-2}. Although all electrodes produced the square wave behaviour expected from the galvanostatic measurement. A deviation in the expected behaviour occurs at 50 mA cm^{-2} during the oxygen evolution. A sudden rise in the potential needed to maintain the current density is indicative of electrode degradation and failure. The electrode degradation could be caused by a number of parameters: (i) Carbon corrosion; (ii) loss/degradation of the electrocatalysts; and (iii) electrode filling with oxygen gas. Any deactivation of the electrocatalysts would occur throughout the potential range of the reaction and was absent from RDE studies. A final possibility is the evolution of oxygen gas blocking the liquid interface of the electrode. The cell was operated at a slight angle ~ 15 – 20° from horizontal to facilitate the removal of gas bubbles from the electrode surface should they accumulate. However, evolved gas was found to diffuse out the air-side of the electrode, being carried away in oxygen gas flow. Typically an electrode suffering from gas bubble evolution into the electrolyte produces a 'saw tooth' type response that is not observed in this data.

The use of high surface area carbon powder in the catalyst layer is a likely source for this electrode failure. However, it was unexpected for the electrode failure to occur within minutes, when the degradation was expected to occur over hours.[40] The carbon is thoroughly mixed with the electrocatalysts and so it is possible the catalysts is also lost from the electrode during any corrosion, leading to the rapid rise in overpotential. It is also possible for the electrode to dry-out at high current densities, effectively starving the catalyst centres of the necessary path for electrons and water to sustain the reaction. This process was only observed for carbon paper electrodes with a Nafion binder. The binder may also play a crucial role in the catalyst layer stability during the OER.

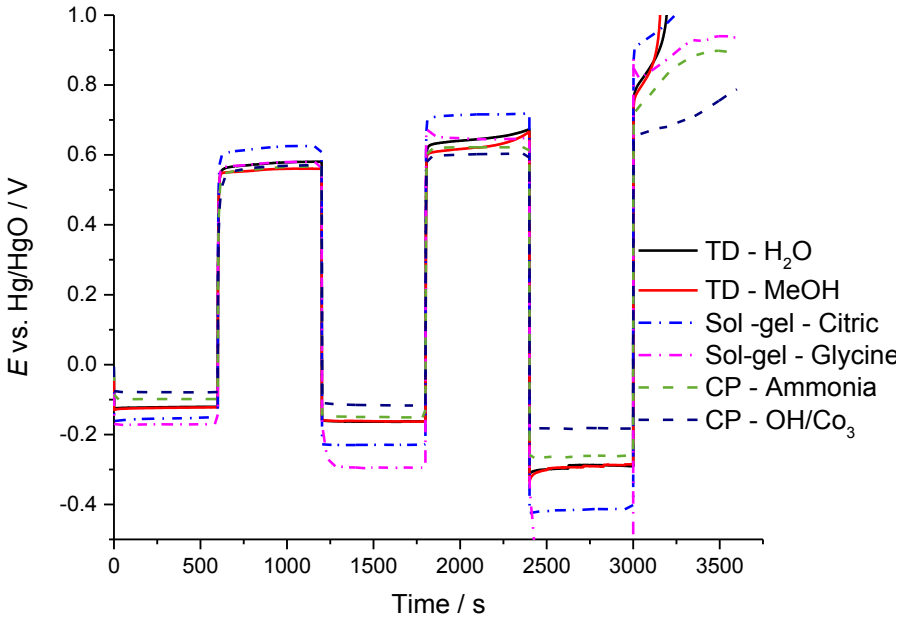

Figure 63: Galvanostatic ORR and OER measurements at 10, 20 and 50 mA cm^{-2} for different synthesis methods of $NiCo_2O_4$ on carbon paper electrodes in 8 M KOH, 200 cm^3 min^{-1} O_2 at 333 K. Catalyst loading of 100 mg cm^{-2} for all samples.

The $NiCo_2O_4$ was prepared by several methods, with the oxygen activity studied on RDE in Chapter 3. The results in Figure 63 highlight the effect the synthesis method has on the activity of the electrocatalyst. Samples prepared by sol-gel methods required the largest overpotential for OER and ORR when prepared on the carbon electrodes, with a potential gap of 940 mV at 20 mA cm^{-2}. The next best electrocatalysts were formed by thermal decomposition (TD), with the preparation by water or methanol indiscernible when prepared into a gas diffusion electrode. The lowest overpotential was achieved with co-precipitated (CP) $NiCo_2O_4$, with a potential gap between the evolution and reduction reactions of 718 mV at 20 mA cm^{-2}. This trend is in agreement with work carried out on the RDE, where the co-precipitated electrocatalysts appeared to provide greater catalytic activity for the oxygen reactions. The increased surface area of the co-precipitated $NiCo_2O_4$, when compared to the thermally decomposed samples, results in a lower overpotential for the ORR. Furthermore the oxygen evolution reaction was equally observed to improve with the use of a co-precipitated $NiCo_2O_4$.

Table 20: Comparison of different preparations of $NiCo_2O_4$ towards the ORR and OER reactions on carbon paper based GDE. Measured in 8 M KOH electrolyte operating at 333 K with an oxygen gas supply.

Sample	ORR @ 20 mA cm^{-2}	OER @ 20 mA cm^{-2}	Potential gap / mV
TD - H_2O	-162	644	806
TD – MeOH	-162	621	783
Sol-gel – citric acid	-229	716	945
Sol-gel – Glycine	-294	646	940
CP – Ammonia	-150	622	772
CP – OH	-116	602	718

The carbon paper electrodes were shown to successfully provide a GDL for the oxygen reduction and evolution reactions. The composition of the catalyst layer was optimised, with an ideal loading of 20 – 30 wt. % $NiCo_2O_4$ and 80 – 70 wt. % carbon. A high surface area electrocatalyst is recommended for this structure, yielding the lowest overpotential for both the ORR and OER. The potential gap is however still relatively large at 718 mV at 20 mA cm^{-2}. The durability of the carbon electrode is also questionable with a thermodynamic drive towards oxidation of the carbon to CO_2 during the OER that forms the non-conductive carbonate salt in the caustic electrolyte.

4.3.2 Nickel foam

Alternative substrates were evaluated, with a view to replace the carbon gas diffusion layer. Metallic structures were selected due to their relatively high stability in the strong alkali environment and relative low cost. Nickel provides an ideal solution with excellent stability, mechanical strength and good conductivity.

To recreate the porous structure critical for a gas diffusion electrode, a nickel foam structure was selected. The interconnected frame of the nickel foam provides an integrated current collector throughout the structure, whilst the pores of the nickel foam support are easily filled by either a catalyst or inert powder (when mixed with binder) to form a gas diffusion layer.

4.3.2.1 Spinel powder

The gas diffusion layer can be formed from the electrocatalyst, when combined with a binder. To this end, a mixture of $NiCo_2O_4$ and PTFE was found to form a dough-like structure that could be packed into porous nickel foam. Using iterative testing of the electrode, it was observed a thermal treatment to activate the electrode was required to achieve current densities for the oxygen reduction above 10 mA cm^{-2}. This was possible in the form of either hot pressing to a temperature above the glass transition temperature of the PTFE or more importantly, heating the electrode to 573 K resulting in the removal of the surfactant used in the PTFE dispersion. The addition of a thin-layer of electrocatalyst by thermal decomposition onto the electrode was found to further enhance the activity greatly, when compared to carbon (Figure 64) and without a dip-coat (Figure 65).[62,63]

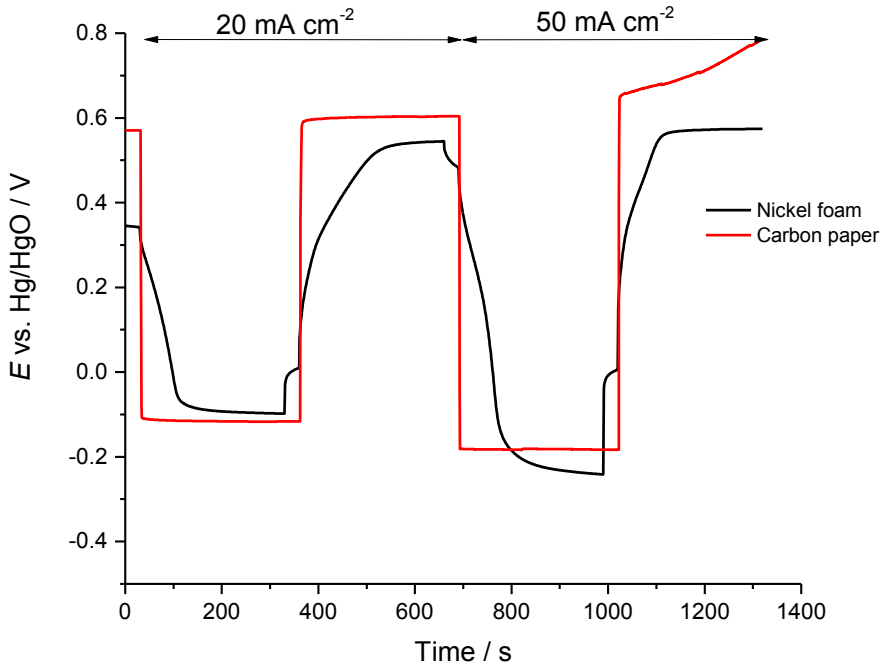

Figure 64: Galvanostatic measurements of the ORR and OER at 20 and 50 mA cm^{-2} of $NiCo_2O_4$ on nickel foam electrode (Black) and carbon paper electrode (red). Carried out in 8 M NaOH electrolyte at 333 K with 200 cm^3 min^{-1} of oxygen. The $NiCo_2O_4$ catalyst loading was 10 mg cm^{-2} on carbon paper and 100 mg cm^{-2} on Nickel foam.

The $NiCo_2O_4$ electrode provides a large pseudo-capacitive response, as shown in Figure 64, during the initial part of the ORR and OER cycles. The region of low overpotential occurs for a period of 120 – 150 seconds and is attributed to the oxidation and reduction of the catalyst film providing additional current at a lower overpotential than that of the OER and ORR. (Cyclic voltammetry of

the $NiCo_2O_4$ in chapter 3 has already identified a reversible surface redox couple is observed before the OER occurs. The peak current was found to be proportional to the scan rate for the range 1 – 300 mV s^{-1}, in addition the charge passed for the oxidation and reduction were equivalent confirming the charge is limited by the availability of a surface species.) The small amount of charge passed, approx. 1.5 mC cm^{-2}, provides further evidence of a surface process and not a bulk change of the catalyst. The electrical charge available with a low overpotential is a desirable feature for the electrode by providing vastly improved voltage efficiency for short periods of battery operation. Increasing the charge that benefits from this region of low-overpotential is limited by the available liquid interface of the either the catalyst or bulk nickel powder. Increasing the surface area of either the catalyst or the nickel powder would increase the charge available with a relatively low overpotential. However, the catalyst is prepared with the highest surface area possible and any alterations to the nickel powder will impact the tortuosity of the gas diffusion layer, with a negative effect on the electrodes overpotential during the oxygen evolution and oxygen reduction reactions.

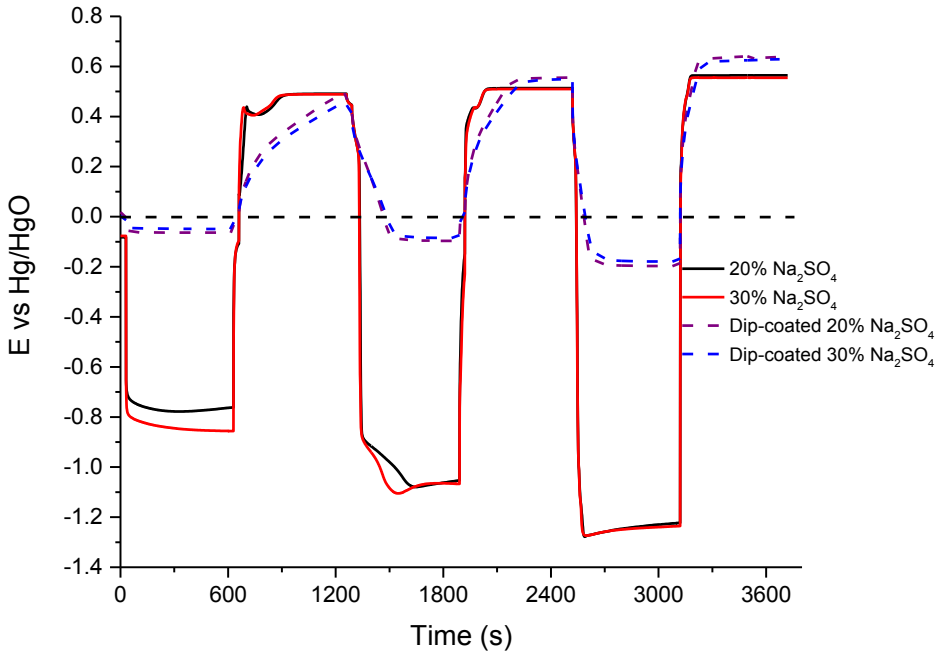

Figure 65: Galvanostatic measurements of the ORR and OER at 10, 20 and 50 mA for dip-coated and non-dip-coated electrodes. Electrodes were prepared using a Na_2SO_4 pore former and $NiCo_2O_4$ loading of 100 mg cm^{-2}. Measured in 8 M NaOH at 333 K.

The nickel foam and carbon electrodes at 20 mA cm^{-2} operate with nearly identical overpotential for the oxygen reduction. At the higher current density of 50 mA cm^{-2}, the overpotential is significantly greater than that of the carbon paper electrode. This would suggest that the

structure is not optimised for the oxygen reduction reaction. It is possible that the gas diffusion into the structure is poor or the catalyst layer is partially flooded, leading to a reduction in the three-phase boundary layer and lowering of the available electrocatalyst sites.

The oxygen evolution reaction, however, requires significantly lower overpotential on the nickel foam electrode. The potential gap between the oxygen reduction and evolution reactions was -96 and 544 mV for the nickel foam compared to -144 and 603 mV for carbon paper. The potential gap at 50 mA cm^{-2} is relatively low at 814 mV. This demonstrates that, even with relatively poor oxygen reduction activity, the metal foam provides an electrode capable of greater voltage efficiency than a carbon based electrode.

The dip-coat has been isolated as providing an important benefit to the metal foam electrodes. When comparing a series of electrodes prepared with and without the inclusion of the dip-coat provide poor activity towards the ORR. Those electrodes prepared without dip-coating typically required an additional 200 - 400 mV overpotential at 20 mA cm^{-2} than that of dip-coated electrodes.

Table 21: The ORR and OER potentials of $NiCo_2O_4$ packed Ni foam and $NiCo_2O_4$ supported on carbon paper in 8 M KOH at 333 K.

Sample	ORR @ 20 mA cm^{-2}	OER @ 20 mA cm^{-2}	Potential gap / mV
Carbon with PTFE binder	-114	603	717
$NiCo_2O_4$ on Ni foam	-96	544	640
$NiCo_2O_4$ + Ni powder	-114	541	655
$NiCo_2O_4$ + MnO_2 powder	-60	527	587

It is unclear, at this time, the role of the PTFE bound powder and the dip-coat deposit on the overall activity of the electrode. It is challenging to distinguish the effect either the spinel or nickel powder have on the OER, as both are able to catalyse this reaction. This can be viewed as benefit for the inclusion of nickel into the electrode structure, as a relatively low cost co-catalyst. To discern the effect of the PTFE bonded diffusion layer material compared to the dip-coated $NiCo_2O_4$ film, a small quantity of the $NiCo_2O_4$ powder was replaced with either nickel powder or MnO_2 to identify a change in the overpotential for either the ORR or OER.

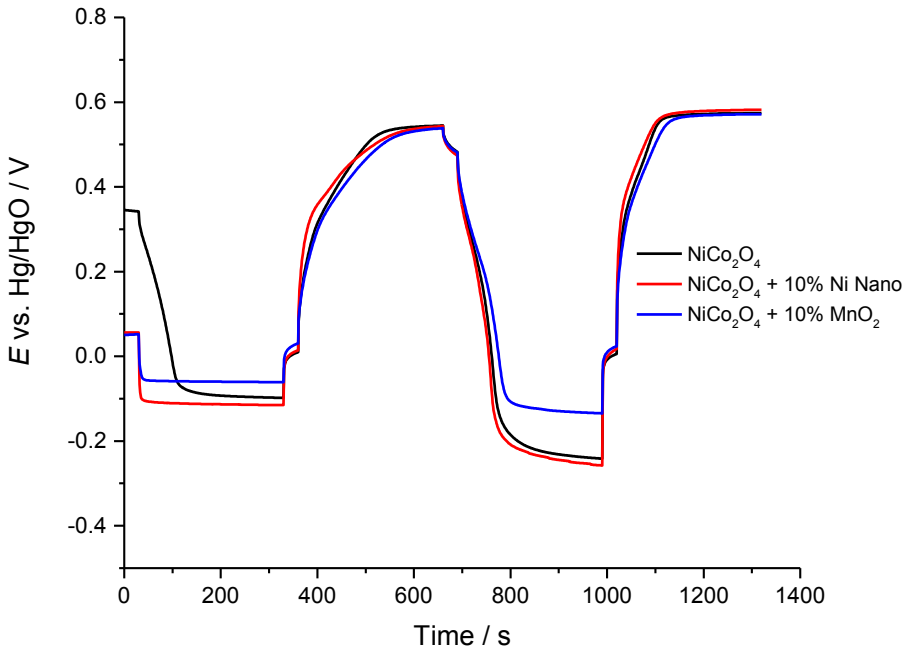

Figure 66: Galvanostatic plot for the ORR and OER for electrodes prepared from $NiCo_2O_4$ (black), the replacement of 10 wt.% $NiCo_2O_4$ with nickel powder (red) and 10 wt.% MnO_2 (blue). All electrodes prepared dip-coated $NiCo_2O_4$ layer. Measurements carried out in 8 M NaOH at 333 K and 200 cm^{-3} min^{-1} O_2.

Nickel powder, with a particle size of 5 – 8 μm (Ni nano in Figure 66), was added to improve conductivity, without altering the ORR activity. (The OER is not considered at this time due to the inability of the gas diffusion layer to fully cover the entirety of the nickel foam structure and thus this will already be having an effect on the result with a $NiCo_2O_4$ based GDL.) The addition of nickel shows little impact on the electrochemical response with a small increase in the overpotential for the ORR of 18 mV at 20 and 50 mA cm^{-2}. The pure $NiCo_2O_4$ electrode starts with a high OCP value, caused by a previous measurement at 10 mA cm^{-2} partially oxidising the electrode and can be ignored in this comparison as the measurement of the Ni nano modified electrode was not subjected to the same pre-treatment. The difference in particle size of the nickel powder (5 – 8 μm) compared to the $NiCo_2O_4$ (< 1μm) may provide a slight change to the packing of particles in the GDL, but appears to have little to no effect on the overpotential ORR, with the variation in overpotential between a nickel modified and pure $NiCo_2O_4$ within the reproducibility of the electrodes.

The addition of MnO_2, commonly employed as an oxygen reduction catalyst in alkaline batteries, does provide an improvement to the overpotential (Figure 66). The oxygen reduction at 20 and 50 mA cm^{-2} shows a reduction in overpotential of 37 mV and 101 mV respectively, when

compared to the pure $NiCo_2O_4$ GDL. This result would suggest the bulk layer does play a role in the catalysis. The particle packing and distribution for the MnO_2 powder is expected to be comparable to the nickel powder as they have similar particle sizes (approx. 10 μm) for MnO_2. However, MnO_2 is not an ideal additive as, with further cycling of the electrode, the overpotential for the ORR increased with each subsequent cycle, requiring greater overpotentials than pure $NiCo_2O_4$ samples within 3 cycles of ORR and OER. It is likely that during the oxygen evolution reaction the MnO_2 catalysts is degraded/deactivated, resulting in this sharp loss of performance after the third or fourth cycle.

4.3.2.2 Nickel powder

The current generation of nickel foam electrodes requires approximately 100 – 150 mg cm^{-2} of $NiCo_2O_4$, but this high-loading of catalyst is unsustainable for large-scale electrodes. Although the spinel electrocatalyst is a relatively low-cost material when compared to platinum and ruthenium catalysts, of the two metals the cobalt is the more valuable and an electrode that uses lower cost materials is always desirable. To further reduce the cost of an electrode a based on a nickel foam an alternative to the $NiCo_2O_4$ powder used in the GDL was required.

As with most electrocatalysts the bulk of the activity is derived from the surface sites, and the reactions that it can catalyse. A nickel powder therefore replaced the $NiCo_2O_4$ in the bulk of the electrode structure. The $NiCo_2O_4$ catalyst layer was subsequently applied through the dip-coating process, saving time and valuable nickel and cobalt catalysts.

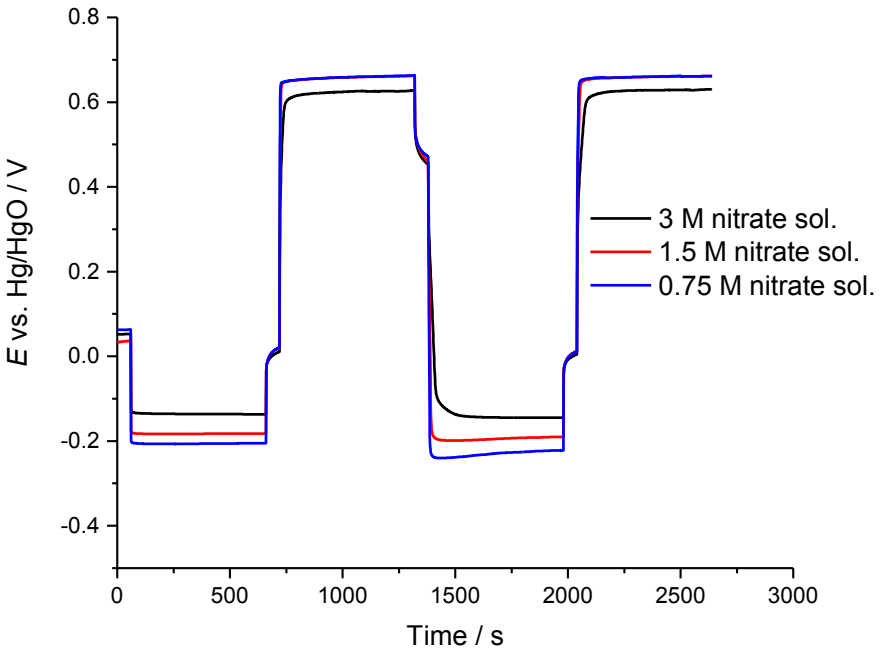

Figure 67: Galvanostatic ORR and OER response of nickel powder GDL dip-coated in $NiCo_2O_4$ in solutions of varying concentrations of the metal nitrate salts. Two cycles of ORR and OER at 50 mA cm^{-2} in 8 M NaOH, 333 K with 200 cm^{-3} min^{-1} O_2.

The standard preparation of the nickel foam electrode required dipping into a solution of nickel and cobalt nitrates at a stoichiometric ratio to attain the desired $NiCo_2O_4$. The previous results were based on using a 0.75 M solution of metal nitrates with a $NiCo_2O_4$/PTFE mixture on nickel foam to form a GDL. The electrochemical response for a pure nickel powder GDL produces a distinct square wave response, similar to that observed on carbon electrodes. This is likely due to the significantly reduced loading of 3-5 mg cm^{-2} compared to >100 mg cm^{-2} for the previous nickel foam electrodes.

The performance is reasonable (882 mV for nickel powder *vs.* 810 mV for $NiCo_2O_4$ powder), with a slight increase in overpotential when compared to the previous electrodes. However, for the nickel/PTFE GDL the concentration of the metal nitrate solution determines the final catalyst loading for the electrode. Increasing the concentration of the metal salts leads to a reduction in overpotential for both the ORR and OER. A further reduction in the potential gap from 882 mV to 772 mV was achieved by increasing the nitrate solution from 0.75 M to 3 M. The 3 M metal nitrates concentration increased the catalyst deposit from 3-5 mg cm^{-2} up to 6-8 mg cm^{-2}, well below the target of 10 mg cm^{-2} for the catalyst loading.

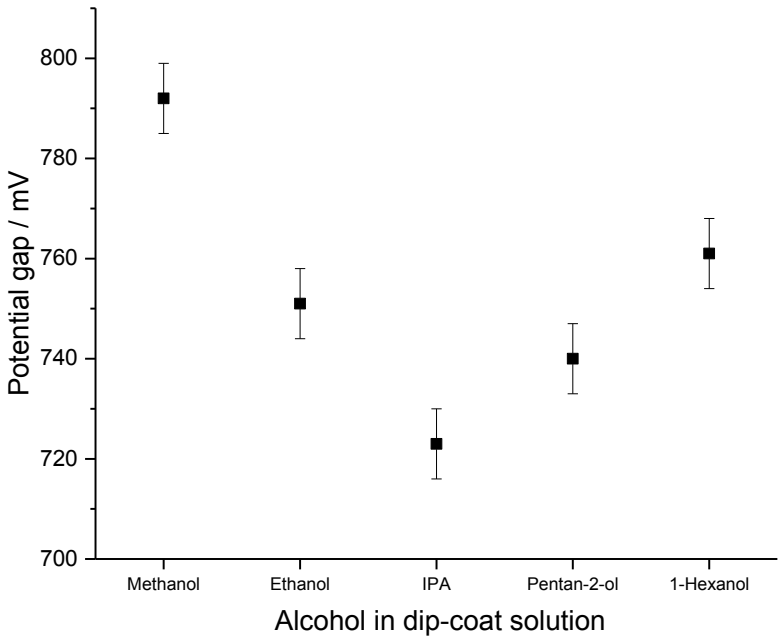

Figure 68: Effect of metal-nitrate solvent in the dip-coating solution on the potential gap between oxygen reduction and oxygen evolution at 50 mA cm^{-2}.

The dip-coating solution was varied to provide an insight into the effect on the catalyst loading and electrochemical response. The GDL is likely to form hydrophobic and hydrophilic regions, due to areas rich in the PTFE binder and those with low concentrations of PTFE respectively. A standard solution was prepared consisting of 3 M metal nitrate solution was prepared with a 1:1 ratio of water and alcohol. Subsequent solutions replaced the alcohol with those of increasing chain length (Figure 68). The increasing chain length, and thus increasing polarity, density and lower solubility in water of the alcohol will affect how the metal nitrate solution permeates the structure of the GDL. The alcohol chain length produced a potential gap dependency for the dip-coated electrode. An optimal solution for the metal nitrates was found to be a mixture of water and IPA, resulting in a potential gap between the ORR and OER of 720 mV at a current density of 50 mA cm^{-2}.

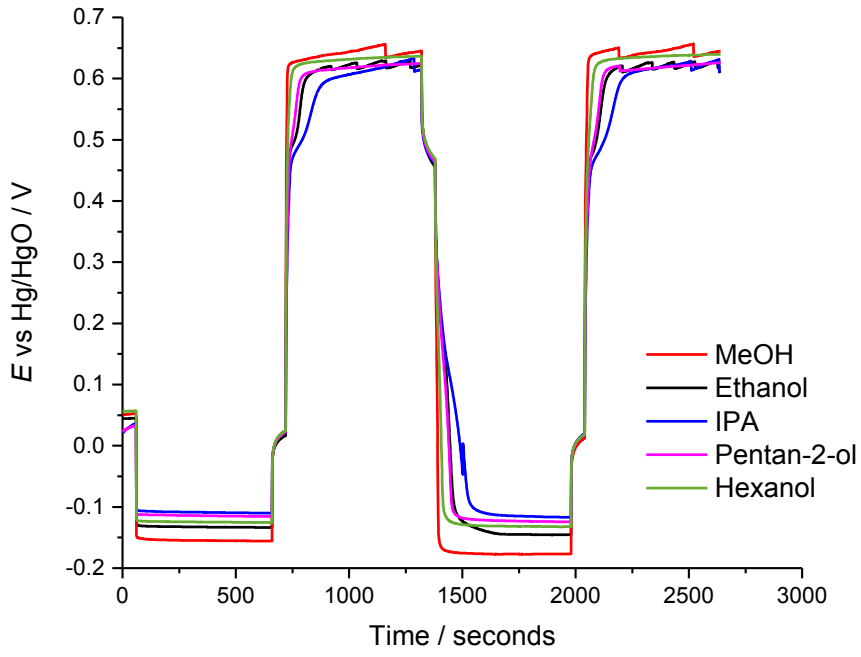

Figure 69: Galvanostatic measurement of the ORR and OER of dip-coated Ni foam electrodes at 50 mA cm^{-2} in 8 M KOH with 200 cm^3 min^{-1} O_2 at 333 K.

The smaller potential gap between the ORR and OER would suggest: (i) the catalyst loading was increased; (ii) the surface area of the catalyst deposit was improved/increased; or (iii) the metal nitrate solution was impregnated further in to the electrode. However, we are unable to determine which of the effects is dominant.

The distortion from a square wave does however provide an insight into the electrochemical surface area of the catalyst. The electrodes were twice cycled at 50 mA cm^{-2} for ORR and OER (Figure 69). Focusing on the second of the two cycles, it is clear the distortion from a square wave closely follows the trend found for the potential gap, with the smallest distortion for the methanol and hexanol samples through to the largest distortion for the IPA sample. As the charge associated with the deviation is related to the number of redox sites on the surface of the catalyst, it is reasonable to assume the IPA either increases the catalyst loading or the resulting surface area for the thermally decomposed catalyst that is formed.

The alcohol was a reasonable liquid medium for the PTFE/dispersant used in the preparation of the GDL. This would reduce the surface tension and promote ingress of the metal solution into the electrode. At the same time as metal nitrates penetrate the electrode structure, the PTFE binder can be lost through dissolution in the solvent. This is believed to be the source of the differences in performance of the dip-coated electrodes. Further, electrodes made to these

specification have been reported to run for greater than 100 hours continuous operation, with minimal loss in performance, highlighting the stability of these electrodes in the long-term.[62,63]

The force applied to the Ni foam electrode was also considered as a property of the manufacturing process that may influence the electrochemical response. A series of electrodes was produced, with increasing compression forces applied when combing the Ni powder/PTFE and the Ni foam current collector. As can be seen in Figure 70, the samples prepared with a low force (1 kN cm^{-2}) resulted in the lowest overpotential for ORR and OER.

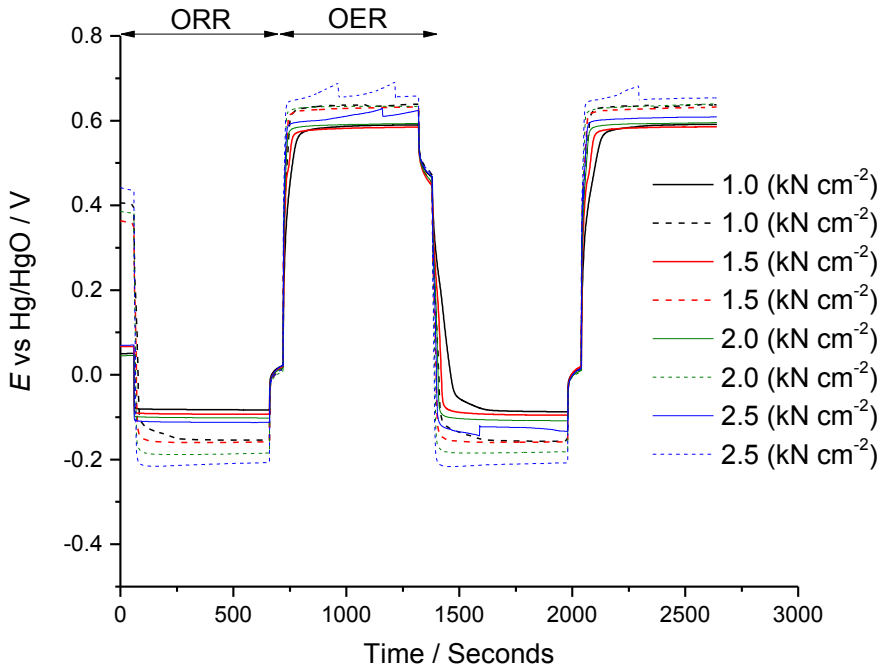

Figure 70: Plot of the galvanostatic measurement for the ORR and OER using Ni powder electrodes prepared on nickel foam, compressed at different forces. Samples measured in NaOH, at 333 K at 20 mA cm^{-2} (solid) and 50 mA cm^{-2} (dashed).

The degree of deviation from the square wave response follows a trend with the applied force, where the lowest force coincides with the greatest deviation. This deviation is associated with a charge available at a reduced overpotential during the first 10s of seconds during the OER and ORR constant current measurements. The electrode with the lowest overpotential throughout the constant current measurement was the Ni foam electrode produced with 1 kN cm^{-2}. The reduced force is likely to yield a more diffuse structure, however increasing in surface area were unreliable in determining a difference. The deviation in the square wave response, associated with surface sites on the catalyst, would suggest an increase in the number of catalytic surface sites has occurred.

4.3.3 Metallic mesh

Nickel foam electrodes are capable of operating at 100 mA cm^{-2} with low overpotentials and excellent durability. However, the resulting structure is relatively thick at approximately 500 µm, when compared with <150 µm for carbon-based electrodes. To reduce the material costs of the electrode and any Ohmic losses due to electrode thickness, a new metallic mesh electrode was developed.

A spray-coated the electrodes were prepared as outlined in section 4.2.2.3. The $NiCo_2O_4$ and PTFE layer applied to the woven metal acts as a gas diffusion layer. Although the GDL is composed of electrocatalyst, the PTFE appears to coat the electrocatalysts particles sufficiently to inhibit oxygen catalysis at current densities >10 mA cm^{-2}. To overcome this barrier a thin-film of $NiCo_2O_4$ is added by thermal combustion of nickel and cobalt nitrates on to the electrode, provided through the dip-coating process used in the nickel foam electrodes. TGA analysis, as shown in section 4.2.5, suggested the electrode was stable to 653K, before further loss of mass occurred, likely due to the decomposition of the PTFE. The dip-coated layer achieves a loading of approximately 3 – 5 mg cm^{-2} for a 1.5 M solution of nickel and cobalt nitrates, after three successive coatings.

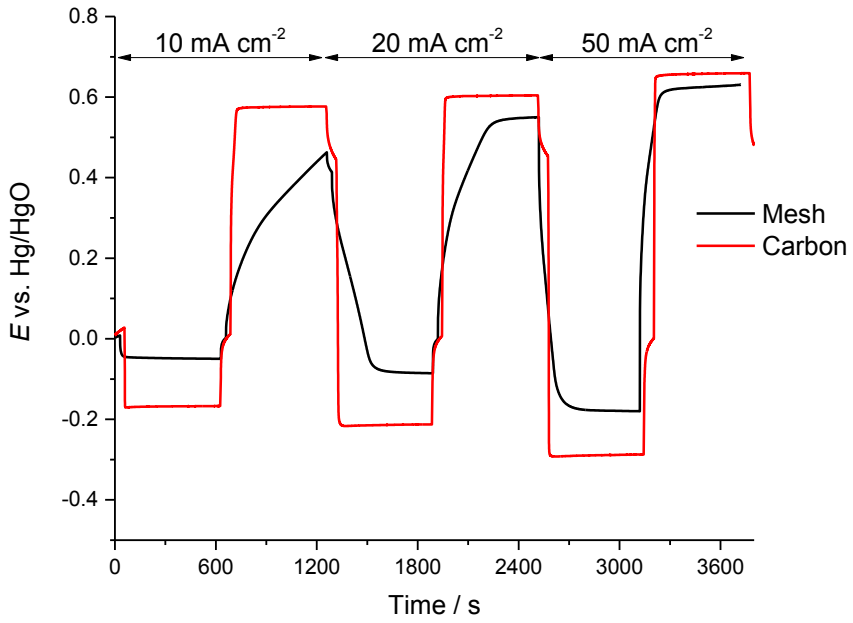

Figure 71: Plot of the galvanostatic response for ORR and OER of spray-coated mesh gas diffusion electrode with $NiCo_2O_4$ dip-coating (black) and $NiCo_2O_4$ on carbon paper (red), operating under galvanostatic control at 10, 20 and 50 mA cm^{-2}, cycling

between ORR and OER. Measured in 8 M NaOH electrolyte at 333 K, with a 200 cm^3 min^{-1} supply of oxygen.

The electrochemical performance of the mesh electrode deviates from that previously observed for the carbon paper and nickel foam electrodes (Figure 71) and is similar to that observed for nickel foam electrodes. The potential response during the oxygen reduction of the first cycle shows the expected square wave response with the potential remaining constant, and a variation of <1 mV for the 10 minutes of ORR.

The subsequent OER and ORR cycles display a distortion to the expected square wave response due to the $NiCo_2O_4$ redox couple. As already mentioned, the current that is available at a potential below the oxygen evolution potential is due to the oxidation of the catalyst. As this is attributed to sites at the surface of the catalyst and any changes in the amount of charge available at a reduced overpotential are directly correlated with catalyst loading. The electrode structure is composed of a higher loading of $NiCo_2O_4$ than previously found in the nickel foam electrodes (20 mg cm^{-2} on mesh electrode compared to 6 mg cm^{-2} for nickel foam). The increased catalyst loading provides a reasonable explanation for the larger current available at a low overpotential, when compared to other carbon or nickel foam electrodes.

The overpotentials at 20 and 50 mA cm^{-2} for the ORR and OER are lower than that of carbon electrodes, but greater than the nickel foam electrodes. At the lower current density of 20 mA cm^{-2} the potential gap was 635 mV, the smallest potential gap for a $NiCo_2O_4$ electrode. At 50 mA cm^{-2} the oxygen reduction occurred at -179 mV, whilst the oxygen evolution at 627 mV resulting in a potential gap of 806 mV, but nickel foam electrodes can achieve the same current density with a potential gap of only 725 mV. The disproportionate rise in overpotential from 20 to 50 mA cm^{-2} for the ORR may suggest the electrode structure is limiting the overall electrode performance. Therefore, with further work this structure could be further optimised to provide lower overpotentials for the ORR at higher current densities.

4.3.3.1 Electrode durability

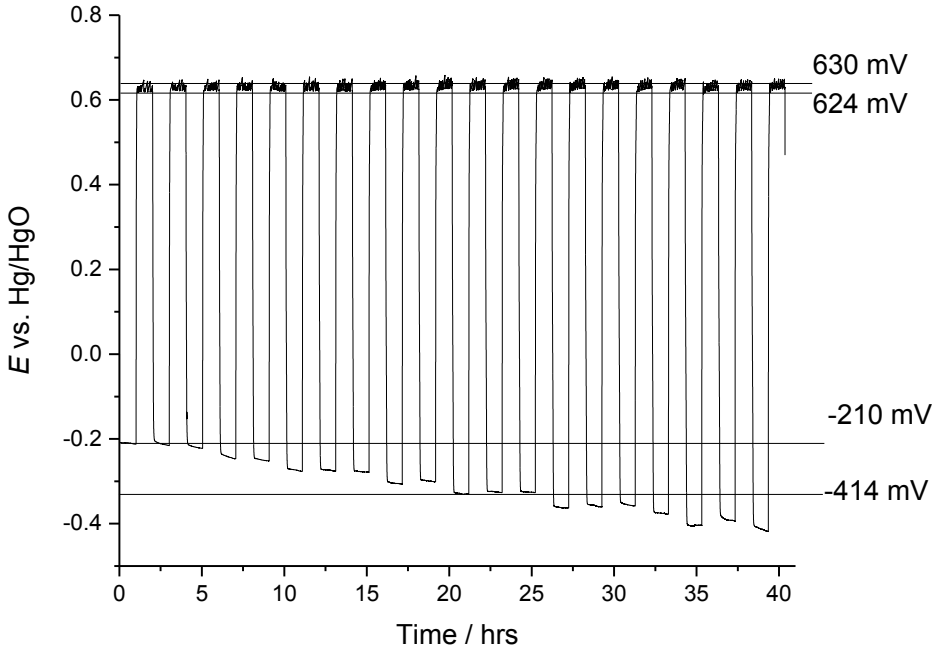

Figure 72: Galvanostic cycling of spray-coated gas diffusion electrode with $NiCo_2O_4$ dip-coating at 50 mA cm^{-2} ORR followed by OER cycles. Measurements carried out in 8 M NaOH, 333 K, 200 cm^{-3} min^{-1} of O_2.

The long-term cycling performance of the electrodes was later reviewed (Figure 72). Electrodes were required to operate for two-hour cycles (one hour ORR + one hour OER) at 50 mA cm^{-2}. The electrodes showed reasonable mechanical stability, with no observable loss of the catalyst layer during operation.

The oxygen evolution reaction was maintained with a potential of 625 – 630 mV through the full 40 hours of operation. The small variation in overpotential was due to the formation of oxygen gas on the electrolyte face of the electrode. This results in a reduction in the effective electrode area, requiring a higher overpotential to maintain the 50 mA cm^{-2}, until the evolved gas dislodges from the electrode with an accompanying drop in overpotential.

The oxygen reduction initial potential of -210 mV is comparable to other electrodes of this construction. The overpotential rises quickly with each subsequent cycle, up to -400 mV within 20 hours of cell operation. This level of degradation is not acceptable for electrodes that ideally need to achieve 1000's of hours of operation for stationary power applications. The fact that it is limited only to the ORR would suggest the catalysts is still active and deactivation is unlikely as this should also present a rise in overpotential for the OER. An alternative explanation for the

rising overpotential is flooding of the electrode. A steady hydrostatic pressure from the electrolyte may fill the electrode, reducing the effective three-phase boundary layer and losing reactive centres for the ORR.

4.3.3.2 Bi-layer spray-coated mesh electrodes

A further understanding of the interactions and formulation of the electrode layer was required, to optimise the structure for activity and stability. Typically, electrodes were prepared with a single layer of packing material ($NiCo_2O_4$ or nickel powder) mixed with a binder at a fixed ratio. This ratio was altered to achieve the lowest overpotential for the oxygen reduction and evolution reactions. However, the mesh electrodes demonstrated a loss in hydrophobicity with cycling. This would suggest that the surface charge pf the layer is changing, which is not an unreasonable assumption with the observed redox couple, or that the PTFE in the structure is deteriorating, as this is the material providing the hydrophobicity in the structure. Cyclic voltammetry measurements have suggested the changes to the surface species undergo a reversible process, so an oxidation state change is an unlikely source for electrode degradation.

To evaluate the electrochemical activity bi-layer electrodes were prepared. Each layer was produced with a different ratio of catalysts to PTFE (5 wt. % PTFE or 30 wt. % PTFE). All the metal electrodes reported earlier in this chapter have utilised a PTFE loading of 30 wt. %. Lower loadings can result in lower overpotentials, but the electrodes typically fail by the electrolyte leaking through the electrode. The bi-layer structure produces regions of high hydrophobicity, from the higher concentration of PTFE, at the cost of conductivity in the layer. The layer with less PTFE and lower hydrophobicity is likely to suffer from flooding with electrolyte. The oxygen evolution and overall conductivity would be promoted by lower PTFE. In contrast the ORR will benefit from an increased three-phase boundary layer of a PTFE rich electrode.

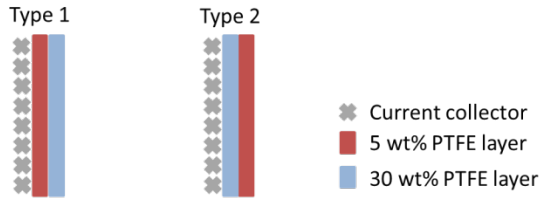

Figure 73: Schematic of the bi-layer electrodes prepared onto current collectors.

Electrodes were prepared by spray coating the desired compositions onto the woven mesh until a loading of 10 mg cm^{-2} was achieved. Followed by spray-coating the next layer with an equal loading of the alternate composition. All electrodes were further hot-pressed and dip-coated to form thin-films of $NiCo_2O_4$ before use. The catalyst layer was always the side exposed to the electrolyte, with the reverse supplied with oxygen.

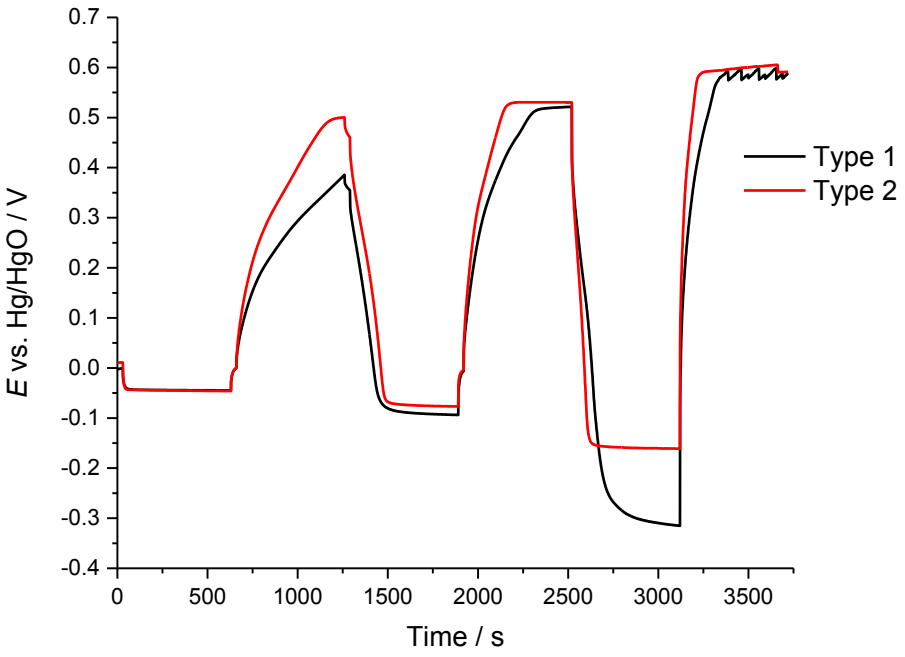

Figure 74: Plot of galvanostatic cycling of different compositions of spray-coated bi-layer electrodes. Type 1 (black) consist of high PTFE loading on a low PTFE loading and type 2 (red) were formed by depositing lower PTFE onto a high PTFE layer. Measured at 10, 20 and 50 mA cm^{-2} in 8 M NaOH electrolyte at 333 K with 200 cm^3 min^{-1} of oxygen.

The electrochemical responses for the two electrode layer types are presented in Figure 74. The electrodes with high concentration of PTFE at the electrolyte interface appear to provide marginally improved OER overpotential, however it is within the tolerance for manufactured electrodes by this method. This result may be due to a slightly increased electrochemical surface area, with the pseudo-capacitance providing a larger effect that is dependent upon the area of exposed electrocatalysts. The oxygen reduction overpotential is comparable for the two electrodes at 10 and 20 mA cm^{-2}. However, at 50 mA cm^{-2} the overpotential rises for the type-1 structure, likely caused by flooding of the electrode. A bi-layer gas diffusion electrode typically consists of a highly hydrophobic backing layer, with catalyst layer of lower hydrophobic polymer content in which the three-phase boundary layer is formed. The type-1 electrode reversing this formation is likely to result in flooding of the oxygen channels in the low PTFE region of the electrode, requiring disproportionate overpotential to drive the current density higher.

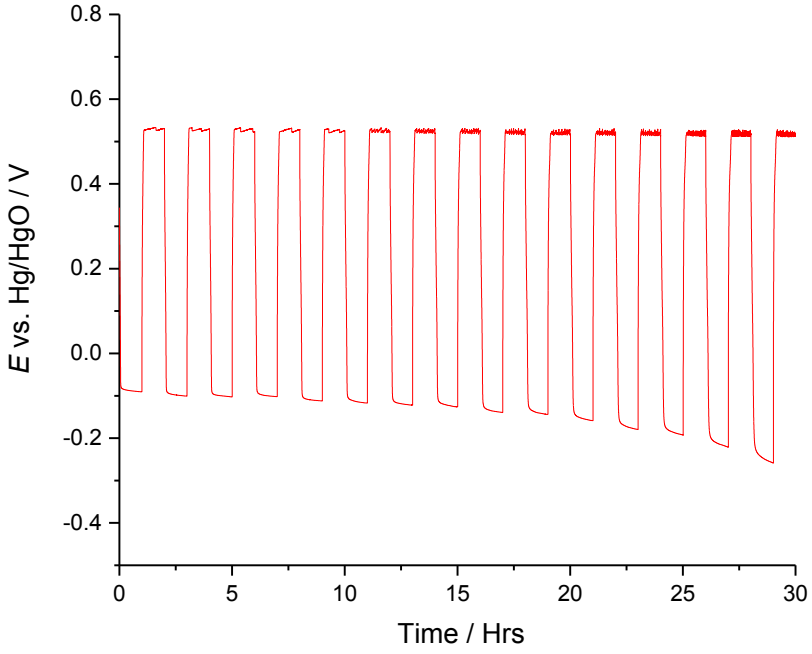

Figure 75: Galvanostatic measurements for extended cycling of a type-2 bi-layer electrode switching between ORR and OER (1 hour each) at 20 mA cm^{-2}. Carried out in 8 M NaOH, 333 K, 200 cm^3 min^{-1}.

The type-2 electrode was further evaluated by cycling for 20 hours, switching between oxygen reduction and evolution every hour. The oxygen evolution potential was consistent throughout the measurement, with a slight reduction (9-10 mV) over the duration of the experiment. The reason for this slight reduction in overpotential is not clear, however, it may be explained by: (i) evaporation of the electrolyte causing a lowering of the pH, or, more likely, (ii) the slow flooding of the electrode, effectively increasing the electrocatalyst area for the reaction.

The overpotential for the ORR on the bi-layer electrode was excellent during the early stages of operation at 20 mA cm^{-2}. However, the overpotential rose steadily throughout the operation of the electrode, with a total increase of 100 mV in 20 hours. This would suggest either loss/deactivation of the electrocatalysts or, as suggested from the OER result, the electrode is slowly flooding. The ingress of electrolyte into the electrode reduces the three-phase boundary layer and requires high overpotential for the ORR.

4.3.4 Catalyst loading on mesh electrode

Electrodes were prepared with high and low loading of $NiCo_2O_4$ to understand the differences in activity observed between the nickel foam and mesh electrodes. The GDL layer on the nickel foam

was prepared in excess of 150 mg cm^{-2}; this loading could not be achieved on a mesh electrode, as above 90 mg cm^{-2} the oxygen reduction was severely limited (<10mA cm^{-2}). Two electrodes with a loading of 20 mg $cm^{-2}$and the other 86 mg cm^{-2} of $NiCo_2O_4$/PTFE at a ratio of 10:3 were prepared to compare the effect the GDL has on the mesh electrodes.

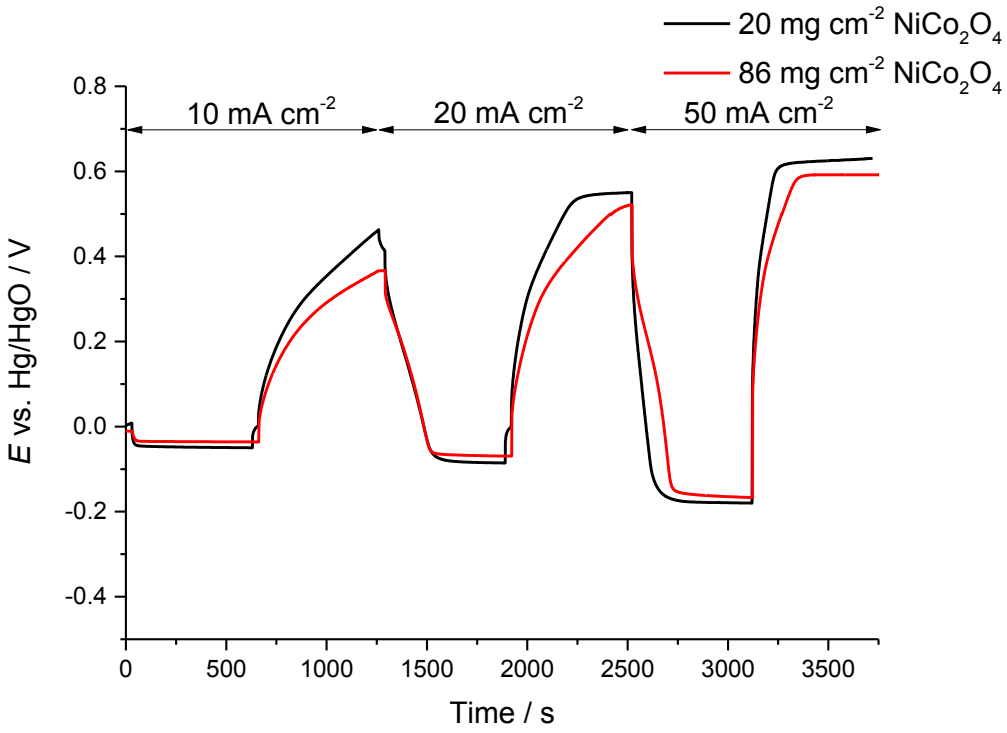

Figure 76: Galvanostatic cycling between ORR and OER for $NiCo_2O_4$ Mesh electrodes in 8 M NaOH at 333 K 200 cm^{-3} min^{-1} O_2.

The overpotential for both the OER and ORR is lower for the sample with more $NiCo_2O_4$ (Figure 76). However, the small improvement in overpotential could not justify the four-fold increase in catalyst/GDL loading. The charge associated with the $NiCo_2O_4$ surface redox couple has increased with thicker gas diffusion layer, providing further evidence that this effect is related to catalyst and not due to the nickel powder or metal current collector.

4.3.5 Brush coated foam

The relatively high loadings of electrocatalysts on electrodes remained a limitation for mass production, particularly with the inclusion of platinum group metals into the catalyst layer. Efforts were undertaken therefore to apply brush-coating of the electrocatalysts onto metallic GDL.

4.3.5.1 Nickel foam gas diffusion layer

Electrodes were prepared with a nickel foam current collector and a GDL formed from a mixture of nickel powder and PTFE as outlined in section 4.2.2.2. The brush-coated electrode was formed by applying a layer an ink of $NiCo_2O_4$ with PTFE (10:3) onto the compacted nickel foam GDL, as outlined in section 4.2.2.5. This method of electrode preparation reduced electrocatalyst loading from 3-8 mg cm^{-2}, for previous dip-coated nickel foam GDL, down to 0.7 mg cm^{-2} $NiCo_2O_4$.

The brush coating was noticeably improved when applied from diluted ink (10 mg of catalysts in 6 mL of (1:1) water/IPA). Each layer was dried at 453 K until the desired loading was achieved. This method provided excellent control of the loading onto the electrode. Previous electrode structures required catalyst loadings of 20 – 150 mg cm^{-2} for mesh and foam electrodes, when using the $NiCo_2O_4$ powder. The nickel foam packed with nickel powder allows lower loadings on the order of 3 – 8 mg cm^{-2}, but with limited control of the loading. Previous electrodes prepared by the dip-coating process required thermal cycling of the electrode to form the catalyst layer, an undesirable process when attempting to increase the scale of the electrodes to >100 cm^{-2}. The brush coated electrodes improved control of the catalyst loading, whilst avoiding thermal cycling of the electrode that may lead to deformation during large-scale (>100 cm^3) electrode production.

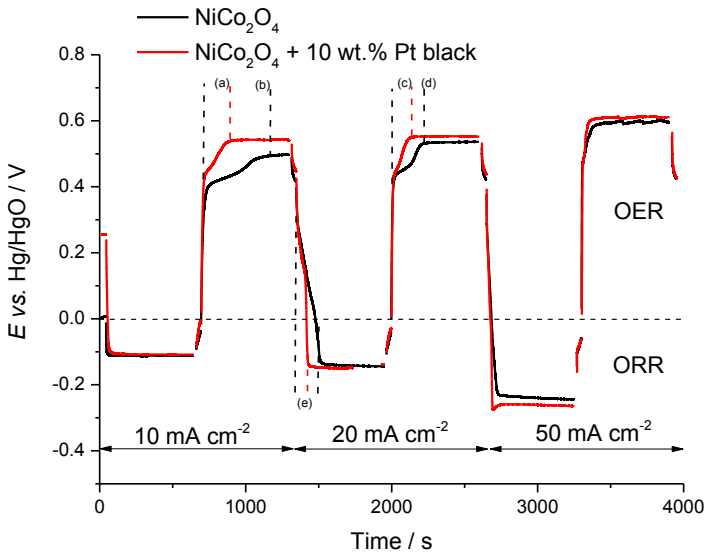

Figure 77: Plot of galvanostatic measurements of nickel foam GDL with brush coated $NiCo_2O_4$ catalyst layer operating at 10, 20 and 50 mA cm^{-2}, alternating between ORR and OER. Measurement carried out in 8 M KOH at 333 K with 200 cm^3 min^{-1} oxygen gas supply.

The brush coated $NiCo_2O_4$ layer provides excellent electrochemical response. A deviation from the square wave response is observed with the first oxygen evolution, as shown in parts (a) and (b) in Figure 77, which is associated with the oxidation of the electrocatalyst surface. The period of time

that it lasts reduces with increasing current density, as highlighted by (c) and (d) compared to (a) and (b) in Figure 77. The associated charge during these periods is roughly equal for the OER in parts (c) and (d) and the ORR, shown in part (e) of Figure 77, suggesting the process is reversible. Any differences may occur through: (i) degradation of the layer via deactivation; (ii) mechanical loss of the electrocatalysts during the OER; and (iii) slow filling of the electrode with electrolyte, resulting in a change to electrochemical surface area.

The potentials during oxygen reduction show a rising potential with each subsequent increase in current density; an equal and opposite response is observed for the oxygen evolution reaction. However, the ORR displays a disproportionate rise in the overpotential, compared to the OER, for the increase in current density. The increase in overpotential from 10 to 20 mA cm^{-2} was 30 mV compared to the 99 mV rise from 20 to 50 mA cm^{-2}; in comparison the OER takes an increase of 40 mV for 10 to 20 mA cm^{-2} and a further 50 mV to achieve 50 mA cm^{-2}. The need for greater overpotential for each increase in current density for the ORR than OER would suggest the ORR is limited by more than just overpotential. The additional limitation may be either a chemical or structural factor is further limiting the electrochemistry on this electrode.

Table 22: Comparison of operating potentials for different electrodes in 8 M KOH* and 8 M NaOH at 333 K with O_2 gas supply.**

Electrode	ORR/OER potentials / mV		
	@10 mA cm^{-2}	@20 mA cm^{-2}	@50 mA cm^{-2}
*Carbon – brush coat	-168/576	-212/604	-287/658
**Nickel foam – dip coat	N/A	-81/590	-154/638
**Mesh – dip coat	-45/500	-76/535	-160/597
*Nickel foam – brush coat	-112/496	-142/536	-243/596

The brush-coated structure results in a low overpotential for the OER at 20 and 50 mA cm^{-2}, when compared to carbon supported $NiCo_2O_4$ (Table 22). The oxygen reduction also demonstrates an improvement of 60 mV, compared to carbon based electrodes. At the lower current densities the ORR yields a consistent response, whilst at 50 mA cm^{-2} a slight rise in the overpotential is observed. The rise in overpotential for the ORR continues with subsequent cycling limiting operational lifetime.

4.4 Conclusion

A comparison of all the gas diffusion electrodes prepared in this series provides clear evidence of improvements that are possible, through electrode design. The carbon paper electrode, with a catalysts loading of 8 mg cm^{-2}, provides the largest overpotential for both the ORR and OER throughout the current range tested, as shown in Figure 78.

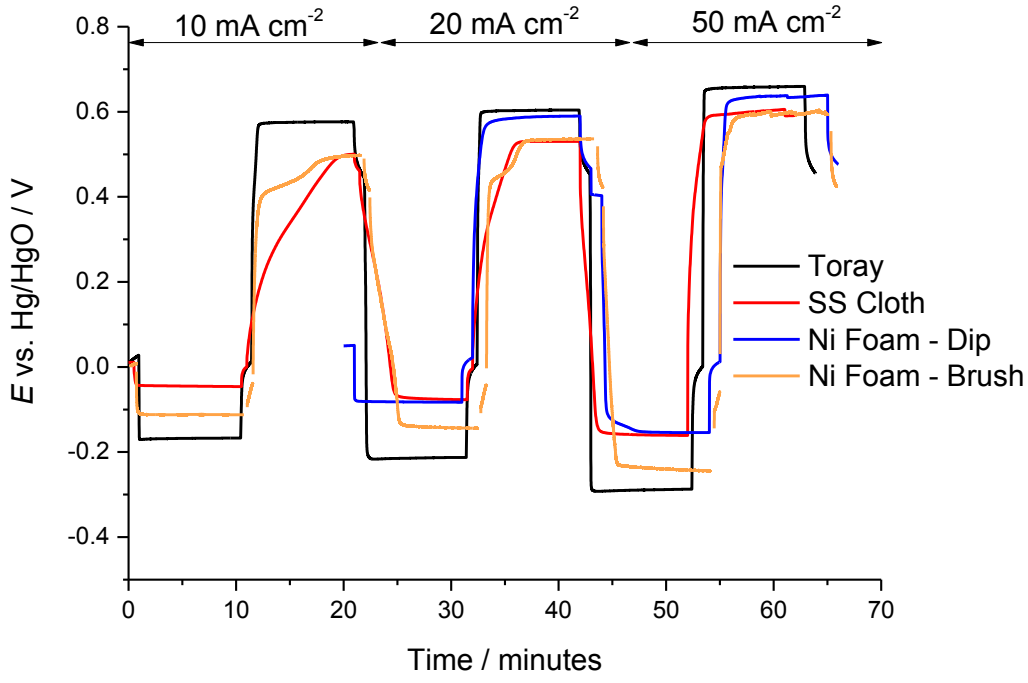

Figure 78: The effect the gas diffusion electrode has on the overpotential of the air electrode at 10, 20 and 50 mA cm^{-2} in 8 M alkali at 333 K with an oxygen supply of 200 cm^3 min^{-1}.

Table 23: Potential gap between ORR and OER for gas diffusion electrodes in 8 M KOH* or 8 M NaOH‡ at 333 K with 200 cm^3 min^{-1}.

Electrode	Potential gap / mV		
	@10 mA cm^{-2}	@20 mA cm^{-2}	@50 mA cm^{-2}
*Carbon – brush coat	744	816	945
‡Nickel foam – dip coat	-	671	792
‡Mesh – dip coat	545	611	757
*Nickel foam – brush coat	608	678	839

The difference in the potential between OER and ORR is an important factor for all of the electrodes developed to date, as the voltage efficiency is a key metric for the financial return on investment from the power being stored in the cell. It is that clear the structure for the lowest potential gap and therefore the highest voltage efficiency is the dip-coated mesh electrode. The potential gap can be reduced to 725 mV by using increased metal nitrate concentrations on nickel foam electrodes; however, it is unclear how this may transfer to mesh electrodes.

Further considerations must also include the long-term electrode stability, as stationary power applications are expected to sustain 1000's of cycles. Therefore the nickel foam electrodes are more suitable, with greater cycle life.[62,63] Finally, for cost reasons the new brush coated electrocatalysts should not be excluded; with electrocatalysts loading one-third of that found in dip-coated electrodes, the reduction in cost is significant.

In this chapter a series of carbon-free electrocatalysts structures have been presented and evaluated for their efficiency and activity as bi-functional oxygen electrodes.

Nickel foam electrodes are presented as a novel structure when filled with either $NiCo_2O_4$ or nickel powder and dip-coated with a $NiCo_2O_4$ film for the OER and ORR reactions. The electrode provides excellent mechanical properties capable of extended electrochemical cycling. The structure does, however, suffer from large material costs with 100 – 150 mg cm^{-2} of catalyst required to fill the foam pore structure. The high loading required to form the gas diffusion layer and general thickness of the foam results in a relatively thick electrode of 300 – 500 µm. This electrode type has achieved the lowest potential gap of only 725 mV at 50 mA cm^{-2} when the catalyst loading was increased and prepared using a solution of water and IPA.

The electrode thickness was reduced significantly (50 - 100 µm) through the use of spray-coating a metallic mesh. Electrodes based on this structure required loadings of 10 – 30 mg cm^{-2} of $NiCo_2O_4$ to act as a GDL. The dip-coating process provided a thin-film of $NiCo_2O_4$ onto the structure, to act as a catalyst layer, with a loading of approximately 3 mg cm^{-2}. These electrodes produced the second lowest potential gap between the ORR and OER of only 757 mV at 50 mA cm^{-2}. The mesh electrode does however reduce the catalyst loading by up to 50 % with a 90 % reduction of total material used in construction when compared to previous foam electrodes. The stability of these electrodes is limited, with flooding believed to be the primary cause of failure. As such, the inclusion of anion exchange membranes or separators to reduce the hydrostatic pressure would likely extend the electrode life.

Finally, brush-coated nickel foam electrodes provide the minimum electrocatalyst loadings of all the electrodes evaluated at <1 mg cm^{-2}. Lower loadings are possible but require further study. Electrochemical performance is reasonable in comparison to other metal electrodes, with low overpotential for the OER. The ORR requires higher overpotential, likely due to the electrocatalysts being applied to the electrolyte side of the GDL. This catalyst layer is, therefore, more prone to flooding than the dip-coated layers, which are dispersed throughout the structure of the electrode. These electrodes could be enhanced by using a vacuum to draw the catalyst ink further into the structure or the addition of an anion exchange membrane to reduce the hydrostatic pressure and avoid flooding the electrode.

4.5 References

(1) Litster, S.; McLean, G. *Journal of Power Sources*. May 2004, pp 61–76.

(2) Wilson, M. S.; Gottesfeld, S. *Journal of Applied Electrochemistry*. Kluwer Academic Publishers 1992, pp 1–7–7.

(3) Wei, Z.; Huang, W.; Zhang, S.; Tan, J. *Journal of Power Sources*. 2000, pp 83–85.

(4) Arai, H.; Müller, S.; Haas, O. *Journal of the Electrochemical Society*. The Electrochemical Society October 1, 2000, pp 3584–3591.

(5) Wang, X.; Sebastian, P.; Smit, M.; Yang, H.; Gamboa, S. *Journal of Power Sources*. 2003, pp 278–284.

(6) Watanabe, M.; Tomikawa, M.; Motoo, S. *Journal of electroanalytical chemistry and interfacial electrochemistry*. November 1985, pp 81–93.

(7) Paganin, V. A.; Ticianelli, E. A.; Gonzalez, E. R. *Journal of Applied Electrochemistry*. Kluwer Academic Publishers March 1996, pp 297–304.

(8) Pearson, G. *Philosophical Transactions of the Royal Society of London*. The Royal Society January 1, 1797, pp 142–158.

(9) LEROY, R. *International Journal of Hydrogen Energy*. 1983, pp 401–417.

(10) Ayers, K. E.; Anderson, E. B.; Capuano, C.; Carter, B.; Dalton, L.; Hanlon, G.; Manco, J.; Niedzwiecki, M. *ECS Transactions*. The Electrochemical Society October 1, 2010, pp 3–15.

(11) Mehta, V.; Cooper, J. S. *Journal of Power Sources*. February 2003, pp 32–53.

(12) Bacon, F. T. *Electrochimica Acta*. April 27, 1969, pp 569–585.

(13) Vogel, W. M.; Lundquist, J. T. *Journal of the Electrochemical Society*. January 1, 1970, pp 1512–1516.

(14) Vogel, W. M.; Klinedinst, K. A. *Electrochimica Acta*. August 7, 1976, pp 1385–1388.

(15) Giner, J.; Hunter, C. *Journal of the Electrochemical Society*. January 1, 1969, pp 1124–1130.

(16) Rockett, J. A.; Brown, R. *Journal of the Electrochemical Society*. January 1, 1966, pp 207–213.

(17) Tang, H.; Wang, S.; Pan, M.; Yuan, R. *Journal of Power Sources*. 2007, pp 41–46.

(18) Fischer, A.; Jindra, J.; WENDT, H. *Journal of Applied Electrochemistry*. Kluwer Academic Publishers 1998, pp 277–282.

(19) Selvarani, G.; Sahu, A. K.; Sridhar, P.; Pitchumani, S.; Shukla, A. K. *Journal of Applied Electrochemistry*. 2008, pp 357–362.

(20) Ramasamy, R. P.; Kumbur, E. C.; Mench, M. M.; Liu, W.; Moore, D.; Murthy, M. *International Journal of Hydrogen Energy*. July 1, 2008, pp 3351–3367.

(21) Carlsson, L.; Öjefors, L. *Journal of the Electrochemical Society*. January 1, 1980, pp 525–528.

(22) *platinum.matthey.com*.

(23) Zeis, R.; Mathur, A.; Fritz, G.; Lee, J.; Erlebacher, J. *Journal of Power Sources*. February 2007, pp 65–72.

(24) Cavarroc, M.; Ennadjaoui, A.; Mougenot, M.; Brault, P.; Escalier, R.; Tessier, Y.; Durand, J.; Roualdès, S.; Sauvage, T.; Coutanceau, C. *Electrochemistry Communications*. April 2009, pp 859–861.

(25) Gasteiger, H. A.; Panels, J. E.; Yan, S. G. *Journal of Power Sources*. March 2004, pp 162–171.

(26) Jorissen, L. 2006; Vol. 155, pp 23–32.

(27) Bidault, F.; Brett, D. J. L.; Middleton, P. H.; Brandon, N. P. *Journal of Power Sources*. 2009, pp 39–48.

(28) Cheng, F.; Chen, J. *Chemical Society Reviews*. 2012, pp 2172–2192.

(29) Li, Y.; Dai, H. *Chemical Society Reviews*. Royal Society of Chemistry 2014, pp 5257–5275.

(30) Chakkaravarthy, C.; Waheed, A.; Udupa, H. *Journal of Power Sources*. 1981, pp 203–228.

(31) Neburchilov, V.; Wang, H.; Martin, J. J.; Qu, W. *Journal of Power Sources*. 2010, pp 1271–1291.

(32) Carmo, M.; Fritz, D. L.; Mergel, J.; Stolten, D. *International Journal of Hydrogen Energy*. April 2013, pp 4901–4934.

(33) Pettersson, J.; Ramsey, B.; Harrison, D. *Journal of Power Sources*. pp 28–34.

(34) Tseung, A.; Botejue, J. *International Journal of Hydrogen Energy*. Elsevier 1986, pp 125–127.

(35) Trasatti, S. *Electrochimica Acta*. May 2000, pp 2377–2385.

(36) Godwin, I.; Lyons, M. E. G. *ECS Transactions*. The Electrochemical Society October 8, 2013, pp 21–31.

(37) Marini, S.; Salvi, P.; Nelli, P.; Pesenti, R.; Villa, M.; Kiros, Y. *International Journal of Hydrogen Energy*. August 2013, pp 11496–11506.

(38) King, W. J.; Tseung, A. *Electrochimica Acta*. 1974.

(39) Bockris, J. O.; Otagawa, T. *Journal of Physical Chemistry*. American Chemical Society July 4, 1983, pp 2960–2971.

(40) Li, Y.; Gong, M.; Liang, Y.; Feng, J.; Kim, J.-E.; Wang, H.; Hong, G.; Zhang, B.; Dai, H. *Nature Communications*. Nature Publishing Group May 7, 2013, p 1805.

(41) Shimizu, Y.; Uemura, K.; Matsuda, H.; Miura, N.; Yamazoe, N. *Journal of the Electrochemical Society*. January 1, 1990, pp 3430–3433.

(42) Lee, C. K.; Striebel, K. A.; McLarnon, F. R.; Cairns, E. J. *Journal of the Electrochemical Society*. January 1, 1997, pp 3801–3806.

(43) Bursell, M.; Pirjamali, M.; Kiros, Y. *Electrochimica Acta*. 2002, pp 1651–1660.

(44) Tseung, A. C. C.; Bevan, H. L. *Journal of electroanalytical chemistry and interfacial*

electrochemistry. August 2, 1973, pp 429–438.

(45) UR-RAHMAN, S.; AL-SALEH, M. A.; AL-ZAKRI, A. S.; GULTEKIN, S. *Journal of Applied Electrochemistry*. Springer Netherlands 1997, pp 215–220.

(46) Shimizu, Y.; Uemura, K.; Matsuda, H.; Miura, N.; Yamazoe, N. *Journal of the Electrochemical Society*. The Electrochemical Society November 1, 1990, pp 3430–3433.

(47) Takasu, Y.; Fukunaga, H.; Yang, H.-S.; Ohashi, T.; Suzuki, M.; Sugimoto, W. *Electrochimica Acta*. August 2013, pp 224–229.

(48) Kannan, A. M.; Shukla, A. K. *Journal of Power Sources*. July 1991, pp 113–121.

(49) Sajdl, B.; Micka, K.; Krtil, P. *Electrochimica Acta*. 1995, pp 2005–2011.

(50) Sieminski, D. *Twelfth Annual Battery Conference on Applications and Advances*. IEEE 1997, pp 171–180.

(51) Li, N.; Yan, X.; Jin, Y.; Li, S.; Lin, B. *Journal of Applied Electrochemistry*. 1999, pp 1351–1354.

(52) Roche, I.; Chainet, E.; Vondrak, J.; Chatenet, M. *Journal of Applied Electrochemistry*. 2008, pp 1195–1201.

(53) Yuasa, M.; Nishida, M.; Kida, T.; Yamazoe, N.; Shimanoe, K. *Journal of the Electrochemical Society*. The Electrochemical Society May 1, 2011, pp A605–A610.

(54) Dong, H.; Yu, H.; Wang, X.; Zhou, Q.; Feng, J. *Water Research*. November 2012, pp 5777–5787.

(55) Ohkuma, H.; Uechi, I.; Imanishi, N.; Hirano, A.; Takeda, Y.; Yamamoto, O. *Journal of Power Sources*. February 2013, pp 319–324.

(56) Yuasa, M.; Tachibana, N.; Shimanoe, K. *Chemistry of Materials*. American Chemical Society July 25, 2013, pp 3072–3079.

(57) Benhangi, P. H.; Alfantazi, A.; Gyenge, E. *Electrochimica Acta*. March 2014, pp 42–50.

(58) Langlois, S.; Coeuret, F. *Journal of Applied Electrochemistry*. Kluwer Academic Publishers January 1989, pp 51–60.

(59) Arisetty, S.; Prasad, A. K.; Advani, S. G. *Journal of Power Sources*. February 2007, pp 49–57.

(60) Bidault, F.; Brett, D. J. L.; Middleton, P. H.; Abson, N.; Brandon, N. P. *International Journal of Hydrogen Energy*. August 1, 2009, pp 6799–6808.

(61) Gorman, S. F. Development and Operation of an Electrically Rechargeable Zinc-Air Flow Battery.

(62) Li, X.; Pletcher, D.; Russell, A. E.; Walsh, F. C.; Wills, R. G. A.; Gorman, S. F.; Price, S. W. T.; Thompson, S. J. *Electrochemistry Communications*. September 1, 2013, pp 228–230.

(63) Price, S. W. T.; Thompson, S. J.; Li, X.; Gorman, S. F.; Pletcher, D.; Russell, A. E.; Walsh, F. C.; Wills, R. G. A. *Journal of Power Sources*. August 2014, pp 43–49.

Chapter 5: Nanoparticle modifications

5.1 Introduction

The materials with the greatest activity for the oxygen reduction and evolution reactions are based upon platinum and ruthenium, respectively. However, due to the low abundance of these metals in the earth's crust and associated cost of extraction, they are prohibitively expensive for many applications. Attempts to increase utilisation of the electrochemically active surface have focused either on forming nanoparticles of a relatively low cost transition metal, with a skin of precious metal (core-shell)[1-4], or through the production of smaller nanoparticles by dispersion on stable and conductive supporting materials such as carbon, tin dioxide or tungsten oxide.[5-8] The dispersion of small nanoparticles has been critical in developing low loadings of platinum on carbon for fuel cells.[9] The synthesis of such materials typically occurs via impregnation of the precious metal salt (e.g. Chloroplatinic acid) into carbon followed by chemical reduction with a reducing agent (e.g. sodium borohydride). An array of alternative methods exist for the synthesis of nanoparticles from chemical reduction, refluxing of metal salts in ethanol, thermal decomposition, and Sol-gels.[10-12]

The use of supporting materials can in some cases which provide an interesting electronic effect on the formed nanoparticles that alters the catalytic activity and stability.[13] Bimetallic platinum alloys such as, Pt_3Co and Pt_3Ni, have been reported to achieve the optimal composition for the oxygen reduction reaction.[14] Although the alloys can provide increased activities, the stability of the alloys is likely to be less than that found for pure platinum. One possible failure mode is the slow dissolution of the transition metal incorporated into the structure. Although the dissolution process would most likely be less problematic in alkali electrolyte, the catalyst would need to remain price competitive with perovskites and spinels capable of similar performance.

Although these precious metal catalysts are typically supported on high surface area carbon, the carbon is an unsuitable supporting material for OER electrocatalysts in alkali as it can be oxidised to CO_2 and form insoluble potassium carbonate on the electrode over time. Metal-carbides also are unlikely to provide the necessary long-term stability needed for stationary power applications. As such a material with excellent stability in the potential ranges of ORR and OER is required for alkaline solution.

Avoiding the use of supporting materials in the catalyst layer is possible. One solution utilised a physical mixture of precious metals (30 wt.% Pt-Ru/C) and transition metal oxide ($LaNiO_3$) catalyst, in a ratio of 5:95 respectively, and this does appear to provide a relatively robust, if simple, solution to the problem.[15] The reduction in OER overpotential of 80 mV (from 760 mV to 680 mV)

at 100 mA cm^{-2} was observed to be stable for 50 hours. It is however, unclear how the electrode compares to a pure Pt-Ru/C sample. The high catalyst loading (86 mg cm^{-2}) will operate for a significant length of time before degradation effects are observed but implementation in commercial applications is limited by the cost.

Iridium and ruthenium have been substituted into spinel and perovskite structures, in place of the cobalt cation.[16,17] The addition of small amounts of iridium into the perovskite appears to lower the overpotentials for both the ORR and OER. The greatest success of such metal utilisation is observed for pyrochlores.[18]

The iridium and ruthenium binary oxides typically show poor activity (200 μA cm^{-2} at 0.7V *vs.* RHE) towards the ORR[19-21], but are highly active for the OER (1 A cm^{-2} at 1.6V *vs.* RHE).[22] However, the associated costs for iridium would be a deterrent for its use in future catalysts, although the high cost of the iridium additive could be offset by the use of a supporting material to improve catalyst utilisation and lower the precious metal loading for the desired electrochemical performance. An example is the use of antinomy tin oxide (ATO) as a stable supporting material that provides a conductive path through the catalytic layer and improves catalyst dispersion, reducing the necessary catalyst loading with minimal impact on the overpotential.[23]

It is also possible to add precious metals onto perovskite and spinel electrocatalysts.[24-26] Combining valuable precious metals onto low cost transition metal electrocatalysts, is able to achieve the same result as the ATO example, but with the added benefit the supporting material can also contribute to the electrochemical reaction. The addition of silver has been shown to enhance the OER when supported onto a perovskite.[24] The addition of silver provides increased conductivity and a reduction of overpotential by 40 mV at 50 mA cm^{-2}. A similar improvement to OER can be achieved with the combination of silver on MnO_x.[27]

Further to simple metal oxide additions to the spinel, ruthenium oxide nanowires have been coated with Co_3O_4 to promote the oxygen evolution, with the combination operating at lower overpotentials than either pure Co_3O_4 or RuO_2.[28] This study suggests an interaction between the cobalt and ruthenium oxides is able to improve the activity beyond that of either pure sample. As the material forms a distinct two-layer structure, it is likely the interface between the two metal oxides provides an environment with improved centres of activity.

The oxygen evolution reaction has been studied with transition metal nanoparticles supported on platinum in alkaline electrolyte.[29] A trend was observed for the first row transition metals tested, with the overpotential for the OER increasing for Ni<Co<Fe<Mn. All modified electrodes demonstrated a lower overpotential than platinum for the OER, with the strength of the M-OH

bond suggested as the primary reason. The OER was believed to operate on a mono-functional basis, limited only by the transition metal. The hydrogen evolution reaction, however, the catalyst appears to provide a bi-functional response suggesting the reactivity occurs at the edges of the metal clusters in close proximity to the platinum surface.

The incorporation of precious metals into and onto mixed metal oxides is a method to improve catalytic activity for the ORR and OER. To further understand which materials provide the greatest improvement this chapter will discuss the effect of adding precious metals (Pt, Ag, Ru, Pd and Au) as supported nanoparticles onto the surface of $NiCo_2O_4$.

5.2 Methods

5.2.1 List of Reagents

Table 24: List of reagents and materials used inclusive of suppliers

Material/Reagent	Supplier
Aqueous Hydrazine (64 wt.%)	Sigma-Aldrich
Aqueous Nafion® solution (10.85 % solids)	Johnson Matthey
Isopropyl Alcohol	Fisher
Ruthenium Nitosyl Nitrate (31.3 % min)	Alfa Aesar
Potassium Hydroxide (> 98 %)	Sigma-Aldrich
Silver Nitrate (>99.9 %)	Sigma-Aldrich
Tetra Amine Platinum Nitrate (99.99 %)	Alfa Aesar
Palladium (II) acetyl-acetonate (99 %)	Sigma-Aldrich
Water (18 MΩ cm)	Purite water purifier

5.2.2 Synthesis

An example of the synthesis is outlined below. The method was amended by exchanging the silver nitrate for a comparable precious metal salt from Table 24 to create the series of metal modified spinel catalysts. All precursor metal salts were selected with a labile ligand and a stoichiometric ratio added for the synthesis to achieve the desired loading.

$NiCo_2O_4$ (0.1000 g) was suspended in 1 mL H_2O and irradiated with ultrasonic radiation for 20 minutes. A metal precursor (typically with a nitrate anion) was added, e.g. $AgNO_3$ (0.0315 g), the sample was irradiated with ultrasonic radiation for 20 minutes followed by heating on a hotplate to dryness. The sample was then re-suspended in 1 mL H_2O, followed by the addition of 1 mL Hydrazine (6.4 wt. %). The sample was placed in an ultrasonic bath for 20 minutes and subsequently heated at 353K until dry. The sample was then transferred to a porcelain crucible and calcined at 648 K for four hours, to yield a black powder.

5.2.3 TEM

Transmission electron microscopy identified the formation of polygonal nanoparticles on the surface of $NiCo_2O_4$ platelets (Figure 79).

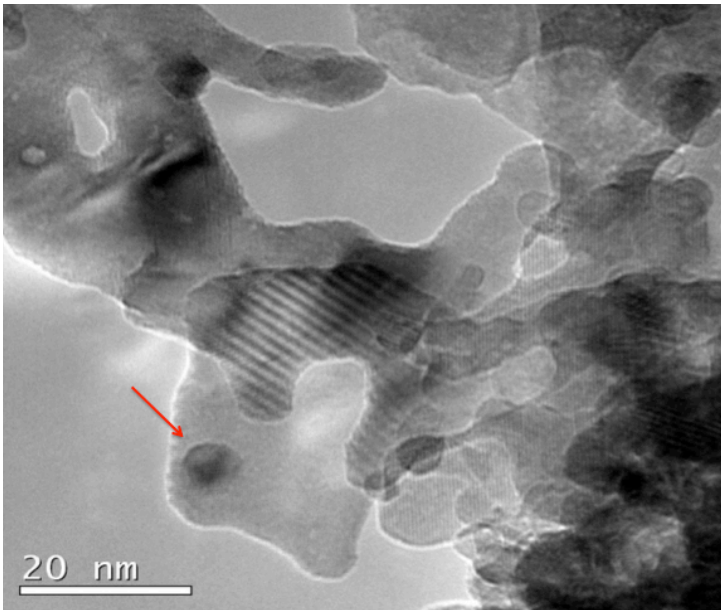

Figure 79: TEM micrograph of AgO_x supported on $NiCo_2O_4$.

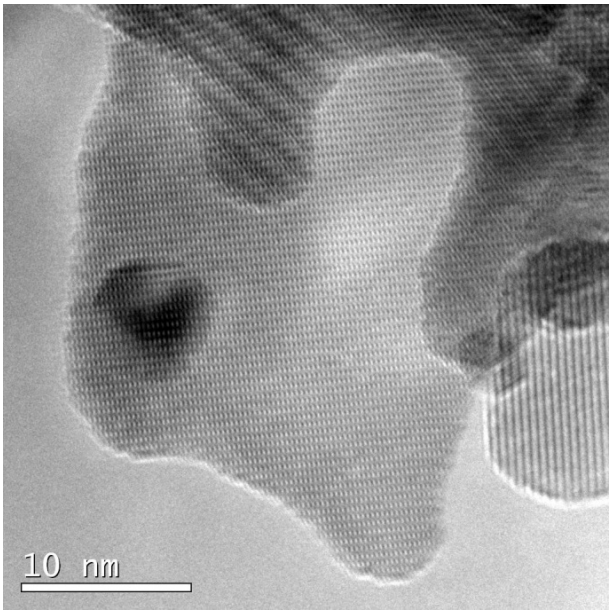

Figure 80: High resolution TEM micrograph of individual AgO_x nanoparticle on $NiCo_2O_4$ platelet.

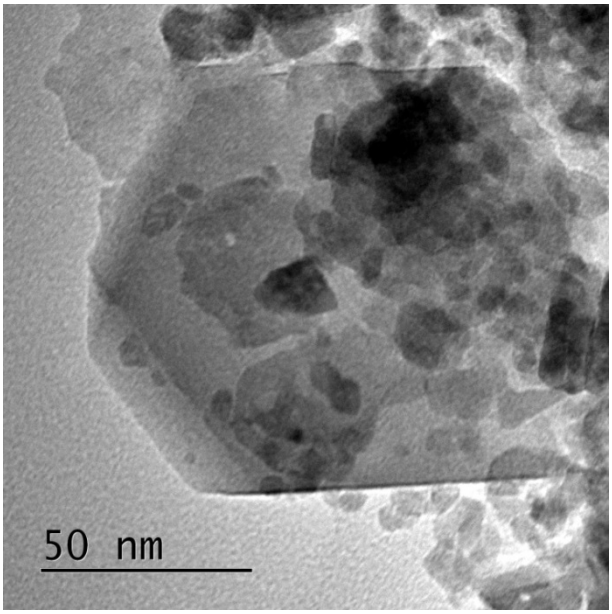

Figure 81: TEM micrographs of RuO_x (irregular polygonal dark objects) supported on $NiCo_2O_4$ (hexagonal polygons).

The silver nanoparticles appear to reside upon a platelet of the $NiCo_2O_4$ (Figure 80). The silver nanoparticles were identified as dark circular shapes in the micrographs that appear on a brighter particle. The dark polygonal particles were absent from all $NiCo_2O_4$ samples prepared in the absence of silver or other metal particle doping. The average particle size of the silver nanoparticles was approximately 8 nm, with an error of ±2 nm as determined by comparing 35 particles.

The ruthenium nanoparticles on the $NiCo_2O_4$ appear similar to the silver, by appearing as polygonal particles. The particles appear to vary in size from 10 to 20 nm, with non-uniform shape.

5.2.4 SEM/EDX

The precious metal loading was determined by SEM-EDX.

Table 25: EDX analysis of ruthenium modified $NiCo_2O_4$.

Sample	Ru wt.%	Ni wt.%	Co wt.%
5 wt.% Ru/$NiCo_2O_4$	12.7	25.2	62.1
10 wt.% Ru/$NiCo_2O_4$	21.6	22.7	55.7
20 wt.% Ru/$NiCo_2O_4$	23.1	21.1	55.8
40 wt.% Ru/$NiCo_2O_4$	54.2	13.1	32.8

5.2.5 XRD

The diffraction patterns for the metal-doped samples were compared with that of the expected metal dopants. Peaks were assigned to the likely form of the metal/metal oxide that was supported on the $NiCo_2O_4$.

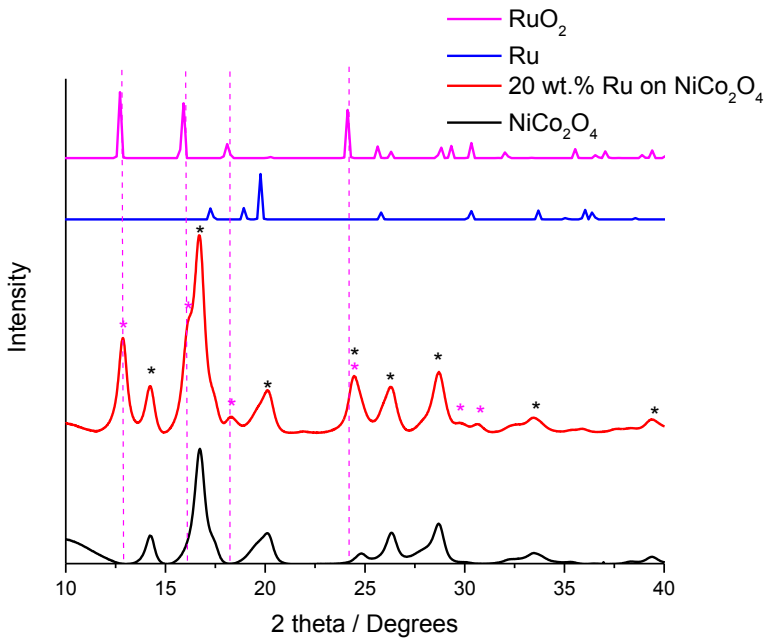

Figure 82: XRD of 20 wt. % RuO_x on $NiCo_2O_4$ compared with $NiCo_2O_4$ and literature differaction patterns for ruthenium.

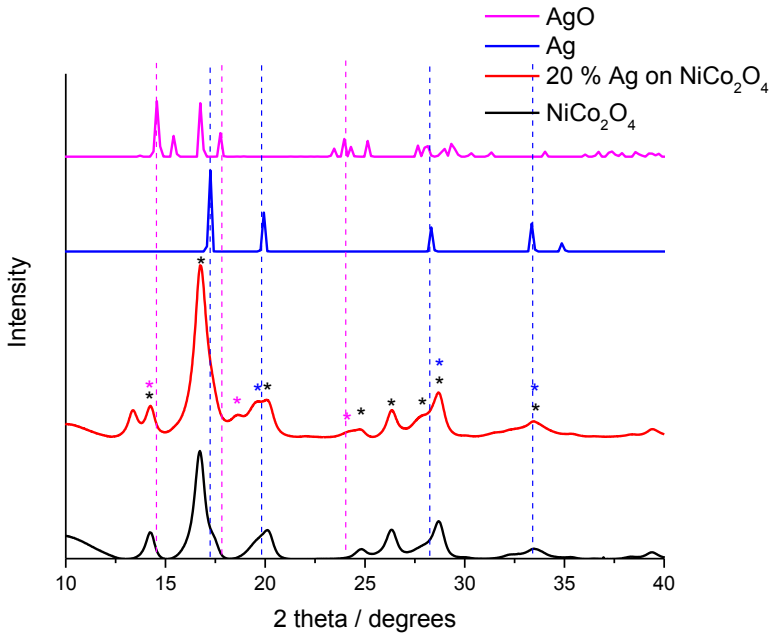

Figure 83: X-ray diffraction data for silver supported nanoparticles on $NiCo_2O_4$.

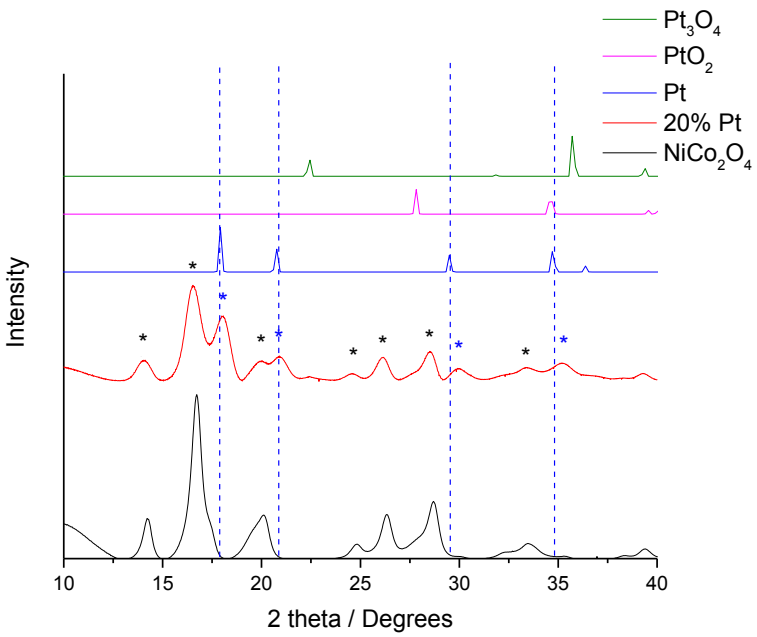

Figure 84: X-ray diffraction pattern for platinum supported on $NiCo_2O_4$.

The diffraction pattern for the ruthenium sample, (Figure 82), suggests that the ruthenium is predominately in the RuO_2 form. A low concentration may be present in a different form, RuO_4, or be non-crystalline, but there is no evidence of this from the XRD or TEM results. The silver sample, (Figure 83) appears to yield a mixture of silver as both metal and metal oxide. In comparison the platinum appears to form metallic platinum (Figure 84).

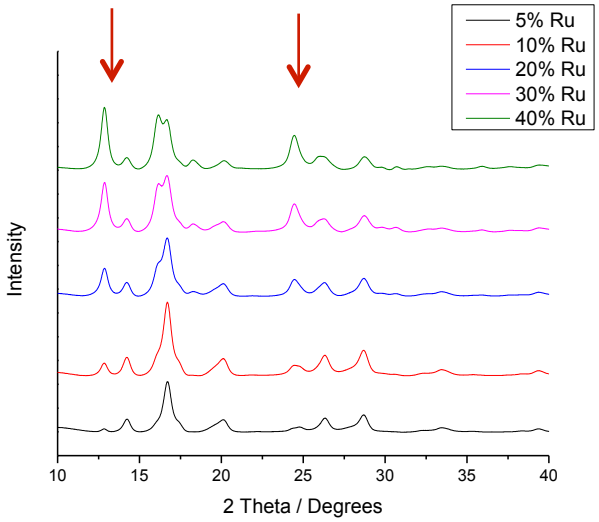

Figure 85: XRD patterns for increased loading of ruthenium onto $NiCo_2O_4$.

The increased loading of ruthenium dioxide on $NiCo_2O_4$ is clearly observed in the diffraction pattern (Figure 85), with new peaks occurring at 2θ = 12.5 and 25 degrees. Crystallite sizes were observed to increase with increased RuO_x loading. The increased loading is likely to result in larger

RuO_x particles. These larger particles would also allow for large crystallite sizes, as determined by the XRD.

Table 26: Crystallite size of ruthenium oxide supported on $NiCo_2O_4$.

Sample	Crystallite size / Å
5 wt. % $RuO_x/NiCo_2O_4$	6.7
10 wt. % $RuO_x/NiCo_2O_4$	8.1
20 wt. % $RuO_x/NiCo_2O_4$	10.8
30 wt. % $RuO_x/NiCo_2O_4$	13.2
40 wt. % $RuO_x/NiCo_2O_4$	11.3

5.3 Electrochemistry of precious metal nanoparticles supported on $NiCo_2O_4$

The electrochemical response was determined from thin-film layers on GC RDE. The formation of RuO_x is not expected to be particularly beneficial for the ORR, and no sample has demonstrated a reduced overpotential through the addition of RuO_x. The oxygen reduction reaction provided a range of responses depending upon which precious metal was used in the synthesis. Typically a sigmoidal curve with a plateau region would be expected for the ORR, as observed for palladium and ruthenium samples. The $NiCo_2O_4$ has been included as a reference for the activity of the supporting material. The oxygen reduction on the spinel has already been identified as a mostly 4-electron oxygen reduction process as described in chapter 3. We observe a rough trend in the plateau, with the majority of samples achieving 0.3 mA cm^{-2} which is comparable with the limiting current observed on a platinum disc electrode.

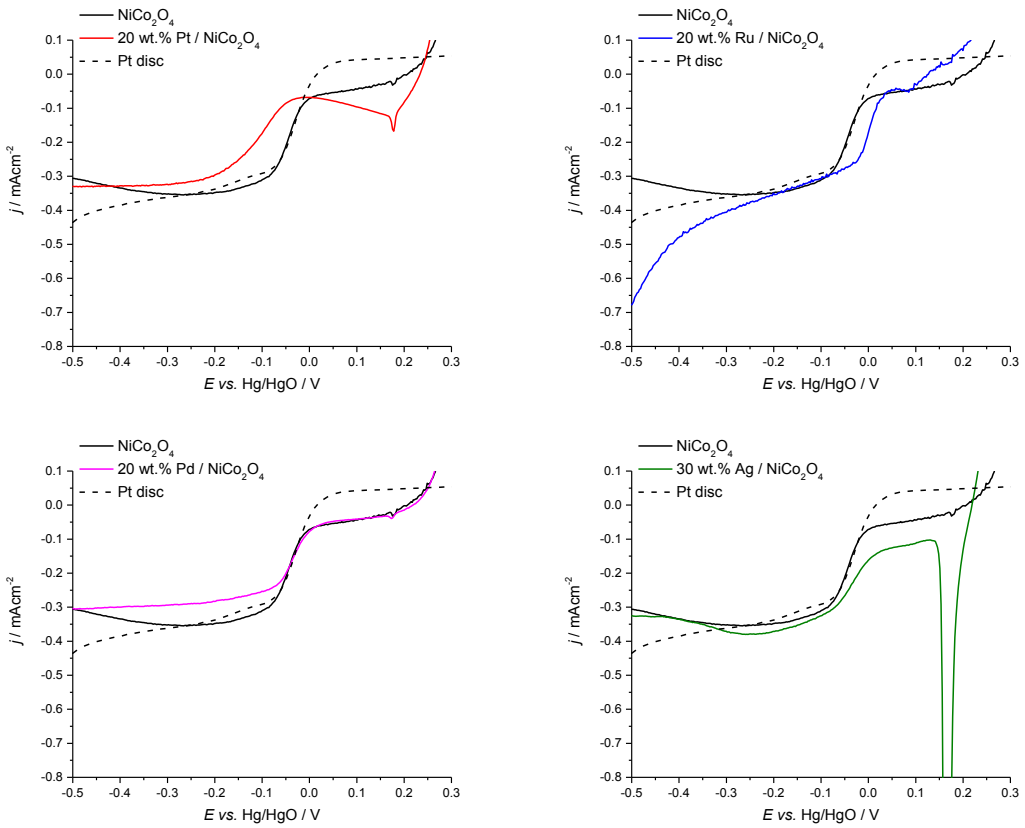

Figure 86: Comparison of ORR polarisation curves of nanparticle modified $NiCo_2O_4$ and $NiCo_2O_4$ in oxygen saturated 4 M KOH at 333 K, rotated at 400 rpm.

Although several studies have suggested the addition of silver nanoparticles to promote the oxygen evolution and oxygen reduction reactions[25,30], the ability to cycle the electrode is limited due to detrimental reactions that occur at potentials between those for the two oxygen reactions. With the addition of silver nanoparticles the polarisation yields a large peak at 170 mV (part (d) in Figure 86), associated with the reduction and subsequent dissolution of solid Ag_2O_3 to $Ag(OH)_{(aq)}$.[31] Although the overpotential for the ORR is reduced, the dissolution of silver from the electrode would result in rapid degradation of the catalyst as the silver is lost to the electrolyte reservoir in a working flow-battery.

The addition of platinum to the sample produces a polarisation curve (red line in Figure 86) with an increased overpotential for oxygen reduction. The platinum was expected to improve the activity; however the Platinum may have formed a surface oxide, which is inhibiting the activity towards the ORR and is not as readily reduced as platinum particles supported on carbon.

Palladium modified $NiCo_2O_4$ (part (c) in Figure 86) results in a sigmoidal curve similar in nature to that of pure $NiCo_2O_4$. A change to the conductivity could be possible at lower current densities, however it falls well within the error of several mV for this measurement. A slight reduction in the limiting current region is observed, this could be from experimental error in the preparation of

the catalyst layer (e.g. excess binder in the thin-film which may supress the rate of reaction with a vast excess of reactant) or the palladium metal sites are blocking a number of $NiCo_2O_4$ sites critical for the ORR.

The addition of ruthenium (part (b) in Figure 86) produces an anodic current measured positive of the OCP of 0.06 V. A small region with a constant current is then observed before the onset of the ORR. A sigmoidal response is observed for the ORR, with a sloping plateau for the mass transport limited region. This sloping plateau could be attributed to the reduction of RuO_4, but without further evidence it is unclear of the source of this cathodic current observed for the ruthenium sample. The limiting current can be extrapolated from the plateau region -0.25 and -0.20 V to be -0.45 mA cm^{-2}, which is similar to that observed for the pure $NiCo_2O_4$ and platinum disc.

Table 27: Comparison of ORR activity for precious metal modified $NiCo_2O_4$ on GC RDE in oxygen saturated 4 M KOH at 333 K, rotated at 400 rpm.

Sample	ORR at -150 μA cm^{-2} / mV	Tafel slope / mV dec^{-1}	j_L @ -500 mV / mA cm^{-2}
Pt - disc	-32	43	-0.44
$NiCo_2O_4$	-34	99	-0.31
20 wt. % Ru / $NiCo_2O_4$	5	74	-0.68
20 wt. % Pt / $NiCo_2O_4$	-88	159	-0.33
20 wt. % Pd / $NiCo_2O_4$	-32	126	-0.30
30 wt. % Ag / $NiCo_2O_4$	9	236	-0.32

A comparison of the overpotential for the ORR was made at -150 μA cm^{-2}, as comparison at lower current densities was not possible due to the large current from the silver oxide reduction interfering with the onset of the ORR. The lowest overpotential for the ORR is observed for samples with ruthenium and silver nanoparticles. These were closely followed by platinum, $NiCo_2O_4$ and palladium modified $NiCo_2O_4$. Although the ruthenium and silver modified samples produce the lowest overpotentials towards the ORR at low current densities, the Tafel slope of 40 mV dec^{-1} for platinum is less than the 74 or 236 mV dec^{-1} for ruthenium and silver modified $NiCo_2O_4$ and this may inhibit the usefulness of these catalysts when operating at higher operating current densities.

A small positive shift in the ORR potential, whilst maintaining the apparent 4-electron transfer for the ORR, was achieved through the addition of RuO_x nanoparticles on to the surface of the $NiCo_2O_4$. The oxygen evolution reaction, where the addition of RuO_x was believed to present the greatest gain, was then evaluated.

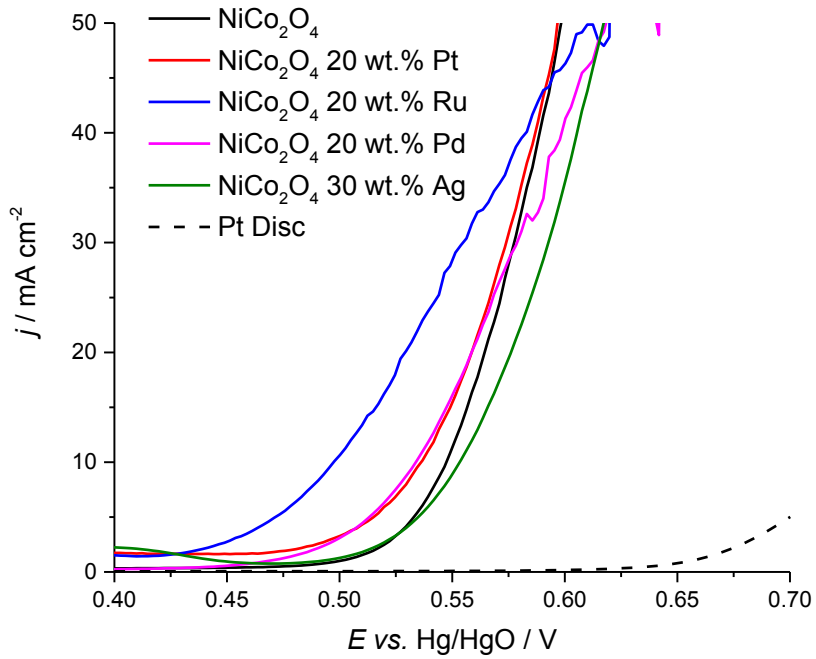

Figure 87: Polarisation curve for the OER for nanparticle modified $NiCo_2O_4$ in oxygen saturated 4 M KOH at 333 K.

The voltammetry from polarisation curves at 1 mV s^{-1} were carried out on glassy carbon RDE, sweeping positive from 0.3 to 0.7 V *vs.* Hg/HgO. The addition of metals onto the $NiCo_2O_4$ yields a mixed result (Figure 87). All samples present a lower overpotential for the OER in comparison to the platinum disc. Silver appears to achieve the same onset, however, at higher currents a larger overpotential is required. The increased activity of the silver may be due to the surface area of the particles, with small nanoparticles observed by TEM, but it is unclear why silver would preferentially form smaller nanoparticles in comparison to other precious metals when using the same preparation method. The high conductivity of silver was hoped to improve the activity, but the OER overpotentials are greater than the unmodified $NiCo_2O_4$. The oxidised silver particles are therefore likely to act as surface inhibitors on the spinel in this case.

Table 28: Acitivity of precious metal modified $NiCo_2O_4$ electrodes towards the OER. Carried out in oxygen saturated 4 M KOH at 333 K and rotated at 400 rpm.

Sample	*E* @ 10 mA cm^{-2} / mV	Tafel slope / mV dec^{-1}
Pt - disc	715	60
$NiCo_2O_4$	547	46
20 wt. % Ru / $NiCo_2O_4$	497	85
20 wt. % Pt / $NiCo_2O_4$	537	73
20 wt. % Pd / $NiCo_2O_4$	533	65
30 wt. % Ag / $NiCo_2O_4$	553	58

The addition of platinum and palladium appear to produce almost identical voltammetry. They both demonstrate a small reduction in the overpotential at 10 mA cm^{-2}, of 10 mV, when compared to pure $NiCo_2O_4$. Further reduction in overpotential is observed with the addition of ruthenium onto the $NiCo_2O_4$. The overpotential for 10 mA cm^{-2} at 50 mV was recorded for the addition of 20 wt. % ruthenium onto the spinel, the lowest overpotential of all the different compositions (doping into and onto the spinel structure).

Table 29: The difference in potential between the oxygen reduction and evolution reactions in oxygen saturated 4 M KOH, 333K on GC RDE rotated at 400 rpm.

Sample	Potential gap / mV
Pt – disc	747
$NiCo_2O_4$	581
20 wt. % Ru / $NiCo_2O_4$	492
20 wt. % Pt / $NiCo_2O_4$	625
20 wt. % Pd / $NiCo_2O_4$	565
30 wt. % Ag / $NiCo_2O_4$	544

The difference in potential between the ORR and OER reactions has been improved by the addition of PGMs onto the surface of $NiCo_2O_4$. The greatest improvement is observed through the addition of ruthenium, reducing the potential gap by 90 mV. However, the associated high value of precious group metals will result in any final catalysts composition requiring the lowest loading of these metals as possible.

5.3.1 The effect of ruthenium loading

The ruthenium loading was explored to determine the effect on oxygen activity. The same synthesis method, as outlined in section 5.2.2, was used for the preparation of all samples, with the ruthenium loading, as wt.% with respect to the $NiCoO_4$ and ruthenium, controlled through the addition of the corresponding quantity of ruthenium nitrosyl nitrate precursor.

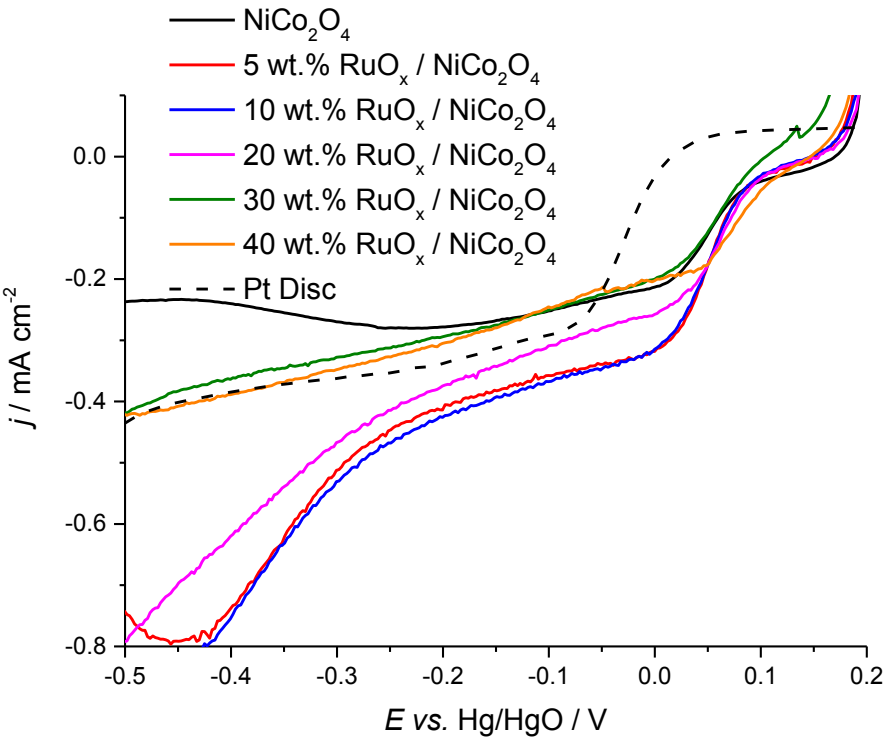

Figure 88: Plot of polarisation curves for the ORR for a series of ruthenium loadings on $NiCo_2O_4$, measured in oxygen saturated 4 M KOH at 333 K, rotated at 400 rpm.

The voltammetry for the ORR is consistent for all samples, with a sigmoidal response for the kinetic limited and sloping plateau in the mass transport limited regions, as seen in Figure 88. At high overpotential, samples with a low loading of ruthenium (<20 wt. % Ru) exhibit a secondary wave at potentials below -0.3 V. The hydrogen evolution reaction at such a positive potential is unlikely. Previous studies on ruthenium and ruthenium dioxide catalysts in alkali have suggested the oxygen reduction curve is stable and constant to -1.0V *vs.* Hg/HgO, before the HER occurs.[18,32] Although these studies were carried out at room temperature and in 1 M KOH, not 4 M KOH used in this current work. In addition, the rising current is most pronounced on the samples with the lowest loadings of RuO_x. Further, the XRD results suggest the reduced ruthenium loading coincides with a reduction in crystal size. The smaller ruthenium particles may be unstable, with any under co-ordinated sites being reduced more easily than that observed for larger nanoparticles.

In the data shown in this set of experiments (section 5.3.1) the polarisation curves for the OER and ORR were observed to have shifted positive relative to the previous results using $NiCo_2O_4$, as shown in Figure 89. However the potential gap remains consistent between measurements for the 20 wt. % sample. This would suggest either a dramatic change to the equilibrium potential in the oxygen reaction on this catalyst, or a shift in the reference electrode between measurements,

with the latter being more likely. Unfortunately time restrictions meant that these measurements were not reproduced using a different reference electrode.

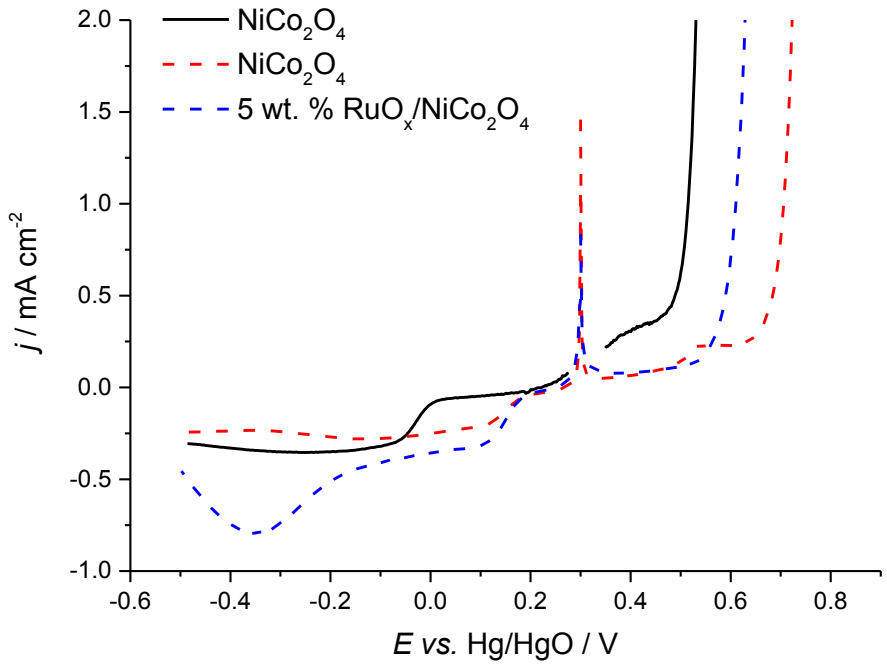

Figure 89: Plot of polarisation curves for $NiCo_2O_4$ and Ruthenium nanoparticle modified spinel in 4 M KOH. The result from the original reference electrode (dashed) and the freshly prepared (solid).

Further evidence of a shift in the reference electrode potential is obtained by examining the potential gap between the ORR and OER reaction, which remained constant, suggesting the oxygen reduction and evolution reactions are not affected. Thus we conclude that the potential of the laboratory manufactured reference electrode has shifted by approximately +150 mV compared to the other measurements.

The reference electrodes were found to degrade after extended use at 333 K in 4 M KOH due to the failure of the glass wool packing material used in the construction. The glass wool is used to provide mechanical support to the mercury-mercury oxide junction. As a result, further measurements have been carried out in section 5.3.2 to confirm the observed activity of ruthenium modifiedruthenium-modified spinels. A new set of operating conditions, of 1 M KOH at 298 K, was used to confirm the potentials for the ORR and OER. These conditions reduce degradation to the reference electrodes, but also provide a direct comparison to previous measurements carried out on the $NiCo_2O_4$.

Table 30: The effect of of ruthenium loading on the $NiCo_2O_4$ has on the ORR activity. Measured using GC RDE, 400 rpm, in oxygen saturated 4 M KOH, at 333 K.

Sample	ORR at -150 μA cm^{-2} / mV	Tafel slope / mV dec^{-1}	j_L @ -500 mV / mA cm^{-2}
Pt – disc	-32	43	-0.44
$NiCo_2O_4$	41	89	-0.24
5 wt. % RuO_x / $NiCo_2O_4$	56	75	-0.74
10 wt. % RuO_x / $NiCo_2O_4$	56	64	-0.75
20 wt. % RuO_x / $NiCo_2O_4$	58	63	-0.62
30 wt. % RuO_x / $NiCo_2O_4$	39	39	-0.36
40 wt. % RuO_x / $NiCo_2O_4$	61	81	-0.39

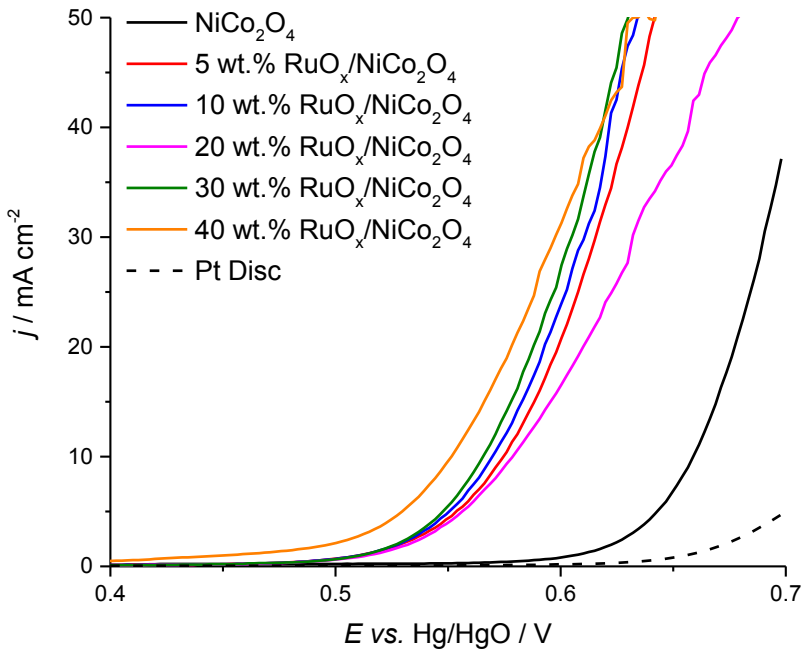

Figure 90: Plot of polarisation curves for the OER of RuO_x nanoparticles on $NiCo_2O_4$.Measured on GC RDE at 400 rpm, in oxygen saturated 4 M KOH, at 333 K.

Measurements of the oxygen evolution yield a typical exponential wave upon the onset of the reaction, followed by a linear rise at high overpotential (Figure 90). The addition of ruthenium

results in a reduction in the overpotential of 80-100 mV compared to unmodified $NiCo_2O_4$ for the OER at 10 mA cm^{-2}. The presence of RuO_x on the surface of the $NiCo_2O_4$ provides sites with high activity towards the OER. A further reduction of 10 mV on the ORR overpotential is possible. The most positive overpotential for the ORR was observed for the sample with the lowest loading of ruthenium, in contrast to the OER which benefits from the maximum loading of ruthenium. Rietveld analysis of the XRD suggests a lower loading of RuO_x coincides with reduced crystallite size (Table 26). This reduced size is a likely source of variation for the observed electrochemical response. A smaller crystallite size would coincide with an increased surface area for the equivalent mass of ruthenium.

Table 31: Comparison of ruthenium loading on OER activity on GC RDE in oxygen saturated 4 M KOH at 333 K.

Sample	*E* @ 10 mA cm^{-2} / mV	Tafel slope / mV dec^{-1}
Pt – disc	714	58
$NiCo_2O_4$	659	52
5 wt. % RuO_x / $NiCo_2O_4$	573	63
10 wt. % RuO_x / $NiCo_2O_4$	568	58
20 wt. % RuO_x / $NiCo_2O_4$	575	61
30 wt. % RuO_x / $NiCo_2O_4$	565	54
40 wt. % RuO_x / $NiCo_2O_4$	551	73

The addition of ruthenium to the nickel cobalt spinel lowers the overpotential for the OER by 108 mV, with a 40 wt.% loading. A lower loading of 5 wt.% ruthenium would be more cost effective yet still achieve a reduction in overpotential of 86 mV for the OER. The Tafel slope for all samples is approximately 60 mV dec^{-1}. These values are greater than the values purported at 298 K due to the increased temperature to 333 K.

5.3.2 The effect of electrolyte concentration on activity

To compare the results collected in 4 M KOH at 333 K, the measurements were repeated in 1 M KOH at 298 K using a glassy carbon disk and platinum ring RRDE. The change in temperature and electrolyte concentration alters the pH of the solution, solubility of oxygen and will impact the overpotential for both the ORR and OER reactions.

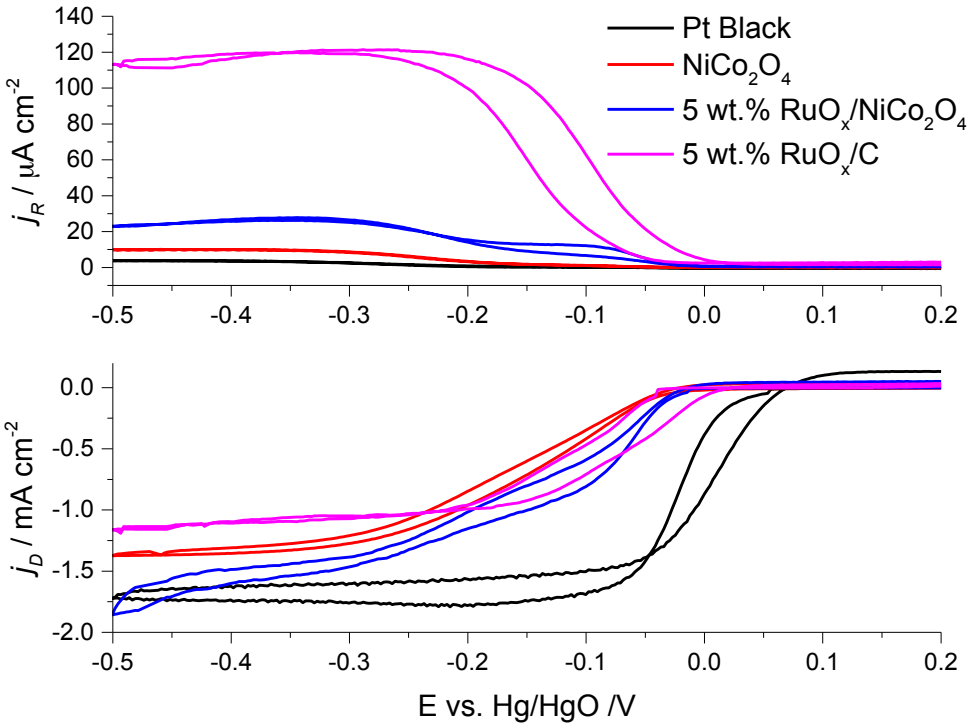

Figure 91: Plot of the polarisation curves for ORR on GC-Pt RRDE for ruthenium modified $NiCo_2O_4$ in oxygen saturated 1 M KOH at 298 K, the ring currents are reported in the top panel and those for the disc in the lower.

Ruthenium nanoparticle modified $NiCo_2O_4$ samples were measured using cyclic voltammetry at slow sweep rates (5 mV s^{-1}) to ensure a steady state response. The polarisation curve closely follows that of RuO_x with an early onset for the ORR with a reduction in the gradient of the slope between -0.1 and -0.2 V (Figure 91). At potentials negative of -0.2 V a second wave can be seen. This set of two waves is closely followed with the current on the ring, where two waves are apparent during the cathodic and anodic sweeps. This would suggest either a change to the mechanism as a function of potential or, new active centres (potentially $NiCo_2O_4$) are only electrochemically active at the more cathodic potentials.

The oxygen reduction on RuO_x/C operates via a 2-electron process, producing hydrogen peroxide as the minor (28%) but significant product. Although carbon is known to be a highly active catalyst for the reduction of oxygen to hydrogen peroxide, the reaction typically occurs at potentials negative of that for $NiCo_2O_4$ (see chapter 3 for further details). It is therefore reasonable to suggest that the active species, at least at low overpotentials is the ruthenium and not carbon. As two polarisation curves are observed for both RuO_x/C and $RuO_x/NiCo_2O_4$ it is most likely the ruthenium is the source of this response.

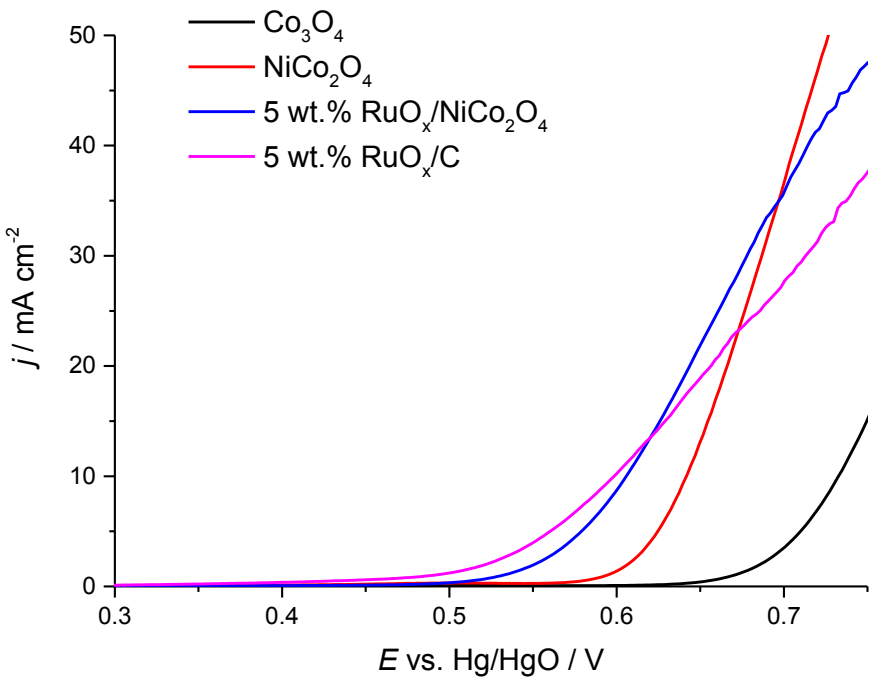

Figure 92: Plot of polarisation curve of OER on ruthenium modified spinel and carbon in oxygen saturated 1 M KOH at 298 K.

response.The oxygen evolution reaction is where the true benefit of ruthenium nanoparticles is realised. From the polarisation curve in Figure 92, at low overpotentials the catalyst with the greatest activity (lowest overpotential) is RuO_x/C, which is closely followed by $RuOx/NiCo_2O_4$. At potentials above 15 mA cm^{-2} the ruthenium modified spinel requires lower overpotentials than ruthenium. The ruthenium modified catalyst outperform the pure $NiCo_2O_4$ and Co_3O_4 catalysts, capable of achieving 10 mA cm^{-2} at approx. 595 mV compared to 640 and 720 mV respectively for the pure spinel samples (Table 33), a gain of 40 mV at 298 K. These results follow the same trend as those found earlier in this chapter, when measured in 4 M KOH and at 333 K, with the ruthenium modified spinel providing an excellent alternative to RuO_x/C, especially at higher current densities.

Table 32: Comparison of the oxygen evolution activity for ruthenium catalysts, measured in 1 M KOH at 298 K.

Sample	*E* @ 10 mA cm^{-2} / mV	Tafel slope / mV dec^{-1}
Co_3O_4	721	51
$NiCo_2O_4$	637	43
5 wt. % RuO_x / $NiCo_2O_4$	597	66
5 wt. % RuO_x / C	589	96

5.3.3 Alternative supports for ruthenium nanoparticles

The reduction in overpotential for the OER is significant (40 mV at 298 K in 1 M KOH and 86 mV at 333 K in 4 M KOH) when RuO_x nanoparticles are prepared onto the surface of $NiCo_2O_4$ in comparison to an unmodified $NiCo_2O_4$ sample. The reduction in overpotential is likely due to the intrinsic activity of the RuO_x towards the oxygen evolution reaction; however, the effect of supporting nanoparticles on $NiCo_2O_4$ is unknown.

In acidic conditions precious metal nanoparticles are susceptible to changes in activity towards the ORR[33-35] and OER[26] when supported on metal oxides and carbides or prepared as solid solutions with cobalt[36]. It is unclear how ruthenium modified $NiCo_2O_4$ compared compares with RuO_x supported on alternative materials. To further resolve the source of the improved activity, samples of carbon and nickel powder were prepared with RuO_x nanoparticles. The samples were produced by the same synthesis method (5.2.2) as the $RuO_x/NiCo_2O_4$, by simply exchanging the supporting material ($NiCo_2O_4$, carbon or nickel powder). In addition, ruthenium was doped into the structure $NiCo_{2-x}Ru_xO_4$, to identify if the insertion of ruthenium into the spinel compares to formation of RuO_x nanoparticles on a surface.

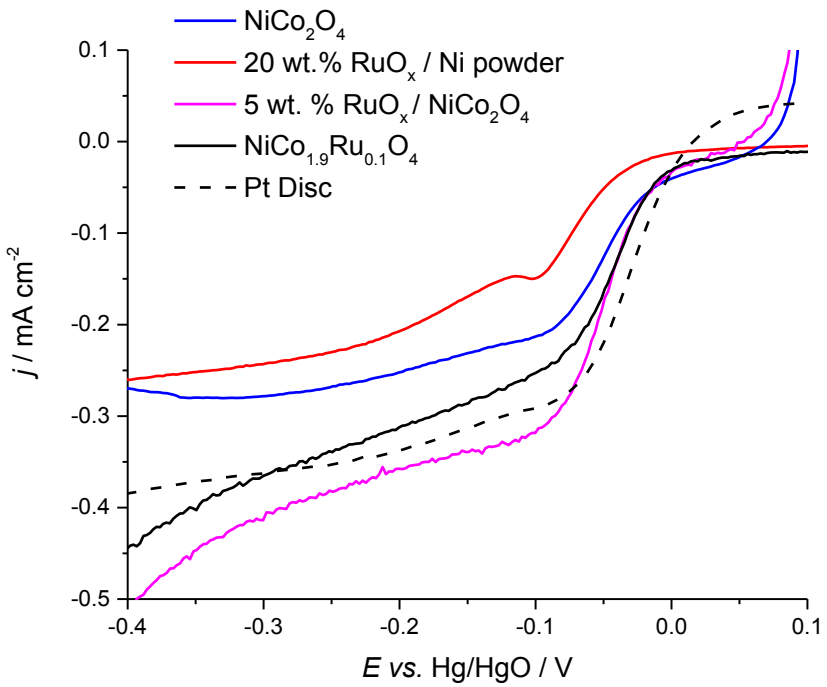

Figure 93: Polarisation plot of ruthenium modified thin-film electrodes on GC-RDE in 4 M KOH at 333 K, rotated at 400 rpm.

A comparison of the voltammetry for the oxygen reduction on thin-film electrodes cast onto glassy carbon RDE (Figure 93) demonstrates that all samples are active. All samples produce a sigmoidal curve, with a sharp rise in current observed with the onset of the ORR, followed by a plateau region for the mass transport limited response. The unmodified $NiCo_2O_4$ is included as a point of reference, along with a platinum disc electrode. All ruthenium doped samples produce non-linear plateau, likely from further reaction of the ruthenium on the surface of the nanoparticles.

Table 33: Comparison of ruthenium modified electrodes towards the ORR in oxygen saturated 4 M KOH at 333 K.

Samples	ORR at -150 μA cm^{-2} / mV	Tafel slope / mV dec^{-1}	j_L @ -500 mV / mA cm^{-2}
Pt disc	-32	43	-0.44
$NiCo_2O_4$	-58	90	-0.27
5 wt. % RuO_x / $NiCo_2O_4$	-44	75	-0.74
$NiCo_{1.9}Ru_{0.1}O_4$	-45	61	-0.45
20 wt. % RuO_x / Ni	-100	77	-0.26

The sample requiring the greatest overpotential for the ORR is that of the RuO_x supported on nickel powder. It is possible that the difference in particle size between the nickel powder and the $NiCo_2O_4$ will contribute towards a difference in activity observed on the RDE. The larger particles of the nickel powder (approx. 5- 10 μm in diameter) will provide a smaller proportion of contact to the glassy carbon surface, relative to its bulk, than that of a smaller particle such as the $NiCo_2O_4$ (200 nm in diameter). This reduced contact may produce an increased overpotential for the kinetically controlled portion of the slope, with a larger resistance for active sites at a further distance from the glassy carbon electrode.

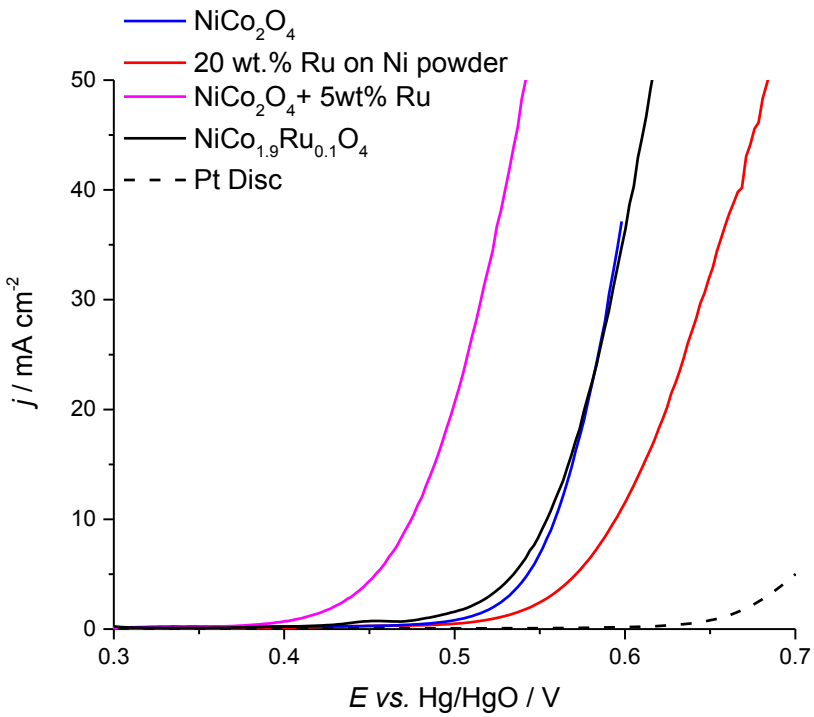

Figure 94: Comparison of ruthenium modified thin-film electrodes on GC-RDE in 4 M KOH at 333 K, rotated at 400 rpm.

The oxygen evolution reaction produces similar voltammetry to previous results, with a negligible current observed until the rapid rise in current due to the OER at potentials positive of 0.45 V. The addition of RuO_x to the spinel lowers the overpotential for the oxygen evolution reaction to 473 mV at 10 mA cm^{-2}, compared to 559 mV for pure $NiCo_2O_4$. The $NiCo_2O_4$ and $NiCo_{1.9}Ru_{0.1}O_4$ produce very similar responses, in terms of polarisation curve shape and overpotential, suggesting the ruthenium, when replacing cobalt in the spinel, is inactive. It is possible that the ruthenium is not present in the surface or the geometry required for the ruthenium to catalyse the OER is not possible in a spinel structure. The ruthenium oxide is believed to operate through a nearby oxygen site in the rutile structure[37], however, this would not be available in the cubic spinel structure.

Table 34: Comparison of ruthenium modified electrodes towards OER in 4 M KOH at 333 K.

Sample	*E* @ 10 mA cm^{-2} / mV	Tafel slope / mV dec^{-1}
Pt – disc	714	58
$NiCo_2O_4$	559	52
5 wt. % RuO_x / $NiCo_2O_4$	473	63
$NiCo_{1.9}Ru_{0.1}O_4$	555	69
20 wt. % RuO_x / Ni	591	67

These results suggest that, although the addition of small concentrations of ruthenium onto the $NiCo_2O_4$ provides little effect towards the ORR activity. However, they do provide an 80 mV reduction in overpotential, when compared to an unmodified $NiCo_2O_4$ for the OER or RuO_x on nickel powder.

5.4 Gas diffusion electrodes

The use of thin-film electrodes on RDE has been commonly employed to determine the activity of electrocatalysts. A significant difference occurs when translating the performance of the catalyst layer from RDE, with a planar geometry on a polished smooth surface of glassy carbon, to a tortuous and porous gas diffusion electrode.

Measurements carried out on the gas diffusion electrodes are not directly comparable to those on RDE, not only due to the changes in electrode structure and gas supply to the catalyst centre, but also the electrolyte is 8 M KOH, as opposed to 4 M KOH used in previous studies. Catalyst loadings are also significantly greater 75 μg cm^{-2} *vs.* 1 – 10 mg cm^{-2} for rotating disc and gas diffusion electrodes respectively.

5.4.1 Carbon GDE

A thin-film catalyst layer was prepared onto carbon GDL as outlined in chapter 4 section 4.2.2. Although carbon is known to be unstable at the potentials for OER in alkali, it is commonly used to compare electrocatalyst activity over short time periods.

Measurements were carried out under galvanostatic control to cycle between the ORR and OER reactions at 10, 20 and 50 mA cm^{-2}. These currents were selected as targets for the overall project

and compare reasonably with current vanadium flow batteries that typically operate at 10 – 50 mA cm^{-2}.[38]

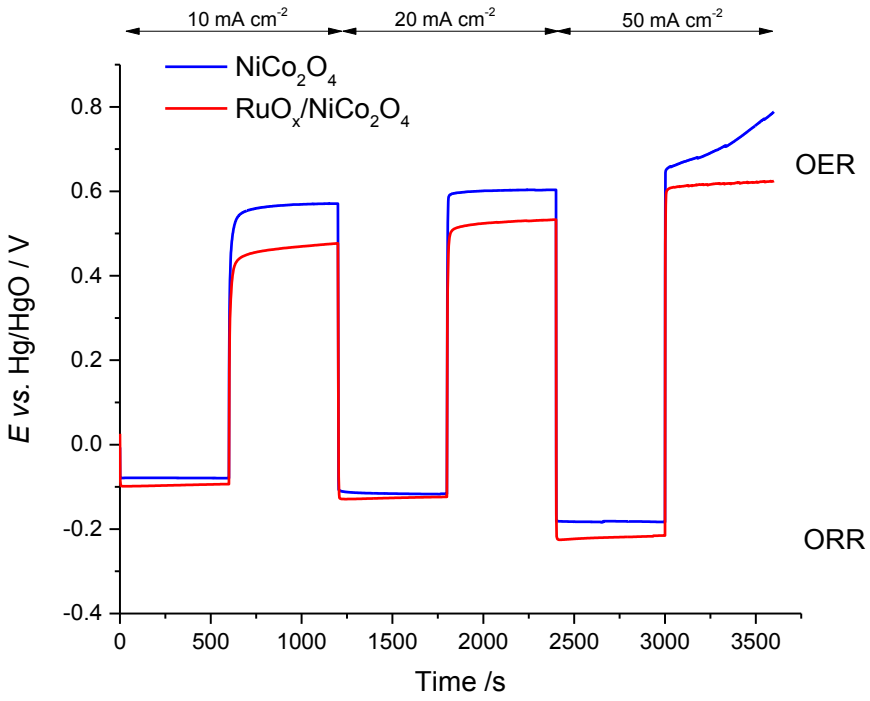

Figure 95: Comparison of Toray GDE with various $NiCo_2O_4$ based electrocatalyst layers at 10, 20 and 50 mA cm^{-2}, alternating between oxygen reduction and evolution in 8 M KOH at 333 K and gas flow of 200 cm^3 min^{-1} O_2.

The galvanostatic measurements are expected to produce a sequence of square waves from the change in potential over time to achieve the desired current. This electrochemical response is observed for the samples prepared on carbon as shown in Figure 95. The unmodified $NiCo_2O_4$ commonly produces a small slope when switching between the oxygen reduction and evolution reactions. The reduced overpotential occurs for only short lengths of time and is most easily identified at lower current densities. This result is consistent with a surface redox couple of the $NiCo_2O_4$ catalyst, and has been discussed in chapter 4. The pseudo-capacitance behaviour of the surface redox couple for the $NiCo_2O_4$ has been of interest in other studies for applications in super-capacitors, where the charge capacity is improved by preparing high surface area spinels and the stability of the 'charged' state extends to hundreds of seconds.[39-41] The addition of an electrocatalyst that also provides a small amount of charge available with a low overpotentials is a beneficial side effect, by improving the electrical efficiency of a battery during short charge/discharge cycles.

The desired current densities were achieved by all samples during both the oxygen reduction and evolution reactions. If the electrode is stable, a constant potential should be observed. Both samples demonstrate this response at 10 mA cm^{-2} and 20 mA cm^{-2}. However, for the unmodified $NiCo_2O_4$ a rising potential at 50 mA cm^{-2} during the oxygen evolution reaction suggests that the electrode is failing. The instability is attributed to loss of electrocatalyst at high current densities. Three possible methods for this electrode failure are as follows. Firstly, the mechanical failure of the electrode layer due to gas evolution, although no electrocatalyst was observed in the electrochemical cell. Secondly, the addition of high surface area carbon in close contact to the electrocatalysts may cause rapid decomposition of the carbon and loss of connection to the electrode surface. Finally, the increase in the potential may be a result of $O_2(g)$ being trapped in the electrode structure at these higher current densities, which simply blocks the available electrode area.

This same increase in the potential during the OER is not observed for the ruthenium doped $NiCo_2O_4$. The difference in stability is unclear, but could be explained through either improved mechanical layer stability or the separation of the OER primarily occurring on the ruthenium sites, which avoids a closer interaction between reactive oxygen species and the carbon. Such a large difference in corrosion rates is unusual and would need to be confirmed by analysis of the evolved gas mixture.

In addition to improved stability, the overpotential towards the oxygen evolution is reduced significantly with the addition of ruthenium to $NiCo_2O_4$. The overpotential throughout the selected current range shows a reduction in overpotential of 70 – 100 mV. The overpotential does however show an increase during the oxygen reduction reaction of 10 – 20 mV. This is likely caused by the ruthenium blocking sites of the $NiCo_2O_4$ that would otherwise be active towards the ORR. The difference between the OER (charge) and ORR (discharge) voltage represents a significant loss in efficiency but with the addition of ruthenium, this can be reduced from approx. 750 mV to 650 mV at 20 mA cm^{-2}.

5.4.2 Nickel GDE

An alternative electrode structure devoid of carbon was developed that would be suitable for both the ORR and OER (Chapter 4). Briefly the electrodes were prepared by a mixture of nickel powder and PTFE solution pressed into nickel foam and calcined, before being brush coated with the desired catalyst and PTFE ink followed by a final heat treatment to form the electrode. This structure eliminates the degradation of the catalyst layer through carbon corrosion. In addition, this method of electrode preparation also allowed a reduction in catalysts loading from 7 mg cm^{-2}

down to 0.7 mg cm^{-2}. The measurements were carried out in 8 M KOH at 333 K, but include a delay of 30 seconds between each chronopotentiometry measurement to determine how the OCP may change with cycling.

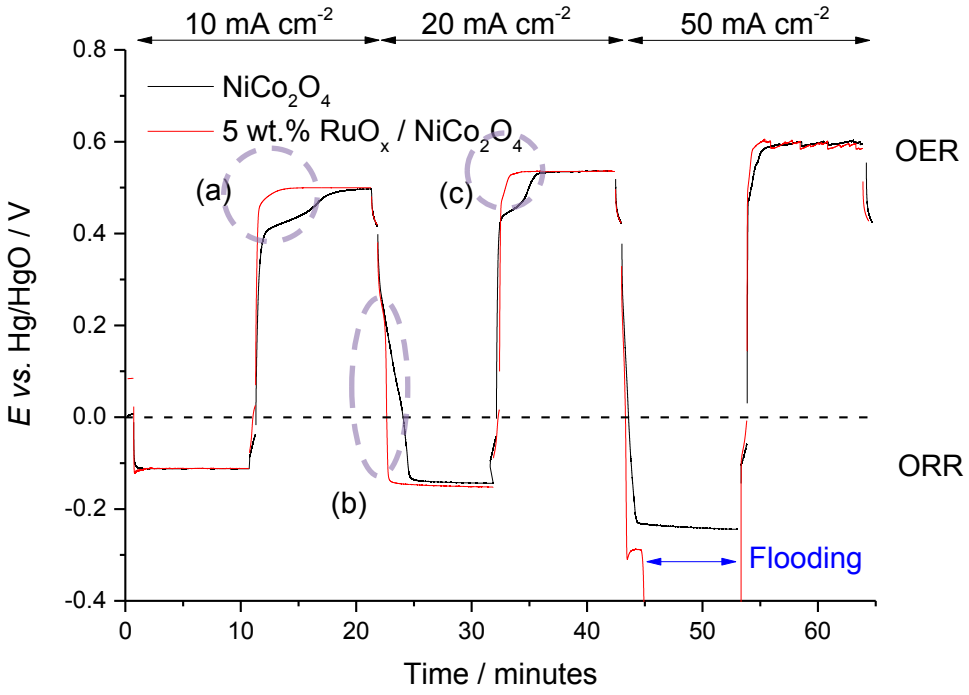

Figure 96: Galvanostatic measurements of ORR and OER on $NiCo_2O_4$ (black) and $RuO_x/NiCo_2O_4$ (red) brush-coated nickel foam GDE in 8 M KOH at 333 K and 200 cm^3 min^{-1} of O_2 supplied to the back of the electrode.

The ruthenium-doped sample was examined using SEM before and after measurement to determine loss of RuO_x (Table 38). The GDE flooded via a slow electrolyte leak during the measurement, observed as a sudden rise in the potential during the oxygen reduction at 50 mA cm^{-2}. This slow outflow of electrolyte limited the maximum current density achieved on the oxygen reduction, with minimal effect to the oxygen evolution result. Increasing the loading of the nickel powder reduces the possibility of such electrode failure.

The oxygen reduction and evolution both produce a distortion of the expected square wave response, due to the $NiCo_2O_4$ surface redox couple. The initial portion of the measurement after the OER shows a reduced overpotential, noticeable when comparing the ruthenium modified and pure $NiCo_2O_4$ results from Figure 96. The area highlighted as part (a) in Figure 96 was used to estimate the charge passed due to the surface redox couple. The areas (b) and (c) of Figure 96 corresponding to approximately 2.4 C for the OER and a reduction of 2.3 C during the ORR. This result is only an approximation, as the oxygen evolution and reduction reactions are likely to also

occur during a portion of the calculated time periods (approx. 2 minutes) when approaching the steady state response. In addition to the determination of the precise limit for the region of low overpotential is a graphical judgement, so the error is likely to these the range of the two values. From previous measurements on GDE electrodes covered in chapter 4, in combination with what appears to be a consistent charge before the ORR and OER would strongly suggest the process of distorting the square wave is reversible.

The result does, however, suggest a negligible difference between the activity of $NiCo_2O_4$ and $RuO_x/NiCo_2O_4$ when supported on nickel foam GDE. This would suggest the GDE is providing a different environment for the electrocatalyst. A more likely explanation would suggest the nickel foam GDE is the limiting factor for this type of electrode. Previously the electrocatalysts were supported on highly conductive glassy or thin (150 μm) Toray® electrodes, the nickel foam electrode is comparatively thick at >3000 μm. The nickel powder may become oxidised during the OER, resulting in an increased resistance of the electrode. The use of thinner nickel mesh gas diffusion electrodes is likely to further improve the response, however, the potential gap for these nickel foam GDEs is still small at 550 mV for a current density of 20 mA cm^{-2}, but is comparable to the results on the carbon GDE.

5.5 XANES measurements

X-ray absorption near edge spectroscopy was used to measure the oxidation state of ruthenium for the prepared samples (Ex-situ). Samples with increasing loading of ruthenium were compared to provide an insight into how the ruthenium is formed on the $NiCo_2O_4$. Further measurements were carried out in alkaline solution (In-situ) at open circuit potentials, to observe any shift with the introduction the electrolyte. In addition, potentiostatic measurements were carried out to identify the active species during the OER and ORR reactions.

5.5.1 Ex-situ XANES

Powdered samples of $RuO_x/NiCo_2O_4$, as in the previous electrochemical measurements, were used to determine the oxidation state of the ruthenium. Briefly, samples were prepared by grinding with (1:1) polypropylene (Mw ~340,000) from Sigma-aldrich) until a homogenous black/grey product was formed. The sample was then pressed at 10 tons to form a disc that was measured in transmission mode. Measurements were carried out on the B18 beamline at the Diamond light source.

The raw XAS data, produced by the beamline, requires several stages of processing. In this work, the data was processed by and analysed using the ATHENA and ARTEMIS software programmes, which are part of the Demeter software suite.[42]

The raw data was initially processed by importing into ATHENA, where the data can be normalised, calibrated and the background subtracted. For XANES analysis, only the normalisation and calibration steps are required. XAS spectra were normalised to a value of 1, as per Figure 97. Normalisation was carried out by (1) fitting a linear function to the pre-edge, extrapolated to the maximum energy; (2) fitting a quadratic function to the post-edge data, ensuring it passed through the midpoint of the oscillations of the data; and finally, (3) subtracting both from the raw data.

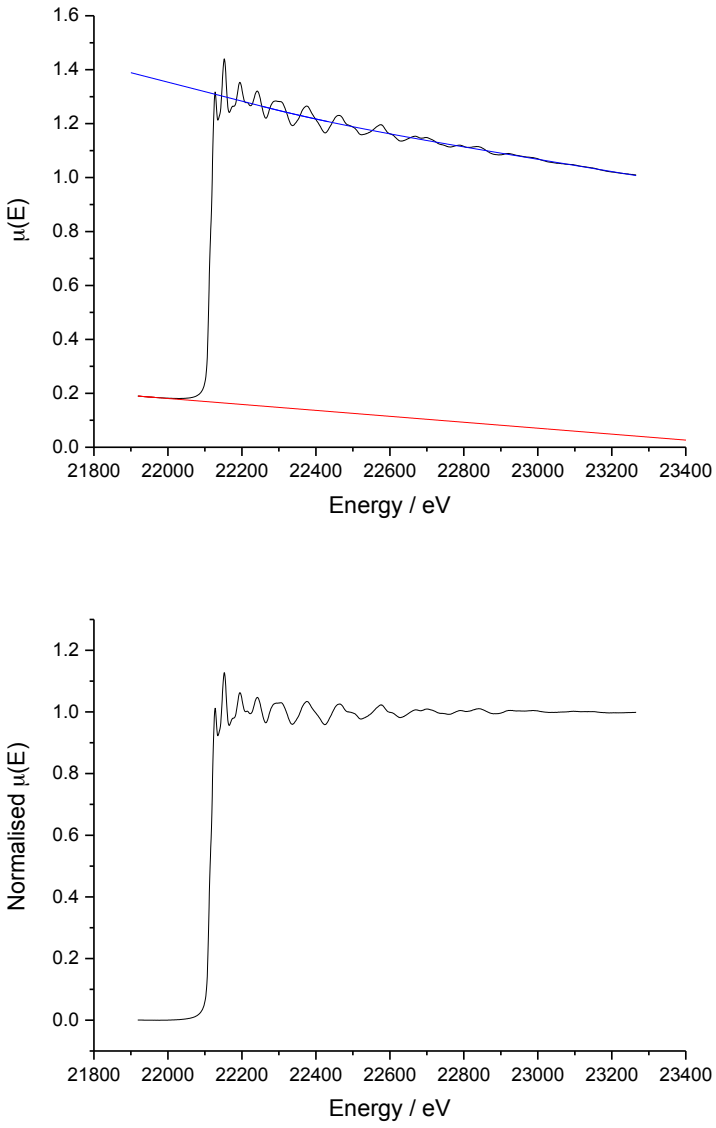

Figure 97: Plot of the XAS spectra for ruthenium foil before normalisation (top), and after (bottom).

Each measurement carried out in transmission geometry also includes a spectrum for ruthenium metal foil that was used to calibrate each sample. This is commonly achieved by aligning the peak of the first derivative of the metal foil reference samples to the tabulated absorption energy.[43] This shift in energy was then applied to the sample data and produces spectra with a consistent energy scale.

Post normalisation and calibration, the signal to noise ratio was improved by merging multiple spectra collected for each sample. This process allows data collected from different experiments at the same edge to be compared.

The absorption edge energy (E_o) of the sample data was then identified. Due to the broad nature of the absorption peak, it is hard to define the point at which the energy to the core electron is fulfilled. As such, the E_o is commonly selected as either half-way up the absorption edge, the peak of the white line or the first peak in a plot of the first derivative of the spectrum. In this work the E_o was selected as half-way up the absorption edge.

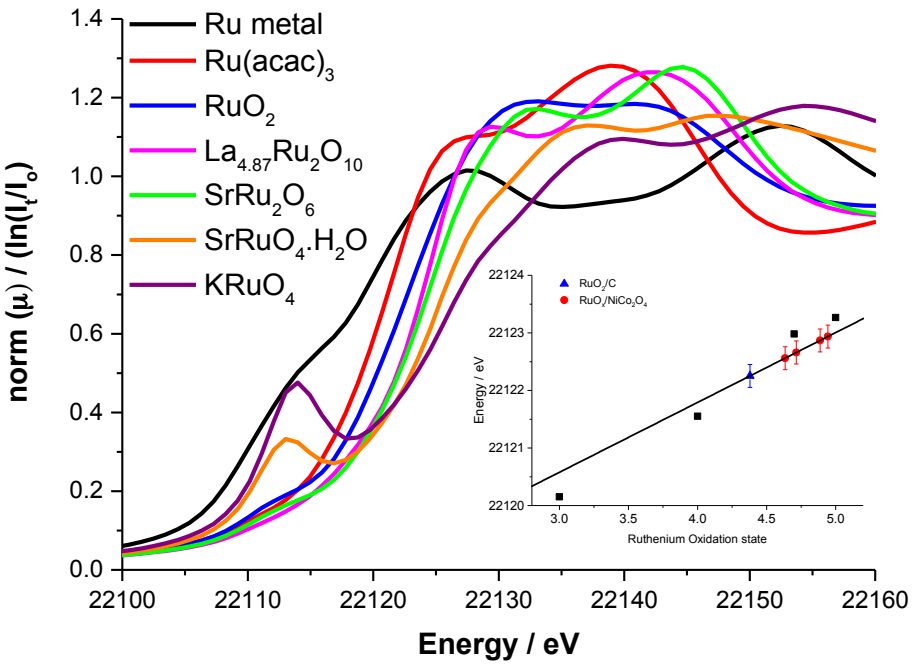

Figure 98: Comparison of spectra for ruthenium reference compounds with increasing oxidation state. Insert:Oxidation state of RuO_2/C and $RuO_x/NiCo_2O_4$ on a calibration curve formed from the reference ruthenium materials.

A series of reference samples were prepared by Walton et al.[44] to provide a calibration, used in the determination of the ruthenium oxidation state. The measured spectra were processed as outlined above. The spectra produce a calibration curve with reasonable fit to the data (Figure

98). The presence of pre-edge features for the $SrRuO_4.H_2O$ and $KRuO_4$ from the 1s to 4d transition is likely to increase the error of oxidation state derived from the calibration curve.

Table 35: List of oxidation states and corresponding absorption energy for the ruthenium reference samples.

Sample	Oxidation state	Energy / eV (±0.1)
Ru (metal)	0	22113.8
$Ru(acac)_3$	3+	22116.9
RuO_2	4+	22118.2
$La_{4.87}Ru_2O_{10}$	4.7+	22119.7
$SrRu_2O_6$	5+	22120.0
$SrRuO_4.H_2O$	6+	22121.1
$KRuO_4$	7+	22121.9

The E_0 for the RuO_x supported on carbon occurs at 22122.1 (±0.1) eV, which corresponds to an oxidation state for the ruthenium of 4.25+, instead of the expected 4+ for RuO_2. The slightly elevated value for the RuO_2/C oxidation state could be explained either by the formation of a small impurity of RuO_4, or the surface oxidation state of the ruthenium nanoparticles may differ to that of the bulk. The small size of the nanoparticles means the surface has a disproportionate effect relative to the bulk, and such a contribution could explain the shift in the overall oxidation state of the measured ruthenium.

The error in the oxidation state obtained from the XANES can be determined by two methods. A statistical analysis of the linear fit used in the calibration can be used to provide an error, but is a referenced value to the quality of the calibration samples used. Alternatively, the detector on the beamline is capable of measuring the XANES with an energy resolution of 0.1 eV, which corresponds to shift in the oxidation state of 0.09 by use of the calibration curve. As the XANES is a direct measure of the energy of the sample with the error predominately in the absolute value of the oxidation state, this was selected for the error determination presented in this work.

Table 36: A comparison of ruthenium absorption energy and corresponding oxidation state for carbon and mixed metal oxide supports, as determined by XAS.

Sample	Ruthenium oxidation state (±0.09)	Energy / eV (±0.1)
5 wt. % RuO_2/C	4.25	22122.1
5 wt. % RuO_x/$NiCo_2O_4$	4.99	22123.0
10 wt. % RuO_x/$NiCo_2O_4$	4.94	22122.9
20 wt. % RuO_x/$NiCo_2O_4$	4.81	22122.8
30 wt. % RuO_x/$NiCo_2O_4$	4.74	22122.7

The addition of RuO_x to $NiCo_2O_4$ results in a positive shift to the XAS spectra (Figure 98), correlating to an increased oxidation state, when compared to RuO_2 on carbon. The rise in oxidation state occurs for all samples regardless of ruthenium loading (Table 36). However, the loading does influence the ruthenium oxidation state, with a slightly increased oxidation state observed for samples with a lower loading of the ruthenium.

The synthesis of the RuO_2 on carbon used the same reducing agent as when preparing on RuO_x on $NiCo_2O_4$. An identical oxidation state with loading relationship is reproduced when preparing samples with a different reducing agent (sodium borohydride), suggesting the reason for a difference in oxidation state is the reducing agent used in the chemical reduction step.

The reducing agent is likely to also reduce the metals in $NiCo_2O_4$. A sample of $NiCo_2O_4$ that has been exposed to hydrazine (equivalent to 20 wt.% of the sample) does show a loss in activity from measurements on the RDE. A thermal treatment, at the same calcination temperatures used in the synthesis of the $NiCo_2O_4$, was included to promote the re-formation of the spinel; however, it appears ineffective against the permanent change caused by the reducing agent to the mixed metal oxide. The reduction in activity was mostly observed to affect the OER, another explanation for the ruthenium providing the most benefit as a nanoparticle modification.

The increased loading of ruthenium does yield larger crystallite sizes, 7 nm *vs.* 13 nm. This larger crystallite size suggests larger particles are likely formed with increased loading, thus the ratio of ruthenium atoms on the surface of the nanoparticle, compared to bulk, will reduce. As one of the possible explanations for the increased oxidation state is oxygen-enriched ruthenium at the surface, this would explain the trend observed for the ruthenium oxidation state.

5.5.2 In-situ XANES

The determination of the oxidation state during operation is key to understanding the active species during the reaction. Samples were therefore prepared onto gas diffusion electrodes and sealed into the XAS electrochemical flow-cell. This allowed the electrocatalyst to be in contact with electrolyte and under electrochemical control, whilst XAS fluorescence measurements were carried out through the thin layer of carbon paper and Kapton® backing window. Further details of the experimental conditions are discussed in Chapter 2 section 2.6.

Electrodes were hydrated with water before being loaded into the cell. The electrolyte, 1 M KOH, was circulated for several minutes to equilibrate the electrode. A continuous low flow rate of electrolyte was passed over the electrode to ensure rapid removal of any evolved gas. The initial measurements were used to determine the open circuit voltage (OCV), with subsequent measurements increasing the potential from 0.1 V to 0.5, 0.6 and 0.7 V for the oxygen evolution reaction. The potential was then stepped back to 0.1 V and -0.2 V for the oxygen reduction reaction.

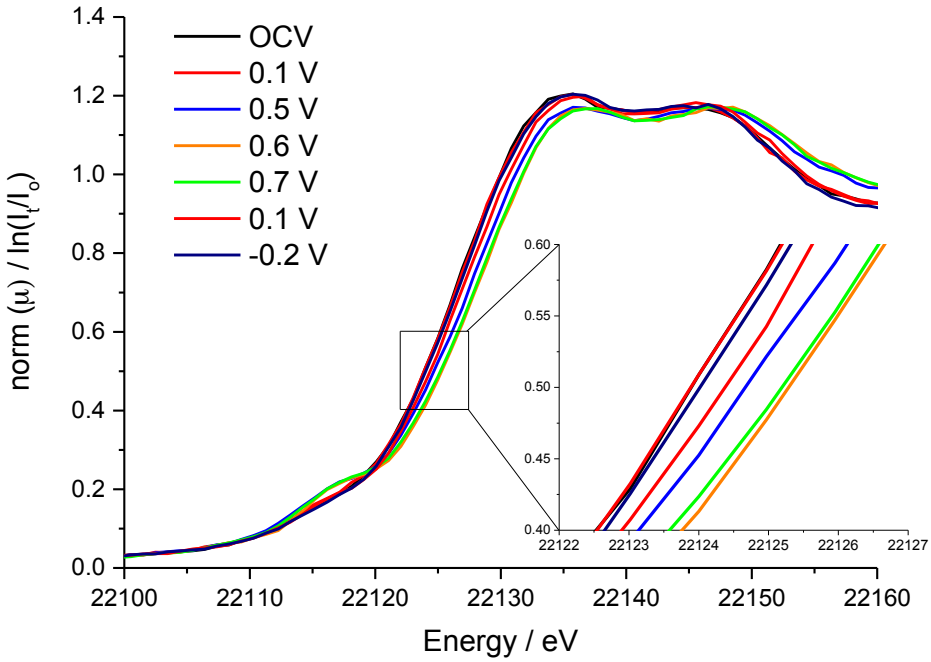

Figure 99: Plot of the In-situ XAS spectra of RuO_x on $NiCo_2O_4$ in 1 M KOH at room temperature.

In-situ measurements were carried out using 5 wt. % RuO_x supported on $NiCo_2O_4$ and carbon. After the electrode with $RuO_x/NiCo_2O_4$ achieved a stable OCV (0.005V *vs.* Hg/HgO), the ruthenium oxidation state was measured. The oxidation state at the OCV was determined as +7.12 ±0.09, a large rise from the value determined from ex-situ measurements of +4.74 ±0.09. This suggests the

ruthenium spontaneously undergoes reaction with the electrolyte to form a hydroxy-oxide species or, possibly, a combination of elevated oxidation states, such as +5 and +8.[45] A similar response was observed for RuO_2/C, with a rise in the ruthenium oxidation state from +4.25 ±0.09 to +6.78 ±0.09 when immersed in 1 M KOH. This would agree with a spontaneous reaction of the ruthenium with the electrolyte.

Table 37: Comparison of ruthenium oxidation states derived from the absorption energy of the XAS spectra.

Potential *vs.* Hg/HgO	RuO_2/C (±0.09)	$RuO_x/NiCo_2O_4$ (±0.09)
OCV	7.12	6.78
-0.2	7.10	6.91
0.1	7.22	6.80
0.5	7.50	7.57
0.6	7.73	8.02
0.7	7.72	7.94

Application of a potential (0.1 V *vs.* Hg/HgO) close to the OCV (0.005 V) results in a nominal shift in the oxidation state that is well within the error of the measurement. At increasing potentials, the oxidation state of the ruthenium rapidly rises when supported on both $NiCo_2O_4$ and carbon. The $RuO_x/NiCo_2O_4$ achieves a higher oxidation state at 0.6 V and 0.7 V of +8.0 compared with +7.7 for the RuO_2/C. This rapid rise in oxidation state, the positive current (5 - 10 mA cm^{-2}) and the gas evolved during the reaction were all indicative that the OER was occurring. The $RuO_x/NiCo_2O_4$ yielded a higher current density for the applied overpotential (7.6 mA cm^{-2}) than RuO_x/C (5.6mA cm^{-2}).

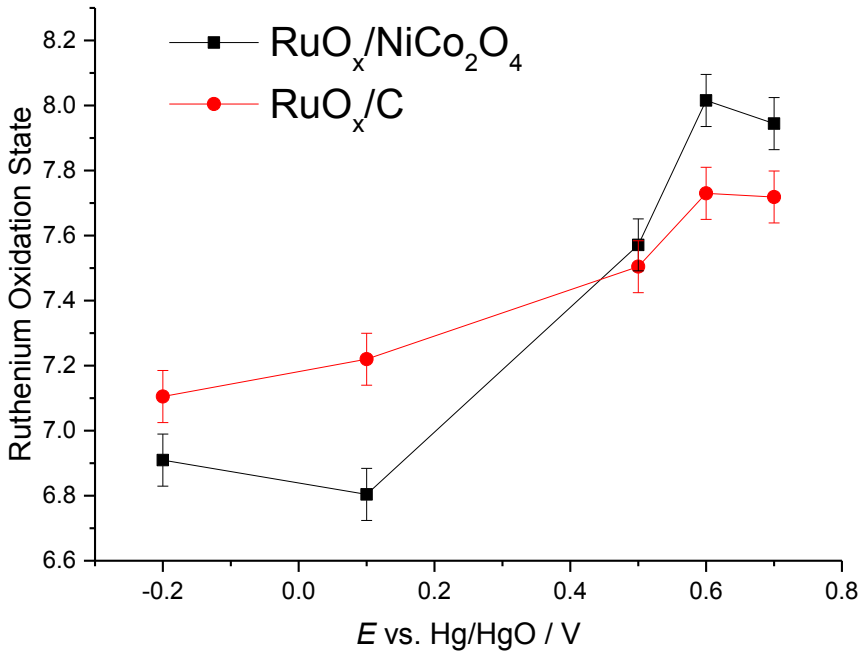

Figure 100: Plot of the change in the ruthenium oxidation state as a function of potentiostatic control for RuO_x on carbon (Red circles) and $RuO_x/NiCo_2O_4$ (Black squares) in flowing 1 M KOH.

The elevated potential and corresponding oxidation state (Figure 100) is likely to enhance the dissolution of the ruthenium oxide through the formation of soluble RuO_4. The Pourbaix diagram, shown in Figure 101, would suggest the ruthenium forms $RuO_2.2H_2O$ or RuO_4 species at potentials for the ORR and $HRuO_3^-$ for potentials for the OER. However, the signal, during the measurements, was observed to only yield a small reduction in intensity, suggesting if this process occurs it may be relatively slow. The OER in acidic media also suggests the formation of hydrous ruthenium species $RuO_2.2H_2O$ or RuO_4. However, in-situ XANES measurements have shown that ruthenium complexes typically form 4+ and 5+ oxidations states. The oxidation state then increases with the application of overpotential for the OER.[44] The increase in oxidation state has been suppressed through substitution of iridium into the pyrochlore structure. This suggests the metal-oxygen binding energy may determine the activity and the addition of iridium to pure ruthenium pyrochlores lowers their activity and oxidation state. In the alkaline conditions a change in the oxidation state of the ruthenium species is observed when prepared as nanoparticles on $NiCo_2O_4$ and carbon during the OER and ORR.

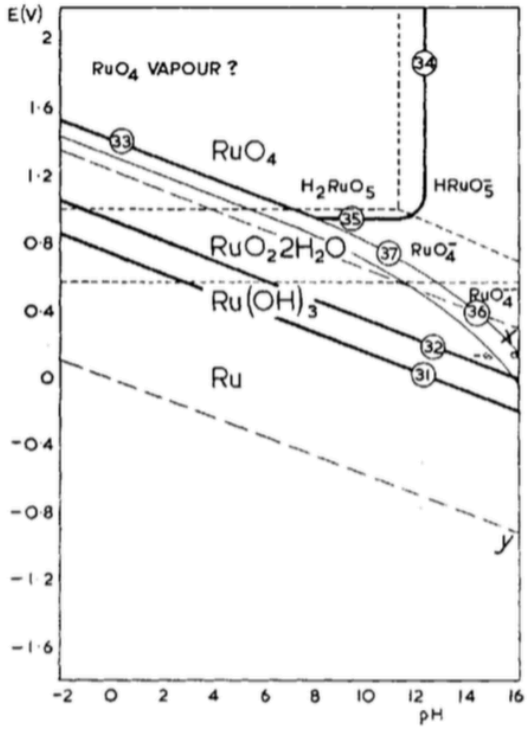

Figure 101: Pourbaix diagram for Ruthenium at 298 K.[46]

An electrode with 0.7 mg cm^{-2} of $RuO_x/NiCo_2O_4$ was prepared onto nickel foam GDL to evaluate the ruthenium stability further. The initial ruthenium loading of 8 wt. % fell to 4 wt. % after 30 hours of operation at OER potentials (650 mV); Samples were measured using SEM-EDX before and after extended operation, with results tabulated in

Table 38. A side view of the electrode after operation (Figure 102) suggests the majority of the ruthenium resides on the electrode surface after operation. A large variation in the concentration of the ruthenium is apparent, suggesting the sample is inhomogeneous. The large variation in ruthenium loading stems from the application of the catalyst to the electrode.

Table 38: EDX results of fresh and aged ruthenium modified electrodes. Aged electrodes operated for 30 hours at 650 mV in 8 M KOH at 333 K for 30 hours.

Element	Fresh electrode / wt.%	Aged electrode / wt.%
Cobalt	54 ± 5	60 ± 10
Nickel	38 ± 6	36 ± 8
Ruthenium	8 ± 1	4 ± 2

The results also show an overabundance of nickel to be present in the sample. The excess nickel is likely contribution from the nickel present in the foam and GDL distorting the relative ratios of nickel and cobalt.

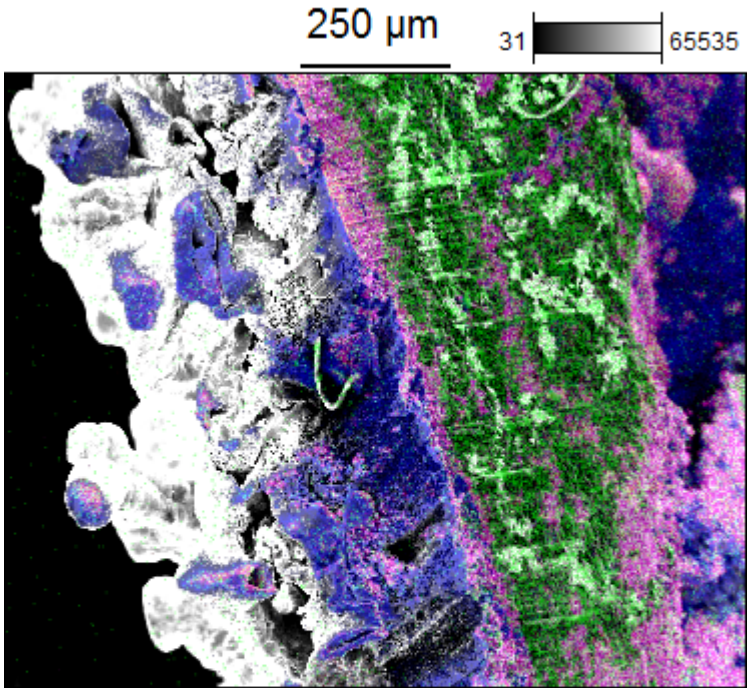

Figure 102: SEM-micrograph of $RuO_x/NiCo_2O_4$ electrode after 30 hours at 650 mV *vs.* Hg/HgO. False colour overlay from EDX for Ru (green), Co (red) and Ni (blue).

The ruthenium oxidation state is reduced when taken into the potential range for oxygen reduction (-0.2V *vs.* Hg/HgO). The oxidation state for the $RuO_x/NiCo_2O_4$ was found to be +6.9, compared to +7.1 when supported on carbon. This may suggest any enhancement in activity is an effect of electronic interaction between the RuO_X and the support. Another explanation could suggest the ruthenium has a relatively high affinity towards hydroxide and at the boundary between the ruthenium and spinel a region of high activity is achieved. In either case, the addition of ruthenium to the $NiCo_2O_4$ provides an increase in activity when compared to either RuO_x/C or $NiCo_2O_4$.

5.6 Conclusion

The modification of $NiCo_2O_4$ with ruthenium dioxide nanoparticles lowers the potential gap between the oxygen evolution and reduction reactions. This reduction in overpotential, of approximately 80 mV, is also observed on carbon gas diffusion electrodes, when operating at a current density of 20 mA cm^{-2}. This result confirms the improved activity of the catalyst from the addition of ruthenium.

However, when implemented on nickel based gas diffusion electrodes, no discernible change in the operating potentials for the modified and unmodified $NiCo_2O_4$ was observed. The modified electrode operates with a square wave response, suggesting the $NiCo_2O_4$ surface species has been covered. This is currently believed to be an issue relating to the structure of the nickel foam, as opposed to a lack of activity from the electrocatalyst. Increased catalysts loadings on the nickel GDE would likely provide an improved comparison to the results from the carbon-electrodes.

The effect of platinum and other precious group metals do not provide any measureable improvement when formed as nanoparticles on the $NiCo_2O_4$. Platinum is most active when formed as metal nanoparticles; however samples synthesised with the $NiCo_2O_4$ predominately formed an oxide structure, likely due to thermal treatment and oxygen rich surface of the $NiCo_2O_4$. Electrochemical reduction was unsuccessful in reducing the platinum without also further reducing the $NiCo_2O_4$ and a further loss of activity towards both oxygen evolution and oxygen reduction reactions.

X-ray absorption measurements of the ruthenium supported nanoparticles were successfully carried out ex-situ and in-situ. Ex-situ measurements found the oxidation state of the ruthenium oxide nanoparticles to be significantly higher when prepared on $NiCo_2O_4$, than carbon. Increasing the loading of the ruthenium oxide leads to a reduction in the oxidation state, suggesting the size of the particle affects the oxidation state.

Beam time limitations did not allow this relationship to be further explored in-situ. However, in-situ measurements of 30 wt. % RuO_x on $NiCo_2O_4$ and RuO_2/C demonstrate a significant change to the ruthenium oxidation state occurs upon contact with the 1 M KOH electrolyte. This spontaneous reaction is believed to comprise the formation of ruthenium hydroxy-oxide. A small pre-edge feature would suggest a possible similarity to the higher oxidation state reference samples.

The results from potentiostatic control suggest the ruthenium oxidation state is further increased when extending the potential into the region of the oxygen evolution reaction (>0.5V *vs.* Hg/HgO). During the OER, the ruthenium in $RuO_x/NiCo_2O_4$ accesses higher oxidation states (+8.0) than RuO_2/C (+7.7). During the ORR, the oxidation state of ruthenium in $RuO_x/NiCo_2O_4$ was found to be +6.9 compared to +7.1 for RuO_2/C. These results suggest that although the ruthenium is likely to undergo dissolution and be lost with time, the support does allow for a change to the electronic state of the RuO_x when supported on a mixed metal oxide. In future, mixed metal oxide supports may provide a means for stabilising the ruthenium nanoparticles, avoiding dissolution, extending their life as electrocatalysts, with minimal impact on the activity towards the OER.

The synthesis of ruthenium nanoparticles onto the $NiCo_2O_4$ produces an enhancement in activity beyond that capable with either RuO_2/C or $NiCo_2O_4$ for the oxygen evolution and oxygen reduction reactions. Current limitations to implementation are: (i) stability of the ruthenium species in alkaline electrolyte for extended periods during the OER; (ii) the increased cost of using such metals in the electrocatalyst. However, with time it is hoped the development of carbon-free GDEs suitable for low loadings of electrocatalyst may permit the use of small amounts of precious metal to be viable in the future.

5.7 References

(1) Crabb, E. M.; Marshall, R.; Thompsett, D. *J. Electrochem. Soc.* **2000**, *147*, 4440–4447.

(2) Crabb, E. M.; Ravikumar, M. K.; Thompsett, D.; Hurford, M.; Rose, A.; Russell, A. E. *Phys. Chem. Chem. Phys.* **2004**, *6*, 1792–1798.

(3) Crabb, E. M.; Ravikumar, M. K. *Electrochim. Acta* **2001**, *46*, 1033–1041.

(4) Lima, F. H. B.; Salgado, J. R. C.; Gonzalez, E. R.; Ticianelli, E. A. *J. Electrochem. Soc.* **2007**, *154*, A369–A375.

(5) Schmidt, T. J.; Gasteiger, H. A.; Stäb, G. D.; Urban, P. M.; Kolb, D. M.; Behm, R. J. *J. Electrochem. Soc.* **1998**, *145*, 2354–2358.

(6) Cui, X.; Guo, L.; Cui, F.; He, Q.; Shi, J. *J. Phys. Chem. C* **2009**, *113*, 4134–4138.

(7) Elezović, N. R.; Babić, B. M.; Gajić-Krstajić, L.; Ercius, P.; Radmilović, V. R.; Krstajić, N. V.; Vračar, L. M. *Electrochim. Acta* **2012**, *69*, 239–246.

(8) Li, G.; Yu, H.; Wang, X.; Sun, S.; Li, Y.; Shao, Z.; Yi, B. *Phys. Chem. Chem. Phys.* **2013**, *15*, 2858–2866.

(9) Wilson, M. S.; Gottesfeld, S. *J. Electrochem. Soc.* **1992**, *139*, L28–L30.

(10) Deivaraj, T. C.; Lee, J. Y. *J. Power Sources* **2005**, *142*, 43–49.

(11) Marie, J.; Berthon-Fabry, S.; Achard, P.; Chatenet, M.; Pradourat, A.; Chainet, E. *Journal of Non-Crystalline Solids* **2004**, *350*, 88–96.

(12) SMIRNOVA, A.; DONG, X.; HARA, H.; VASILIEV, A.; SAMMES, N. *Int. J. Hydrogen Energ.* **2005**, *30*, 149–158.

(13) Greeley, J.; Stephens, I. E. L.; Bondarenko, A. S.; Johansson, T. P.; Hansen, H. A.; Jaramillo, T. F.; Rossmeisl, J.; Chorkendorff, I.; Nørskov, J. K. *Nat. Chem.* **2009**, *1*, 552–556.

(14) Stamenkovic, V. R.; Mun, B. S.; Arenz, M.; Mayrhofer, K. J. J.; Lucas, C. A.; Wang, G.; Ross, P. N.; Marković, N. M. *Nat. Mater.* **2007**, *6*, 241–247.

(15) Soares, C. O.; Carvalho, M. D.; Tavares, A. C.; Jorge, M. E. M.; Gomes, A.; da Silva Pereira, M. I. *J. Electrochem. Soc.* **2013**, *160*, F1138–F1142.

(16) Chang, Y.-M.; Wu, P.-W.; Wu, C.-Y.; Hsieh, Y.-C. *J. Power Sources* **2009**, *189*, 1003–1007.

(17) Chang, Y.-M.; Chang, Y.-F.; Wu, P.-W.; Wu, C.-Y.; Lin, P. *J. Electrochem. Soc.* **2010**, *157*, B900–B905.

(18) Prakash, J.; Tryk, D. A.; Aldred, W.; Yeager, E. B. *J. Appl. Electrochem.* **1999**, *29*, 1463–1469.

(19) Pettersson, J.; Ramsey, B.; Harrison, D. *J. Power Sources* **2006**, *157*, 28–34.

(20) Yoshinaga, N.; Sugimoto, W.; Takasu, Y. *Electrochim. Acta* **2008**, *54*, 566–573.

(21) Takasu, Y.; Yoshinaga, N.; Sugimoto, W. *Electrochem. Commun.* **2008**, *10*, 668–672.

(22) Cruz, J. C.; Hernández, A. R.; Guerra-Balcazar, M.; Chávez-Ramirez, A. U.; Ledesma-García, J.; Arriaga, L. G. *Int. J. Electrochem. Sci.* **2012**, *7*, 7866–7876.

(23) Cruz, J. C.; Rivas, S.; Beltran, D.; Meas, Y.; Ornelas, R.; Osorio-Monreal, G.; Ortiz-Frade, L.; Ledesma-García, J.; Arriaga, L. G. *Int. J. Hydrogen Energ.* **2012**, *37*, 13522–13528.

(24) Zhuang, S.; Huang, K.; Huang, C.; Huang, H.; Liu, S.; Fan, M. *J. Power Sources* **2011**, *196*, 4019–4025.

(25) Wang, Y.; Lu, X.; Liu, Y.; Deng, Y. *Electrochem. Commun.* **2013**, *31*, 108–111.

(26) Da Silva, L. M.; Boodts, J. F. C.; De Faria, L. A. *Electrochim. Acta* **2001**, *46*, 1369–1375.

(27) Slanac, D. A.; Lie, A.; Paulson, J. A.; Stevenson, K. J.; Johnston, K. P. *J. Phys. Chem. C* **2012**, *116*, 11032–11039.

(28) Ko, J. W.; Ryu, W.-H.; Kim, I.-D.; Park, C. B. *Chem. Commun.* **2013**, *49*, 9725–9727.

(29) Subbaraman, R.; Tripkovic, D.; Chang, K.-C.; Strmcnik, D.; Paulikas, A. P.; Hirunsit, P.; Chan, M.; Greeley, J.; Stamenkovic, V.; Marković, N. M. *Nat. Mater.* **2012**, *11*, 550–557.

(30) Soares, C. O.; Carvalho, M. D.; Melo Jorge, M. E.; Gomes, A.; Silva, R. A.; Rangel, C. M.; da Silva Pereira, M. I. *J. Appl. Electrochem.* **2012**, *42*, 325–332–332.

(31) Pourbaix, M. J. N.; Van Muylder, J.; de Zoubov, N. *Platinum Metals Review* **1959**, *3*, 100–106.

(32) Anastasijević, N. A.; Dimitrijević, Z. M.; Adžić, R. R. *J. Electroanal. Chem. Interfacial Electrochem.* **1986**, *199*, 351–364.

(33) Stamenkovic, V. R.; Fowler, B.; Mun, B. S.; Wang, G.; Ross, P. N.; Lucas, C. A.; Marković, N. M. *Science* **2007**, *315*, 493–497.

(34) Duong, H. T.; Rigsby, M. A.; Zhou, W.-P.; Wieckowski, A. *J. Phys. Chem. C* **2007**, *111*, 13460–13465.

(35) Leont'ev, I. N.; Guterman, V. E.; Pakhomova, E. B.; Guterman, A. V.; Mikheikin, A. S. *Nanotechnol. Russia* **2009**, *4*, 170–175.

(36) Jirkov*s.*ký, J.; Makarova, M.; Krtil, P. *Electrochem. Commun.* **2006**, *8*, 1417–1422.

(37) Lee, Y.; Suntivich, J.; May, K. J.; Perry, E. E.; Shao-Horn, Y. *J. Phys. Chem. Lett.* **2012**, 399–404.

(38) Kear, G.; Shah, A. A.; Walsh, F. C. *Int. J. Energy Res.* **2012**, *36*, 1105–1120.

(39) Jiang, H.; Ma, J.; Li, C. *Chem. Commun.* **2012**, *48*, 4465–4467.

(40) Wu, Y. Q.; Chen, X. Y.; Ji, P. T.; Zhou, Q. Q. *Electrochim. Acta* **2011**, *56*, 7517–7522.

(41) Wang, C.; Zhang, X.; Zhang, D.; Yao, C.; Ma, Y. *Electrochim. Acta* **2012**, *63*, 220–227.

(42) Ravel, B.; Newville, M. *J Synchrotron Radiat* **2005**, *12*, 537–541.

(43) McMaster, W. H.; Kerr Del Grande, N.; Mallett, J. H.; Hubbell, J. H. *Compilation of X-Ray Cross Sections*; Report UCRL-50174; Lawrence Livermore National Laboratory, 1969.

(44) Sardar, K.; Petrucco, E.; Hiley, C. I.; Sharman, J. D. B.; Wells, P. P.; Russell, A. E.; Kashtiban, R. J.; Sloan, J.; Walton, R. I. *Angew. Chem.* **2014**, *126*, 11140–11144.

(45) David A McKeown; Patrick L Hagans; Linda P L Carette; Andrea E Russell; Karen E Swider, A.; Debra R Rolison. *J. Phys. Chem. B* **1999**, *103*, 4825–4832.

(46) Pourbaix, M. J. N.; Van Muylder, J.; de Zoubov, N. *Platinum Metals Rev.* **1959**, *3*, 100–106.

Chapter 6: Future work – A comparison of electrocatalysts towards oxygen activity

6.1 Introduction

This chapter will discuss the electrochemical response of electrocatalysts with a perovskite or spinel structure towards the oxygen reduction and evolution reactions. The work in this chapter is incomplete, but contributes to furthering the understanding of mixed metal oxide electrocatalysts activity towards oxygen reduction and evolution reactions. The experiments carried out are to provide a context when discussing catalytic activity between spinel and perovskite electrocatalysts using the same electrochemical system.

The results reported in this chapter include work carried out by Dr. Stephen Price and myself, as part of the POWAIR project on developing zinc-air flow-batteries. Dr. Price prepared several perovskite samples and carried out electrochemical analysis. Samples prepared by myself include the following perovskites: $LaNiO_3$; $CeNiO_3$; $La_{0.6}Ca_{0.4}CoO_3$. In addition, I am responsible for all work on spinel and modified spinel samples

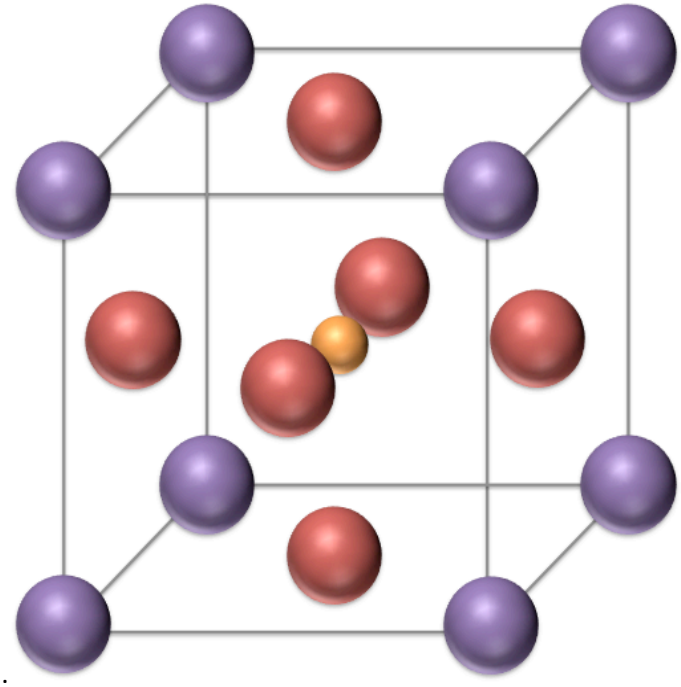

Figure 103: Schematic of the cubic perovskite unit cell. Purple spheres represent the A cations, orange sphere for the B cations and Red spheres for the oxygen atoms.

Initially a series of perovskite samples, defined by their crystal structure as ABO_3, were prepared to compare the electrochemical response towards the oxygen reduction and evolution. The $LaNiO_3$ sample was characterised with XRD, TEM and SEM-EDX to confirm the successful

synthesis. Other perovskite samples were evaluated electrochemically, with physical properties still to be completed. A synthesis method was always selected from the literature.[1-6]

Early studies focused heavily on the nature of transition metal oxides as oxygen reduction and evolution reactions.[7-9] The perovskite structure (unit cell shown in Figure 103) allows for control of oxidation states through the preference for transition metals on the B-site and lanthanide on the A-site.[10] The requirements to achieve the perovskite structure are discussed further in the literature.[11,12] The perovskites have been extensively studied, with larger ionic radii of the lanthanide linked to improved ORR activity.[13] Although lanthanum provides the highest activity, it is reported to be potentially unstable after 10s of hours of operation in hydroxide where it is believed to decompose into $La(OH)_3$.[14]

Other efforts have focused on lowering the overpotential for either the ORR or OER of the mixed metal oxide catalyst to provide a low cost alternative to platinum or ruthenium based electrocatalysts that provide some of the highest activities to-date. Typically, this is carried out with lanthanum in the A-site in a 3+ oxidation state and the B-site filled with one or more transition metals, e.g. $LaCoO_3$ or $LaNiO_3$. The addition of alkali metals onto the A-site, in place of the lanthanide, can further enhance the activity of the perovskite, as seen with the addition of Sr, Ba or Ca to the structure. Recent efforts have explored the electron filling of the B-site metals as a descriptor for the ORR and OER.[10,15-17] Early results suggest the elevated oxidation states of the Co and Ni provide optimal activity, whilst recent work suggests the e_g filling level to be a key parameter, where both low and high oxidation states can provide equivalent specific activities. One proposed mechanism for the ORR on a perovskite electrocatalyst is shown in Figure 104.

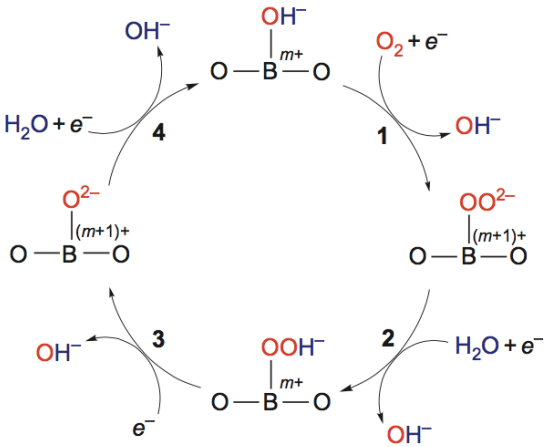

Figure 104: Proposed mechanism for the ORR on perovskite oxide catalysts in alkaline media.[6]

Recent work has noted the addition of carbon to a perovskite catalyst layer provides a change in the overall activity of the sample.[18] An example of this phenomenon can be found with $Ba_{0.5}Sr_{0.5}Co_{0.8}Fe_{0.2}O_{3-\delta}$ (BSCF) catalyst, where hydrogen peroxide is the major product during the

ORR when either the BSCF or carbon is used separately. However, when these materials are combined in a single composite layer the production of peroxide drops and the overpotential for the ORR also is lowered.[19] Similar results are found for other perovskites in the literature, whereby the addition of carbon, to form a carbon composite electrode, yields lower overpotentials for the ORR.[20,21] The change in overpotential towards the ORR and was found to correlate with increased loading of carbon in the electrode.[22] The effect of carbon in the perovskite layer is clearly important for the ORR, but is likely to be detrimental in a bi-functional oxygen electrocatalysts, with the carbon corroding at potentials necessary for the OER. It is for this reason this work has excluded the use of carbons in the catalysts films on RDE.

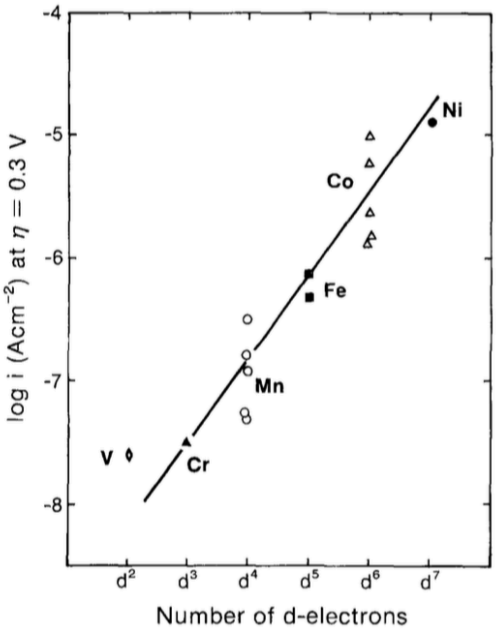

Figure 105: Current density at 0.3V against the number of d-electrons of transition metal ions in perovskites.[1]

The conductivity of perovskites ranges from insulators through to metallic conductors depending upon the composition, where an increasing number of d-electrons is suggested to result in an increased conductivity.[10,23] Modifications to the composition of the perovskite were created to identify factors that influence the activity towards the ORR and OER. The initial starting composition was selected as $LaMO_3$ (M=Co, Ni, Mn), providing electrocatalysts with 4, 6 and 7 d-electrons in their structure.[17] The d-band structure of perovskite transition metal oxides has been suggested as the source of increased conductivity and catalytic activity, as shown by the increased current at a fixed potential in Figure 105.[24] The catalytic activity is suggested to require an interaction with the π* orbitals of oxygen, which can be used in calculating the adsorption energy for OH^- and O intermediate species.[25] Perovskite transition metal-oxides with a greater number of d-band electrons were proposed to yield an optimal affinity towards the O and OH^-

intermediates.[26] However, for bifunctional materials, the gains on either the ORR or OER typically come at the expense of a lower activity (greater overpotential) for the other reaction. This effect was highlighted when comparing the activity of several perovskite electrocatalysts, with the optimal e_g filling level different for the oxygen reduction and evolution reactions, as shown in Figure 106.[16] In this work efforts are focused on identifying the perovskite electrocatalysts that will yield the lowest potential gap between the ORR and OER.

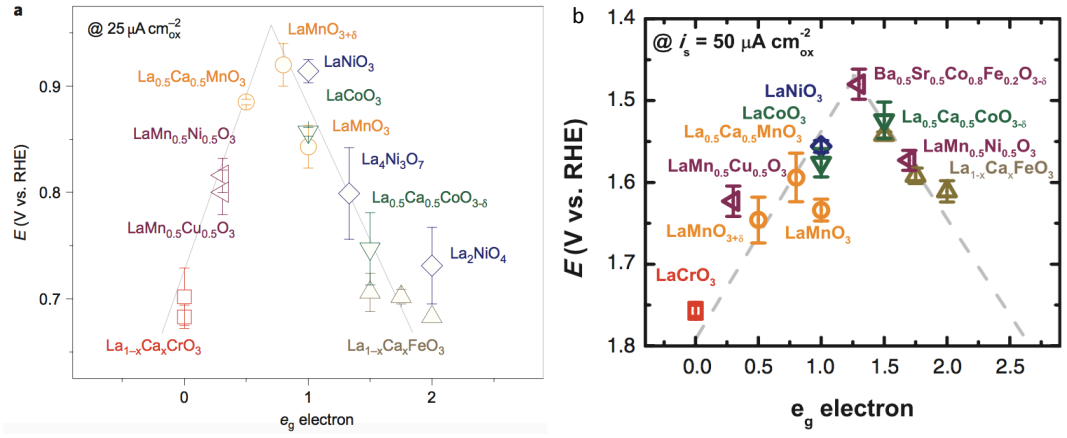

Figure 106: Plot of the ORR (a) and OER (b) overpotential against e_g electron filling level for perovskite electrocatalysts.[6,16]

Following the comparison of the perovskites, a series of $NiCo_2O_4$ spinel samples were modified by substitution of either the A or B site with transition metals. This was carried out to determine if the oxygen activity has a dependence upon the affinity towards oxygen and overall oxidation state of the sample.

The addition of nickel to a cobalt spinel already presents a significant improvement in the ORR and OER overpotentials, as seen in chapter 3. Theoretical studies suggest the improvement in activity can, in part, be due to the presence of Co^{3+} on surface sites of the β-CoOOH.[27] Physical characterisation of the $NiCo_2O_4$ have suggested the structure is complex, with a mixture of oxidation states for the nickel and cobalt distributed in both the octahedral and tetrahedral sites.[28-31] The enrichment of the surface structure with nickel was not accounted for in the theoretical model, neither was the complex distribution of the cations in the structure observed from the neutron, magnetisation, XPS and EXAFS results. The physical characterisation was carried out ex-situ and as such is not able to demonstrate how the surface may change in the presence of strong alkali electrolyte. Current understanding of the catalytic species in the spinel is limited by direct measurements during operation. The percentage of nickel doping has also been linked to the number of electrons in the ORR, with an optimal nickel composition between $0.8 < x < 1.2$ for $Ni_xCo_{3-x}O_4$.[32] Preparing samples outside of this optimal composition, the ORR produces significantly more hydrogen peroxide.

The composition of the spinel has been varied in the hopes of further improving the activity towards either the ORR or OER. The addition of lithium to Co_3O_4 is reported to promote the oxygen activity.[33-39] Further to this, manganese spinels also have demonstrated excellent ORR activity, but typically result in poor OER overpotentials.[40-45] Copper has also been a popular addition to spinels in an effort to promote the OER.[44,46-48] The increased activity was linked to the strength of the M-O or M-O_2^- bond, which is suggested to be weaker for the copper doped samples than pure Co_3O_4 resulting in a lower overpotential for the OER when using copper doped spinels.[46]

Unlike the perovskites, the electron filling has not been reported as a descriptor for the oxygen activity of spinel electrocatalysts, but the activity appears dependent upon the oxidation state of the surface species. The cobalt is suggested to spontaneously form Co-OOH surface on contact with alkali. The cyclic voltammogram yields an oxidation peak, before the OER occurs and this is likely to be due to a change in the oxidation state of the cobalt species from Co^{3+} to Co^{4+}, with the conversion of the surface Co-OOH to CoO_2.[27,46] The oxidation state has not been measured directly during the OER for either cobalt or nickel, and so the evidence is limited by interpretation of the electrochemical response. The addition of small concentrations of other transition and alkali metals to the spinel may provide a shift in the oxidation state of the active cobalt species on the spinel. This is likely to be observed as a shift in the overpotential towards either the oxygen reduction or evolution reactions.

In this chapter a range of samples were screened for electrochemical activity towards the ORR and OER. These samples include a number of substituted perovskites and spinels. The results were used to identify the composition that achieves the lowest potential gap between the ORR and OER.

6.2 Methods

6.2.1 Catalyst synthesis

Electrocatalysts were prepared by the following general methods, with the metal composition varied to produce the desired stoichiometric ratio.

6.2.1.1 Perovskites

$LaNiO_3$, $LaMnO_3$, $LaCa_{0.4}Co_{0.6}O_3$ and $CeNiO_3$ were prepared by thermal decomposition of stoichiometric ratios of metal nitrates dissolved in water. Thermal decomposition was carried out

at 1073K, for a period of four hours. The resulting black powders were ball milled and sieved to < 50 μm before preparation into catalyst inks, as described in section 6.2.3.

6.2.1.2 Spinel – Citric acid synthesis

A modified method reported by Muller et al.[49] and El Baydi et al.[3] was used to prepare the $NiM_xCo_{2-x}O_4$ samples. A solution of $Ni(NO_3)_2.6H_2O$ (2.9079 g), $Co(NO_3)_2.6H_2O$ (5.8206 g) and citric acid (0.5764 g, 0.03 M) were added to 100 mL of water (red solution). The solution was transferred to an evaporating dish and heated (353 K) to dryness (dark red gel). The gel was transferred to a porcelain crucible with a lid and decomposed and calcined at 648 K for four hours. Resulting black powder was ball milled to fine homogenous product. Substituted samples were prepared as outlined above, substituting a stoichiometric molar ratio of cobalt nitrate with the desired metal nitrate salt of Cu, Fe, La, Mn, Ba or Sr.

6.2.2 Physical characterisation

6.2.2.1 SEM-EDX

The elemental composition of samples was determined by SEM-EDX.

Table 39: SEM-EDX analysis results for perovskite samples.

Sample	1st A – site / At. %	2nd A – site / At. %	B – site / At. %
$LaNiO_3$	20.7 ±3.4%	-	11.6 ±5.6%
$CeNiO_3$	17.3 ±4.3%	-	12.1 ±4.8%
$LaMnO_3$	16.7 ±0.4%	-	13.8. ±5.0%
$LaNi_{0.5}Co_{0.5}O_3$	7.4 ±3.3%	6.2 ±5.2%	17.1 ±2.9%
$La_{0.6}Ca_{0.4}CoO_3$	8.2 ±2.4%	7.6 ±2.6%	16.9 ±4.9%
$La_{0.6}Ca_{0.4}NiO_3$	9.1 ±4,6%	6.1 ±5.9%	15.9 ±1.9%
$La_{0.6}Ca_{0.4\,M}nO_3$	14.4 ±7.9%	14.6 ±6.0%	6.1 ±3.4%

Table 40: SEM-EDX analysis results for spinel samples.

Sample	Ni / At. %	Co / At. %	Dopant / At. %
$NiCo_{1.9}Cu_{0.1}O_x$	15.7 ±3.6%	29.7 ±1.7%	0.5 ±28%
$NiCo_{1.9}Fe_{0.1}O_x$	15.4 ±0.2%	31.4 ±2.9%	0.7 ±3.1%
$NiCo_{1.9}La_{0.1}O_x$	15.8 ±0.3%	31.3 ±0.9%	0.9 ±3.2%
$NiCo_{1.9}Mn_{0.1}O_x$	16.4 ±3.8%	32.4 ±2.6%	0.3 ±16%
$NiCo_{1.9}Ba_{0.1}O_x$	20.0 ±1.2%	26.7 ±12%	0.3 ±56%
$NiCo_{1.9}Sr_{0.1}O_x$	24.2 ±1.6%	30.4 ±4.1%	0.4 ±29%

6.2.2.2 XRD

X-ray diffraction results for selected samples confirmed the desired phase of either perovskite or spinel was formed.

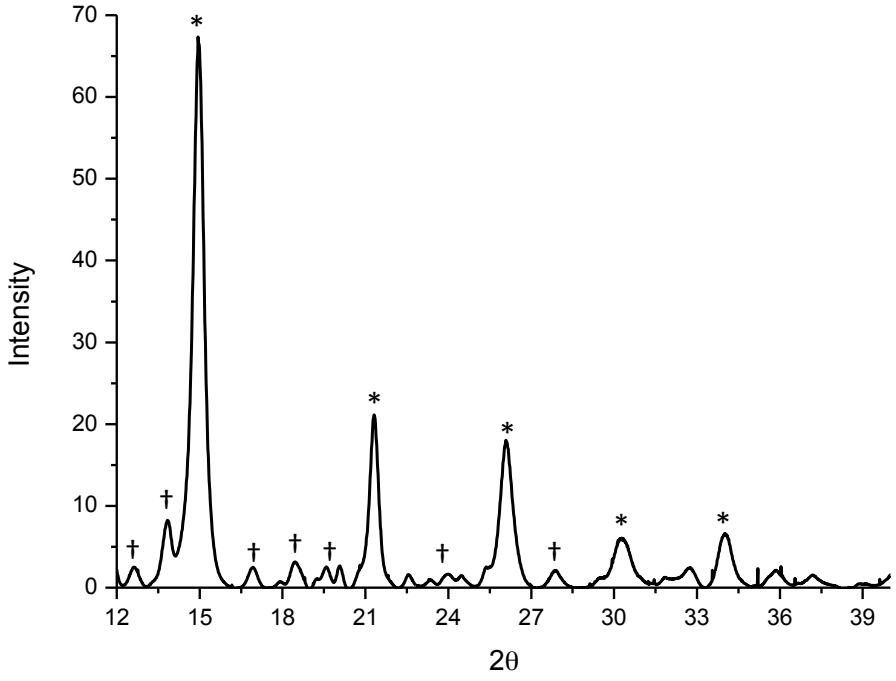

Figure 107: Diffraction pattern for LaNiO3. $LaNiO_3$(*) and trace metal oxide impurities(+).

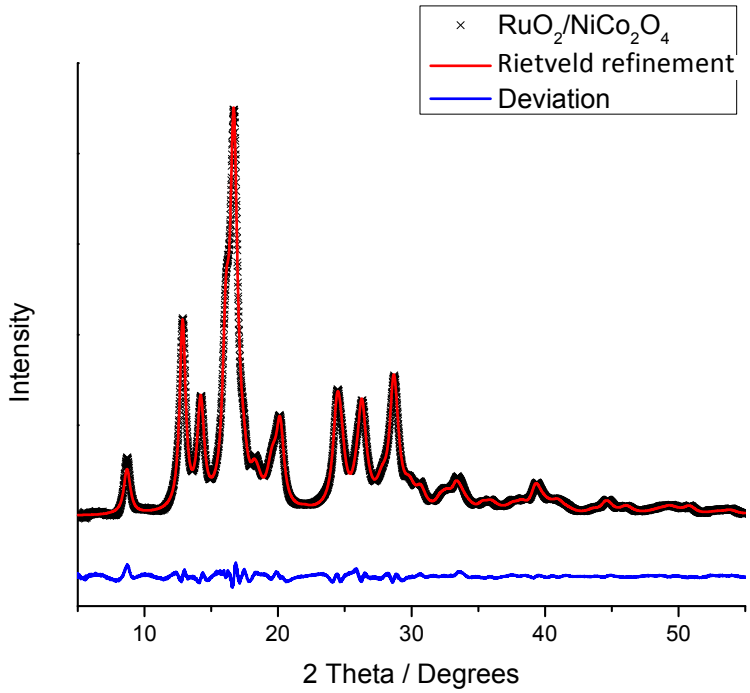

Figure 108: X-ray diffraction patter for $NiCo_2O_4$ after Rietveld fit.

6.2.3 Electrochemical results

For rapid screening of a wide array of potential electrocatalyst materials the rotating disc electrode was used to determine the electrochemical kinetics. Electrodes were prepared as outlined in chapter 2 section 2.3, with electrocatalyst loading of 500 μg cm^{-2}. The increased loading (over the standard 75 μg cm^{-2}) improves coverage of the catalyst film across the GC RDE. The rotation rate of the RDE was maintained at 400 rpm for all steady state measurements. Uncompensated resistance correction and Tafel slope analysis was carried out using a graphical correction method as outlined in chapter 3 section 4.5.1.

Chapter 3 discussed results carried out in 1 M KOH at 298 K. In contrast, the results presented here were obtained in 4 M KOH and the operating temperature increased to 333 K to provide closer approximation to the conditions in a flow-battery. The increase in electrolyte concentration and temperature results in a reduction in the oxygen solubility and lowering of the limiting current. As such, the results are no longer directly quantitatively comparable, although trends can be identified to allow qualitative comparison of the results.

6.3 Results and discussion

6.3.1 Perovskite electrocatalysts

A series of perovskite transition metal oxides, defined by their composition of ABO_3, were prepared to determine the activity towards the oxygen reduction and evolution reactions. The mixture of oxides was selected to isolate a small range of d-electron and e_g filling levels. These two factors have previously been suggested as activity descriptors for perovskite electrocatalysts.[11,17]

6.3.2 Oxygen reduction reaction

Samples were prepared by thermal decomposition methods, as outlined in section 6.2.1, and evaluated for their electrochemical activity towards the ORR using RDE.

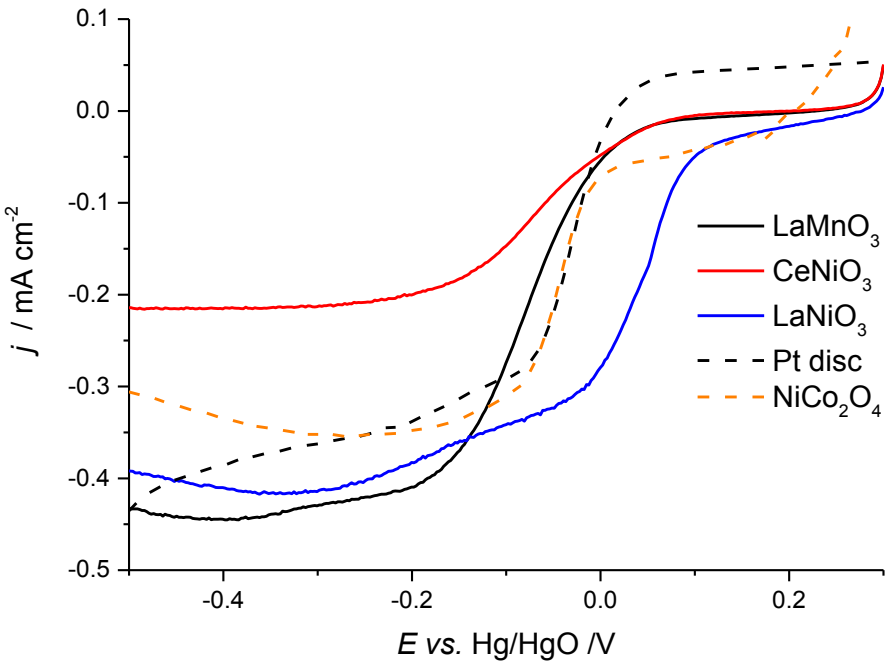

Figure 109: Plot of polarisation curves comparing Perovskite electrocatalysts activity towards the ORR on GC RDE at 400 rpm, in oxygen saturated 4 M KOH at 333 K.

A cathodic linear sweep of the $CeNiO_3$ produces a clear sigmoidal response for the ORR (Figure 109). The polarisation curve initially provides an anodic current when the sweep begins at 0.3 V due to the starting point being positive of the OCP, which rapidly drops to a very small current as the potential shifts negative. A large slope is observed for the kinetically controlled region, before

tailing off with an independent response to further applied overpotential from the mass transport controlled region of the polarisation curve.

The onset potential, slope and limiting current were found to be variable, depending upon the perovskite composition (Figure 109). Previous studies on $LaNiO_3$ and $LaMnO_3$ suggest they catalyse the ORR to form hydroxide, with a near 4-electron transfer.[50] The limiting current of approximately 0.4 mA cm^{-2} attained by both the $LaNiO_3$ and $LaMnO_3$ would agree with this representing the 4-electron transfer limiting current.

The $CeMnO_3$ sample yields a limiting current half that of the other two perovskites, of approximately 0.2 mA cm^{-2}. This would suggest either the reaction is inhibited in some way, with an extremely slow chemical step, or the number of electrons in the reaction have been reduced by a factor of two. A rotation rate dependent study with rotating ring-disc electrodes would provide proof of any hydrogen peroxide generated on $CeMnO_3$ during the ORR. Although this was not completed owing to time constraints.

A slight oscillation is visible in the limiting current response. This is attributed to a small concentration of oxygen in the catalyst layer formed on the RDE. The solution was purged with oxygen for a minimum of 15 minutes before measurements; in this time oxygen can be trapped on the electrode, producing a non-linear response, where by the additional overpotential allows further reduction of trapped oxygen. For this reason the limiting current is typically derived from the value at -0.5V, where the effect is least contributing.

The ORR on $LaNiO_3$ occurs at potentials positive of that for the $LaMnO_3$, demonstrating the importance of the metal in the B-site of the perovskite. The high activity of $LaNiO_3$ has previously been reported when prepared in gas diffusion electrodes[4] and on RDE[17] where even samples with low surface areas (0.1-5 m^2 g^{-1}) were capable of operating at high currents with low overpotentials.

6.3.2.1 Perovskite dopants

To elucidate the effect that the electronic structure has on the perovskite activity, a series of samples were produced based upon manganese, cobalt and nickel on the B-site. A baseline was established with the A-site occupied by lanthanum. The electronic structure was then modified by the addition of calcium into the A-site, which will be balanced by a change to the oxidation state of the B-site transition metal.

The addition of Ca^{2+} into the predominantly La^{3+} A-site produces a corresponding increase in the Co oxidation state from Co^{3+} to a mixture of Co^{3+} and Co^{4+}. This trend is not quite a linear

relationship, suggesting oxygen vacancies further reduce the need for Co^{4+}.[51] A similar relationship was observed for Sr-doped $La_{1-x}Sr_xCoO_3$ perovskite with the cobalt accounting for the majority of the change in oxidation state, with a small portion caused by oxygen deficiencies.[52,53]

To utilise the known shifts in the oxidation state of B-site metal, $La_{0.6}Ca_{0.4\ M}O_3$ (M=Mn, Co, Ni) were combined with the non-doped versions to provide a range of electrons filling the d-band. The $LaMO_3$ provides samples with d-electrons ranging 4,6 and 7.[23] Extrapolating from Mastin et. al.[51], the addition of calcium produces a reduction of 0.3 in the B-site atoms' oxidation state. Applying the shift in oxidation state for all modified samples, the number of electrons in the d-band is 3.7, 5.7, and 6.7 for the Mn, Co, and Ni samples, respectively.

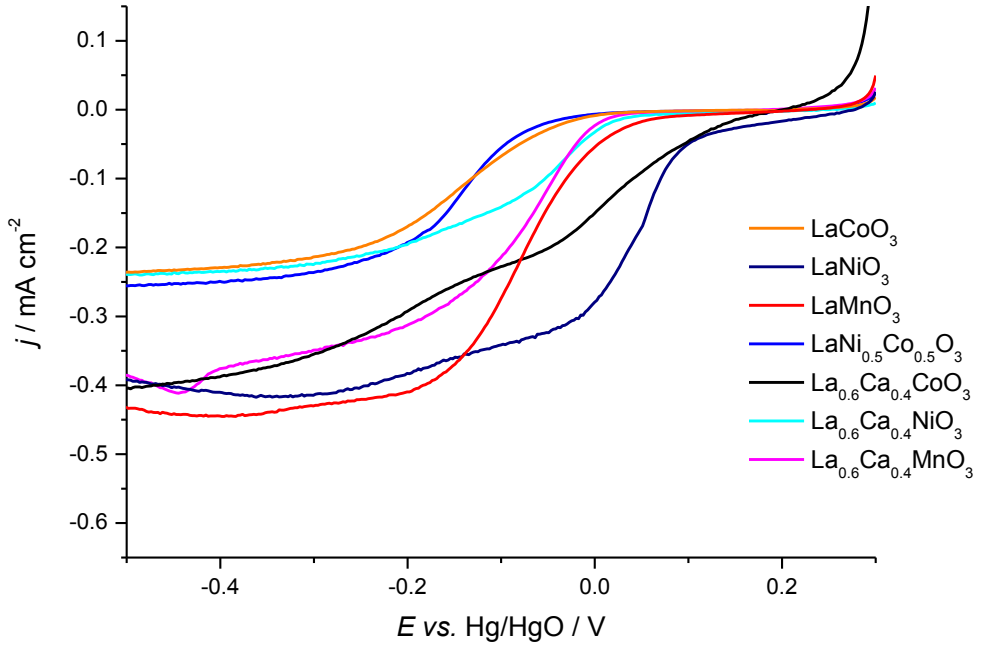

Figure 110: Plot of the polarisation curve of oxygen reduction for doped perovskite samples, on GC RDE, in oxygen saturated 4 M KOH at 333 K.

The electrochemical responses from polarisation curves for the prepared samples are presented in Figure 110. A clear sigmoidal curve is observed for all samples. A double wave is observed for the $La_{0.4}Ca_{0.6}CoO_3$, this unusual response may mark a shift in the mechanism of the ORR for this sample but without another electrochemical technique, such as rotating ring-disc measurements, it is not possible to discern any specific change in the oxygen reduction reaction. A sharp slope is observed in the polarisation curve corresponding to the onset of the oxygen reduction reaction, followed by a shift in the gradient of the slope, before a plateau region for the limiting current

independent of overpotential is observed. For the purpose of screening the samples the potential required to achieve a current of -50 μA cm^{-2} was compared (Figure 111).

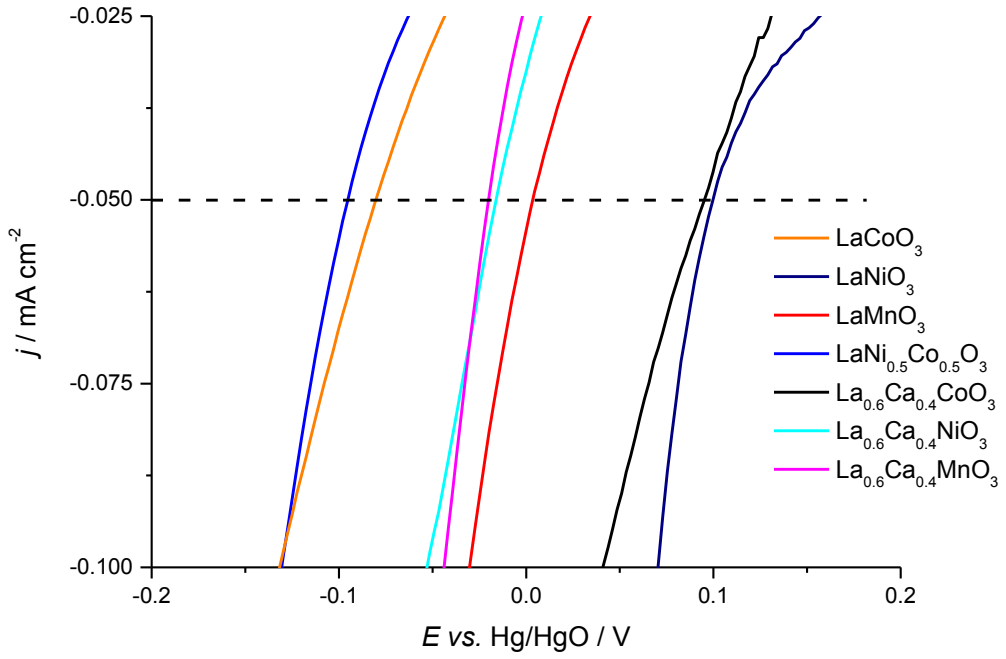

Figure 111: Plot of potential sweeps for the ORR on various perovskite electrocatalysts. Carried out in oxygen saturated 4 M KOH at 333 K.

As with previous studies[4,9,49,54] the $LaNiO_3$ and $La_{0.6}Ca_{0.4}CoO_3$ samples demonstrate high activity towards the ORR, with the lowest overpotential for the ORR of the perovskite samples tested in this study. The highest overpotentials are associated with the $LaCoO_4$ and $LaNi_{0.5}Co_{0.5}O_3$ samples.

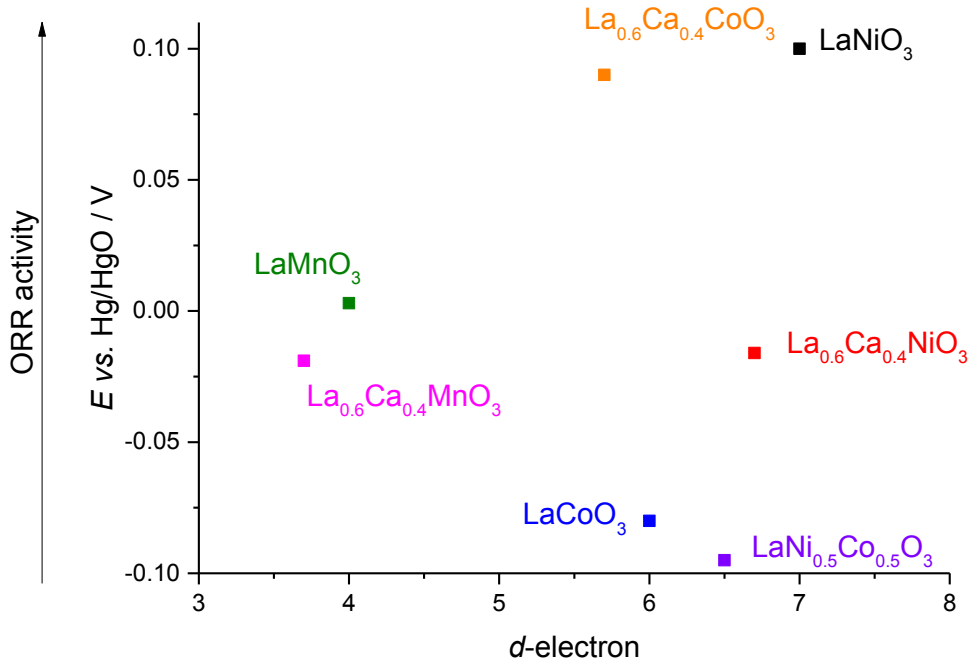

Figure 112: Measure of ORR activity. Plot of potential at -50 μA cm^{-2} as a function of d-electron filling for perovskite samples on GC RDE at 400 rpm in oxygen saturated 4 M KOH, 333 K.

Previous work has suggested a trend in the activity of the perovskite with the number of d-electrons or e_g filling level (shown in Figure 113).[9,17,26,55] These reports would propose the $LaMnO_3$ and $LaNiO_3$ are able to catalyse the ORR with the lowest overpotentials. The overpotential at -50 μA cm^{-2} as a function of the number of d-electrons for samples prepared in this work are plotted in Figure 112. There is no apparent simple relationship between d-electron filling and the mass activity of the perovskite samples presented here. Therefore, it is possible the d-electron filling is not a descriptor for ORR activity for perovskites.

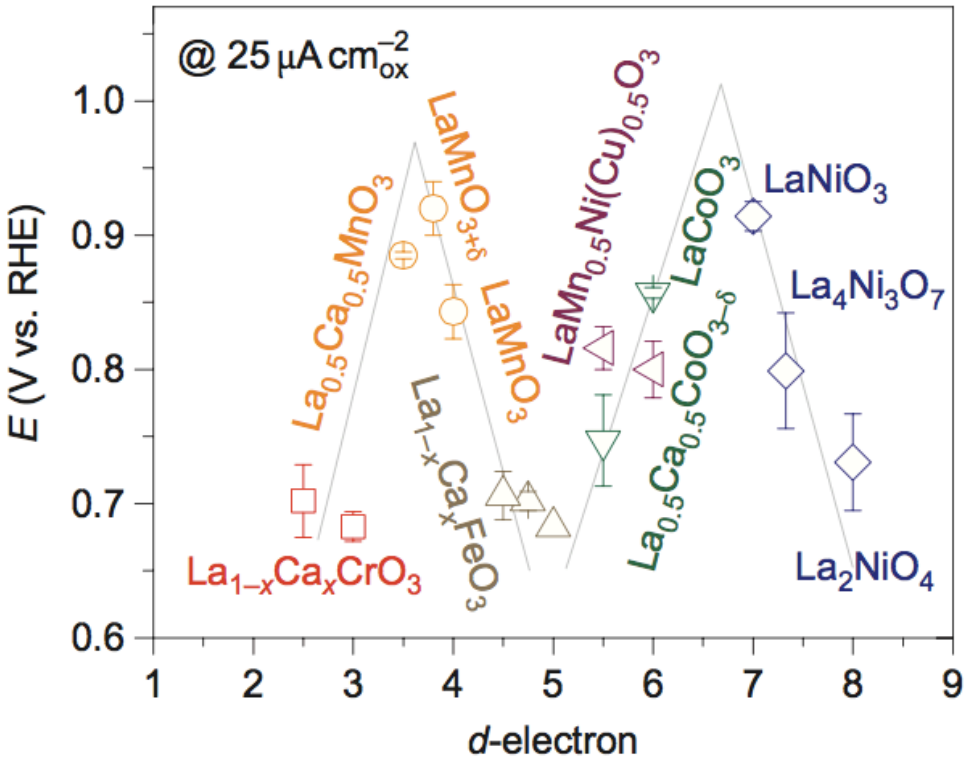

Figure 113: Plot of potential to achieve 25 μA cm^2 against the number of d-electrons in the transition metal cation in the perovskite catalyst.[6]

A comparison with e_g filling levels is also unlikely to reveal a simple trend as the $LaMnO_3$ ($t_{2g}^3 e_g^1$), $LaCoO_3$ ($t_{2g}^5 e_g^1$) and $LaNiO_3$ ($t_{2g}^6 e_g^1$), all provide the same e_g filling level, but require dissimilar overpotentials for the ORR. The addition of the calcium to each structure results in a reduction of the e_g filling for all samples by 0.3 electrons. However, the $La_{0.6}Ca_{0.4}MnO_3$ and $La_{0.6}Ca_{0.4}NiO_3$ result in an increase in overpotential and $La_{0.6}Ca_{0.4}CoO_3$ reduces the overpotential by >100 mV when compared to the non-doped samples. The results do not correlate with the e_g filling level; therefore it is likely another factor is affecting the catalytic activity.

The results in this work are based upon the mass activity of the electrocatalyst. It is therefore likely the surface area is different between samples, resulting in no discernible trend in the catalysts activity. It is possible to normalise the electrochemical response for the surface areas of electrocatalysts using BET measurements, if only the physical surface area is considered. An alternative electrochemical method uses the linear response between capacitance of the double layer with various scan rates to calculate the surface area of the sample. As the scan rate is increased, so too does the measured double layer current which can be used to determine the capacitance of the layer (Equation 33).[56] This can be converted to an approximate area by use of a reference value, typically C^*= 60 μF cm^{-2} for mixed metal oxides (Equation 34).[9]

Equation 33

$$C = \frac{dQ}{dE} = \frac{idt}{dE} = \frac{i}{(dE/dt)}$$

Equation 34

$$Area = C/C^*$$

In results from the literature the current was normalised for physical surface area, as determined by SEM and BET.[17] Although the results suggest an approximate error to the area as a factor of 3 and the error of mass loading as a factor of 2, these measurements have not accounted for electrochemical surface area. In addition, the surface areas determined by BET are on the order of 0.1 – 5 $m^2 g^{-1}$, which is lower than the 10 – 30 $m^2 g^{-1}$ for samples prepared in this work. These two factors would suggest the results are not directly comparable and may account for the difference in catalyst activity.

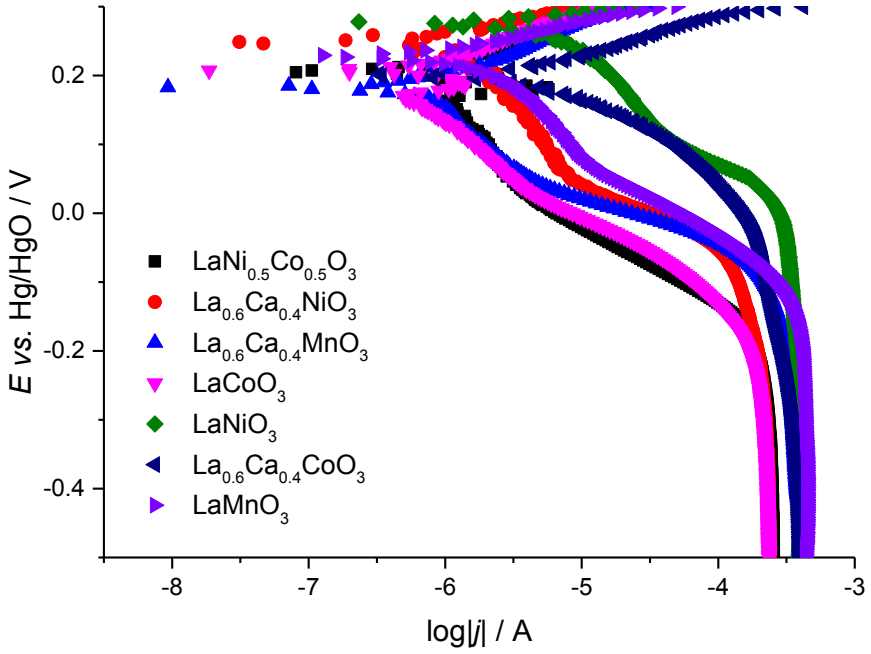

Figure 114: Tafel plots of the ORR on perovskite electrocatalysts in 4 M KOH at 333 K.

The Tafel slope for the perovskite samples, shown in Figure 114, was found to vary significantly from 60 to 110 mV dec^{-1}. Such a shift in the slope likely indicates a change to the RDS in the ORR mechanism. Lower Tafel slopes coincided with the addition of calcium into the perovskite and also for the $LaNiO_3$ sample.

Table 41: Comparison of perovskite transition metal oxides activity for the ORR.

Sample	ORR at -50 μA cm^{-2} / mV	Tafel slope / mV dec^{-1}	j_L @ -500 mV / mA cm^{-2}
Pt	-5	-43	-0.43
$NiCo_2O_4$	-15	-94	-0.31
$LaCoO_3$	-80	-110	-0.24
$LaNiO_3$	100	-90	-0.39
$LaMnO_3$	3	-100	-0.43
$LaNi_{0.5}Co_{0.5}O_3$	-95	-110	-0.26
$La_{0.6}Ca_{0.4}CoO_3$	90	-97	-0.40
$La_{0.6}Ca_{0.4}NiO_3$	-16	-81	-0.24
$La_{0.6}Ca_{0.4\ M}nO_3$	-19	-61	-0.39

6.3.3 Oxygen evolution

The oxygen evolution reaction is highly influenced by the composition of the electrocatalyst, as shown in Figure 115.

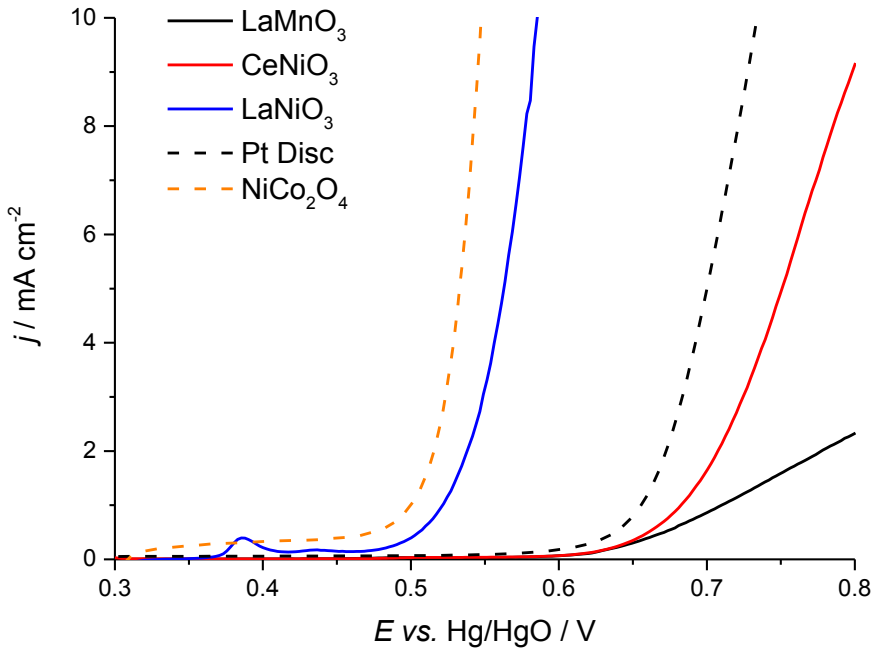

Figure 115: Plot of polarisation curves for the OER on ABO_3 perovskite electrocatalysts in oxygen saturated 4 M KOH at 333 K.

The electrochemical response for the transition metal oxide perovskite electrocatalysts in alkali electrolyte is consistent for all samples. The voltammogram yields an initial response independent of the overpotential, followed by exponential rise in the current correlating with the OER. A small peak is observed for the $LaNiO_3$ sample at approximately +385 mV and is attributed to a small NiO impurity present in the sample producing a Ni^{2+} to Ni^{3+} oxidation.

The $LaMnO_3$ requires a larger overpotential to drive the oxygen evolution reaction (Table 42). The previously poor ORR electrocatalyst $CeNiO_3$ achieves a four-fold increase in current at 800 mV when compared to $LaMnO_3$. This shift in current highlights the affinity some catalysts can demonstrate towards either the ORR or OER. The onset for both samples is >100 mV positive of that achieved by $LaNiO_3$.

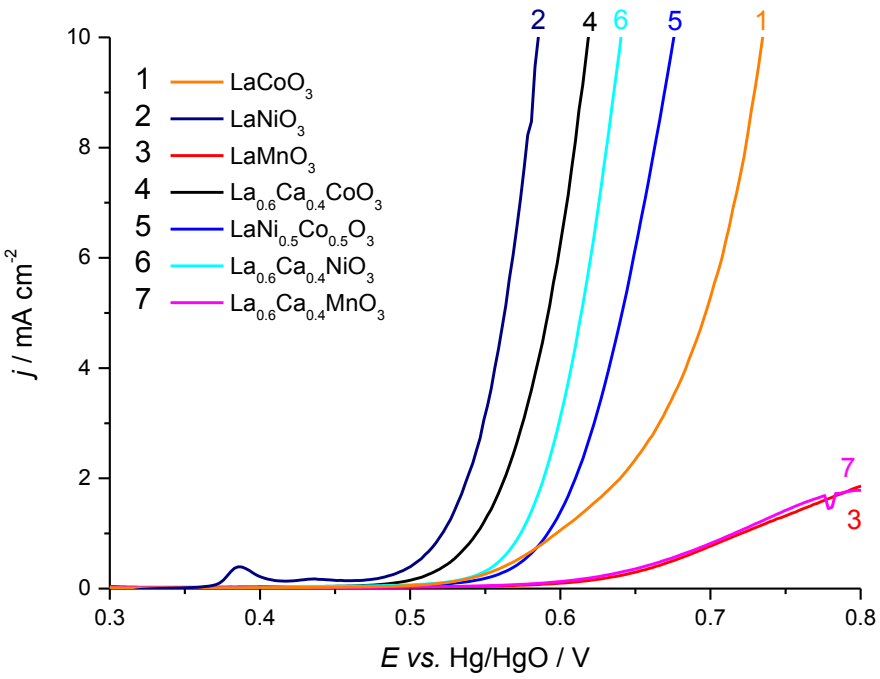

Figure 116: Plot of the polarisation curves to study the OER on perovskite electrocatalysts on GC RDE at 400 rpm, in oxygen saturated 4 M KOH at 333 K.

The substitution of metal dopants into the structure has already been considered as a source of variation for the oxidation state of the B-site metal during the ORR study. This same variation in the oxidation state provides a strong influence on the OER activity (Figure 116). The samples with manganese on the B-site demonstrated relatively poor performance, with a large overpotential (>800 mV *vs.* Hg/HgO) required to achieve 10 mA cm^{-2}. Samples containing cobalt and nickel generally required significantly lower overpotential for the OER. The lowest overpotential for the OER was observed for the $LaNiO_3$, achieving 10 mA cm^{-2} at 577 mV.

The substitution of calcium in place of cobalt in the perovskite sample must be balanced by an equal increase of Co^{4+} in the structure. This is likely to be beneficial as the Co^{4+} is believed to be an active site for the OER. The substitution of calcium in place of the nickel in the $La_{0.6}Ca_{0.4}NiO_3$ appears to result in a reduction in the OER activity. This shift in activity with substitution, may be due to a change in electrochemical surface area of the sample or potentially a change in the rate determining step.

If the rate determining step for the reaction changes, depending on the composition of the sample, it should coincide with a change in the Tafel slope. A Tafel slope of 60 (±10) mV dec^{-1} was cfound for the majority of the perovskite samples (Table 42). The samples with manganese yield

Tafel slopes of ~110 mV dec^{-1}, and this would suggest a change in the mechanism for the OER. The spinel catalyses the OER at an overpotential of 547 mV compared to the $LaNiO_3$ 577 mV.

Table 42: Comparison of OER performance and Tafel slope of perovskite electrocatalysts on GC RDE in oxygen saturated 4 M KOH at 333 K.

Catalyst	*E vs.* Hg/HgO at J = 10 mA cm^{-2} / mV iR corrected	Tafel slope / mV dec^{-1}
Pt- disc	714	58
$NiCo_2O_4$	547	46
$LaCoO_3$	651	58
$LaNiO_3$	577	56
$LaMnO_3$	809	104
$LaNi_{0.5}Co_{0.5}O_3$	656	61
$La_{0.6}Ca_{0.4}CoO_3$	602	56
$La_{0.6}Ca_{0.4}NiO_3$	623	49
$La_{0.6}Ca_{0.4\ M}nO_3$	810	111

6.4 Modification of the $NiCo_{2-x}M_xO_4$

In the case of the perovskite transition metal oxides, modifications of the oxidation state to the B-site were possible through replacement of the A-site with alkali metals and the localisation of the electrons in the structure. The spinel, however, is believed to operate with a greater delocalisation of the electrons. The delocalisation of electrons is proposed through the Co t_{2g} and Ni e_g bands, possible with a suggested structure combining equal amounts of $Co^{3+}\left(t_{2g}^4 e_g^2\right)/Ni^{3+}\left(t_{2g}^6 e_g^1\right)$ and $Co^{2+}\left(t_{2g}^5 e_g^2\right)/Ni^{4+}\left(t_{2g}^6 e_g^0\right)$ in the octahedral site[30], however, it is unusual to have the both Co^{3+}/Ni^{3+} and Co^{2+}/Ni^{4+} in the same crystal structure.

This sharing of electron density in the d-band of the octahedral site complicates the possible effect of doping the spinel with other metals. Several studies have already demonstrated the activity of the spinel to fall rapidly as you deviate from the ideal metal ratios.[32] This could be

explained by the previous suggestion of a delocalised structure easily disrupted through the addition of other metals in to the structure.

The substitution of small concentrations of metals for the cobalt, $NiCo_{2-x}M_xO_4$ (M= Mn, Fe, Cu, La; x=0.1), was evaluated. The oxygen reduction reaction appears mostly independent of the effect of doping (Figure 117). At low currents (-50 μA cm-2), the required overpotential for the lanthanum doped sample is 2 mV *vs.* Hg/HgO, with the transition metal dopants ranging -12 to -14 mV.

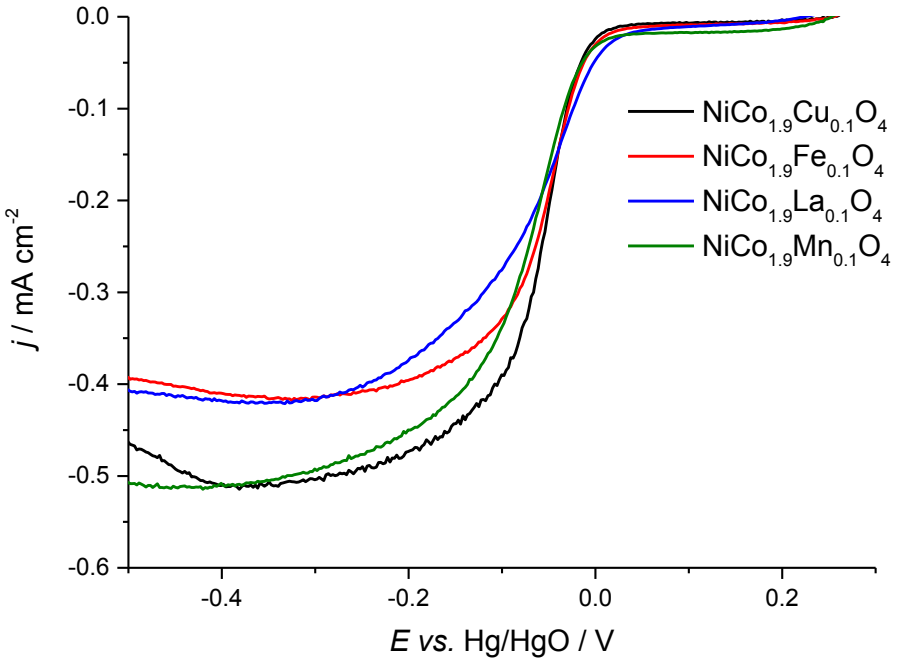

Figure 117: Plot of the polarisation curve for the ORR of $NiCo_{1.9}M_{0.1}O_4$ (M=Cu,Fe,La,Mn) on GC RDE at 400 rpm in oxygen saturated 4 M KOH at 333 K.

The current measured at the half wave potential, $E_{1/2}$, demonstrates a different trend, where the addition of iron and copper resulted in a slightly reduced overpotential. The difference in the polarisation curves is well within the error, typically in the range of ±10 mV, of measurements on these samples. The Tafel slope does correspond with this observation, whereby the lowest slope was observed for the copper doped sample. The Tafel slope increased with dopants Cu<Fe<Mn<La, rising from approximately 50 to 70 mV dec^{-1}. This shift in Tafel slope would suggest the addition of the dopants is affecting the spinel activity.

Table 43: Comparison of ORR activity on doped spinel samples.

Sample	$E_{\frac{1}{2}}$ / V	E @ -0.2 mA cm^{-2} / V	Tafel slope / mV dec^{-1}
$NiCo_{1.9}Cu_{0.1}O_x$	-0.058	-0.049	-48
$NiCo_{1.9}Fe_{0.1}O_x$	-0.053	-0.052	-55
$NiCo_{1.9}La_{0.1}O_x$	-0.064	-0.060	-71
$NiCo_{1.9}Mn_{0.1}O_x$	-0.072	-0.059	-67

The oxygen evolution reaction is influenced by the effect of the doping to a greater degree. The polarisation curves (Figure 118), would suggest the addition of iron provides a greater activity than the other metals tested. The response is distorted at higher currents by oxygen gas bubble formation on the surface of the electrode and the growing influence of iR drop.

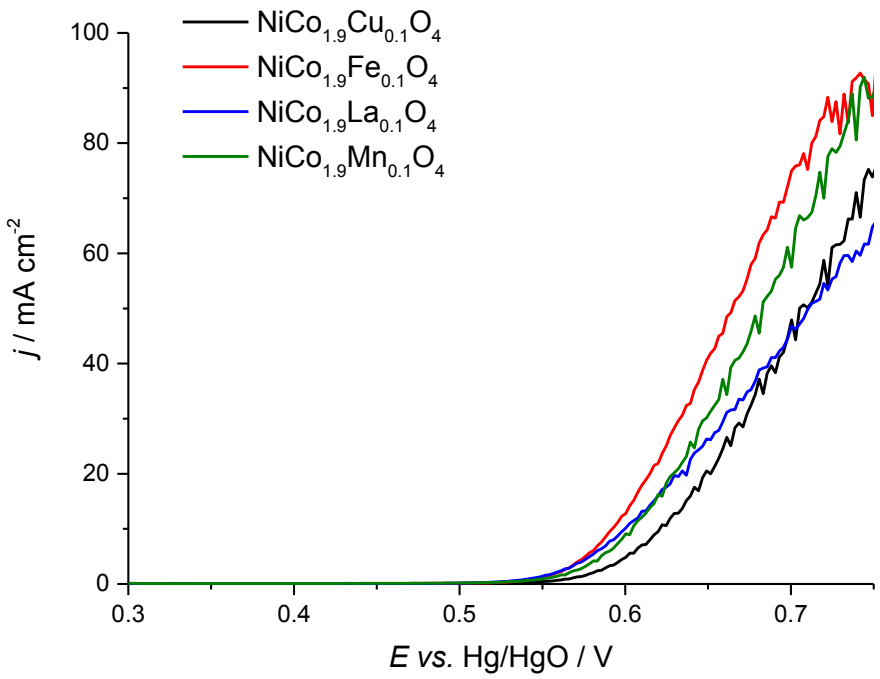

Figure 118: Polarisation curve for the oxygen evolution on $NiCo_{1.9}M_{0.1}O_4$ (M = Mn, Fe, Cu, La) on GC RDE at 400 rpm, in oxygen saturated 4 M KOH at 333 K.

Analysis of the Tafel slope yields a value of 40 (±10) mV dec^{-1} for all samples. A minor shift in the mechanism could be suggested from the rising Tafel slope for the least active lanthanum and

manganese samples. The pure $NiCo_2O_4$ achieved a Tafel slope of 40 mV dec^{-1}, suggesting a similar mechanism is maintained until the addition of the dopant produces a change.

Table 44: Comparison of $NiCo_{1.9}M_{0.1}O_4$ (M = Mn, Fe, Cu, La) towards the OER.

Catalyst	*E vs.* Hg/HgO at *J* = 10 mA cm^{-2} / mV iR corrected	Tafel slope / mV dec^{-1}
$NiCo_{1.9}Cu_{0.1}O_x$	642	44
$NiCo_{1.9}Fe_{0.1}O_x$	614	39
$NiCo_{1.9}La_{0.1}O_x$	624	47
$NiCo_{1.9}Mn_{0.1}O_x$	636	50

The addition of transition metals and lanthanides into the structure provides a mixture of possible oxidation states for the transition metals. The degree to which they can interact with the nickel and cobalt d-electrons and the occupancy of the octahedral site is unclear without further neutron diffraction and magnetic moment measurements to determine the site occupancy and relative spin states to determine the oxidation state for the nickel and cobalt cations.[28,57] The addition of alkali metals will reduce the variable oxidation states attained in the structure. This study considers the resulting electrochemical activity towards the oxygen evolution and reduction reactions from doping the spinel with lithium, barium and strontium.

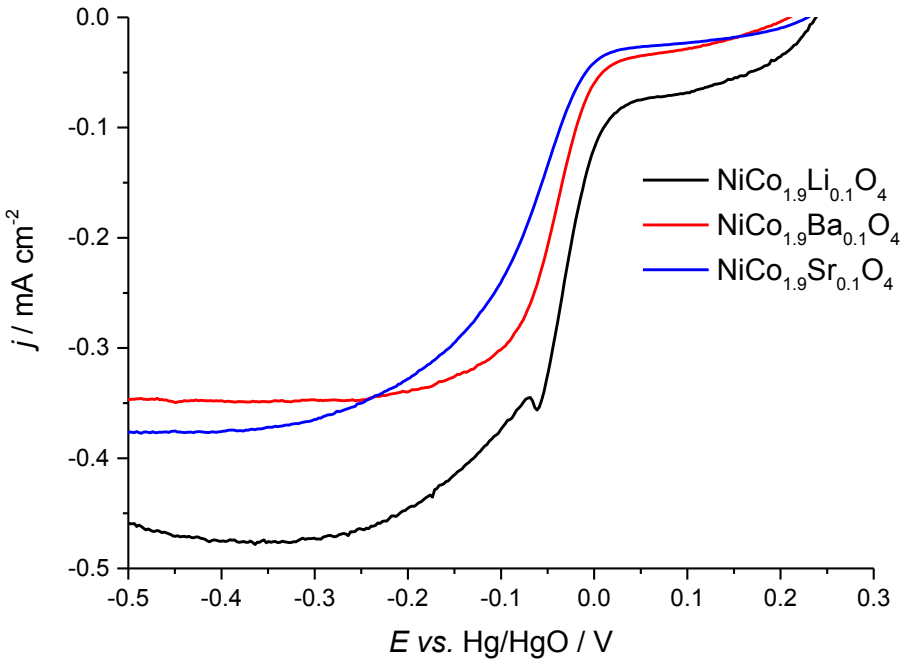

Figure 119: Plot of the polarisation curve for alkali metal doped-spinel on GC RDE at 400 rpm to study the ORR, in oxygen saturated 4 M KOH at 333 K.

The electrochemical response for the alkali metal doped samples in oxygen saturated KOH achieves sigmoidal curves. The sample with lithium consists of significant negative current, increasing from the point of the open circuit potential. In addition a small peak appears during the ORR wave (Figure 119). This peak, at approximately 50 mV during the ORR, reduces in subsequent polarisation curves. The reduction in current from the peak with cycling would suggest the process is irreversible and incompatible with the ORR. As the spinel is known to be stable and absent of peaks in this region the lithium therefore is suggested to be unstable in the structure and the peak current is attributed to reduction and dissolution of lithium from the structure. The size of the lithium is likely limiting the stability of this particular sample during the ORR.

Table 45: Comparison of ORR activity of $NiCo_{2-x}M_xO_4$ on GC RDE in 4 M KOH at 333 K.

Sample	$E_{\frac{1}{2}}$ / V	E @ -0.2 mA cm^{-2} / V	Tafel slope / mV dec^{-1}
$NiCo_{1.9}Li_{0.1}O_x$	-0.023	-0.024	-106
$NiCo_{1.9}Ba_{0.1}O_x$	-0.041	-0.049	-87
$NiCo_{1.9}Sr_{0.1}O_x$	-0.080	-0.078	-96

The barium and strontium doped spinel do not produce a peak during the ORR polarisation curve, suggesting they may offer improved stability over the lithium-doped sample. The sigmoidal

response is consistent with that of the pure spinel and the previous transition metal doped spinel. A plateau region is consistent with previous measurements. The magnitude of the limiting current is lower than that of $NiCo_2O_4$ (-0.31 mA cm^{-2}) and the Pt-disc electrode (-0.43 mA cm^{-2}).

The Tafel slope for all the alkali metal samples was found to be 100 mV dec^{-1}. This result is significantly higher than 40 mV dec^{-1} for the pure Co_3O_4 and $NiCo_2O_4$ spinel. The Tafel slope and higher overpotential towards the ORR are consistent with the spinel sample with a manganese dopant. Assuming the effect of alkali metal dopants is to increase the oxidation state of the Ni or Co active surface sites, this would suggest a lowering of the d-electrons in the structure produces a negative shift for the ORR.

The oxygen evolution reaction appears with similar electrochemical response to that of previous samples. A negligible current is observed in the linear sweep from 0.3 V to the onset of the reaction, denoted by a sharp rise in the current. The current grows exponentially, until a linear response is observed (Figure 120). The addition of lithium and barium in place of the cobalt in the spinel is likely to promote the formation of Co^{4+} in the structure. There is no clear difference between the activity for these two samples, suggesting the Co on the surface is not strongly affected by the addition of the alkali metals or the OER is not influenced by the subtle changes to the oxidation state, but once in solution the surface is remodelled further. The addition of strontium however results in an increased overpotential of 636 mV compared with an approx. 615 mV for the lithium and barium samples, to achieve 10 mA cm^{-2}.

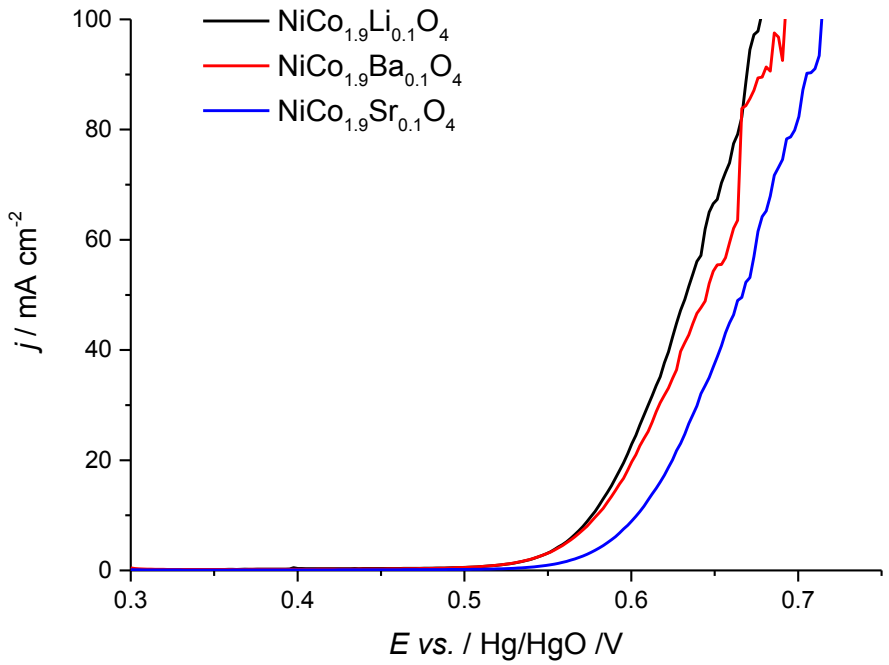

Figure 120: Polarisation curve of the OER for alkali metal doped-spinel on GC RDE at 400 rpm, in oxygen saturated 4 M KOH at 333 K.

The Tafel slopes for the alkali doped spinels are 50 mV ± 10 mV. The pure $NiCo_2O_4$ sample typically achieves 40 mV ± 10 mV, suggesting the mechanism may have undergone a slight shift in the RDS, but further evidence is required to confirm if a change has truly occurred. The addition of alkali metals are unlikely to have caused a significant shift in the reaction mechanism, but was hoped to provide an increased number of Co^{4+} sites believed to be active for the OER.

Table 46: Comparison of oxygen evolution activity of $NiCo_{2-x}M_xO_4$ on GC RDE in 4 M KOH at 333 K.

Catalyst	*E vs.* Hg/HgO at *J* = 10 mA cm^{-2} / mV (iR corrected)	Tafel slope / mV dec^{-1}
TD - Co_3O_4	654	45
Sol-gel - Co_3O_4	639	44
$NiCo_{1.9}Li_{0.1}O_x$	614	53
$NiCo_{1.9}Ba_{0.1}O_x$	617	56
$NiCo_{1.9}Sr_{0.1}O_x$	636	50

6.5 Conclusion

This chapter has confirmed that the modification of perovskite composition is able to strongly influence the activity. The literature suggests the localisation of electrons in the perovskite as a suitable explanation for the effect of the doping. This shift in oxidation state of the sample is believed to be a key parameter determining the intrinsic activity of these electrocatalysts.

When these materials are transferred from thin-film RDE electrodes into gas diffusion electrodes the intrinsic activity is no longer the critical measure of performance. High surface area samples may provide a lower intrinsic activity, but can provide a higher mass activity. For commercial applications the gas diffusion electrode will be considered in terms of catalyst loading by mass and overpotential required to achieve a desired current density. Using this measure, the $LaNiO_3$ and $La_{0.6}Ca_{0.4}CoO_3$ provide the greatest activity of the perovskite samples evaluated.

The modification of the spinel was found to provide only a minimal shift in the activity of both the oxygen reduction and evolution reactions. The doping of transition and alkali metals into the $NiCo_2O_4$ yields a detrimental effect on the activity. The $NiCo_2O_4$ itself has been identified as having an 'optimal' composition between $Ni_xCo_{3-x}O_4$ $0.4<x<1.2$, and beyond these limits not only does the activity reduce, but so does the number of electrons in the ORR reaction.[32] It is possible the addition of the nickel is providing the necessary optimisation of the cobalt surface sites. As all transition metal ternary-modifications fall within the 0.4 – 1.2 range they achieve similar results for low concentrations of doping. Increasing the metal dopant concentration in the spinel may

provide greater deviation in the oxygen activity and enable one to discern if any further improvements are possible.

The addition of lithium to the $NiCo_2O_4$ produces a small improvement to the OER overpotential of 20 mV. During the ORR, the sample yields a sharp peak that reduces with subsequent cycling. This is believed to be the dissolution of lithium from the structure, and was found to be absent for barium and strontium dopants. The relativelly small size of the lithium is a likely reason for the different response to the other alkali metals.

To further develop the spinel, the dopant concentrations should be increased. The electrochemical surface area should be considered, when determining the intrinsic catalytic performance. However, the mass activity is also a necessity when evaluating electrocatalysts and should hold equal weighting when comparing electrocatalysts. The generation of hydrogen peroxide should be determined for all samples.

The spinel presents high surface area (>50 $m^2 g^{-1}$) electrocatalysts, whereas the perovskite samples are limited to <20$m^2 g^{-1}$. This is a combination of the heavy elements in the composition, as well as the relatively dense crystal structure, when compared to the spinel.

6.6 References

(1) Bockris, J. O.; Otagawa, T. *Journal of the Electrochemical Society*. February 1, 1984, pp 290–302.

(2) Takahashi, J.; Toyoda, T.; Ito, T.; Takatsu, M. *Journal of Materials Science*. Kluwer Academic Publishers March 1, 1990, pp 1557–1562.

(3) Baydi, El, M.; Tiwari, S.; Singh, R.; Rehspringer, J.; Chartier, P.; Koenig, J.; Poillerat, G. *Journal of Solid State Chemistry*. 1995, pp 157–169.

(4) Bursell, M.; Pirjamali, M.; Kiros, Y. *Electrochimica Acta*. 2002, pp 1651–1660.

(5) Yuasa, M.; Nishida, M.; Kida, T.; Yamazoe, N.; Shimanoe, K. *Journal of the Electrochemical Society*. The Electrochemical Society May 1, 2011, pp A605–A610.

(6) Suntivich, J.; Gasteiger, H. A.; Yabuuchi, N.; Nakanishi, H.; Goodenough, J. B.; Shao-Horn, Y. *Nature chemistry*. Nature Publishing Group July 1, 2011, pp 546–550.

(7) Bockris, J. O.; Srinivasan, S. *Journal of Electroanalytical Chemistry (1959)*. May 1, 1966, pp 350–389.

(8) Matsumoto, Y.; Yoneyama, H.; Tamura, H. *Journal of electroanalytical chemistry and interfacial electrochemistry*. October 1, 1977, pp 167–176.

(9) Bockris, J. O.; Otagawa, T. *Journal of the Electrochemical Society*. January 1, 1984, pp 290–302.

(10) Goodenough, J. B.; Zhou, J. S. *Chemistry of Materials*. American Chemical Society October 2, 1998, pp 2980–2993.

(11) Goodenough, J. B.; Cushing, B. L. *Oxide-based ORR catalysts*; John Wiley & Sons, Ltd: Chichester, UK, 2010.

(12) Peña, M. A.; Fierro, J. L. G. *Chemical Reviews*. American Chemical Society May 31, 2001, pp 1981–2018.

(13) Hyodo, T.; Hayashi, M.; Miura, N.; Yamazoe, N. *Journal of the Electrochemical Society*. The Electrochemical Society November 1, 1996, pp L266–L267.

(14) Hyodo, T.; Hayashi, M.; Mitsutake, S.; Miura, N.; Yamazoe, N. *Journal of Applied Electrochemistry*. 1997, pp 745–746.

(15) Matsumoto, Y.; Sato, E. *Materials Chemistry and Physics*. May 1986, pp 397–426.

(16) Suntivich, J.; May, K. J.; Gasteiger, H. A.; Goodenough, J. B.; Shao-Horn, Y. *Science*. 2011, pp 1383–1385.

(17) Suntivich, J.; Gasteiger, H. A.; Yabuuchi, N.; Nakanishi, H.; Goodenough, J. B.; Shao-Horn, Y. *Nature chemistry*. July 2011, pp 546–550.

(18) Miyahara, Y.; Miyazaki, K.; Fukutsuka, T.; Abe, T. *Journal of the Electrochemical Society*. The Electrochemical Society January 1, 2014, pp F694–F697.

(19) Fabbri, E.; Mohamed, R.; Levecque, P.; Conrad, O.; Kötz, R.; Schmidt, T. J. *ACS Catalysis*. American Chemical Society March 3, 2014, pp 1061–1070.

(20) Hardin, W. G.; Slanac, D. A.; Wang, X.; Dai, S.; Johnston, K. P.; Stevenson, K. J. *Journal of*

Physical Chemistry Letters. American Chemical Society January 7, 2013, pp 1254–1259.

(21) Malkhandi, S.; Trinh, P.; Manohar, A. K.; Jayachandrababu, K. C.; Kindler, A.; Prakash, G. K. S.; Narayanan, S. R. *Journal of the Electrochemical Society*. The Electrochemical Society January 1, 2013, pp F943–F952.

(22) Poux, T.; Napolskiy, F. S.; Dintzer, T.; Kéranguéven, G.; Istomin, S. Y.; Tsirlina, G. A.; Antipov, E. V.; Savinova, E. R. *Electrocatalysis*. July 30, 2012, pp 83–92.

(23) ArimaTaka-hisa; TokuraYoshinori. *Journal of the Physical Society of Japan*. The Physical Society of Japan July 29, 1995, pp 2488–2501.

(24) Morin, F.; Wolfram, T. *Physical Review Letters*. June 1973, pp 1214–1217.

(25) Fernández, E. M.; Moses, P. G.; Toftelund, A.; Hansen, H. A.; Martínez, J. I.; Abild Pedersen, F.; Kleis, J.; Hinnemann, B.; Rossmeisl, J.; Bligaard, T.; Nørskov, J. K. *Angewandte Chemie, International Edition in English*. WILEY-VCH Verlag June 9, 2008, pp 4683–4686.

(26) Vojvodic, A.; Nørskov, J. K. *Science*. American Association for the Advancement of Science December 9, 2011, pp 1355–1356.

(27) Bajdich, M.; García-Mota, M.; Vojvodic, A.; Nørskov, J. K.; Bell, A. T. *Journal of the American Chemical Society*. American Chemical Society August 14, 2013, pp 13521–13530.

(28) Battle, P.; Cheetham, A.; Goodenough, J. *Materials Research Bulletin*. Elsevier 1979, pp 1013–1024.

(29) King, W. J.; Tseung, A. C. C. *Electrochimica Acta*. December 28, 1974, pp 493–498.

(30) Marco, J. F.; Gancedo, J. R.; Gracia, M.; Gautier, J. L.; Ríos, E. I.; Palmer, H. M.; Greaves, C.; Berry, F. J. *Journal of Materials Chemistry*. Royal Society of Chemistry 2001, pp 3087–3093.

(31) Marco, J. F.; Gancedo, J. R.; Gracia, M.; Gautier, J. L.; Rıos, E.; Berry, F. J. *Journal of Solid State Chemistry*. January 1, 2000, pp 74–81.

(32) HellerLing, N.; Prestat, M.; Gautier, J.; Koenig, J.; Poillerat, G.; Chartier, P. *Electrochimica Acta*. 1997, pp 197–202.

(33) Wu, X.; Scott, K. *International Journal of Hydrogen Energy*. March 1, 2013, pp 3123–3129.

(34) Nikolov, I.; Darkaoui, R.; Zhecheva, E.; Stoyanova, R.; Dimitrov, N.; Vitanov, T. *Journal of Electroanalytical Chemistry*. May 1997, pp 157–168.

(35) Hibbert, D. B.; Churchill, C. R. *Journal of the Chemical Society, Faraday Transactions 1: Physical Chemistry in Condensed Phases*. The Royal Society of Chemistry 1984, pp 1965–1975.

(36) Rasiyah, P.; Tseung, A. *Journal of the Electrochemical Society*. 1983, pp 365–368.

(37) Švegl, F.; Orel, B.; Grabec-Švegl, I.; Kaucic, V. 2000; Vol. 45, pp 4359–4371.

(38) Hamdani, M.; Singh, R. N.; Chartier, P. *International Journal of Electrochemical Science*. January 1, 2010, pp 556–577.

(39) Gardner, G. P.; Go, Y. B.; Robinson, D. M.; Smith, P. F.; Hadermann, J.; Abakumov, A.;

Greenblatt, M.; Dismukes, G. C. *Angewandte Chemie International Edition*. 2012, pp 1616–1619.

(40) Liu, Y.; Wang, Y.; Xu, X.; Sun, P.; Chen, T. *RSC Advances*. The Royal Society of Chemistry 2014, pp 4727–4731.

(41) Nissinen, T.; Valo, T.; Gasik, M.; Rantanen, J.; Lampinen, M. 2002; Vol. 106, pp 109–115.

(42) Nissinen, T.; Kiros, Y.; Gasik, M.; Lampinen, M. *Materials Research Bulletin*. 2004, pp 1195–1208.

(43) Wang, Y.-G.; Cheng, L.; Li, F.; Xiong, H.-M.; Xia, Y.-Y. *Chemistry of Materials*. 2007, pp 2095–2101.

(44) De Koninck, M.; Marsan, B. 2008; Vol. 53, pp 7012–7021.

(45) Cheng, F.; Shen, J.; Peng, B.; Pan, Y.; Tao, Z.; Chen, J. *Nature chemistry*. 2011, pp 79–84.

(46) De Koninck, M.; Poirier, S.-C.; Marsan, B. *Journal of the Electrochemical Society*. 2006, pp A2103–A2110.

(47) De Koninck, M.; Poirier, S.-C.; Marsan, B. *Journal of the Electrochemical Society*. April 1, 2007, pp A381–A388.

(48) Wu, X.; Scott, K. *Journal of Materials Chemistry*. 2011, pp 12344–12351.

(49) Muller, S.; Striebel, K. A.; Haas, O. 1994; Vol. 39, pp 1661–1668.

(50) Suntivich, J.; Gasteiger, H. A.; Yabuuchi, N.; Shao-Horn, Y. *Journal of the Electrochemical Society*. 2010, pp B1263–B1268.

(51) Johann Mastin; Mari-Ann Einarsrud, A.; Grande, T. *Chemistry of Materials*. American Chemical Society February 22, 2006, pp 1680–1687.

(52) Xiyong Chen; Jinsong Yu, A.; Stuart B Adler. *Chemistry of Materials*. American Chemical Society July 20, 2005, pp 4537–4546.

(53) Johann Mastin; Mari-Ann Einarsrud, A.; Grande, T. *Chemistry of Materials*. American Chemical Society November 7, 2006, pp 6047–6053.

(54) Lee, C. K.; Striebel, K. A.; McLarnon, F. R.; Cairns, E. J. *Journal of the Electrochemical Society*. January 1, 1997, pp 3801–3806.

(55) Bockris, J. O.; Otagawa, T. *Journal of Physical Chemistry*. American Chemical Society July 4, 1983, pp 2960–2971.

(56) Trasatti, S.; Petrii, O. A. *Pure and Applied Chemistry*. January 1, 1991, pp 711–734.

(57) Knop, O.; Reid, K. I. G.; Sutarno; Nakagawa, Y. *Canadian Journal of Chemistry*. NRC Research Press January 14, 1968, pp 3463–3476.

Chapter 7: Conclusions

The aim of this thesis has been to prepare mixed metal oxide based electrocatalysts for use in low-cost metal-air batteries. The introduction outlined the primary issues of expensive precious metal electrocatalysts and slow electron-kinetics of oxygen catalysis limiting commercial development of electrochemically rechargeable metal-air batteries. Chapter 3 discusses the use of $NiCo_2O_4$ as a bifunctional oxygen catalyst, with activity approaching that of platinum at a fraction of the cost. Chapter 4 details methods to incorporate the catalysts into carbon-free electrodes, avoiding the degradation and deactivation that carbon would cause. The overpotential for the oxygen evolution reaction is improved through the addition of ruthenium nanoparticles to the $NiCo_2O_4$ in chapter 5. Finally, chapter 6 discusses the modifications of spinel and perovskite catalysts that may impact the oxygen activity.

The work presented in chapter 3 has highlighted the importance of the synthesis method of the $NiCo_2O_4$ and how that impacts the catalytic activity. The mass activity of the spinel was closely linked to improvements in surface area, brought about by the co-precipitation synthesis method. This was confirmed by TEM, particle size analysis, BET and XRD, all confirming a reduction in particle size for co-precipitated samples. Rietveld refinement of the $NiCo_2O_4$ x-ray diffraction pattern confirmed a solid solution with a spinel structure. The increase in surface area promoted both the oxygen reduction and evolution reactions, with those relating to the ORR providing the greatest impact on the overall activity.

The $NiCo_2O_4$ was shown to operate by a mostly 4-electron reduction of oxygen, with only a small fraction of hydrogen peroxide generated. The proportion of hydrogen peroxide generated increased depending upon the synthesis method. The synthesis method also would define the surface area samples, such as those produced by thermal decomposition having lower surface area than samples prepared by co-precipitation. The literature has proposed the co-precipiation and thermal decomposition methods yield $NiCo_2O_4$ with different nickel and cobalt oxidation states on the surface. It is therefore likely that a hydroxy-oxide species is involved in a mechanism for the oxygen reduction as the hydrogen peroxide species is observed. The co-precipitated sample appears to provide a surface far more active in the reduction of hydrogen peroxide than when $NiCo_2O_4$ is prepared by other methods (e.g. Thermal decomposition from H_2O or methanol or using other precipitating agents). The $NiCo_2O_4$ has been demonstrated to have high electrochemical activity towards hydrogen peroxide, one possible explanation for the low concentration of hydrogen peroxide observed during the RRDE measurements.

The kinetic activity of $NiCo_2O_4$ was observed to change by the physical mixture with carbon, with the addition of carbon lowering the overpotential at higher currents. For the majority of samples,

the addition of carbon did not increase the proportion of hydrogen peroxide generated. The high activity, in terms of oxygen and hydrogen peroxide reduction, of the spinel surface is likely the cause for this behaviour. However, the addition of carbon is undesirable for the long-term stability during OER.

The development of a gas diffusion electrode is an essential component to the Powair project for a zinc-air flow battery. The spinel has been integrated into a range of gas diffusion electrodes based upon the current collector (e.g. carbon paper, Ni foam and stainless steel mesh). Carbon electrodes are capable of operating at 50 mA cm^{-2}, but appear to undergo corrosion during the OER. The results highlight similarities between the electrochemical response on the RDE and GDE, but significant differences in electrolyte concentrations and low solubility of oxygen in alkaline solution limits the comparison to qualitative analysis. In both cases the ORR operates at approximately -100 mV *vs.* Hg/HgO and the OER occurs positive of 500 mV *vs.* Hg/HgO.

Ni foam gas diffusion electrodes provide increased corrosion resistance and mechanical durability of the electrode, when compared to carbon paper in OER potentials. The Ni foam electrodes are capable of operating for 100s of cycles at 20 and 50 mA cm^{-2} in 8 M hydroxide electrolyte at 333 K.

The replacement of catalyst with nickel powder reduced the catalyst loading from ~100 mg cm^{-2} to 6 mg cm^{-2} for Ni foam electrodes. The dip-coating solution used to prepare the $NiCo_2O_4$ layer appears to alter the catalyst active area and is of interest in further developments. The spinel loading was lowered further by taking the pressed Ni foam packed with Ni powder/PTFE gas diffusion layer and brush coating with <1 mg of spinel/PTFE ink to form a catalyst layer on the electrolyte side of the air-electrode.

Using spray-coated mesh electrodes reduced the total material loading and electrode thickness, compared to the Ni foam electrodes. A stainless steel mesh structure could be reliably filled with < 20 mg cm^{-2} of powder. The packed layer may be comprised of either spinel powder of Ni powder to form a gas diffusion layer, to which a catalyst lay can be either formed by thermal decomposition (via dip-coating) or brush coating. These electrodes were stable for 10s of hours at 50 mA cm^{-2}.

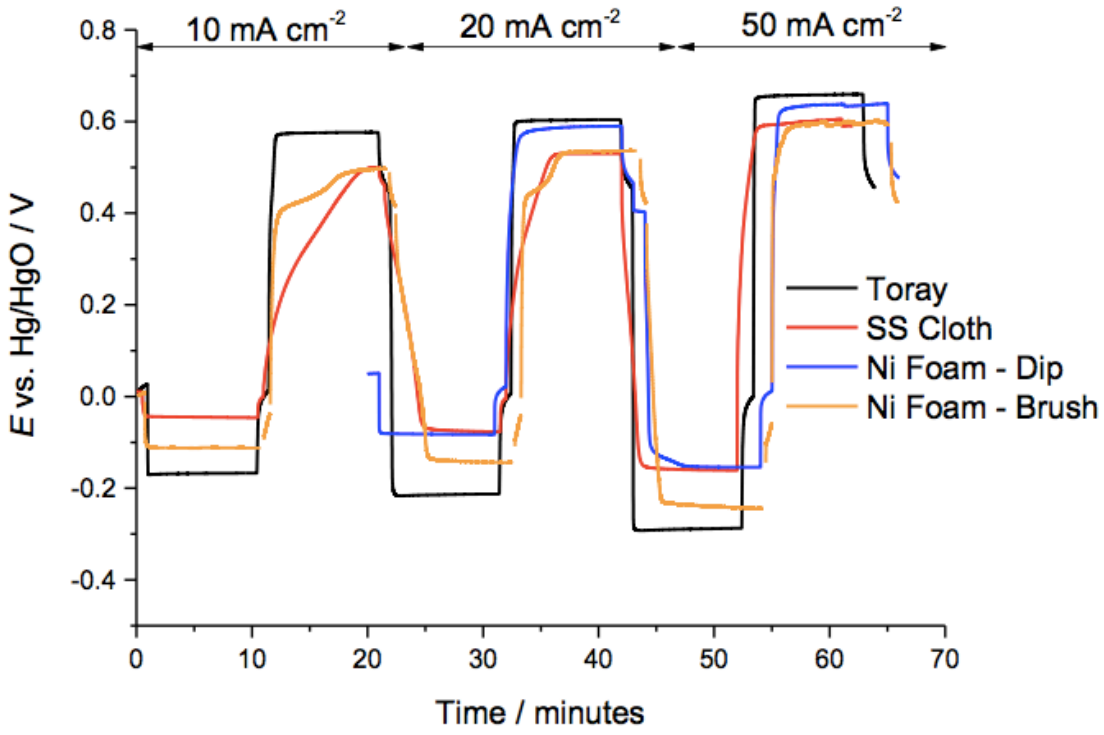

Figure 121: Comparison of galvanostatic response of GDE with $NiCo_2O_4$ catalyst layers towards the ORR and OER, in 8 M hydroxide at 333 K.

The results are promising for the implementation of low cost mixed metal oxide bi-functional electrocatalysts. The manufacturing method provides a wide array of variables with the proportion of PTFE (ideally 10:3 ratio of catalyst to PTFE) and compression force (ideally ≤ 1 kN cm^{-2}) demonstrating clear trends impacting on the electrode performance. Through the electrode development the catalyst loading was lowered from 200 mg cm^{-2} to less than 1 mg cm^{-2}, with only a small increase to the overpotential on the ORR, as shown in Figure 121. It is believed with further development of anion-exchange membranes, the performance of the electrode could be greatly improved, increasing the current densities and extending the operating times.

The catalyst can be altered by the addition of precious metal nanoparticles onto the surface of the spinel, which results in improved activity towards the OER. Ruthenium formed an oxide structure when prepared as spherical particles on the surface of the spinel. The ruthenium loading shows a clear trend, with increasing quantities of ruthenium the overpotential for the OER is lowered at 10 mA cm^{-2}.

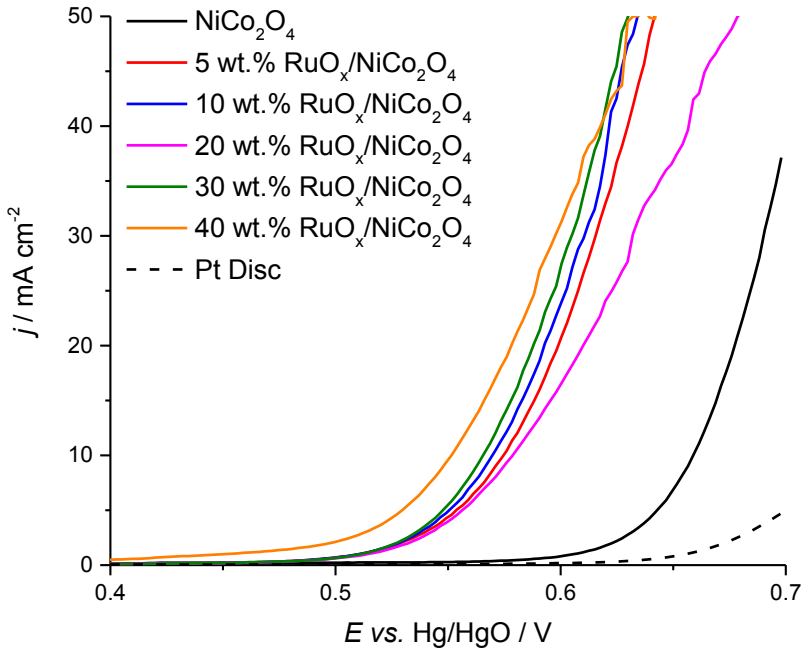

Figure 122: Increased ruthenium loading on $NiCo_2O_4$ on GC RDE in 4 M KOH.

The oxidation state for the ex-situ XANES measurement is analogous to RuO_2 from the XRD. However, the in-situ XAS measurements show the oxidation state increases from ~ 4.5+ to >6+ when the sample is exposed to the electrolyte at the OCP. The application of positive overpotential, towards the OER region, increases the ruthenium oxidation state when it is prepared on carbon and $NiCo_2O_4$. The oxidation state of the $Ru/NiCo_2O_4$ is lower than the RuO_x/C in the region of the OER, this difference may suggest an interaction with the supporting material in this case carbon and $NiCo_2O_4$, as shown in Figure 123. This may suggest the selection of supporting material can extend beyond stability, conductivity and surface area and include a method to lower to provide an electronic state change to an active species.

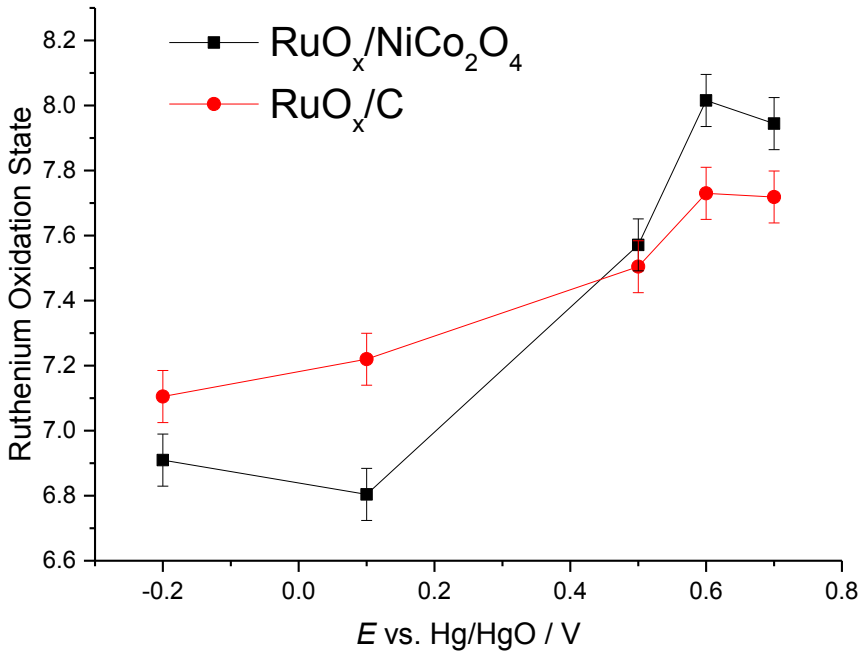

Figure 123: Ruthenium oxidation state as a function of overpotential as determined by in-situ XANES.

The need to discern trends and descriptors for the activity of mixed metal oxide electrocatalysts towards ORR and OER has been fundamental for the overall advancement of the low-cost electrical energy storage technology. Several reports have suggested the perovskites activity is linked to the electron filling level of the B-site transition metal for perovskites.[1,2] However, this trend has not been observed for the samples prepared in this work. The elemental composition of the mixed metal oxide does clearly impact the resulting catalytic activity. Applying small changes to the spinel composition provides negligible changes to the ORR and OER activity. A wider range of samples encompassing a broader range of dopants is necessary to expand on this work before further understanding can be reported. Overall the trends in mixed metal oxides are complex and hard to predict. It is possible that a monotonic trend is not possible, but equally the true activity descriptor may yet to be determined.

Although the catalyst activity is an important parameter when developing the air-electrode, the cost of the mixed metal oxides electrocatalysts has been outlined as one of the motivations for this work. Limiting the analysis to consider only the raw material costs, currently nickel is £6,977 per tonne and cobalt £19,363 per tonne,[3] in comparison ruthenium is £0.9 million and platinum £20 million per tonne,[4] therefore replacement of precious metals with transition metals represents a clear cost benefit, but is dependant on the loading as the activity on spinel is lower than that of the precious metals. The precious metals loadings in PEMFC and water electrolysers

is typically on the order of 0.1 mg cm^{-2}, therefore to achieve comparable costs with or Ni powder would require a 10,000 fold increase in loading or approximately 100 mg cm^{-2} of mixed metal oxide in the air electrode. Other costs relating to the electrode have been excluded such as ionomer, polymer membrane, gas-diffusion layer and flow field plates, as they are likely to be included in both scenarios.

Table 47: Cost analysis of spinel electrodes.

Material	Loading	Cost / £ m^{-2}
Spinel	@ 100 mg cm^{-2}	1190
Spinel	@ 8 mg cm^{-2}	80
Nickel powder	@ 100 mg cm^{-2}	20
Nickel foam	-	300
PTFE powder	@ 33 mg cm^{-2}	420
Ruthenium	@0.3 mg cm^{-2}	3

The nickel foam electrodes were packed with approximately 100 mg of either spinel or nickel powder. The use of nickel powder in place of the spinel would reduce the cost (Table 47) as it avoids the need for the more valuable cobalt (commonly employed in secondary lithium batteries). The nickel powder is unlikely to cause problems with availability as it is already commonly used in nickel battery chemistry. It is available in tonne quantities from several manufactures in china for as a little as £20 per kg, representing siginifcant cost saving compared to the $NiCo_2O_4$. The air-electrode composition and manufacturing costs are susceptible to scale of production and are likely to hinder acceptance into the wider market without significant initial investment.

In conclusion, this work has demonstrated it is possible to replace platinum and ruthenium as ORR and OER electrocatalysts with a low cost bi-functional mixed metal oxide. Carbon free gas diffusion electrodes suitable for extended operation have been shown, with low catalyst loadings. Selection of the appropriate catalyst and electrode design is a compromise between activity, stability, durability and cost. This work has highlighted possible direction for further research and commercial manufacture of electrocatalysts and electrodes for zinc-air flow batteries of the future. Future work should focus on descriptors of catalytic activity for mixed metal oxide electrocatalysts. In-situ EXAFS of the catalysts during the ORR and OER reaction would be an ideal

starting point. The gas diffusion electrodes suffered a range of failure modes, from flooding to slow degradation and mechanical failure and present a problem for long-term stability of electrodes. Investigations into optimisation the electrode structure and reducing thickness would reduce cost and electrode layer resistance, which become increasingly important when attempting to increase scale to the prototype stage. The development of stable and highly conductive anion-exchange membranes for investigations on gas diffusion electrodes would be desirable for new air electrodes, to improve mechanical stability.

7.1 References

(1) Suntivich, J.; May, K. J.; Gasteiger, H. A.; Goodenough, J. B.; Shao-Horn, Y. *Science*. 2011, pp 1383–1385.

(2) Suntivich, J.; Gasteiger, H. A.; Yabuuchi, N.; Nakanishi, H.; Goodenough, J. B.; Shao-Horn, Y. *Nature chemistry*. July 2011, pp 546–550.

(3) *London Metal Exchange http://lme.com*. August 1, 2015.

(4) *Johnson Matthey Precious Metal Prices http://platinum.matthey.com*. May 1, 2015.